UNIVERSITÀ DEGLI STUDI DI TRIESTE

UNIVERSITÀ DEGLI STUDI DI UDINE

Dottorato di Ricerca Interateneo in

Ingegneria Civile–Ambientale e Architettura

Curriculum: Strutture

Settore Scientifico Disciplinare: ICAR/09

XXXV Ciclo

PO FRIULI VENEZIA GIULIA - FONDO SOCIALE EUROPEO 2014/2020

Numerical fragility assessment and structural performance analysis of glass façade systems including post-fracture residual capacity

Dottorando
Silvana Mattei

Coordinatore
Prof. Alberto Sdegno

Supervisore di Tesi
Prof. Chiara Bedon

Co-Supervisore di Tesi
Prof. Claudio Amadio

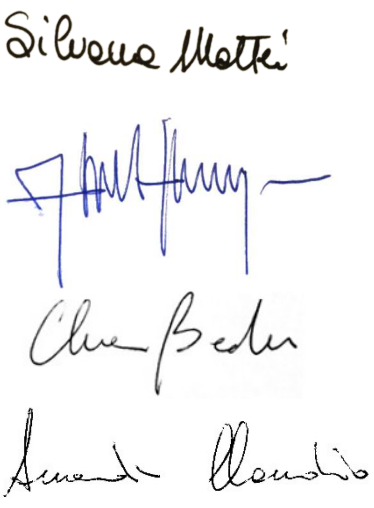

Anno Accademico 2021/2022

Istruitevi, perché avremo bisogno
di tutta la nostra intelligenza.
Agitatevi, perché avremo
bisogno di tutto il nostro entusiasmo.
Organizzatevi, perché avremo
bisogno di tutta la nostra forza.

A. Gramsci

Ringraziamenti

È per me un piacere oltre che un dovere, chiudere il mio percorso di dottorato, con i più sentiti ringraziamenti a tutti coloro che hanno contribuito a farmi giungere fino a qui.

Il contesto in cui si è svolto il mio percorso di studi è stato sicuramente atipico e per certi versi irripetibile, segnato da una pandemia in atto che se da una parte mi ha impedito di vivere appieno la vita quotidiana all'interno delle aule universitarie e dei laboratori di ricerca, dall'altra ha intensificato i rapporti interpersonali attraverso i moderni mezzi di comunicazione.

Così mi sono ritrovata a vivere ed operare con la costante presenza del mio Supervisore, che anche nei momenti più pesanti della pandemia, non mi ha mai abbandonato, spronandomi a lavorare con diligenza e assiduità. La Prof. Chiara Bedon è stata anche colei che non ha mai perso la fiducia nella certezza che il sempre "troppo poco tempo" a disposizione per portare a compimento tutte le pubblicazioni, gli articoli, le ricerche che ho effettuato in questi tre anni, potesse bastare. È evidente inoltre che la sua grande umanità si coniuga con una ancora maggiore passione e competenza per i temi che man mano mi aiutava a svolgere, segnando appieno il mio percorso attuale e futuro. A Lei dunque il mio più sentito e infinito "grazie".

Anche a tutti i colleghi che mi hanno accompagnato in questo percorso, va' la mia riconoscenza per essere riusciti ad affiancarmi con discrezione, tollerando a volte perfino i miei momenti di ansia e tensione.

Né posso dimenticare gli altri prof e tantomeno la cortese e collaborativa disponibilità del caro prof. Amadio, che fino alla fine mi ha fornito preziosi suggerimenti.

Infine la mia famiglia, sempre pronta a supportarmi e Pasquale, colui che è stato sempre presente e che non smetterò mai di ringraziare per la stima e la fiducia che ripone in me tale da alimentare ed amplificare tutte le mie energie.

È con l'animo pieno di riconoscenza e di soddisfazione che si chiude questo importante percorso che si è rivelato formativo a trecentosessanta gradi, anche oltre le mie stesse aspettative.

Table of contents

Abstract 1

Sommario 3

Introduction 6

Motivation and scope of the research 6

Framing of the activity 6

Part A: Numerical fragility assessment of glazing curtain-walls

A.1 The structural use of glass 9

A.1.1 Glass type and properties 9

A.1.2 Glass structures 12

A.1.2.1 Glass members 12

A.1.2.2 Glass floors 14

A.1.2.3 Glass shells 14

A.1.2.4 Balustrades 15

A.1.2.5 Glass curtain-wall systems 16

A.1.3 Design criteria 18

A.1.4 Reliability of structures 21

A.1.4.1 Level III methods 22

A.1.4.2 Level II methods 23

A.1.4.3 Level I methods and limit states 23

A.1.5 Design actions and strength 25

A.1.6 References 27

A.2 Seismic performance of façades 30

A.2.1 Seismic design 31

A.2.2 Current regulations 33

A.2.2.1 European Standard: Eurocode 8 34

A.2.2.2 National Standard: Norme Tecniche per le Costruzioni 2018 35

A.2.2.3 American Standard: FEMA 450 36

A.2.2.4 Japanese Standard: JASS14 39

A.2.2.5 New Zealand Standards 40
A.2.3 References 43
A.3 Seismic risk 45
A.3.1 Vulnerability assessment 47
A.3.1.1 Fragility assessment 51
A.3.2 Cloud method for fragility derivation 52
A.3.2.1 Record selection and fragility parameters definition 54
A.3.3 References 56
A.4 Finite Element Modelling 59
A.4.1 Selected glass configurations 59
A.4.2 Numerical code: ABAQUS/CAE 62
A.4.3 Case study 1: Glass panel 64
A.4.3.1 Geometries of case-studies 64
A.4.3.2 Material characteristics 66
A.4.3.3 Boundary conditions and interactions 68
A.4.4 Case study 2: Full-scale application 70
A.4.4.1 Primary steel frame 70
A.4.4.2 Geometric and material properties 73
A.4.5 References 76
A.5 Discussion on the results 78
A.5.1 Description of numerical structural response 78
A.5.1.1 Full-scale application (CS#2) 78
A.5.1.2 Glass panels (CS#1) 82
A.5.2 Component fragility derivation 87
A.5.3 References 96

Part B: Experimental and numerical investigations on post-failure behaviour of glass fitted with ASFs

B.1 The use of ASFs in architectural glass 97
B.1.1 ASF composition 99
B.1.1.1 Polyethylene terephthalate (PET) tape 100
B.1.1.2 Pressure sensitive adhesive (PSA) 101

B.1.2 References 102
B.2 Experimental program 104
B.2.1 Static characterization 104
B.2.1.1 Tensile tests 104
B.2.1.2 Peel Tests 105
B.2.1.3 Three-Point bending tests 107
B.2.2 Material investigation of PET-film 109
B.2.2.1 Differential Scanning Calorimetry 110
B.2.2.2 Fourier Transform Infrared spectroscopy 110
B.2.3 Accelerated ageing protocols 111
B.2.4 References 113
B.3 Adhesion: theoretical approach 114
B.3.1 Fracture mechanics basics applied to peel test 114
B.3.2 Application of the classic approach to the specific peel test configuration 117
B.3.3 References 120
B.4 Finite Element Modelling 121
B.4.1 Geometric and material proprieties 121
B.4.1.1 Peel Test simulations 121
B.4.1.2 Three-Point bending test simulations 122
B.4.2 Cohesive Zone Model (CZM) 124
B.4.3 References 127
B.5 Discussion on the results 128
B.5.1 Film results 128
B.5.1.1 Material properties 128
B.5.1.2 Mechanical properties of PET: tensile test 130
B.5.1.3 Adhesion properties of PSA: peel test 132
B.5.2 ASF fitted glass results 145
B.5.3 References 149
Conclusions 150
Nomenclature 153
List of Figures 156

Part A: Numerical fragility assessment of glazing curtain-walls 156
Part B: Experimental and numerical investigations on post-failure behaviour of glass fitted with ASFs 158
Appendix A 160
List of Tables 162
Part A: Numerical fragility assessment of glazing curtain-walls 162
Scientific publications 163
Scientific papers 163
Conference papers 164
Appendix A i

Abstract

In modern civil engineering the ability to adopt models for the assessment of the seismic vulnerability of structures, especially for structures consisting of materials whose design is still characterized by a huge amount of uncertainties, is an important means for the assessment of seismic risk and therefore for the mitigation of losses due to stochastic events.

Glass as a building material has always been an integral part of structures for aesthetic/functional purposes only such as to bring light to environments or to provide ventilation to them. In recent years, due to the development of new technologies for the production of glass elements, civil engineering has given space to the construction of structural works consisting entirely of glass. Until a few decades ago, it was impossible to think of entrusting brittle elements the load-bearing capacity, therefore it only served as a frame to the design.

However, although today there is greater awareness of the use of this material, the design criteria for these types of construction are still lacking. And in particular, there is no way in the calculation codes of the whole world to predict the inter-storey displacement that can cause the achievement of a specific damage state of glass systems. Thus, it is impossible to define the structural damage thresholds for particular limit states. The main objective of this thesis is therefore to provide means and solutions related to increasing the reliability of these structures, and in particular for façade systems against seismic action.

In this thesis, the first results are presented in terms of fragility curves, built with a numerical approach on glass panels and overall buildings obtained by means of post-processing cloud analysis results, using non-scaled seismic records on FE models (built in Abaqus/CAE) inspired by scientific literature, providing a comparison with an analytical and experimental approach. The Cloud analysis is simpler than the method characterized by incremental dynamic analysis (IDA) because the latter has climbed to the collapse of the structure and therefore burdens a greater computational effort. In particular, the considered models were chosen because representing a wide range of existing solutions in the context of glass constructions, exposing the results for several types of structural glass (monolithic and laminated) and various configurations (in terms of glass-to-frame clearance). In detail, the results obtained from the non-linear analyses were analysed using linear regression analyses, through the application of a Maximum Likelihood Estimate, assuming a constant standard deviation.

Finally, this work focuses on some peculiar issues in using PET films on glass panels. In the structural field, they are mainly used to reduce the risks related to the fragmentation of glass following sudden and exceptional events such as seismic events; explosions, and impacts. In particular, the material characterization of the commercial multilayer product used in the conducted experimental campaign and the following

study of the influence that these safety sheets offer on the bending mechanical response of glass, are addressed by combining the experimental results with the calibration analyses carried out by a three-dimensional model in a FE software (such as Abaqus/CAE). This last step allows stating the adhesion parameters, such as the fracture energy, G, using a typical cohesive zone model (CZM) taking into account the influence of displacement-rate and ageing protocols.

Keywords: Seismic design; Structural glass; Glazing Curtain-Walls; Fragility curves; Engineering Demand Parameters (EDPs); Finite Element (FE) numerical models; Cloud analysis; Anti-shatter films; Cohesive zone model (CZM); Accelerated ageing.

Sommario

Nell'ingegneria moderna la capacità di poter adottare modelli per la valutazione della vulnerabilità sismica delle strutture, specie che per le strutture costituite da materiali la cui progettazione ad oggi è ancora incerta, risulta un importante mezzo per la valutazione del rischio sismico e quindi per la mitigazione delle perdite dovute ad eventi di tipo stocastico.

Il vetro come materiale da costruzione, è da sempre parte integrante delle strutture per scopi unicamente estetico/funzionali, per portare luce agli ambienti o per fornire aerazione agli stessi. Negli ultimi anni, a causa dello sviluppo di nuove tecnologie per la realizzazione di elementi in vetro, l'ingegneria civile ha dato spazio alla costruzione di opere strutturali costituite interamente in vetro. Fino a qualche decennio fa infatti era impossibile pensare di affidare ad un elemento fragile come il vetro, la capacità portante, pertanto esso forniva solo da cornice alla progettazione.

Tuttavia, sebbene ad oggi si abbia maggiore consapevolezza sull'uso di questo materiale, risultano ancora carenti i criteri di progettazione relativi a tali tipologie costruttive. Ed in particolare non esiste, nei codici di calcolo di tutto il mondo, un modo per prevedere lo spostamento di interpiano che potrebbe causare il raggiungimento di uno specifico stato di danno per sistemi vetrati. Pertanto si riscontra l'impossibilità di definire le soglie di danneggiamento strutturale per particolari stati limite. L'obiettivo principale di questo lavoro di tesi è quindi quello di fornire mezzi e soluzioni legati ad incrementare l'affidabilità di tali strutture, ed in particolare per sistemi di facciata nei confronti dell'azione sismica.

In questa tesi, si espongono i primi risultati, in termini di curve di fragilità, costruite con un approccio di tipo numerico su pannelli in vetro ed edifici completi ottenuti per mezzo dei risultati di un'analisi Cloud, utilizzando record sismici non scalati, su modelli agli elementi finiti (costruiti in Abaqus/CAE) ispirati alla letteratura scientifica e fornendo un confronto con un approccio analitico e sperimentale. L'analisi Cloud risulta più semplice del metodo caratterizzato dall'analisi dinamica incrementale (IDA) poiché quest'ultima necessariamente deve raggiungere il collasso della struttura scalando gli accelerogrammi di input e pertanto grava di uno sforzo computazionale maggiore. In particolare, i modelli considerati sono stati scelti perché rappresentativi di una vasta gamma di soluzioni esistenti nel contesto delle costruzioni in vetro, esponendo i risultati per più tipologie di vetro strutturale (monolitico e laminato) e varie configurazioni (in termini di glass-to-frame clearance). Nel dettaglio i risultati ottenuti dalle analisi non lineari, sono stati post-processati secondo una Stima di Massima Verosimiglianza utilizzando una regressione lineare adottando un metodo semplificato con deviazione standard costante.

Sommario

In ultimo, tale lavoro si concentra sul tema relativo all'uso delle pellicole in PET su pannelli in vetro. In ambito strutturale sono utilizzate principalmente per ridurre i rischi connessi alla frammentazione del vetro in seguito ad eventi di tipo improvviso ed eccezionale come: eventi sismici; esplosioni ed impatti. In particolare, la caratterizzazione del prodotto multistrato commerciale utilizzato nella campagna sperimentale e il seguente studio sull'influenza che offrono sulla risposta meccanica a flessione del vetro, sono affrontati combinando i risultati sperimentali con le analisi di calibrazione effettuate con un modello tridimensionale in Abaqus. Quest'ultimo passaggio consente di indicare i parametri di adesione, come l'energia di frattura (G), utilizzando un tipico modello di zona coesiva (CZM) tenendo conto dell'influenza delle velocità di applicazione del carico e dei protocolli di invecchiamento accelerato.

Parole chiave: Progettazione sismica; Vetro strutturale; Facciate continue in vetro; Curve di fragilità; Parametri di domanda ingegneristica (EDP); Modelli numerici agli elementi finiti (FEM); Analisi Cloud; Pellicole di sicurezza; Cohesive zone model (CZM); Invecchiamento accelerato.

Introduction

Motivation and scope of the research

The devastating effects generated by earthquakes in various parts of the world in recent decades, has increased the attention towards seismic engineering. This branch of structural engineering is concerned with the study of the behaviour of structures subject to a telluric event and develops design methods aimed at avoiding collapse or limiting the damage to buildings.

The aim of this PhD dissertation can be summarized in two objectives which are given below:

- Investigation of seismic behaviour of glazing curtain wall and derivation of fragility functions by means of numerical method
- Fundamental knowledge on adhesion parameters of Anti Shatter Films (ASFs) and quantification of actual benefit in ensuring post-failure behaviour of fitted glass.

In brief, the herein reported research activity has been concerned with Finite Element (FE) numerical analyses of glass mechanical behaviour. Overall, the Ph.D. activities have been developed with a focus on two major aspects of technical interest. The first examined issue is related to glass performance and capacity under dynamic accidental loads (such as seismic action). In parallel, a key issue of uncertain quantification is represented by the measure and prediction of its post-fracture capacity (with a focus on bending performance), especially when glass elements are retrofitted by anti-shatter films. In the first case, major efforts took advantage of literature background documents and FE numerical simulations. In the second case, experimental activities were carried out and extended by FE computations.

Framing of the activity

In the present section, an outline of the developed research project is exposed. In addition, a primary distinction should be provided: Part A and Part B deal with two topics rhetorically distant but held together by the primary purpose of this study, namely the vulnerability analysis of glazed systems investigating the reliability in choosing Anti-Shatter Films as solution albeit temporary.

Each part is organized into five separate main chapters.

Chapter A.1 presents the background on the use of structural glass in civil constructions, investigating the existing glazing systems and their main issues to be addressed, pointing out its innovative features as building material and the subsequent little-broad knowledge about mechanical behaviour, especially in post-failure field, due

to the scepticism in entrusting primary tasks to this brittle material. Moreover, the structural reliability and the methodologies used for its assessment are discussed together with the basic principles of design practice with regards to glass structures in different forms.

Chapter A.2 focuses on seismic performance of glazing façades, highlighting the motivations at the base of this study are expressed and an overview of the worldwide standing regulations. While in Chapter A.3, an overall review of existing fragility methods, available in literature, is carried out (i.e., empirical; analytical; expert judgment elicitation, and hybrid approaches) and special mention is given to the used Cloud methodologies.

In Chapter A.4, the selected case-studies under consideration and the main characteristics of the finite element modelling phase are described in terms of problem geometry, model discretization and material parameters adopted. Details are also given on the main features of the calculation platform used in this work (the FE code ABAQUS Standard v.6.12) with particular attention to the integration procedures of the available dynamic field equilibrium equations.

Moreover, a brief overview of the existing fragility functions, derived by analytical and empirical approaches, is introduced in order to justify the selection of glazing systems analysed.

Finally, in Chapter A.5 the results of the analyses are presented, in the form of comparisons, in terms of the history of accelerations, displacements and stresses on the structural elements and tensile and deformative paths at various points of the domain.

Part B concerns the investigation of structural performance of safety films as a useful and low-cost retrofitting solution for improving the reliability of glazing systems. The addressed numerical calibration

Chapter B.1 introduces the wide field of application of protective films, providing a geometric description of the one used in this treatment and focusing on the essential aspects of the main properties of PET (= tape's material) and PSA (= adhesive layer).

Chapter B.2 presents the experimental methods used for the characterization of materials and their chemical and mechanical properties and Chapter B.3 offers a comprehensive analysis of the theoretical framework underlying the study of the adhesion phenomenon.

In Chapter B.4, after introducing some basic principles of fracture mechanics, it is discussed its application to the specific case study by discussing the formulations that will then be calibrated on the experimental results through the use of a Finite Element Software (Abaqus/CAE). Finally, Chapter B.5 contains the main outputs.

The work ends with a final chapter, in which a summary of the main conclusions and further additional insights to inform future development and opportunities for innovation are presented and discussed.

Part A: Numerical fragility assessment of glazing curtain-walls

A.1 The structural use of glass

In the design of a building and its different components (Haldimann 2006, Haldimann et al. 2008, UNI 2022), the architectural evolution has seen the glass cover progressively different roles, although its main role has always been to repair and protect from the external actions and ensure the light supply towards the interior of the rooms. However, the potentialities which permit the widespread use of glass in the construction field concern also sustainability, from the manufacturing process to recycling. Generally, glass has always been chosen in the construction field to use natural sunlight to brighten up indoor spaces, or – as the architect F. L. Wright intended - to provide the harmony of form and function in a building and to ensure that the external context is fully integrated with the built environment. Several architectural examples, once considered utopian or impossible, have been produced from the intensive research and technological progress of the manufacturing industries. Although the visual, acoustic and thermal comfort are not negligible, the mechanical performance is an issue particularly sensitive due to its intrinsic brittleness. As opposed to other materials, a knowledgeable approach to design is needed to achieve levels of reliability similar to those obtained in the case of more traditional structures, such as steel or reinforced concrete. Even though, unlike both, glass doesn't have a plastic phase or a plastic adaptation capacity.

A.1.1 Glass type and properties

Among the different glass types available, depending on the manufacturing process, the main references are float glass and cast glass, which appear in the construction field in two different primary compositions (soda-lime silicate glass and borosilicate glass) (Cagnacci et al. 2010).

Soda-lime silicate glass is a solid material consisting of silica (SiO_2), in the form of sand, and soda ash (Na_2CO_3) to which are added other substances in order to improve their chemical and mechanical characteristics and the workability both at the time of its production in flat glass, both in subsequent machining. Glass with a sodium-calcium

composition is also used for melded and ornamental glass, structural glass and U-shaped glass, as well as in the case of plates having a considerable thickness.

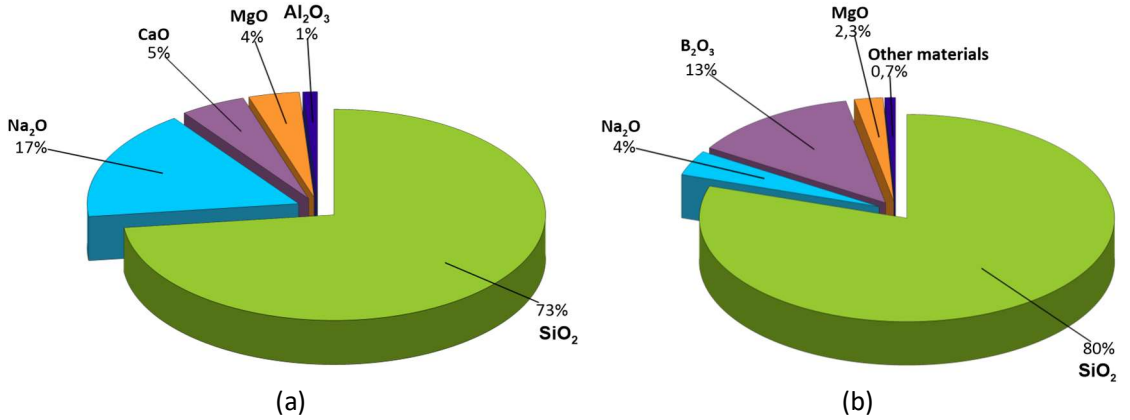

Figure A.1-1 Chemical composition of soda-lime glass and borosilicate glass (Schittich et al. 2007; GRANTA 2014)

Nowadays, technological evolution concerns especially borosilicate glass. In fact, despite being less low-cost that the float one, the cast glass is widely used in the building industry, particularly when it comes to structural elements in the form of tubes, by coupling a modest thermal expansion to greater resistance.

As far as the glass curtain walls are concerned, it is of paramount importance to direct attention to the float glass process. According to Pilkington (Pilkington 1969), who developed this process in 1959, glass is obtained by continuous casting and flotation in a metal tin bath controlled atmosphere. In summary, there are three consecutive chambers in which the glass is melted (~1500°C) and refined, floated, and then annealed to relieve stresses, otherwise responsible for breaking. This last phase is necessary because during the critical cooling step the onset of slight tension and compression structural stresses is unavoidable, as a result of differential cooling rates on the two surfaces of the glass plate.

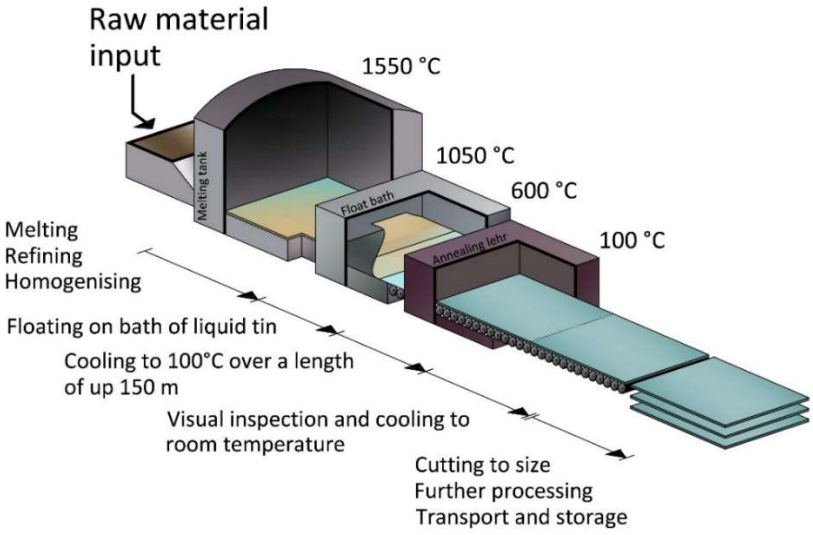

Figure A.1-2 Schematic image of a float line (figure © S. Mattei)

A.1 The structural use of glass

The density of the glass varies according to its composition: about 2.5 g/cm^3, or 2.15 g/cm^3 for borosilicate glasses and, on the contrary, even double for those with lead oxide. Density can be a valuable means of controlling glass homogeneity.

Among the physical properties of glass, transparency is certainly peculiar and primarily directs its use in buildings by providing specific architectural qualities. Moreover, the glass has a fairly high hardness, of the order of about 6 on the Mohs scale (resistance to nicking) and between 400 and 500 on the Knoop scale of hardness. Nevertheless, various minerals, for example, quartz, orthoclase and steel, may affect the glass.

Generally, the glasses used for construction are annealed, heat-strengthened (partially tempered), toughened (fully tempered) and laminated (Ledbetter et al. 2015; CNR-DT210 2013). However, it is important to point out that annealing does not lead to a strengthening of the mechanical strength as in the other cases mentioned before.

Through tempering, to the glass is given a state of surface pre-stressing that provides a greater strength because the fracture propagation of the inevitable surface defects isn't allowed. These micro-fractures, inclusions and scratches have, at the boundary, a state of compression effort unfavourable to the opening of the crack and its propagation. In particular, these inclusions are defects equivalent to micro-fracturing, such as air bubbles; in tempered glass, heat treatment reduces these, and accuracy in the production process reduces inclusions. In the core of the plate, instead, pull forces are generated and these induced compressive and tensile forces must be distributed in such a way as to be in reciprocal equilibrium. For this reason, tempered glass is also referred to as "safety glass", since, in case of breakage, the glass breaks down into small splinters with no sharp edges. The tempering process is basically of two types, thermal and chemical. The former is far more important in structural applications. In fact, the tensile strength in this type of glass is of the order of 200-250 MPa, which is two or three times higher than that of simply annealed glass. As an indication, in a plate subject to uniform pressure (i.e., wind pressure) the tempered glass is about four times stiffer than ordinary glass; moreover, it has an impact resistance of about doubled. The chemical tempering process, instead, involves effects only in thicknesses of a few hundredths of a millimetre below the surface of the glass. Thus, chemically hardened glass is more sensitive to surface damage.

Table A.1-1 Main physical properties of soda-lime silicate and borosilicate glass

Property	Units	Soda-lime silicate glass	Borosilicate glass
Density	kg/m^3	2250 - 2750	
Thermal resistivity	m°C/W	0.909 – 1.11	0.769 – 0.909
Thermal expansion coefficient	µm/(mK)	9.1 – 9.5	3.2 - 4
Tensile strength	MPa	30 – 35	22 - 32
Compressive strength	MPa	300 - 420	260 - 350
Young's Modulus	GPa	68 – 72	61 – 64

Hardness	Kg/mm^2	440 – 485	84 – 92
Cost	€/kg	1160 – 1370	3430 – 5150

Finally, in order to remedy the typical fragility of glass, in addition to the mechanical strengthening processes mentioned above, the use of multi-layered sections should be highlighted in the case of the structural façades and the supporting elements of many contemporary structures entirely glazed. The laminated glass consists of a panel composed of, at least, two sheets of glass connected by a polymeric interlayer. The most commonly used material is Polyvinyl butyral (PVB) with transparency comparable to vitreous, a contained thickness up to about 1.5 mm or higher for toughened glass plates, or many other materials can be employed to enhance the stiffness of the section (Chaszar 2003). The properties of laminated glass, especially the fracture pattern, are based on several interlinked factors: type of glass, the thickness of individual plates, surface conditions of glass and edges, panel geometry and nature of the load, overall thickness, boundary conditions and type of support structure.

Compared to tempered glass, the laminated one absorbs much higher impact energy, remaining in its home, and preventing penetration. However, impact resistance is directly related to the adhesion of interlayer to glass, as the deterioration of the adhesion over time seriously compromises the expected impact safety performance. The location of the crack and the adhesion of the fragments to the plastic layer, limit consequential damage and dangers. These features explain the wide field of application, being the best guarantee of safety that allows structural applications, as well as horizontal and vertical closure, parapet elements, entire staircases, and elevator cages.

A.1.2 Glass structures

A.1.2.1 Glass members

The use of glass for the realization of load-bearing structures of a certain consistency is still limited to a few daring realizations (Carrè et al. 1999, Biolzi et al. 2016); the main difficulties, besides the considerable costs, are linked to the limited size of semi-finished products and the consequences of the sudden failure of the glass on the stability of the structural system.

A glass plate placed vertically with loads applied parallel to the average plane (see Fig. A.1-3) can act as a beam. In glass beams the stress can be calculated with the plate theory or, in case of a high L/H ratio, with the beam theory: however, the bending around the strong axis implies tensile stress along the lower edge. Therefore, the factor determining the effective resistance to bending of the beam is represented by the type of processing carried out on the bottom edge of the slabs, which affects the distribution of micro defects.

A.1 The structural use of glass

Beam performance can be improved by assembling multiple glass sheets, which not only have more resistant material in the tensile stress zone but also have greater stiffness to transverse bending and torsion than monolithic ones.

Figure A.1-3 Connection detail between glass beams[1]

As for the glass columns (see Fig. A.1-4), generally compressed, the glass material would seem to be able to manifest its maximum application, provided that end constraints are created that ensure the complete absence of parasitic bending moments (Bagger et al. 2009). The first difficulty consists of the limited dimensions of the plates that will form the pillar; the glass sheets produced by the float process have a maximum thickness of 19 mm, and only in special cases can be up to 25 mm. Therefore, wanting to limit the slenderness to 1/50 (L/H), it will be necessary to compose the various plates together to obtain sections of acceptable inertia. Although the glass has good compressive strength, the brittle break triggered by possible bending stresses makes the structural reliability of the glass pillars problematic. A redundant structural system can be used to overcome this problem. Another "fail safe" system consists of the use of multi-layer elements, in which there are layers that can replace the load-bearing layer in case of breakage.

Figure A.1-4 Primary glass frames.

[1] Figure reproduced with permission from (Saji et al. 2018) under the terms and conditions of CC-BY license agreement

A.1.2.2 Glass floors

According to the theory of elasticity, a "plate" is considered a solid with the development of two dimensions prevailing over the third (small thickness plate) loaded perpendicularly to its middle plane. This is the prevailing condition of the use of glass sheets with the function of separation (glazing wall) or covering (roofs). If the glass plate is used as a walking element (decks, steps, walkable pavements) the perception of the vertical displacement due to the application of its weight can further amplify the possible discomfort given by a transparent walking surface (Bedon 2018, Royer et al. 2007). Given that the pedestrian slabs are always multi-layered, if the layers were simply superimposed and independent, each of them would be allocated its own part of the load, according to its flexural stiffness. Thus, the choice of properties of the intermediate layer of adhesion is therefore very important, since a very high rigidity is favourable for the bending behaviour, while in case of breakage, it is of great advantage to have a high viscosity, which allows the damaged plates to remain integral, offering a residual strength and avoiding the detachment of fragments in a perspective of post-failure behaviour in order to save people from falling through the fractured glass plate. Traditionally, with regard to the fixing of the slabs to the underlying structure, the most effective and simple one happens by contact along the entire edge of the slab, with more or less elastic support strips, depending on the material chosen (hardwood, EPDM, neoprene, aluminium, silicone or other). Lateral displacement is prevented by elastic spacers placed along the side edges. Finally, care must be taken to ensure the flatness of the supports and to control the deformations of the support structure, so that no peaks of tension arise. A point fixing is also possible, but the local stresses induced by the concentred constraint reactions lead to the slab being assigned high thicknesses.

A.1.2.3 Glass shells

The shell structure is one of the most efficient load-carrying structures that nature ever invented. It is found in many of natural creations because the shape is made to protect and resist any external action. Glass shell has been used for many years to bring light into buildings, whose glass plates were hence connected structurally thanks to metal frames. Concerning shape, shell structures cover a wide range of applications, from simple geodesic domes to modern freeform architecture. Jorg Schlaich's contribution in this field has allowed this technology to take a great evolutionary step (Holgate 1998). The German engineer has developed and manufactured reticular domes and reticular shells, with articulated knots and double diagonal with thin cables. The high degree of standardization and ease of assembly have led to cost-effective solutions for geometrically complex structures, while the slender sections of the rods and cables have made them extremely transparent.

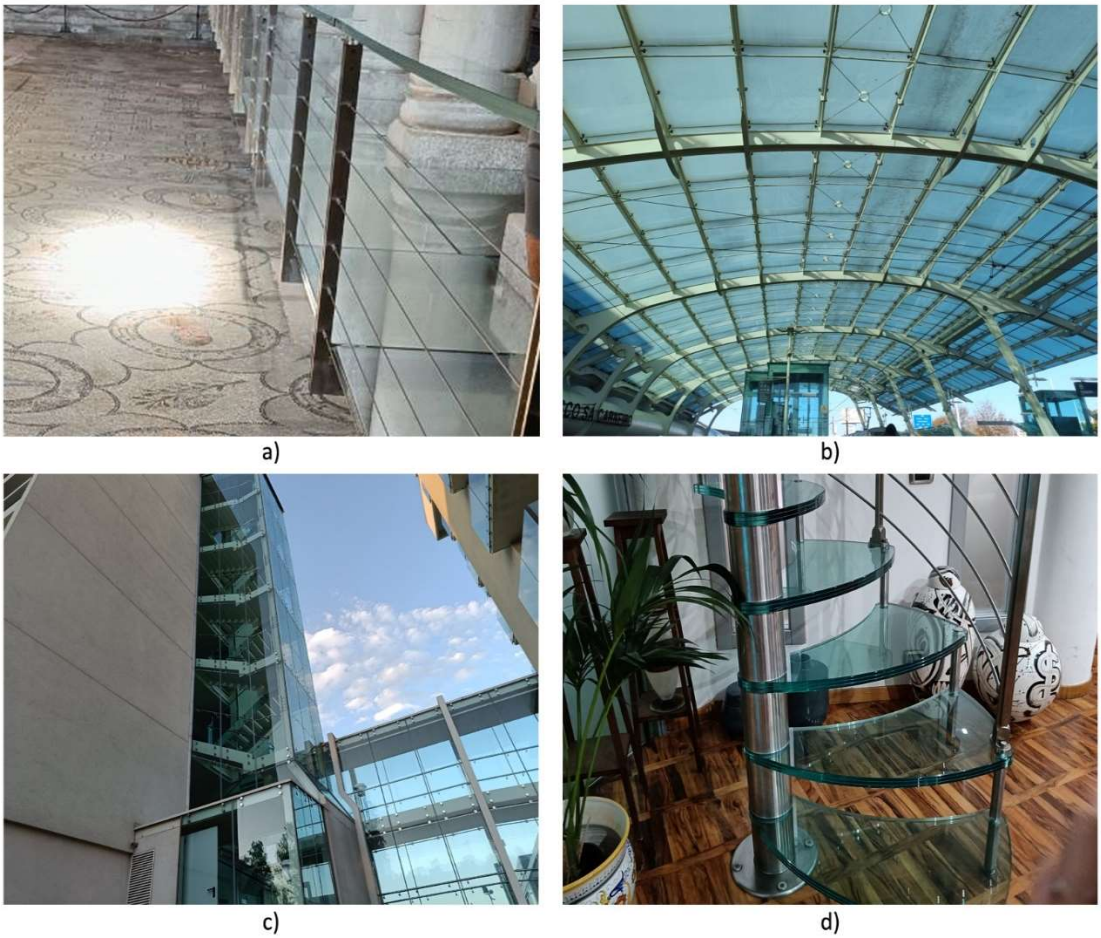

Figure A.1-5 Glass shells – (a) glass pedestrian walkway in Basilica of Aquileia, Italy; (b) glass roof at metropolitan train-station 'Aeroporto do Oporto: Francisco Sá Carneiro', Portugal; (c) glass stair tower in hotel facility in Marotta Italy; (d) glass-steel stair in residential building in Sant'Agata De' Goti, Italy (photos © S. Mattei)

A.1.2.4 Balustrades

A glass balustrade is a building component with the aim of preventing people from falling off balconies, stairways and other places where there's a significant height difference (Hoier et al. 2019). The usual scheme is a freestanding glass cantilevered from the base or supported with four, three or two-edge glazing. Typically, safety glass is used to reduce the likelihood of breakage on impact but the thickness and the compositions of the laminates vary as a function of the manufacture. According to the building codes, this component is considered a secondary element that does not take any loads from the overall structure. Consideration should also be given to the potential risks for pedestrians and for glass to fall from height after breakage. In fact, depending on the application, a classification based on different risks and consequences is addressed in the design stage. Generally, all the components included in a glass balustrade can be categorized as either Class 1 or 2 (EN 1990).

a) b)

Figure A.1-6 Two practical example of glass balustrades in residential buildings, (photos © S. Mattei)

A.1.2.5 Glass curtain-wall systems

Among the main applications of glass architecture, glazed façades are the element of the larger building envelope system, with more or less extensive geometries and typologies.

In façade systems, five essential functional elements can be distinguished (EN 13830):

• the basic element, that is the simple glass plate or the insulating glass;

• the supporting structure, or the structure on which the glass sheets and other glass elements are fixed on, and which all the loads are transmitted to;

• the fixing, that is the system that allows the transmission of the loads from the plate to the main frame;

• the joint, or the set of those elements of correlation and tightness;

• the “setting blocks”, which are two elements under the glass plate with the aim of supporting the weight of the panel in order to reduce the sealant joint size.

The first generation of façades, which appeared in modern buildings during the twentieth century, was generally structured on the so-called "mullions and transoms" system and on the first concepts of prefabrication in building modules. The latter way is especially helpful in order to make the assembly process easier and faster.

Today, the variety of solutions is massive and differs according to the construction and aesthetic needs as their presence is highly noticeable by an eventual observer. This tends to let them become the real protagonists of the analysed architecture, putting the prominent glass surface on the background. The last generation of glazed façades are those integrated into the air conditioning circuit and the photovoltaic ones, thanks to their characteristics.

In brief, Curtain wall systems are grouped into stick-built and unitized. However, the latter type is the most common one, thanks to its high feasibility, as this system lacks the need of any scaffolding during the installation phase on the site.. Despite higher

costs, the pre-assembly procedure in the factory makes positioning easier. On the other hand, stick-built systems use a series of horizontal transoms and vertical mullion frame members which are assembled and glazed on site.

In addition to the first distinction i just explained, the types of structural glass-steel façades built in recent year can also be divided in two large groups, whose difference depends on the condition their glass sheets are laid in. according to this new division, they can either be "slab-independent" or "slab-dependent" façades.

The first group allows the creation of larger glass surfaces where each plate is connected to the supporting structure by at least four points, thanks to specific fixing systems. The loads are then transferred to them, due to their own weight and the external stresses. This happens because said leads flow through glass as well, which is an integral part of the whole structure.

Breakage caused by high wind pressures is not a common occurrence, although this should be considered at the design stage. In the event of accidental breakage of one of the plates, there would be no significant impact on the stability of the overall system.

Since about 1960, the introduction of synthetic gaskets has made it possible to directly glue the glass plate to the frame with silicone adhesives. The definition of a "structural curtain-wall" emphasizes the load-bearing task of glass sheets, in which the silocone no longer serves only as a sealant against atmospheric agents, but also supports part of the load of the plate and transmits the thrust and suction of the wind from the glass to the metal curtain that is hung on the façade or fixed in another mechanical way.

From the static point of view, in addition to their own weight, the glass panels also have to carry the one coming from the pressure of the wind, as well as the one provoked by the slabs. Speaking of this, it is also important to consider that the said wind pressure can be assumed to be evenly distributed on the whole glass surface. The glass panel behaves like a plate, but due to the holes drilled to house the anchoring elements, the ultimate collapse load is strongly influenced by the distance of the hole from the end of the plate. This is a factor that has to be carefully considered in the phase concerning the design, using the help of finite element simulations, able to highlight the areas of the greatest concentration of effort.

In order to reduce the points of stress, it is advisable to arrange special joints, known as "rotules", which, thanks to a spherical connection positioned on the glass top or with elastic washers, allow the free deformation of the sheet that is inflexed by wind pressure.

Being the seismic action the main topic of this thesis, it will be now considered thoroughly. In this regard, a façade is generally considered a non-structural element according to worldwide seismic codes (EN 1998-1; NTC 2018; FEMA 450; ASCE 2013; JASS 14). Obviously, the seismic response of the building depends also on the secondary structure (non-structural elements, such as infill) due to the transfer of the stresses from structural elements to the secondary ones, implying the possibility of serious damage to the latter although less significant than those acting on the load-bearing structure. It is

worth remarking that a non-structural element, by its nature, is not required for the building to resist because its collapse doesn't affect the load-bearing capacity of the whole system. The main issue is the correlated danger to people's lives due to the glass shattering, either outside or inside the building, in addition to the fact that it could affect the behaviour of the supporting structure or make the building unusable for a long time.

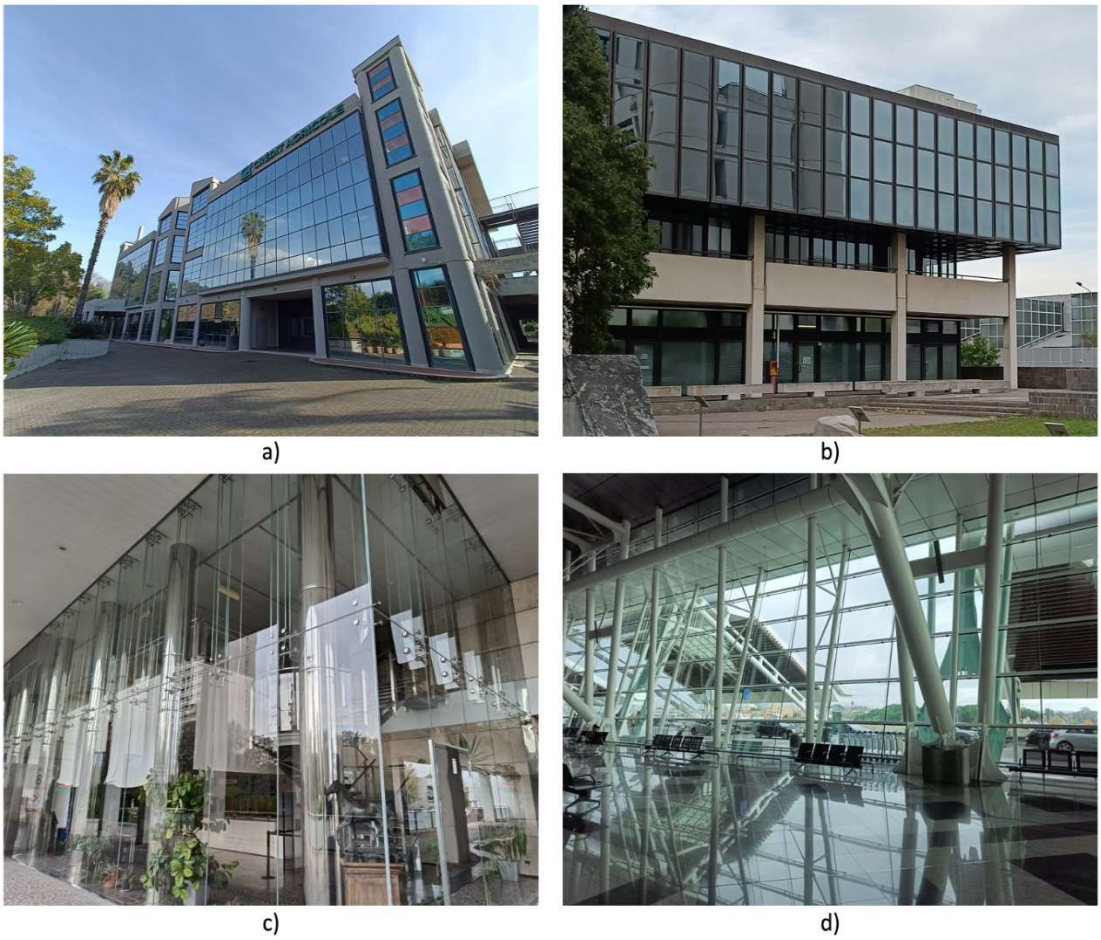

Figure A.1-7 Glass curtain-walls – (a) Unitized system , (b) Mullions and transom system; (c) and (d) Point-supported systems (photos © S. Mattei)

A.1.3 Design criteria

As previously mentioned, there are currently no specific Eurocodes for glass (Feldmann, et al., 2014). However, when glass structures are designed, the philosophy follows the basic concepts of the existing Eurocodes that are applicable to every building structure (CNR-DT210 2013).

The limitation of the use of glass as a structural material came from considering it "too brittle" to be able to safely carry out load-bearing functions. Another limitation (e.g. for beams and columns) was represented until a few years ago by the small size of the manufactured plates. However, an issue related to the connection that introduce localized concentrated stresses is still endured. The design criterion in the presence of possible sudden breakages is the "fail-safe approach", used to predict, already at the

design stage, that some elements may collapse, without affecting the overall stability of the structural system. Three key concepts of this approach are:

- hierarchy;
- robustness;
- redundancy.

The first consists of establishing a function for each of the elements that compose the structure, fixing a hierarchical order of importance, in order to identify those secondary elements as "expendable". The design modelled after the hierarchy is based on the criterion of sizing the structural elements not according to the real transmitted loads but according to the resistance of the connected elements. For example, in the case of a glass mullion used as a fin, the possible collapse of the façade panels has to precede the collapse of the fin itself.

The primary elements, however, must always be well protected and functioning, and indeed in greater numbers than strictly necessary (redundancy). Structural redundancy arises from the structure's ability to redistribute forces within it in a way that the collapse of part of a section, a structural element, or a portion of the structure does not cause the entire structure to collapse.

Designing a robust structural system means designing it so that it can safely withstand:

- the accidental collapse of a structural element (a fin in a façade, a vertical slab in a façade system with hanging slabs, etc.) or a limited portion of the structure;
- the occurrence of localized damage.

In a redundant structure the loads can be supported, in case of damage:

- by the same resistant starting mechanism, but with reduced resistance due to damage (section redundancy),
- through alternative resistant mechanisms that are activated after damage (structural element or system redundancy).

In more detail, section redundancy is the ability of the section of a structural element to maintain a residual resistant capacity following the rupture of a part of it or in an equivalent way, the property that the breaking of a part of the section does not cause it to break completely. This is the case of elements made of laminated glass consisting of 3 or more sheets of glass, where some layers have the task of intervening only in the event of the breaking of the layer in charge of bearing the loads. It should be noted that in glass structures, a low working rate of the material does not give redundancy to the section, unlike for example in a section of reinforced concrete or steel, because the spontaneous breaking of a glass plate can occur even in the presence of low tensional levels.

Finally, according to the definition of robustness, an element or a structure shall not break or lose its load resistance when subjected to ordinary effects. Also in this case, on the element level, the protection against expected loads or impacts can be attained

by using a laminated glass where the outer layer protects the inner resisting section (Feldmann, et al., 2014).

When talking about hierarchy, particular attention is given to the classification of structural glass elements in terms of economic, social and environmental consequences. According to UNI EN1990, three classes of consequences are defined as a function of the construction importance, the position in the building, the social impact corresponding to the probability of the loss of human life as a consequence of the collapse of the glass element. For the sake of completeness, class CC0 is added by the Italian guidelines, in which all specifically non-structural glass construction products are included.

Table A.1- 2 Summary of element classes as a function of consequences classes

Element class	**Consequences class (CC)**	
Class zero	CC0	Non-structural elements whose failure has *extremely limited* consequences in all respects, including in terms of loss of human life.
Class 1	CC1	Structural elements whose failure has *negligible* consequences in all respects, but *limited* consequences in terms of loss of human life.
Class 2	CC2	Structural elements whose failure has *considerable* consequences in all respects, but *medium* consequences in terms of loss of human life.
Class 3	CC3	Structural elements whose failure has *very great* consequences in all respects, but *high* consequences in terms of loss of human life.

For glass, in particular, it is absolutely necessary to know in depth all the physical characteristics and to keep in mind that it has a very resistant structure but is strongly penalized by the presence of micro defects, which generate substantial differences in yield between the different points of a given element. In order to ensure the bearing capacity of a glass structure with adequate safety, it is necessary to know how these micro-defects affect the real strength according to the shape, size and variables related to the boundary conditions. Moreover, the effect of permanent loads is not negligible when the alternation of hygrothermal conditions, especially in the presence of high percentages of relative humidity, can accelerate crack propagation.

It is now recognized that conventional design methods based on the assumption of uniform stress distribution are inadequate to ensure a high level reliability related to the risk of structural failure. The strength of the glass depends on many parameters, among which the main ones are: the surface condition of the glass element; duration of load applied; geometry of the glass element; relative humidity and temperature of the surrounding environment.

Consequently, all these factors must be considered in the design of structural glass in order to carry out a correct safety analysis. A well-executed design phase must be accompanied by a careful choice of products to be used in the realization of the project.

As a matter of principle, complex probability models should be used by taking into account the contribution of various factors (e.g., characteristics of the base material; designing strategy; static scheme) and their correlation. In fact, one of the main characteristics of glass, common also to other materials such as wood and concrete, consists in the fact that the intrinsic strength of the material is influenced by the loads, due to the effects of static fatigue and tension distribution.

A.1.4 Reliability of structures

In general, the reliability of a structure can be defined as the probability that the building will continue to perform the functions for which it was designed and constructed during a fixed period of time. In other words, this probability is the one providing that the useful life of the structure is not inferior to a given value, known as design life, which is determined beforehand. Therefore, a structure can be considered reliable if the P_{succ} (probability that the structure will continue to perform its functions throughout its useful life) will be greater than a fixed acceptability value P* or, reciprocally, if the probability, P_{fail}, that the useful life of the structure is lower than the value of 1-P*, taking into account that the sum of the probability of the occurrence of a certain condition and the probability of its not occurring is equivalent to certainty.

The nominal or design life is defined as the period of time when it's reasonable to that the structure is to be used for its intended purposes, with scheduled ordinary maintenance.

This generic definition of reliability prompts to specify the boundary conditions beyond which the structure is no longer able to perform its functions; these limit conditions or limit states may be divided into service limit states and ultimate limit states; the former are defined as those conditions in which the structure loses at least one of the necessary characteristics for its proper functioning, such as an excessive deformation, but continues to maintain its stability and integrity; the latter are the conditions in which the loss is precisely the stability and/ or structural integrity.

Without losing generality, these limit states can be expressed generically with equality between a given stress S acting on the structure and the resistance R of the structure to this action, overcome which manifest the conditions of loss of fixed functionality. Defined therefore a limit state S=R, the reliability of the structure can generically be defined as:

$$P[S \leq R] \tag{1}$$

The evaluation of this probability obviously requires the determination of the two quantities R and S. Therefore, it is necessary to schematize the structure through a

model; define the actions acting on it; choose a calculation method for the design and check the inequality S≤R, where the equal sign corresponds to the achievement of the limit state.

It is intuitive to understand that in each of these phases there are quantities affected by uncertainties; for instance, in the mathematical model used, the geometric schematizations made, the actual behaviour of the materials and, finally, the random nature of the loads. All these factors have to be taken into account in order to arrive at the result sought, by associating the traditional deterministic calculation techniques with those of random calculation that provide results in terms of safety, or in a complementary way, of the probability of collapse of a structure.

Depending on the level of knowledge about random variables and the type of assessment required, the analyses on structural reliability and the related verifications can be traced back to the categories in the following sections.

A.1.4.1 Level III methods

Developed around the mid-20th century, the level III method aims to assess the probability of collapse and to check that it is below a very small value considered acceptable.

The exact probabilistic approach is characterized by the fact that the resistances of the materials and permanent and variable actions performing on the structure are modelled as random variables and intervene with the respective probability density functions. It should be considered (Casciati et al. 1996):

- The load probability density function;
- The probability density function of materials (strengths).

The relationship between these probability functions and the probability of collapse should be determined, taking into account the non-linearity of the materials.

By defining X as a point in the random variable space representative of the significant input and system parameters; the probability that X is within the U-collapse domain or the S-security domain can be expressed as:

$$P_{fail} = \int_{G(X)\leq 0} f_X(X)dx \tag{2}$$

Where $f_X(X)$ is the joint probability density function of X vector of the random variables characterizing the problem under consideration; and G=G(X) is a defined function such that G>0 and G<0 represent success and failure of the structure, respectively.

The problem of structural reliability is apparently reduced to the solution of the multidimensional integral by Eq. (2); in fact, the closed-form solution of the previous integral is only possible in very rare cases and under very restrictive assumptions where both the performance function and the joint probability density function JPDF can be expressed in a simple way. Only in the case of a two-dimensional problem of

independent variables and linear performance function can a solution be found in closed form. In general, however, this integral can only be solved numerically thanks to Monte Carlo simulations.

A.1.4.2 Level II methods

The main problems related to the calculation of the integral can be summarised in three points (Rotondi et al. 2001):

1. The integration domain shall only be known implicitly;
2. The integration domain is generally "far" from the mean value of the vector X;
3. The value of the integrate function varies rapidly in the integration domain.

The first point makes it difficult to find limits (bounds) for the integration domain and for generating random numbers. The second point also makes an efficient generation of random numbers difficult, while it is necessary to carefully choose the integration scheme as far as the third point is concerned in order not to lose any peak value of the integrand function.

For these reasons, several authors since the 1960s have proposed the idea of assessing reliability by means of a β index, known as the reliability index (Ditlevsen et al. 1996). This index measures, in units of standard deviation, the distance between the mean value of the vector X and the boundary of the breaking domain, that is the distance between the mean value and the point of the performance function that is closer to the mean value (design point). The evaluation of the β index is, therefore, a constrained minimum search problem.

For example, in the case of a two-dimensional space of normal-distributed and independent variables, β can be calculated as follows:

$$\beta = \frac{\mu_R - \mu_S}{\sqrt{\sigma_R^2 - \sigma_S^2}} \tag{3}$$

Where μ and σ represent respectively the mean and standard deviation of the variables indicated in the subscript.

After this index has been calculated it is possible to obtain the probability of collapse and compare it with reference values in order to evaluate the degree of reliability of the structure; obviously the higher the value of β, the lower the probability of collapse.

A.1.4.3 Level I methods and limit states

This method is called *semi-probabilistic method* (in structure modelling and load definition) because the uncertainty present in the structural problem is partly taken into account through the introduction of specific values characteristic of the relative probability distributions. It is a limit state method (in the execution of safety checks) as it assesses the reliability of the considered structure in relation to the specific crisis

modes that may occur. More precisely, it is defined as the limit state of a given structure any condition from which the structure that is being considered (as a whole or in one of its parts) ceases to fulfil partially or totally, the functions for which it was designed and built.

The breaking of a glass panel does not necessarily depend on the maximum tensile force at the surface; the fracture occurs at the point of the surface at which a relatively high level of tensile strength also corresponds to a significant surface defect. The collapse should occur neither at the point of greatest defect nor at the point of greatest stress. It follows that the probability of failure depends on a weighted average of the distribution of the tensile forces. In a probabilistic view, it must be verified that the structure has a sufficient safety margin with respect to each limit state. For this purpose, it is necessary to adequately model all the actions acting on the structure, that is all the causes or sets of causes (static loads, accidental and permanent loads, dynamic loads, deformations enterprises, aggressive agents, etc.), capable of inducing limit states in the structure.

The semi-probabilistic method, also known as the partial safety coefficient method or the I-level probabilistic method, is a simplification of the probabilistic approach in which the calculation of the probability of rupture, is replaced by the verification of critical inequality, introducing instead of random variables R and S the characteristic values of the latter (R_k, S_k) together with the " partial safety coefficients" (γ_s, γ_r).

In this way the designer must verify that the following inequality is respected for the generic limit state:

$$\gamma_S S_k \leq \frac{R_k}{\gamma_r} \tag{4}$$

where R_k and S_k are defined as upper and lower fractions respectively:

Where p-value is a very small value (ranging from 2% to 5%).

According to the “fail-safe approach”, the achievement of the ultimate limit state of collapse of any part of a structure is considered as the ultimate limit state of the whole work or the crisis of an element (or part of the structure) represents the crisis of the entire structure.

However, it should be pointed out that glass structures often have a non-linear geometric behavior (since the plates are very flexible, the greatest displacements exceed half the thickness of the plates), with the activation of a membranal behaviour. A complex structural analysis would therefore be required.

The limit states for glass elements are the Service Limit State (SLS), Ultimate Limit State (ULS) and Collapse Limit State (CLS):

- The SLS considers the structure subjected to the characteristic design loads. In general, the purpose is to ensure the functionality of the building in terms of deflection, vibration, thermal performance and many others. As for structural

functionality, the deformability of the structural element is evaluated and limited.

- The ULSs consider the structure subjected to extreme values of external actions, and aim at guaranteeing the structural integrity of the element.
- The CLSs consider the glass element as fully or partially fragmented.

A.1.5 Design actions and strength

According to UNI EN 1991 and national standards, in the case of not exceptional actions, the design loads are given by the following expression as a function of the relative limit state:

For SLS
$$F_d = G_1 + G_2 + Q_{k,1} + \sum_i \psi_{0,i} Q_{k,i} \quad (5)$$

For ULS
$$F_d = \gamma_{G1} G_1 + \gamma_{G2} G_2 + \gamma_{Q,1} Q_{k,1} + \sum_i \gamma_{Q,i} \psi_{0,i} Q_{k,i} \quad (6)$$

For CLS
$$F_d = \gamma_{G1} G_1 + \gamma_{G2} G_2 + \gamma_{Q,1} Q_{k,1,\tau} + \sum_i \gamma_{Q,i} \psi_{0,i} Q_{k,i,\tau} \quad (7)$$

Where:

- G_1 represents the action value caused by the self-weight (dead load);
- G_2 represents the action value caused by the permanent loads;
- $Q_{k,i}$ are the characteristic value of the variable action, referring to a return period of 50 years (for i=1 the variable action is the main one);
- $Q_{k,I,\tau}$ is the characteristic value of the variable action, referring to a return period (τ) of 10 years (for i=1 the variable action is the main one);
- $\Psi_{0,i}$ denotes the variable load combination coefficient;
- γ_{G1}, γ_{G2}, $\gamma_{Q,i}$ are the partial factor for self-weight, permanent loads and variable actions, respectively.

In addition to what can be found in the specific regulations (e.g., EN 572 for float glass), the design values for the verification can be inferred as follows:

$$R_d = \frac{k_{mod} R_k}{\gamma_m} \quad (8)$$

Where:

- R_k represents the characteristic value of glass strength;
- k_{mod} denotes the coefficient taking into account the load duration and the environmental conditions;
- γ_m is the partial factor for the tensile strength of annealed glass under bending, including model and geometry uncertainties.

A.1 The structural use of glass

The characteristic strength values determined directly by experimental tests have to follow the indications given in EN 1288 (e.g., $f_{g;k}$ = 45 N/mm^2 for float and borosilicate glass). These values were determined by experimental data interpreted with the Weibull distribution for a probability of ruin of 0.005.

The following k_{mod} factor is inserted to consider the phenomenon of glass corrosion under stress in presence of high levels of water or humidity, which depending on the durability of the workers, affects fatigue behaviour.

A.1.6 References

ASCE (2013). “Minimum Design Loads for Buildings and Other Structures”; ASCE: Reston, VA, USA, 2013.

Bagger, A., Petersen, R.I. (2009): “Structural use of glass: cruciform columns and glass portals with bolted connections subjected to bending”, *Proceedings of Glass Performance Days*, pp.381-385.

Bedon, C. (2018). “Vulnerability assessment and dynamic characterisation of a glass footbridge: on-site vibration tests and FE numerical modelling”, *Proceeding GNGTS 2018*.

Biolzi, L., Orlando, M., Piscitelli, L. R., Spinelli, P. (2016). “Static and dynamic response of progressively damaged ionoplast laminated glass beams”, *Composite Structures*, 157, pp.337-347.

Cagnacci, E., Orlando, M., Spinelli, P. (2010) “Il vetro come materiale strutturale”, *Edizioni Poli-stampa*, Firenze.

Carrè, H., Daudeville, L. (1999): “Load-Bearing Capacity of Tempered Structural Glass”. *Journal of Engineering Mechanics*, 125(8).

Casciati, F., Roberts, J. (1996). "Models for structural reliability analysis", CRC Press.

Chaszar, A. (2003). “Hybrid laminations for structural glass.” *Glass processing days 2003*, Tampere, Finland, pp.416-418.

CEN. European standard EN 1990 (2002). “Eurocode 0 – Basis of structural design”.

CEN. European standard EN 1991 (2002). “Eurocode 1: Actions on structures”.

CEN. European standard EN 1998-1 (2004). “Eurocode 8: Design of structures for earthquake resistance – Part 1: General rules, seismic actions and rules for buildings”.

CNR. CNR-DT210. Istruzioni per la Progettazione, L’esecuzione ed il Controllo di Costruzioni con Elementi Strutturali di vetro; Guide for the Design, Construction and Control of Buildings with Structural Glass Elements; National Research Council of Italy (CNR): Roma, Italy, 2013. (In Italian).

Ditlevsen, O., Madsen, H.O. (1996). "Structural Reliability Methods", John Wiley & Sons Ltd, Chichester.

EN 13830 (2015). “Curtain Walling-Product standard”.

Feldmann, M.; Kasper, R.; Abeln, B.; Cruz, P.; Belis, J.; Beyer, J.; Colvin, J.; Ensslen, F.; Eliasova, M.; Galuppi, L.; et al. (2014): “Guidance for European Structural Design of Glass Components—Support to the Implementation, Harmonization and Further Development of the Eurocodes”. Report EUR 26439–Joint Research Centre-Institute for the Protection and Security of the Citizen; Pinto, D., Denton, F., Eds.; European Union: City of Brussels, Belgium, 2014.

GRANTA Design, CES EduPack, 2014.

Haldimann, M. (2006): “Fracture Strength of Structural Glass Elements – Analytical and numerical modeling, testing and design”, Thése EPFL 3671, Ecole Polytechnique Fédérale de Lausanne.

Haldimann, M., Luible, A., Overend, M. (2008): “Structural use of glass”, *International Association for Bridge and Structural Engineering (IABSE)*, Switzerland. ISBN 978-3-85748-119-2.

Hoire, J., Lago, S. (2019). “Numerical Analysis of Point-Fixed Glass Balustrades”.

Holgate, A. (1998). “Art of Structural Engineering: The Work Of Jorg Schlaich and his team” Edition Axel Menges GmbH.

JASS 14 (1996), “Japanese Architectural Standard Specification Curtain Wall”, AIJ, *Architectural Institute of Japan*.

Ledbetter, S.R., Walker, A.R.; and Keiller, A.P. (2006) “Structural Use of Glass”. *Journal of architectural engineering*, 12, pp.137-149.

NTC (2018) “Norme Tecniche per le Costruzioni. Design Standard for Buildings”; Ministero delle Infrastrutture e dei Trasporti: Roma, Italy. (In Italian)

Pilkington L. A. B. (1969). The float glass process. *Proceedings of the Royal Society A: Mathematical, Physical and Engineering Sciences*. 314A, 1.

Royer-Carfagni, G., Silvestri, M. (2007). “A proposal for an arch footbridge in Venice made of structural glass masonry”, *Engineering Structures*, 29, pp.3015-3025.

Rotondi, A., Pedroni, P., Pievatolo, A. (2001). "Probabilità Statistica e Simulazione", *Editore Springer*.

Schittich, C., Staib, G., Balkow, D., Schuler, M., Sobek, W. (2007). "Glass Construction Manual". ISBN 978-3-03461-554-9.

Saji, S.M., Vedic. N. (2018). *"Analysis of Laminated Glass Beam with different Core Thickness"*. International journal of engineering research & technology (IJERT) ETCEA. Volume 6 – Issue 06.

UNI EN 572. "Vetro per edilizia".

UNI EN 1288-2:2001. "Vetro per edilizia - Determinazione della resistenza a flessione del vetro - Prova con doppi anelli concentrici su provini piani, su grandi superfici sollecitate".

UNI Ente Italiano di Normazione (2022). "*Guida al mondo normative e legislative del vetro per edilizia*".

A.2 Seismic performance of façades

Considering the structural feature, rather than thermal and acoustic ones which relate to the comfort and the durability issues, it is worth to highlight that the proper design of a façade is a matter of life safety and cost-saving. As mentioned above, the structural role encompasses resisting gravity and wind loads, transferring this actions to the primary frame and accommodating the movements caused by earthquakes. Especially in high-rise buildings, where the wind pressure could affect in severe ways, the displacements caused by seismic action to the primary bearing system of a building may be considerable and, thus, represent a serious threat to the safety of people inside and outside the building (Behr 2009).

As observed from past damage reports, secondary components are very susceptible to earthquake shaking, and consequently cause high socio-economic losses and activity interruption.

For curtain walls, typical damage consisted in glass fallout due to limited movements of the panels, the warping of the steel or aluminium frame and the integrity loss of connections not properly designed. Fig. A.2-1 show façade damages after (a) Christchurch 2011; (b) Northridge earthquake 1994 and (c) Mexico earthquake in 1985 earthquakes.

One of the major issues is related to the lack of extended and harmonized documentation and technical codes that can regulate the glass design procedure at different levels: basic elements, non-structural components, or stand-alone load-bearing structures; without considering that it is often used in combination with other construction materials (such as aluminium, steel or wood, composites, etc.) (Blyberg 2011; Kido et al.2013). Besides, an in-depth investigation of its mechanical behaviour is still needed. Specifically, the 'brittle' feature is intrinsic in glass applications and regulates the overall building serviceability performance. Thus, according to the Performance-Based Design, the primary deformation capacity under mechanical design loads is limited to established amplitudes, to permit its functional use within the entire building life-cycle (EN 1998, NTC 2018). In this sense, ATC-58 project (ATC 2009), named "Development of Next-Generation Performance-Based Seismic Design Guidelines for New and Existing Buildings", focuses on the definition of a next-generation PBSD procedure, in which the performance predicted of all components in the building is quantitatively addressed in terms of risks. The measures used to quantify losses (in terms of physical, social or economic equity) are presented in probabilistic models by means of cumulative functions based on the mean value (θ) and standard deviation (β) parameters, and can be distributed normally or log-normally.

Basically, the cost of damaged glass and its replacement was higher than the cost of all the other element involved. Thus, with the aim of mitigating the risk of damage,

recent research is moving towards the development of fragility curves for glazing non-structural components at significant damage states, that are useful tools for designers in the assessment of building damage, that is a primary step in the PBSD procedure, on which depends the assessment of building losses.

Figure A.2-1 (a) Glazing damage in Chile, after the 8.8 Chile Earthquake (2010) (FEMA E-74_Figure 6.3.1.4-3); (b) Impact damaged façade at the entrance of the Corte de Apelaciones de Talca , after the 8.8 Chile Earthquake (2010) (FEMA E-74_Figure 6.3.6.1-2); (c) Damaged glazing system in San Francisco (1989), after Loma Prieta earthquake [https://www.earthquakecountry.org/step1/largewindows/ ; California Seismic Safety Commission]

A.2.1 Seismic design

Among the natural actions that cause the greatest number of losses are due to seismic action (Cassese 2017). From a phenomenological point of view, the earthquake derives from the sudden breakage of the rock, thus releasing deformation that had accumulated in the boundary areas of the tectonic plates. The “fault area” where the fracture occurs is an important parameter related to intensity measurements of an earthquake, such as magnitude, Arias intensity or the quantitative peak intensity measures (PGD, PGV and PGA). These latter parameters are of great interest in the field of seismic engineering, being focused on the ground shaking at the construction site. In

fact, the acceleration corresponds to the known term in the motion equation of a structure subjected to a seismic action.

According to empirical evidence and several literature studies, an earthquake is a destructive event that often results in serious consequences on the society, either building assets or people's lives, causing the largest number of losses in terms of victims.

The seismic design of structures has evolved over time, both in relation to the action itself and the response of the structures. In the past, as for all actions of natural origin: landslides, volcanic events, earthquakes; prevention was given to the only historical memory (Cimino 2016) that handed down to future generations a certain event. Nonetheless, the notion of the return period and its repetitive nature was not yet understood or known. Moreover, especially in Italy, the structures were designed in such a way as to exploit the only elastic resistance of the structure, and therefore without considering the plastic development of the same. The result of this modelling was a safe building against gravity actions alone, and less for exceptional ones, such as seismic ones. Today, modern design codes around the world define performance levels to prevent structural collapse or structural damage, and thus limits to the economic losses. (Cassese 2017) In particular, the cost of glass façades in an ordinary or a commercial building can be many times larger than the cost of the main structure, thus the economic value of losses can be actually high (Nuzzo et al. 2020).

The performance level of the curtain walls subject to earthquakes is, as usually happens in the field of civil engineering, differentiated in serviceability limit state (i.e., the ability of the curtain walls to ensure its functionality in terms of water or air tightness) and ultimate limit state (i.e., fall-out or glass cracking).

Since a Curtain Wall Façade is considered a non-structural element attached to the primary building by a brackets system, it has to accommodate the displacements of the supporting system without influencing the overall response of the construction work. Whereas a globally ductile non-structural behaviour is provided by the aluminium frame, which tends to follow easily the stories relative displacements, a sort of displacement capacity, known as clearance, is provided to the glass panels which can move rigidly in-plane or out-of-plane reducing the risk of breakage (CNR-DT210 2013).

The main foreseeable risk is the brittle breaking of the glass panels or the fall-out of the panel from the façade plane and the consequent fall. In particular, it may be the case that, due to the classical façade with mullions and traverses, the vertical load-bearing elements tend to deform in their plane causing changes in shape on the infill that lead to breakage or expulsion from the plane (Poso 2014). Several studies have shown that the glass panel response under in-plane loads can be described in two steps:

- initially it behaves like a rigid element only moving and without deforming until the contact with the frame;
- the first contact causes the creation of the strut and tie-rod; this tension field may result in brittle rupture of the tensile glass or instability of the compressed

strut. In the worst case, the deformation of the panel can completely fall out from the frame.

Furthermore, Sucuoglu and Vallabhan (1997) discuss seismic capacity of the glass relating to the combination of in-plane deformation and out-of-plane resistance of glass, subjected to in-plane loading, by analysing the out-of-plane deflection phenomenon and providing a mathematical formulation of displacement orthogonal to the glass panel. In this regard, a study on the observations of the consequences of seismic events indicates that in-plane deformations are most likely the origin of glass collapse.

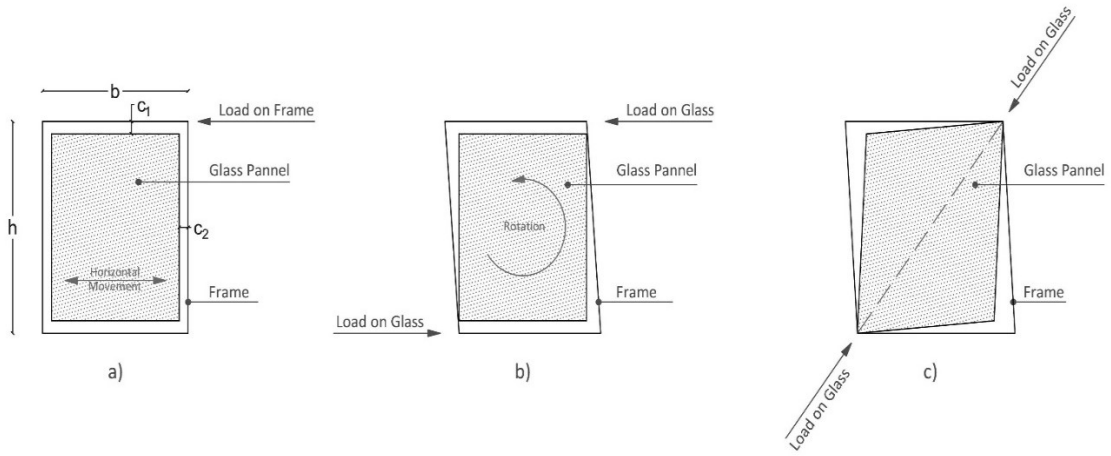

Figure A.2-2 In plane drift mechanism of the framed CW: (a) Rigid horizontal movement of the panel; (b) Deflection of frame by panel horizontal movement; (c) Combined horizontal and rotation movement (figure © S. Mattei)

A.2.2 Current regulations

The comparison of several regulations and their approach to the seismic design of non-structural elements, such as façades, is fundamental in understating all the limits and the necessary studies in this regard.

In the current regulatory scenario, façades are classified both by Eurocodes (EN 1998-EC8) and by the National Regulation (NTC 2018), as secondary or non-structural elements, with many advantages being an affordable option for the exterior of the building in terms of aesthetics and energy efficiency. In particular, Section 7.2.3 of the NTC18 and Section 4.3.5 of Eurocode 8 are reserved for the requirements of non-structural elements. The code focuses on the movements that the main structure transmits to the façade and that the secondary elements “shall, together with their supports, be verified to resist the design seismic action”. A more detailed and specific framework, regarding the design and verification of curtain walls, can be obtained if referring to the regulations of the seismic countries where the development of these technologies has been in progress for a longer time, such as the United States or Japan.

A.2.2.1 European Standard: Eurocode 8

Within the European regulation, in absence of more specific analyses a simplified method is used to assess the seismic effects on the secondary element and consists of applying a static horizontal force F_a defined as follows:

$$F_a = \frac{S_a W_a \gamma_a}{q_a} \tag{9}$$

Where:

- F_a is the horizontal seismic force, applied to the centre of mass of the element in the most unfavourable direction;
- W_a is the weight of the element;
- γ_a is the importance factor as a function of importance classes for buildings and it depends on the consequences of collapse for human life in the immediate post-earthquake period (EC8 § 4.2.5 Table 4.3);
- q_a is the behaviour factor (EC8 §5.2.2.2);
- S_a is the seismic coefficient applicable to non-structural elements, computed as the peak acceleration normalized with respect to the acceleration of gravity. Moreover, in absence of a more accurate evaluation, it can be determined as:

$$S_a = a_g/g \cdot S \cdot R_a \tag{10}$$

with the magnification factor R_a defined as:

$$R_a = max\begin{cases} \dfrac{3(1+Z/H)}{1+(1-T_a/T_1)^2} - 0.5 \\ 1 \end{cases} \tag{11}$$

where:

- a_g/g is the ratio between the peak ground acceleration on type A ground to be considered in the limit state in question and the acceleration of gravity;
- S is the soil factor;
- Z is the height of the centre of gravity of the non-structural element measured from the foundation level;
- H is the building height measured from the foundation level;
- T_a is the fundamental vibration period of the non-structural element;
- T_1 is the fundamental vibration period of the construction in the direction considered.

Eurocode 8 underlines the importance of non-structural elements design for the general safety and for the functionality of the building itself, stating that their failure could expose people to a serious hazard. In this regard, a restriction of movement between floors is provided depending on the non-structural components (as reported in Table A.2-1). In particular, the European code focuses on the design of the fastening and supporting system, requiring their verification to resist the design seismic action. So

it recognizes brackets and other fastening devices to be of great importance in the seismic behaviour of the non-structural element.

Table A.2- 1 Damage limitation criteria in EC 8-1

Non-structural element type	Limitation
Non-structural elements of brittle materials attached to the structure	$d_r \nu \leq 0.005\ h$
Ductile non-structural elements	$d_r \nu \leq 0.0075\ h$
Non-structural elements fixed in a way so as not to interfere with structural deformations	$d_r \nu \leq 0.010\ h$

The parameters in the table are: h is the storey height; d_r represents the design interstorey drift calculated for T_r = 475 year; ν is the reduction factor taking into account the lower return period of the seismic action associated to the damage limitation requirement t (in case of importance class I and II ν = 0.5 and in case of importance class III and IV ν = 0.4).

A.2.2.2 National Standard: Norme Tecniche per le Costruzioni 2018

As previously mentioned, in Section 7.2.3 of NTC 2018 are reported some provisions and design criteria dedicated to secondary elements, without a particular reference to façades. In such way, both the stiffness and strength of these elements are ignored in the analysis of the structural response and designed to withstand only vertical loads. In accordance with the prescriptions provided by the European standard, these elements must be able to absorb the deformations of the structure subject to the design seismic action, maintaining the bearing capacity, and must be verified, together with their connections to the structure, for the seismic action related to the limit state considered. Moreover, when their distribution is highly irregular in plane, their effects have to be assessed and taken into account, as well as for cases of highly irregular distributions in height.

The effects of the seismic action on the building secondary elements can be determined by means of the application of a horizontal force F_a, defined in Eq. 12 as follows:

$$F_a = \frac{S_a W_a}{q_a} \tag{12}$$

Where:

- F_a is the horizontal seismic force, applied to the centre of mass of the element in the most unfavourable direction;
- W_a is the weight of the element;
- q_a is the behaviour factor of the element;
- S_a is the peak acceleration, normalized with respect to acceleration of gravity, that the non-structural element undergoes during an earthquake and corresponds to the limit state considered. In the absence of a more accurate evaluation, it can be determined as Eq. 10.

Furthermore, in terms of damage limitation, the Italian code provides reference values of interstorey drift caused by seismic actions (as reported in Table A.2.2), depending on the performance level required to the overall structure.

Table A.2-2 Damage limitation criteria in NTC-18

Non-structural element type	Limitation
Brittle non-structural elements rigidly attached to the structure	q d_r ≤ 0.005 h
Ductile non-structural elements rigidly attached to the structure	q d_r ≤ 0.0075 h
Non-structural elements fixed in a way so as not to be damaged because of an interstorey drift equal to d_{rp} due to their intrinsic deformability or to the links to the structure.	q d_r ≤ d_{rp} ≤ 0.010 h
Ordinary masonry	q d_r ≤ 0.002 h
Reinforced masonry	q d_r ≤ 0.003 h
Confined masonry	q d_r ≤ 0.0025 h

In the table h is the storey height and d_r is the interstorey drift calculated with linear or nonlinear analyses, on the numerical model not including infill.

A.2.2.3 American Standard: FEMA 450

Based on the main purpose of the *National Earthquake Hazard Reduction Program (NEHRP)*, which is to reduce the level of seismic risk and to enhance public safety, the 2003 edition of the *NEHRP Recommended Provisions for Seismic Regulation of New Buildings and Other Structures* (FEMA 450/2003 edition) consists of criteria and requirements for the design and verification of structures subjected to seismic records.

According to these provisions, the design earthquake may result in both structural and non-structural damage. In particular, Chapter 6 deals with architectural components that are permanently attached to the primary structure, including their supports and attachments, with specific reference to structural glass components.

The design seismic force, F_p, is defined as follows (FEMA 450 §6.2.6):

$$0.3S_{DS}I_pW_p \leq \boldsymbol{F_p} = \frac{0.4a_pS_{DS}W_p}{R_p/I_p}\left(1+2\frac{z}{h}\right) \leq 1.6S_{DS}I_pW_p \qquad (13)$$

Where:

- a_p is the component amplification factor selected in a proper manner according to the code (see Table A.2-3);
- S_{DS} is the short-period spectral acceleration parameter, calculated as $2/3\ F_aS_S$, where F_a is the site coefficient and S_S is the mapped, maximum considered earthquake, 5-percent-damped, spectral response acceleration parameter at 0.2 sec;
- W_p is the weight of the non-structural element;
- R_p is the component response modification factor selected in a proper manner according to the code (see Table A.2-3);
- I_p is the component response modification factor, $I_p \in [1; 1.5]$ depending on some conditions related to the material asset and the required functions;

- z is the height above the base of the fastening point of the component;
- h is the average roof height of the structure above the base.

Table A.2-3 Coefficients for Architectural Components (FEMA 450 2003)

Architectural Component or Element	a_p	R_p
Interior non-structural walls and partitions		
Plain masonry walls	1,0	1,5
All other walls and partitions	1,0	1,5
Cantilever Elements, unbraced or braced (to structural frame) below their centres of mass		
Parapets and cantilevered interior non-structural walls	2,5	2,5
Chimneys and stacks where laterally supported by structures	2,5	2,5
Cantilever elements, braced (to structural frame) above their centres of mass:		
Parapets	1,0	2,5
Chimneys and stacks	1,0	2,5
Exterior non-structural walls	1,0	2,5
Exterior non-structural wall elements and connections		
Wall element	1,0	2,5
Body of wall-panel connections	1,0	2,5
Fasteners of the connecting system	1,25	1,0
Veneer		
High deformability elements and attachments	1,0	2,5
Low deformability elements and attachments	1,0	1,5
Penthouses (except where framed by an extension of the building frame)	2,5	3,5
Ceilings		
All	1,0	2,5
Cabinets		
Storage cabinets and laboratory equipment	1,0	2,5
Access floors		
Special access floors	1,0	2,5
All other	1,0	1,5
Appendages and ornamentation	2,5	2,5
Signs and billboards	2,5	2,5
Other rigid components:		
High deformability elements and attachments	1,0	3,5
Limited deformability elements and attachments	1,0	2,5
Low deformability elements and attachments	1,0	1,5
Other flexible components		
High deformability elements and attachments	2,5	3,5
Limited deformability elements and attachments	2,5	2,5
Low deformability elements and attachments	2,5	1,5

Furthermore, there are some exceptions based on the value of the component period, T_p, as follows:

If $T_p \geq T_{flx} = (1 + \frac{0.25z}{h})S_{D1}/S_{DS}$ the value of F_p may be reduced by the ratio of T_{flx}/T_p.

Finally, the force F_p shall be independently applied to each of the two orthogonal horizontal directions, combined with service loads. In addition, the non-structural element shall be designed for a simultaneous vertical force equal to $\pm 0.2S_{DS}W_p$.

In terms of deformation capacity, the relative seismic displacements (D_p) can be determined in accordance with Eq. 14.

$$D_p = \delta_{xA} - \delta_{yA} \leq (X - Y)\frac{\Delta_{aA}}{h_{sx}} \quad (14)$$

Where:

- X is the height above the base of the upper support attachment (at level x);
- Y is the height above the base of the lower support attachment (at level y);
- δ_{xA} is the deflection at level x of structure A;
- δ_{yA} is the deflection at level y of structure A;
- Δ_{aA} is the allowable storey drift for structure A provided by the code as reported in Table A.2-4 and as a function of a classification assigned to the structure based on its use.

Table A.2- 4 Values for the allowable story drift (FEMA 450 2003)

Structure	Seismic Use Group		
	I	II	III
Structures, other than those using masonry seismic-force-resisting systems, four stories or less in height with interior walls, partitions, ceilings, and exterior wall systems that have been designed to accommodate the story drifts	0.025 h_{sx}	0.020 h_{sx}	0.015 h_{sx}
Masonry cantilever shear wall structures	0.010 h_{sx}	0.010 h_{sx}	0.010 h_{sx}
Other masonry shear wall structures	0.007 h_{sx}	0.007 h_{sx}	0.007 h_{sx}
Special masonry moment frames	0.013 h_{sx}	0.013 h_{sx}	0.010 h_{sx}
All other structures	0.020 h_{sx}	0.015 h_{sx}	0.010 h_{sx}

A very interesting section, in FEMA 450, specifically refers to glazed curtain walls, storefronts or partitions (interior and exterior) in order to provide peculiar seismic drift limits ($\Delta_{fallout}$ by Eq. 15) necessary to avoid the glass fallout from the supporting system and determined in accordance with AAMA 501.4-00 (2001) and AAMA 501.6-01 (2001), in absence of detailed study and in some particular common cases, or by engineering analysis. Thus, during the earthquake, the façade is required to be able to accommodate the relative seismic displacement of the structure for a selected limited state, D_p.

$$\Delta_{fallout} \geq \max(1.25\, I\, D_p; 13\ \text{mm}) \quad (15)$$

Where I is the importance factor of the building.

The most widely used experimental investigations in practice, as previously mentioned, refer to the method by the American Architectural Manufacturers Association (AAMA), which provides a mock-up test guideline for evaluating the behaviour of a storefront system subjected to the inter-storey drift and for determining the seismic drift causing glass fallout from a wall system, respectively AAMA 501.4-09 and AAMA 501.6-09 standards.

The Static racking test, as explained in the former document, has the primary scope of estimating the serviceability performance of wall system specimens following a seismic event, as a result of statically applied in-plane horizontal racking displacements. This methodology concerns a testing sequence which is a combination of air infiltration, water penetration and static load tests.

AAMA 501.6 deals with the ultimate limit state, determining $\Delta_{fallout}$, defined as the "in-plane dynamic drift causing glass fallout from a glazed curtain wall panel, a glazed storefront panel or a glazed partition panel". This technical document provides a

Dynamic racking test focusing on seismic safety by applying a displacement history, consisting of four sinusoidal motions at progressively higher racking amplitudes composed of rump up and constant amplitude intervals. The testing facility (as shown in Fig. A.2-3) is very complex and specific for glass panels, in which the bottom anchorage points are fixed, thereby carrying out the application of in-plane displacement by means of an actuator at the top frame. The Crescendo test run continuously until achievement of one of the following conditions:

- the glass fallout;
- the ratio between drift over the height of the glass panel is at least 0.10;
- the dynamic racking displacement of ±150mm.

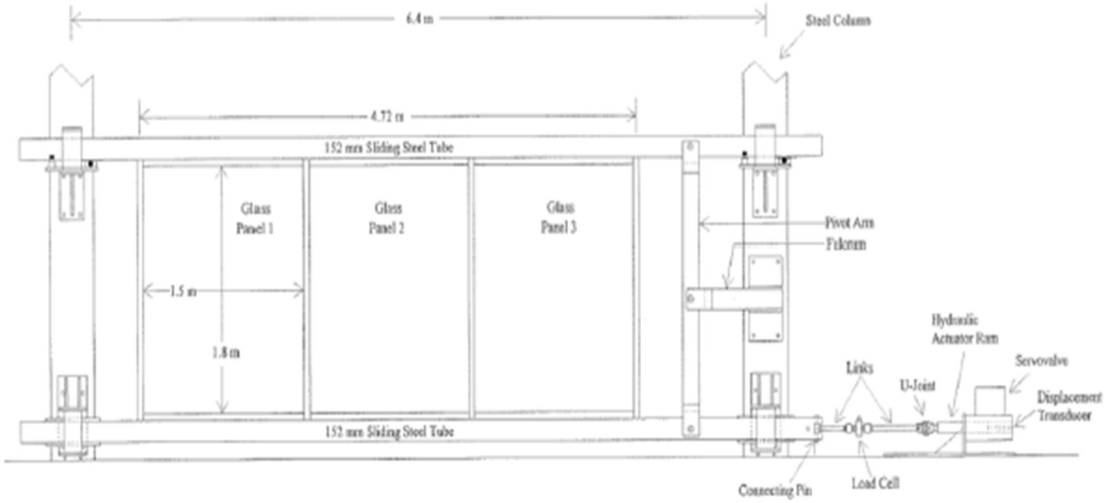

Figure A.2-3 Dynamic racking test facility (AAMA 501.6)

The assessment of the displacement, in accordance with the 2013 document of the American Society of Civil Engineers (ASCE 7-10 2013), may be avoided when the drift causing contact between the glass panels and the frame (Δ_{clear} by Eq. 16) is greater than 1.25 D_p.

$$\Delta_{clear} = 2c_1 \left(1 + \frac{h_p c_2}{b_p c_1}\right) \geq 1.25 D_p \quad (16)$$

Where c_1 indicates the clearance between the vertical glass edges and the frame; c_2 denotes the clearance between the horizontal glass edges and the frame; h and b are the height and the width of the glass panel, respectively.

A.2.2.4 Japanese Standard: JASS14

In and about Japan, one-tenth of earthquakes in the world occur (Matsu'ura 2017). Consequently, the needed development of seismic code has been conducted over years in order to preserve constructions against earthquake events.

As well as the American regulation, also the Japanese code JASS14 (1996) specifies a minimum value of the drift capacity of the façade in relation to the interstorey height,

h, of the buildings. But unlike all the other codes, it is specifically dedicated to façades and curtain walling under seismic actions.

In particular, it establishes threshold values depending on the severity of the seismic event and the probability of occurrence, and it provides special requirements. The design requirements are reported in Table A.2-5.

Table A.2-5 Reference limitations based on JASS14 (1996)

Grade of severity	Limitation
Level 1 - no damage on internal and external components. This is the grade related to the earthquakes that frequently occur in Japan.	h/300
Level 2 - all external components must not exceed the allowable stress. The prolonged use is possible according to the extent in which sealing is repaired. This is the grade of largest scale earthquakes that happened in the past.	h/200
Level 3 - neither the damage of the glass nor the dropout of any components is allowed. This is the grade of largest scale earthquakes that are forecasted to happen in the next 100 years.	h/100

In addition, a force-based check is indicated as a function of the energy released by the different seismic waves in the two main components: Primary waves acting in the vertical direction and Secondary waves in the horizontal directions. According to this approach, the seismic forces calculated with Eq. 17 and 18 have to be applied to the centre of mass of the non-structural components proportionally to the vertical (S_P) and horizontal (S_S) seismic coefficients:

$$F_{P,V} = WS_P \tag{17}$$

$$F_{P,H} = WS_S \tag{18}$$

Where W indicates the weight of the element.

A.2.2.5 New Zealand Standards

In New Zealand, the observation of the damage in non-structural elements during recent earthquakes discloses that non-structural elements performed poorly, but, on the other hand, there are cases in which the detailed design of secondary elements cut lives and costs.

Based on the expected performance under an earthquake, non-structural elements can be classified into 7 categories as proposed by the standard:

Table A.2-6 Parts classification criteria

Category	Criteria	Part risk factor R_p	Structure limit state
P.1	Part representing a hazard to life outside the structure[2]	1.0	ULS
P.2	Part representing a hazard to a crowd of greater than 100 people within the structure[2]	1.0	ULS
P.3	Part representing a hazard to individual life within the structure[2]	0.9	ULS

P.4	Part necessary for the continuing function of the evacuation and life safety systems within the structure	1.0	ULS
P.5	Part required for operational continuity of the structure[3]	1.0	SLS2
P.6	Part for which the consequential damage caused by its failure are disproportionately great	2.0	SLS1
P.7	All other part	1.0	SLS1

The seismic design of non-structural components is based on the Building Act 2004 and several New Zealand standards: NZS 4219 (2009), whereby this element type should be designed and realized within a building to resist earthquake loads, to reduce hazards and to protect all the contents from damage or from the loss of function; and in particular cases, not included in the previous one, such as partitions (also known as non-load-bearing walls), NZS 1170.5 (2004) has to be consulted. In the latter document, the Section 8 embodies all parts of structures including permanent, non-structural components and their connection, and permanent services and equipment supported by structures, and they specify their design of them under the earthquake actions.

In terms of force-based approach, both a vertical and a horizontal action calculated with Eq. 19 and 20, are considered as applied to every single element for its verification.

$$\boldsymbol{F_{pv}} = C_{pv} C_{vd} R_p W_p \leq 2.5 W_p \tag{19}$$

$$\boldsymbol{F_{ph}} = C_p(T_p) C_{ph} R_p W_p \leq 3.6 W_p \tag{20}$$

Where:

- C_{pv} and C_{ph} are, respectively, the vertical and the horizontal response factors, according to the ductility of the component, μ_p;
- C_{vd} corresponds to the vertical design action coefficient for the period of the system supporting the part;
- R_p is the risk factor;
- W_p is the weight of the non-structural element;
- $C_p(T_p)$ represents the horizontal design coefficient of the part, depending on the site hazard, the fundamental period, the spectral shape and a coefficient related to the floor height.

Table A.2-7 Part response factors

Ductility of the part μ_P	**C_{ph} and C_{pv}**
1.0	1.00
1.25	0.85
2.0	0.55
3.0 or greater	0.45

In terms of serviceability checks, the non-structural element connected to the primary structure on more than one level, have to be designed to sustain the actions resulting from the relative deflections that occur for the limit state being considered.

A.2.3 References

AAMA 501.6-01 (2001). “Recommended Dynamic Test Method for Determining the Seismic Drift Causing Glass Fallout From A Wall System”, AAMA, Schaumburg, IL, USA.

AAMA 501.4-00 (2001). “Recommended Static Test Method for Evaluating Curtain Wall and Storefront Systems Subjected to Seismic and Wind Induced Interstory Drifts”, AAMA, Schaumburg, IL, USA.

Applied Technology Council (ATC) (2009). Guidelines for Seismic Performance Assessment of Buildings.

ASCE 7-10 (2013). “Minimum Design Loads for Buildings and Other Structures”; ASCE: Reston, VA, USA.

Behr, R. A. (2009). “Architectural Glass to Resist Seismic and Extreme Climatic Events”, Cambridge, UK, Woodhead Publishing Limite.

Blyberg L. (2011). “Timber/glass adhesive bonds for structural applications”. Licentiate Thesis by Louise Bly- berg, Linnaeus University, School of Engineering, Sweden.

Cassese, P. (2017). “Structural, geotechnical and seismic engineering”. Ph.D. dissertation, University of Naples “Federico II”.

CEN. European standard EN 1998-1 (2004). “Eurocode 8: Design of structures for earthquake resistance – Part 1: General rules, seismic actions and rules for buildings”.

Cimino, G. (2016). “La vulnerabilità sismica del patrimonio edilizio dell’Università di Bologna Metodologia adottata e analisi dei risultati”. Ph.D. dissertation, University of Naples “Federico II” (in Italian).

FEMA 450, (2003). “Recommended provisions for seismic regulations for new buildings and other structures”, FEMA.

FEMA E-74 (2012). “Reducing the Risks of Nonstructural Earthquake Damage – A Practical Guide”.

JASS 14 (1996), “Japanese Architectural Standard Specification Curtain Wall”, AIJ, *Architectural Institute of Japan*.

Kido E.M., Cywin´ski Z. (2013): The new steel-glass architecture of buildings in *Japanese Steel Construction*, 6, pp.229-237.

Matsu'ura, R. S. (2017). "A short history of Japanese historical seismology: past and the present", *Geoscience Letters*, 4, 3.

NTC (2018) "Norme Tecniche per le Costruzioni. Design Standard for Buildings"; Ministero delle Infrastrutture e dei Trasporti: Roma, Italy. (In Italian)

Nuzzo, I., Aiello, C., Bonati, A., Caterino, N., Coppola, O., Occhiuzzi, A. (2020). "Fragility curves of glass façades via analytical simplified modelling". *Proceeding of 17th World Conference on Earthquake Engineering, 17WCEE*.

NZS 4219 (2009). "Seismic performance of engineering systems in buildings". Standards New Zealand.

NZS 1170.5 (2004). "Structural Design Actions" – Part 5, ZEALAND, STANDARDS NEW, Wellington, NZ.

Poso, M. (2014). "Studio del Sistema di connessione alla struttura portante per facciate continue del tipo a cellula sottoposte ad azione sismica", Master's Thesis, Politecnico di Milano (in Italian).

Sucuoglu, H. and Vallabhan, C.V.G. (1997). "Behaviour of window glass panels during earthquakes". *Engineering Structures*, 19, pp.685-694.

A.3 Seismic risk

Recently, the scientific community has been focused on structural risk assessment because the building heritage is out of date and it would be convenient to retrofit or reinforce instead of demolishing and rebuilding.

In this regard, the present studies on the structural behaviour of glazing walls are of paramount importance since the knowledge of the response under exceptional actions is limited to a few experimental results, as reported in literature (Memari et al. 2004). Thus, research in the structural sector has focused heavily on assessing the vulnerability of glass structures, with the aim of understanding and improving structural performance, and safeguarding human life.

In this section, some basic concepts in relation to seismic engineering applied to civil construction are explained. Firstly, the seismic risk is defined as follows:

$$\mathbf{Risk} = \mathrm{f}\,(\,Hazard; Vulnerability; Exposure) \tag{21}$$

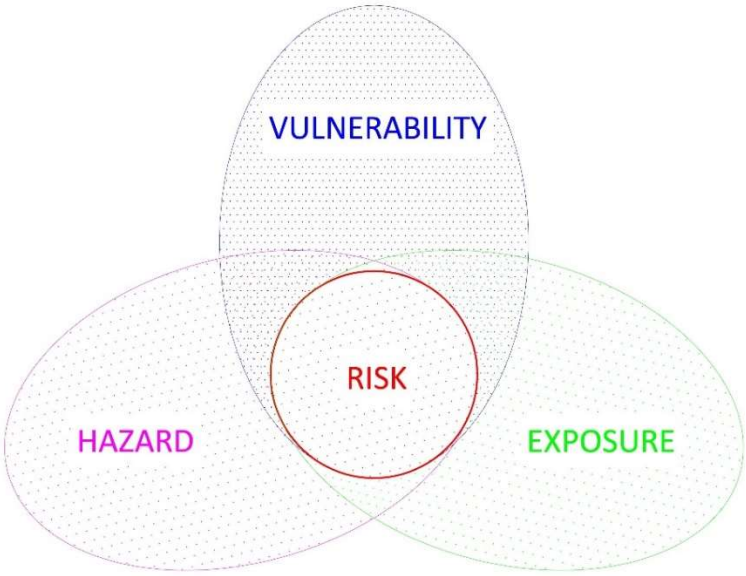

Figure A.3-1 Seismic risk definition as the convolution of parameters (figure © S.Mattei)

The seismic risk denotes, in a quantitative way, the expected losses expressed in terms of human lives and damage, direct and/or indirect, due to an estimated seismic event for the reference area (Faccioli et al. 2005). In probabilistic terms, it defines the probability of collapse, in a time interval of interest (Iervolino et al. 2007), corresponding to a certain limit state exceeded.

In other words, it can be evaluated as a combination of the three factors in Eq. 21; where:

- *Seismic hazard* is tied to the attitude of a site to be affected by earthquakes, which can cause damages and losses. It denotes the probability of exceeding a given intensity threshold, in a predetermined period of time (also known as return of period, T_r). By this logic, a site can have more dangerous hazard than another, given a certain earthquake intensity and different frequency (Cito 2019). The seismic hazard analysis is the basis of the seismic risk assessment and the determination of the seismic actions of the project (Cornell et al. 2000).
- *Vulnerability* represents the susceptibility of a building to be damaged as a consequence of a seismic event. This factor, conversely to the seismic hazard, is the only variable which depends on the construction properties and refers to the assessment of losses in terms of goods, people and activity. Obviously, in the first case, the structure, non-structural components (infill, equipment and accessories) and content (furniture, computers, storage) are taken into account.
- *Exposure* is a measure of the losses due to the expected damages, depending on the Importance Class of the buildings involved, that is based on the classification of constructions in terms of consequences of an interruption of service or collapse (*Class I*: constructions with the only occasional presence of people, agricultural buildings. *Class II*: constructions designed for normal crowd levels, without essential public and social functions. Factories. *Class III*: constructions designed for significant crowd levels. *Class IV*: constructions with important public or strategic functions, including those with relevance in disaster management. (CNR-DT210 2013). Together with the vulnerability, the exposure is an anthropic factor and, therefore, governable through interventions aimed at eliminating the critical issues.

Finally, it is necessary to define the type of risk analysis according to the purpose to be achieved and the preferred methodology: risk analysis relied on a probabilistic approach or scenario analysis based on a deterministic methodology.

In the earthquake risk management, the seismic risk assessment is of paramount importance and the components of risk analysis can be addressed with HAZUS methodology (Molina et al. 2010), which is one of the most widely used methods of assessing seismic vulnerability and developed by the Federal Emergency Management Agency) in collaboration with the National Institute of Building Sciences (NIBS). This method is based on the observation of the damage suffered by buildings during past earthquakes through the use of databases in which information is collected about the post-earthquake structural damage. In general, the information contained in the database is linked to the construction characteristics of a certain building: the place subject to the earthquake, and the characteristics of the earthquake (magnitude, distance, etc...). The HAZUS method identifies smaller classes of buildings, to which a capacity curve and a certain standard deviation are associated, and allows to calculate the probability of a class of damaged structures. This method can be considered

quantitative, although there is a component based on expert judgement and heuristic data.

In last decades, several European projects have been settled in order to contribute in developing tools and methodologies for assessing risk, such as SYNER-G (Pitilakis et al. 2014a; Pitilakis et al. 2014b) or RISK-UE (Mouroux et al. 2006). The latter ('An advanced approach to earthquake risk scenarios with applications to different European towns') began in January 2001 and ended in 2004 and involved the evaluation of multiple seismic scenarios, probable in Europe and, in particular, in seven cities. The research project was born with the main purpose of identifying a way to assess the damage caused by a seismic event, and thus improve emergency management.

This research work aims to underline the importance of improving the seismic design of curtain wall for which the analysis of the performance in terms of force and permissible displacements are still very limited.

A.3.1 Vulnerability assessment

In order to reduce the gap between the widespread use of glass and the actual little knowledge of the involved mechanisms in structural response, which leads to an over-conservative design, the study of vulnerability at different structural levels can be very interesting.

Seismic vulnerability is an intrinsic property of buildings that provides information about the aptitude of a building to resist against a seismic event of defined intensity and its susceptibility to damage following the occurrence of the earthquake. In brief, the *vulnerability* of a building represents the relationship between the seismic action and the damage caused to the structure, and can be evaluated in ways more or less complex depending on the specificity of the study case. The formulation of the chosen methodology is a function of the definition and nature of the criteria that affect the investigated performance. The level of detail in this assessment can go from the expedited evaluation procedures based on visual observation to the most extensive and elaborated based on non-linear modelling strategies (Maio et al. 2015).

With reference to the definition of vulnerability, namely the propensity of a structure to suffer damage in terms of losses (i.e., human, economic, functional, political or social), it is possible to distinguish three types as follows:

- Direct vulnerability when the damage of the single element is investigated. This definition relates structural capacity and demand in terms of strength and/or structure displacement.
- Induced vulnerability when the damage is a consequence of the collapse of a single physical element. This definition is therefore strongly influenced by the context in which the building is located.
- Indirect vulnerability which concerns the effects that occur post-event. And in particular refers to the phases of first emergency.

Furthermore, a classification of the four main approaches to estimate a building's vulnerability lists the following (Porter et al. 2007):

i. Analytical approaches;
ii. Empirical approaches;
iii. Expert judgment elicitation approaches;
iv. Hybrid approaches.

In the following sub-sections an in-depth description is carried out by exposing some case studies by the literature within the European context.

Analytical approaches:

Generally, the analytical fragility function is constructed by taking into account a specific structural model of the asset group where the connection between the building feature and its performance and damage state is uniquely defined. According to Porter (2003), every version of this method consists in four phases (see Fig. A.3-2) by assuming some initial data, such as site location, structural and architectural characteristics, or mechanical and electrical components. After describing the geometry and all the parameters which could be affected by earthquakes (from the structural elements to the facilities), firstly a Hazard Analysis is performed in order to select the ground motion records in terms of acceleration to use during the second step. Secondly, a structural analysis is needed to define the force and the deformation measures which are imported in the identification of the engineering demand parameter (EDP) thresholds according to the significant damage states. Then, the fragility assessment is carried out in the third stage, obtaining probabilistic damage measures. Finally, the aim of the vulnerability analysis is achieved with the last step consisting of a loss analysis or repair cost estimation through the generation of damage-to-loss functions.

The major advantage of the just explained method is the possibility of developing fragility curves of building types have not yet been subjected to a seismic event, or of considering records in an arbitrary way. At the same time, the estimation of building behaviour by means of theoretical approaches or numerical modelling is very time-consuming and the lack of experimental results for the validation could lead to unreliable fragility functions.

In this context, Padgett and DesRoches (2008), developed fragility curves for classes of retrofitted bridge systems through an analytical methodology in order to compare different retrofit measures; and Rota et al. (2010) proposed a new approach based on nonlinear analysis for masonry buildings. Moreover, a comprehensive review on the analytical fragility methods in seismic risk assessment was provided by Moussa et al. (2016) by considering different level of nonlinearity of the materials and models.

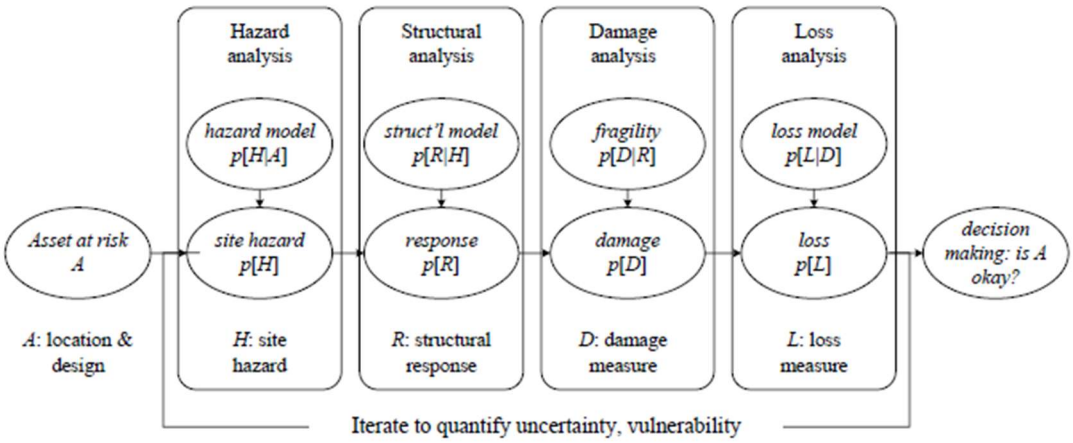

Figure A.3-2 Flowing chart for estimating seismic vulnerability by analytical method[2]

Empirical approaches:

Amongst others, the empirical vulnerability approach is the most desirable due to the increased reliability made possible from the direct observation of laboratory data or results from the real life. In this case, empirical fragility functions are created by approximating experimental data derived as pairs of environmental excitation, such as parameters describing ground motion, and failure condition based on the limit state definition. Despite the credibility of the method, several issues are recognized in the procedure. For instance, in case of results from observations on site, the main limits relate to the lack of data for a homogeneous range of intensity measure, but in particular at high levels of excitation, and to the difficulty in estimating them due to the low number of station sources which record seismic events or to the presence of the background noise. Moreover, with regard to the laboratory experiences, the cost for carrying out specific tests are elevated and thus, the repeatability of the test in not always feasible.

In earthquake engineering, many empirical fragility functions are developed for the most widespread building typologies, at least since Kustu et al. (1982), according to Porter (2007). Moreover, Sarabandi et al. (2004) published some notable works where a set of earthquake-related fragility functions for three building types (i.e., wood, steel and concrete moment resisting frame) were developed for several strong earthquakes, as a function of four different characterization of seismic performance.

The majority of recent study focuses on this vulnerability approach. For instance, Liu et al. (2021) studied the feasibility of implementing empirical method on RC columns by employing an innovative SVM-based model, which is able to provide the mean of column deformation capacities.

[2] Figure adapted with permission from (Porter 2003) under the terms and conditions of CC-BY license agreement

A.3 Seismic risk

In Italy, the effects of the two main seismic events, which are the ones occurred in Irpinia (1980) and L'Aquila (2009) were considered in modelling of empirical fragility curves depending on the building height and the type of design (i.e., gravity and seismic load before and after 1981) by Rosti et al. (2020). Otherwise, a "Compendium and Guide for Selection" for existing empirical vulnerability and fragility functions was drawn up by Rossetto et al. (2015).

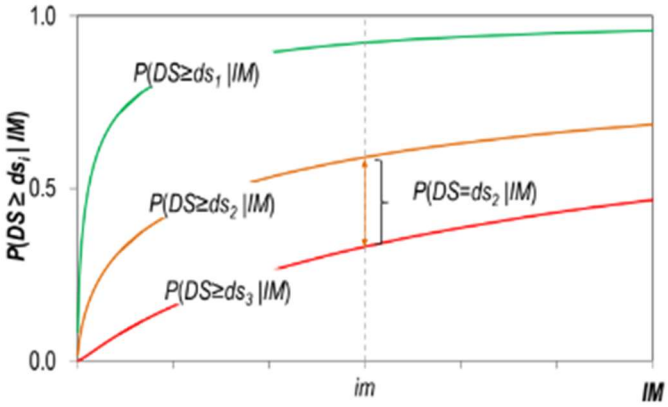

Figure A.3-3 Fragility curves corresponding to a specific damage states for the same building class [3]

A large database of empirical fragility curves for different types of curtain walls in terms of inter-storey drift ratios was developed in the FEMA P-58 (2012) or by O'Brien et al. (2012) based on many previous experimental campaigns.

Expert judgment elicitation approaches:

Expert judgement elicitation approaches are generally used when empirical data are difficult to obtain and analytical models take more time than expected. For these reasons, the expert opinion is very efficient at very low costs. Otherwise, although several authors consider this data paired with the test outputs in their study, the method reliability is affected by the missing cross-validation in case of particular and innovative structural system or the underestimation of uncertainty.

In literature, some expert-opinion fragility functions are based on the possibility to assign to each structure a vulnerability index that is a numerical value determined according to some rules as a function of some parameters not interpreted in a typological meaning, but as symptoms of suitability to withstand earthquake.

According to the Porter's guide (2007), ATC.13 (Applied Technology Council 1985) is one of the best examples where some experienced people, with the asset class under consideration (i.e., buildings, bridges, ect.), guess or judge failure probability as a function of external loads and obtain a huge amount of judgment-based fragility functions for Californian buildings.

[3] Figure reproduced with permission from (Rossetto et al. 2015) under the terms and conditions of CC-BY license agreement

Hybrid approaches:

A common practice consists of the derivation of fragility curves by combining the three above-mentioned approaches, for instance by using different sources of data and the most widely employed integrate empirical data with results from numerical or analytical simulations, such as in Calvi et al. (2006), since the combination of two or more methods should compensate the lack of the others.

Li et al. (2013) proposed a two-step approach for developing fragility curves in structural engineering field by using a combination of analytical and empirical methods. The initial finite element model of Meloland Road Overcrossing bridge was carried out in ZEUS-NL and, successively, some eight experimental cyclic tests based on a particular Bayesian framework were performed on small-scale pier in order to validate the analytical results.

A.3.1.1 Fragility assessment

In risk assessment, vulnerability curves are commonly used to express uncertain loss related to a measure of seismic ground motion intensities by generally referring to a particular asset class. Part of the process of assessing vulnerability, and in particular the representation of the correlation between the physical damage and the earthquake's intensity, involves the development of fragility curves. In this sense, the classification of the building stock considering the characteristics of the investigated structural typology is the most important step which affects the reliability of fragility curves. In literature, many fragility curves are available with regard to ordinary buildings thanks to their relevance as a tool for the seismic risk assessment.

By the theoretical definition, fragility curves express the probability, for a range of earthquake intensities, of reaching or exceeding damage states derived by previous studies related to a specific system or a generic building type that can be grouped for similarities in structural behaviour. Thus, fragility function can be used to obtain a realistic estimation of a certain level of damage that an asset would withstand due to a given seismic event and it is generally formulated as follows (Wen et al. 2004):

$$F_i(IM|EDP_i) = \Phi\left(\frac{\ln\left(\frac{IM}{\mu_i}\right)}{\beta_i}\right) \tag{22}$$

Where:

- Φ denotes the standard normal cumulative distribution function;
- subscript *i* represents the damage state of interest;
- μ_i is the median for IM parameter given EDP_i, derived from a regression analysis;
- β_i is the standard deviation of the natural logarithm derived according to FEMA P-58 guidelines (2012) as expressed by Eq. (23);

$$\beta_i = \sqrt{\beta_r^2 + \beta_u^2} \quad (23)$$

Where:

- β_i is the measure of uncertainty associated with the component;
- β_r expresses the random variability in the experimental data by tests or post-earthquake observations;
- β_u represents tests uncertainty associated to actual installation and loading conditions on the building as compared to the component testing conditions in the laboratory, and the adequacy of sample size in order to accurately represent the real variability.

The ATC-58 Guidelines recommends minimum values of β_u equal to 0.25 if one of the following points occurs; otherwise, a value of 0.10 can be considered:

- the number of tested specimens is five or higher;
- all specimens are tested with the same configuration and subjected to the same loading protocol.

However, it is necessary to distinguish the case in which a single building is to be studied, taking into account all its peculiarities and characteristics, by the analysis of a sample of buildings of a certain area represented by a typological class.

In the second case, a class of buildings that can be represented by macro-parameters (such as shape, size, year of construction, etc…) is considered. In this way, a "medium" structure is analysed with the difficulty of considering, with an analytical approach, the influence of all macro-parameters on its seismic behaviour. For this reason, the fragility curves of typological classes of buildings are constructed empirically through a statistical analysis of the data concerning the behaviour of buildings, all of which can be traced back to the same class.

Instead, in the first case, given the amount and accuracy of the input data, it is possible to go to high levels of motion detail and derive the fragility functions for damage levels data analytically obtained through numerical simulations on the seismic structural response. In general, given the large computational and modelling burden this operation is aimed at buildings with particular strategic or historical monumental value.

A.3.2 Cloud method for fragility derivation

In this thesis, a special mention is given to the Cloud method, an analytical approach for deriving fragility curves. It is easy to understand that the assessment of vulnerability is generally affected by the methodology choice, which is strictly dependent on available observation data, structure type and any suitable probabilistic model in considering epistemic uncertainties (i.e., record-to-record variability, uncertainties in section capacities, in material properties and construction details) which derive from lack of knowledge. In civil engineering, the types of uncertainties involved

in structural modelling, especially in assessing safety, are difficult to consider since the randomness (Kim 2018).

Cloud Method (Jalayer et al. 2015) is a numerical procedure in which a building numerical model is subjected to a series of nonlinear dynamic analyses for a set of unscaled seismic records.

Following the schematic representation of the synthetic framework proposed in Mattei et al. (2021) and represented in Fig. A.3-4, the generation of fragility curves by means of Cloud method comprises some steps, which are later explained.

Firstly, the detailed identification of the case-study is needed to build a Finite Element Model which can grasp the actual system behaviour by taking into account all the possible collapse mechanisms with all the issues these involve. This also concerns the knowledge of primary dynamic properties of the structure, starting from natural frequencies of the system and participating masses through a modal analysis. Then, the fundamental period, T_1, is used for selecting a consistent range of intensity measure (IM) and thus the seismic inputs in the subsequent numerical analyses. The basic principle in the arbitrary collection of earthquake records from European Strong Motion Database relates to provide a more even distribution of cloud data, in order to avoid too high scattering in the analyses outputs.

The nonlinear dynamic analyses are performed in a FE software, and a linear regression analysis can then be employed to fit cloud data for deriving the first two statistical moments of the probability cumulative function by Eq. (22) which describes the fragility curves.

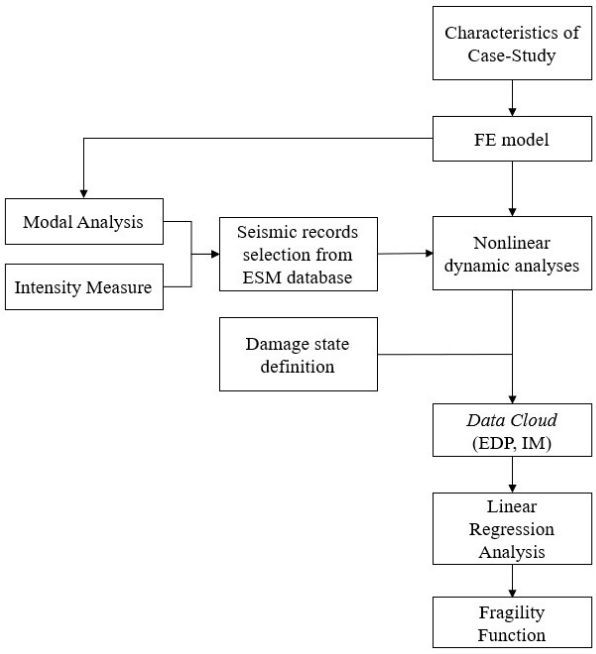

Figure A.3-4 Flow-chart on the numerical implementation of the analytical fragility function[4]

Consequently, the mean and the standard deviation are calculated as follows:

[4] Figure reproduced with permission from (Saji et al. 2018) under the terms and conditions of CC-BY license agreement

$$\vartheta_i = \mathrm{a} + \mathrm{b}\ln(EDP_i) \tag{24}$$

$$\beta_i = \beta_r = \sqrt{\frac{(\ln(IM_i) - (\mathrm{a} + \mathrm{b}\ln(EDP_i))^2}{\mathrm{n} - 2}} \tag{25}$$

Where *a* and *b* are the constant coefficients which represent the intersection with the Y axis and slope of the regression line, respectively. While n is the number of specimens.

Furthermore, the subscript *i* indicates the damage state and its estimation, according to limit state criteria, is an essential step consisting of thresholds identification after the engineering demand parameter (EDP) definition.

In this sense, the knowledge of progressive collapse in case of a façade is explored. Typically, the damage of a glazing curtain wall begins with the gasket degradation which is followed by an initial glass cracking and crushing, both representative of the serviceability damage states that reflect the water permeability and air leakage and other indirect failures. Finally, the glass fallout occurs as an ultimate damage state representing a potential life safety risk.

A.3.2.1 Record selection and fragility parameters definition

The randomness of the seismic action is mainly linked not only to the intensity of the earthquake that, in general, is expressed in terms of peak ground acceleration (PGA), but also to the duration of the earthquake and its frequency. Given the geometric dimensions of glazing system, the stiffness and the masses of the components of the structure, the fundamental period is uniquely determined and the elastic spectral acceleration could be another exhaustive parameter to express the intensity of the earthquake.

Moreover, since the fragility curves are expressed specifically as a function of the intensity measures (IMs), in their generation, they are not considered in the single analysis as a random variable but the entire range of interest is explored. In fact, the selection of records is treated as a discrete variable with constant probability density using a set of 45 natural accelerograms from those identified in the ESD (European Strong-Motion Database) and reported in Appendix A.

In particular, the ground motion records (in Appendix A) used were characterized by a moment magnitude (Mw) between 5.3 and 7.6, an epicentral distances (R) ranging between 32 km and 263.4 km, and a soil class type A or B (EC8 classification). Moreover, the corresponding response spectra are depicted in Fig. A.3-5 highlighting the mean one.

The main difference in using Cloud Analysis refers to the low computational effort due to the smaller number of nonlinear analyses that have to be carried out.

The maximum *drift ratio*, computed as the maximum in-plane displacement in the direction of earthquake excitation divided by the height, was chosen as the reference EDP for the frame.

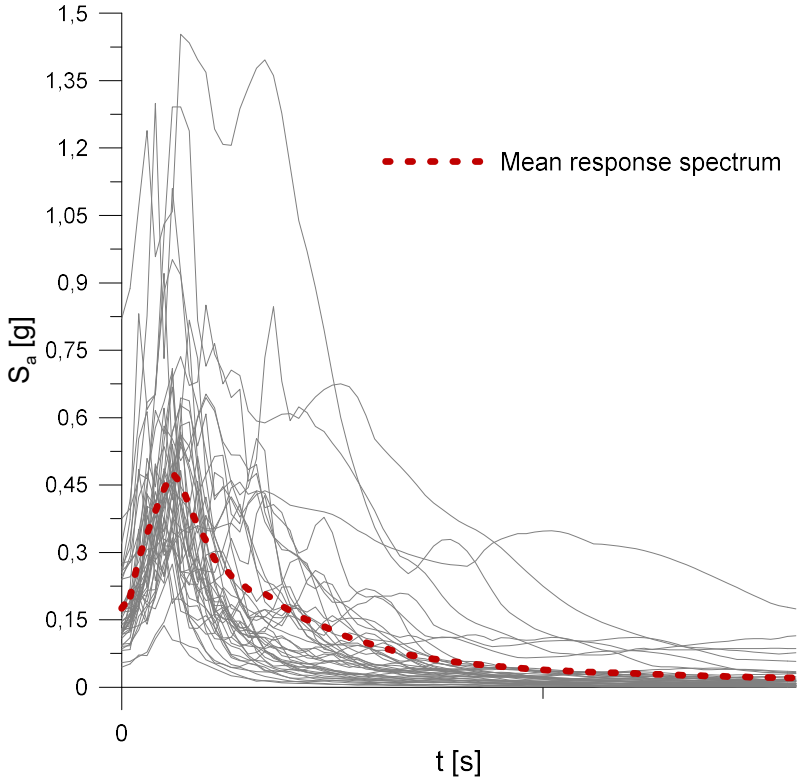

Figure A.3-5 Response spectra of the chosen records

A.3.3 References

ATC-13. (ATC) Applied Technology Council (1985). “ATC-13, Earthquake Damage Evaluation Data for California”. Redwood City, CA, 492 pp.

Calvi, G. M., Pinho, R., Magenes, G., Bommer, J. J., Restrepo-Vélez, L. F., Crowley, H. (2006). “Development of seismic vulnerability assessment methodologies over the past 30 years”.*ISET journal of Earthquake Technology*,43(3), pp.75-104.

Cito, P. (2019) “Tools, methodologies and discussions about single-site, multi-site and sequence-based probabilistic seismic hazard analysis”. Ph.D. dissertation, University of Naples “Federico II”.

CNR. CNR-DT210. Istruzioni per la Progettazione, L’esecuzione ed il Controllo di Costruzioni con Elementi Strutturali di vetro; Guide for the Design, Construction and Control of Buildings with Structural Glass Elements; National Research Council of Italy (CNR): Roma, Italy, 2013. (In Italian).

Cornell, C. A., Krawinkler, H. (2000). “Progress and challenges in seismic performance assessment”. *PEER Center News,* 3(2), pp.1-3.

Wen, Y. K., Ellingwood, B.R., Bracci, J. (2004). “Vulnerability Function Framework for Consequence-Based Engineering”, Mid-America Earthquake Center, CD Release 04-04.

Faccioli, E., Paolucci, R. (2005) “Elementi di sismologia applicati all’ingegneria”, *Pitagora editrice*, Bologna.

Federal Emergency Management Agency (FEMA) (2012). “Seismic Performance Assessment of Buildings”, Volume 1, Methodology. Report No. FEMA P-58-1, Washington DC.

Iervolino, I., Manfredi, G., Polese, M., Verderame, G. M., Fabbrocino, G. (2007). “Rischio sismico di classi di edifici in cemento armato”. *XII Convegno Nazionale “L’Ingegneria Sismica in Italia.*

Kim, J.J. (2018). “Development of Empirical Fragility Curves in Earthquake Engineering considering Nonspecific Damage Information”, Advances in Civil Engineering, pp.1-13.

Kustu, O., D.D. Miller, and S.T. Brokken (1982). Development of Damage Functions for Highrise Building Components, for the US Department of Energy, URS/John A Blume & Associates, San Francisco, CA.

Jalayer, F., De Risi, R., Manfredi, G. (2015). "Bayesian Cloud Analysis: efficient structural fragility assessment using linear regression", *Bulletin of Earthquake Engineering*, 13, pp.1183-1203.

Li, J., Spencer Jr, B. F., Elnashai, A. S. (2013). "Bayesian updating of fragility functions using hybrid simulation". *Journal of Structural Engineering*, 139(7), pp.1160-1171.

Liu, Z., Guo, A. (2021). "Empirical-based support vector machine method for seismic assessment and simulation of reinforced concrete columns using historical cyclic tests", *Engineering Structures*, 237 (2021) 112141.

Mattei, S., Bedon, C. (2021). "Analytical fragility curves for seismic design of glass systems based on cloud analysis", *Symmetry*, 13(8), 1541.

Memari, A. M., Behr, R. A., & Kremer, P. A. (2004). "Dynamic racking crescendo tests on architectural glass fitted with anchored pet film". *Journal of architectural engineering*, 10(1), pp.5-14.

Molina, S., Lang, D. H., Lindholm, C. D. (2010). "SELENA–An open-source tool for seismic risk and loss assessment using a logic tree computation procedure". Computers & Geosciences, 36(3), pp.257-269.

Mouroux, P., Le Brun, B. (2006). "Risk-UE project: an advanced approach to earthquake risk scenarios with application to different European towns". In: Oliveira CS, Roca A, Goula X (eds) Assessing and managing earthquake risk. Springer, Netherlands, pp 479–508.

Moussa, A., Christou, P., Kyriakides, N. (2016). "The developments of the analytical fragility methods in seismic risk assessment – A review". *Journal of Sustainable Architecture and Civil Engineering*, 16.

O'Brien, W. C., Memari, A. M., Kremer, P. A., Behr, R. A. (2012). "Fragility Curves for Architectural Glass in Stick-Built Glazing Systems", *Earthquake Spectra*, 28(2), pp.639-665.

Padgett, J.E., DesRoches, R. (2008). "Methodology for the development of analytical fragility curves for retrofitted bridges", *Earthquake Engineering and Structural Dynamics*, 37, pp.1157-1174.

Pitilakis, K., Crowley, E., Kaynia, A. (eds) (2014a). “SYNER-G: typology definition and fragility functions for physical elements at seismic risk”, vol 27, *Geotechnical, geological and earthquake engineering*. Springer, Heidelberg. ISBN 978-94-007-7872-6.

Pitilakis, K., Franchin, P., Khazai, B., Wenzel, H. (eds) (2014b). “SYNER-G: systemic seismic vulnerability and risk assessment of complex urban, utility, lifeline systems and critical facilities. Methodology and applications”, *Geotechnical, geological and earthquake engineering*. Springer, Heidelberg. ISBN 978-94-017-8834-2.

Porter, K. A. (2003). “An overview of PEER’s performance-based earthquake engineering methodology”. *Proceedings Ninth International Conference on Applications of Statistics and Probability in Civil Engineering (ICASP9)* July 6-9, 2003, San Francisco, CA. Civil Engineering Risk and Reliability Association (CERRA), pp.973-980.

Porter, K. A., Kennedy, R., Bachman, R. (2007). “Creating Fragility Functions for Performance-Based Earthquake Engineering”, Earthquake Spectra, 23, pp.471-489.

Rossetto, T., Ioannou, I., & Grant, D. N. (2015). “Existing empirical fragility and vulnerability functions: compendium and guide for selection”, *Global Earthquake Model Foundation*, Pavia, Italy.

Rosti, A., Del Gaudio, C., Rota, M., Ricci, P., Di Ludovico, M., Penna, A., Verderame, G. M. (2020). “Empirical fragility curves for Italian residential RC buildings”, *Bulletin of Earthquake Engineering*, 19, pp.3165-3183.

Rota, M., Penna, A., Magenes, G. (2010). “A methodology for deriving analytical fragility curves for masonry buildings based on stochastic nonlinear analyses”, *Engineering Structures*, 32(5), pp.1312-1323.

Sarabandi, P., Pachakis, D., King, S., Kiremidjian, A. (2004). “Empirical fragility functions from recent earthquakes”. *Proceedings 13th World Conference on Earthquake Engineering*, Vancouver, B.C., Canada.

Simoes Dias Maio, R., Tsionis, G. (2015). “Seismic fragility curves for the European building stock: review and evaluation of existing fragility curves”. EUR 27635. Luxembourg (Luxembourg): *Publications Office of the European Union*; 2015. JRC99561.

A.4 Finite Element Modelling

A.4.1 Selected glass configurations

This Chapter presents the structural model employed in the Cloud Analysis in the case of different curtain wall configurations from a wide database of architectural glass experimental testing results that were performed by researchers at the Pennsylvania State University and University of Missouri and presented in several research papers (Behr et al. 1996, Behr 1998, and Memari et al. 2003), to which are added some further experimental tests conducted by O'Brien et al. (2012). In the latter study, that can be considered as a representative starting point for assessing component fragility, fifteen samples are used. As already mentioned, nine of these were chosen based on the amount of data available from past published research which consists of the most common glazing systems used on buildings, while the last six samples were introduced because of particular interest in the authors. These configurations (Table A.4-1) contain different glazing characteristics that are known to affect the seismic performance of glass, which include glass type, system type (Mid-Rise Curtain Wall or Storefront), aspect ratio, glass configuration (monolithic, Laminated, or IGU), aspect ratio, and glass-to-frame clearances. The various glass configurations have a square corner geometry, cut (or raw as termed by some glass manufacturers) corner and edge finish conditions, dry-glazed and used aluminium Kawneer 1600^{TM} CW framing.

For sake of clarity, the experimental campaigns consisted of crescendo tests that was carried out as introduced in Section 3.2.3. It deals with an in-plane dynamic tacking tests performed on the configurations summarized in the Table A.4-1 using the racking facility according to AAMA 501.6 (2001), as shown in Fig. A.2-3, which consists of two horizontal steel tubes situated on roller assemblies. The drift amplitude is applied to glass components through a hydraulic actuator arm placed at the lower horizontal. In particular, the drift protocol consists of a series of ramp-up and constant drift amplitudes with different frequencies depending on the total applied racking displacements (i.e., 0.8 Hz up to 75 mm and 0.4 Hz for higher values of drift). The drift corresponding to the glass fallout, for each set of specimens that counts a minimum number equals to three, refers to the occurrence of the first one of the following conditions: (1) by definition of 'glass fallout', when the area of the shattered fragments is higher than 650 mm^2; (2) a drift index divided by the panel height is higher than 10%; (2) the drift amplitude achieve the maximum value in the 'crescendo test', which is 150 mm.

It is worth to mention that, during the phase of data observation, the differences between Serviceability or Ultimate limit states are very subtle. The main damage states indicated by the experimental tests can be listed as follows: glass cracking, gasket seal degradation and glass fallout. The first two damage states are considered serviceability,

whereas glass fallout is considered an ultimate failure, because is a life safety hazard disrupting normal building operations and exposing the building interior to external actions.

Table A.4-1 Configuration characteristics (O'Brien et al. 2012)

Config. ID	System	Glazing Type	Glass Panel (H x B)	Clearance	Aspect ratio	No. of Specimens
1	MR	6 mm – AN monolithic	1829 x 1524 mm	11 mm	6:5	7
2	MR	25 mm – AN IGU	1829 x 1524 mm	11 mm	6:5	7
3	MR	6 mm inner AN/ 6 mm outer AN LAM (0.030 in. PVB) – IGU	1829 x 1524 mm	11 mm	6:5	6
4	MR	6 mm inner AN/ 6 mm outer AN LAM (0.060 in. PVB) – IGU	1829 x 1524 mm	11 mm	6:5	6
5	MR	6 mm inner AN/ 13 mm outer AN LAM (0.030 in. PVB) – IGU	1829 x 1524 mm	11 mm	6:5	6
6	MR	6 mm AN LAM (0.030 in. PVB)	1829 x 1524 mm	11 mm	6:5	24
7	SF	6 mm – AN monolithic	1829 x 1524 mm	10 mm	6:5	12
8	SF	25 mm – AN IGU	1829 x 1524 mm	15 mm	6:5	12
9	SF	6 mm AN LAM (0.030 in. PVB)	1829 x 1524 mm	10 mm	6:5	9
10	MR	6 mm – AN monolithic	1829 x 1524 mm	0 mm	6:5	2
11	MR	6 mm – AN monolithic	1829 x 1524 mm	3 mm	6:5	2
12	MR	6 mm – AN monolithic	1829 x 1524 mm	6 mm	6:5	3
13	MR	25 mm – AN IGU	1829 x 1524 mm	6 mm	6:5	1
14	MR	6 mm – AN monolithic	2438 × 1219 mm	11 mm	2:1	2
15	MR	6 mm – AN monolithic	1219 × 2438 mm	11 mm	1:2	2

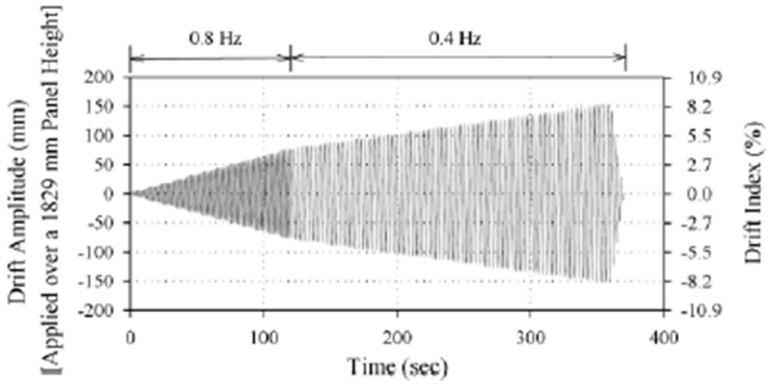

Figure A.4-1 The entire time history of the crescendo test [5]

[5] Figure reproduced with permission from (Memari et al. 2003) under the terms and conditions of CC-BY license agreement

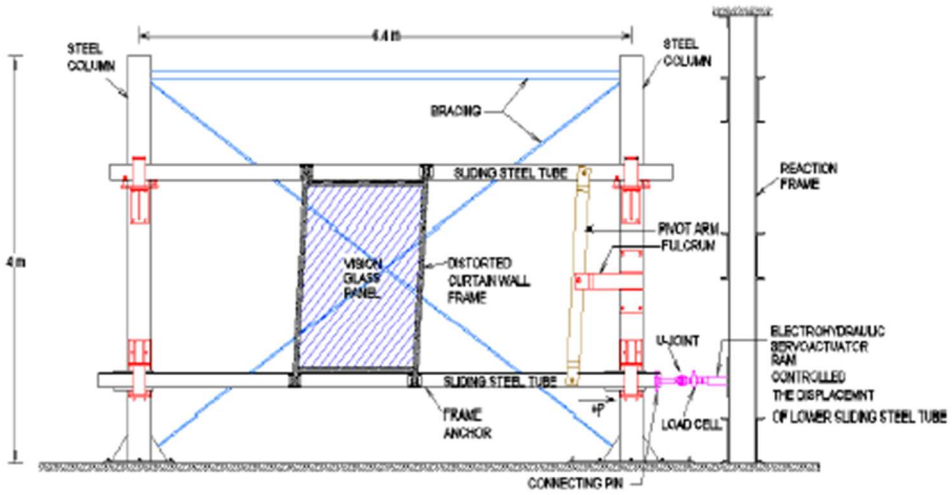

Figure A.4-2 Racking facility and setup used for the mid-rise CW testing[6]

All the configurations analysed in the present study have been selected from the work conducted by O'Brien et al. (2012) for developing empirical fragility curves giving fundamental indications related to the damage state involved in the seismic performance of a glazing system.

The performance of glass subjected to lateral loading is known to be sensitive to its glass-to-frame clearance, but as of yet no studies have been performed which isolate this glazing detail. In this regards, the selection consider some configurations characterized by the same materials and geometry and a varying glass-to-frame clearance from 3 mm to 11 mm.

The chosen glazing case studies consist of a 6 mm annealed (AN) monolithic panel, an aluminium mid-rise framing system, and rubber gaskets are used for the dry connection between the two materials along the entire perimeter. Moreover, a laminated glass unit with a thickness of 6.76 mm (3 mm annealed glass + 0.76 mm PVB + 3 mm annealed glass) has been also considered keeping a constant clearance of 11 mm, that corresponds to the recommended value for practical building installations.

Table A.4-2 Geometric characteristics of the investigated configuration

Config. ID	System	Glazing Type	Glass Panel (H x B)	Clearance	Aspect ratio
A	CW	6 mm – AN monolithic	1829 x 1524 mm	3 mm	6:5
B	CW	6 mm – AN monolithic	1829 x 1524 mm	11 mm	6:5
C	CW	6 mm AN LAM (0.030 in. PVB)	1829 x 1524 mm	11 mm	6:5

[6] Figure reproduced with permission from (Behr et al. 1995) under the terms and conditions of CC-BY license agreement

In addition, Memari et al. (2004) conducted a pilot study, with a very limited number of specimens, on the evaluation of seismic capacity of glass curtain walls fitted with anchored PET film. The benefits in using this type of additional tools have been investigated, with experimental tests and numerical analysis, and exposed in a dedicated Part of this dissertation (i.e., Part B).

A.4.2 Numerical code: ABAQUS/CAE

Finite element analysis (FEA) is intended as the computer simulation technique used in engineering analysis and is based on the finite element method (FEM), which aims to solve generic problems represented by differential equations. This method allows the transition from a continuous problem to a discrete problem through the application of successive steps necessary to obtain the solution to the problem. In particular, starting from the fundamental equations that regulate the phenomenon to be studied, introducing appropriate approximations of the variables involved, a solution is sought that, although approximate, tends to the exact solution as the number of discrete variables increases.

For the numerical simulations covered by this paper, the commercial calculation code ABAQUS Standard v6.12 (2017) has been chosen.

The choice fell on a commercial calculation code, instead of a specific computing platform developed for research purposes, since the application of this study is based on the substantial know-how accumulated as a result of the previous activity relating to the material, whose the mechanical response under seismic action has been investigated.

Abaqus can solve complex design problems that span relatively simple linear analyses or more demanding nonlinear simulations, in which the non-negligible effects related to geometric nonlinearity are related to materials and boundary conditions. Any geometry ca be practically modelled and the behaviour of a multiplicity of materials can be simulated. For the analysis of models constituted by more elementary parts, it has the faculty to associate each of them with the respective model of material and to define the interactions between them. Abaqus has two main products for the analysis: Abaqus/Explicit and Abaqus/Standard. Abaqus/Explicit is particularly suitable for the simulation of impulsive dynamic events while Abaqus/Standard is the ideal solution for dynamic and static low-speed events.

Generally, there are several methods to obtain numerical solutions approximated to the equation of the motion of a structure based on the characteristics of the problem to be analysed, which can be linear or non-linear, and according to the degree of accuracy required.

Moreover, the integration methods of the motion equation may be classified as implicit or explicit. The explicit methods obtain the values of dynamic quantities such as displacement, velocity and acceleration at time ($t + \Delta t$) starting only from the values of

these quantities at time t, and are characterized by being conditionally stable. In general, the stability limit, that is the maximum value of the time step Δt for which the solution converges towards the solution of the problem, can be approximated as the time taken by an elastic wave to pass through the smallest element in the system. The implicit methods of integration of the equation of motion, exceed the limit due to the maximum dimension of the time step basing the solution of the equation at time (t + Δt) not only on the values of the dynamic quantities at time t but also on some of the same quantities at time (t + Δt) and for this reason they are called implicit.

Recalling the D'Alembert's principle of dynamic equilibrium, a system is in equilibrium at each time instant if the sum of all the forces acting on the mass is zero including the fictitious inertia force. Thus, the overall dynamic equilibrium equation between external (F) and internal (I) applied forces, for each instant of time, by Eq. (26):

$$\mathrm{F} - \mathrm{I} = \mathrm{M}\ddot{\mathrm{u}} \tag{26}$$

Where $\mathrm{M}\ddot{\mathrm{u}}$ denotes the nodal accelerations and M is the mass matrix.

The explicit central-difference operator satisfies the equilibrium at the beginning of the increment, t; the accelerations at that time are used to advance the velocity ($\dot{\mathrm{u}}$) and the displacement (u) solutions to the next step, calculated by Eq. (27) and Eq. (28).

$$\dot{\mathrm{u}}_{\left(\mathrm{i}+\frac{1}{2}\right)} = \dot{\mathrm{u}}_{\left(\mathrm{i}-\frac{1}{2}\right)} + \frac{\Delta \mathrm{t}_{(\mathrm{i}+1)} + \Delta \mathrm{t}_{(\mathrm{i})}}{2} \ddot{\mathrm{u}}_{(\mathrm{i})} \tag{27}$$

$$\mathrm{u}_{(\mathrm{i}+1)} = \mathrm{u}_{(\mathrm{i})} + \Delta \mathrm{t}_{(\mathrm{i}+1)} \dot{\mathrm{u}}_{\left(\mathrm{i}+\frac{1}{2}\right)} \tag{28}$$

Where:

- u corresponds to a degree of freedom;
- i refers to the increment number;
- $\dot{\mathrm{u}}_{\left(\mathrm{i}-\frac{1}{2}\right)}$ and $\mathrm{u}_{(\mathrm{i})}$ are the velocity and the displacement from the previous increment, respectively.

It is worth to note that an explicit algorithm is conditionally stable. Moreover, the stable time increment in the numerical analysis depends on element density, size and stiffness. Since it is calculated for each mesh element, the smallest one is consider as the stable time for the complete model. An approximation of Δt can be obtained as follows:

$$\Delta t \approx \frac{L_{min}}{c_d} \tag{29}$$

Where L_{min} represents the smallest mesh element dimension and cd is the dilatational wave speed as function of λ_0 and μ_0, defined in terms of material moduli from the relative constitutive law.

In implicit algorithms, on the other hand, the temporal step solution is obtained through the knowledge of the solution (accelerations, velocities and displacements) at step i and the conditions imposed at step (i+1). An example of this approach is the

Newmark method (1959) or a method derived from and implemented in ABAQUS/Standard, the so-called HHT method (Hilber et al. 1978). In general, for structural applications, the implicit integration methods usually provide acceptable solutions with some precautions about time steps depending on the stability limit of simple explicit schemes, but the response is increasingly diverted from the actual one to the increase in time,Δt. Consequently, the main disadvantage regards the cost in terms of time; and a solution is not always achievable due to nonlinearities. Eq. (30) and (31) express the dynamic equations to be solved implicitly.

$$u_{(i+1)} = u_{(i)} + \Delta t \dot{u}_{(i)} + \Delta t^2 \left[\left(\frac{1}{2} - \beta\right) \ddot{u}_{(i)} + \beta \ddot{u}_{(i+1)}\right] \quad (30)$$

$$\dot{u}_{(i+1)} = \dot{u}_{(i)} + \Delta t\left[(1-\gamma)\ddot{u}_{(i)} + \gamma \ddot{u}_{(i+1)}\right] \quad (31)$$

Where:

- u corresponds to a degree of freedom;
- i refers to the increment number;
- $\ddot{u}_{(i)}$, $\dot{u}_{(i)}$ and $u_{(i)}$ are the acceleration, the velocity and the displacement from the previous increment, respectively;
- $\ddot{u}_{(i+1)}$, $\dot{u}_{(i+1)}$ and $u_{(i+1)}$ are the acceleration, the velocity and the displacement from the consecutive increment, respectively.

According to Hilber et al. (1978), β is calculated as $\frac{1}{4}(1-\alpha)^2$ and γ is derived as $\frac{1}{2} - \alpha$. Each time step size change introduces some numerical noise into the solution of the dynamic problem. For this reason, a modest level of numerical damping, introduced by the HHT algorithm, appears necessary to overcome the inconvenience of the automatic incrementing procedure. A parameter value of α is 0=05 in most applications seems to quickly remove high frequency numeric noise, without having any noticeable effect on system response at the most significant frequencies (low frequencies).

A.4.3 Case study 1: Glass panel

A.4.3.1 Geometries of case-studies

Of paramount importance is the fine-tuned modelling in Abaqus/CAE as shown in Figure A.4-4. All glass configurations were characterized by the same glass size (h x b = 1829 x 1524 mm). In particular, the three-dimensional solid model consists of a panel modelled with a perfectly linear elastic behaviour; while an elastoplastic mechanical type was chosen for the aluminium frame and the transparent interlayer of PVB. However, the simplified assumption on glass behaviour is monitored by controlling that the tensile strength has never been achieved. Finally, the stiffness of axial connectors used for reproducing gaskets performance in the plane of the glass panel was calculated

as a function of typical mechanical parameters, mesh dimensions and different clearances.

The first phase of the modelling step consists of creating all the different elements, which establishes the glass panel totally framed, in the *Part* module. In this module it is possible to define each part of the model specifying if you want to define a three-dimensional geometry, flat or with an axis of symmetry and if they are deformable rather than rigid elements. Depending on the choices made, the geometry will be drawn through solid shapes, shells, wires or points. The created parts are 3 for each configuration, including the 2 mullions, 2 transoms and the glass panel because of the possibility of replicability of the aluminium components, and have all been designed directly on the software in the section Sketches. All elements are modelled as brick elements (C3D83 type).

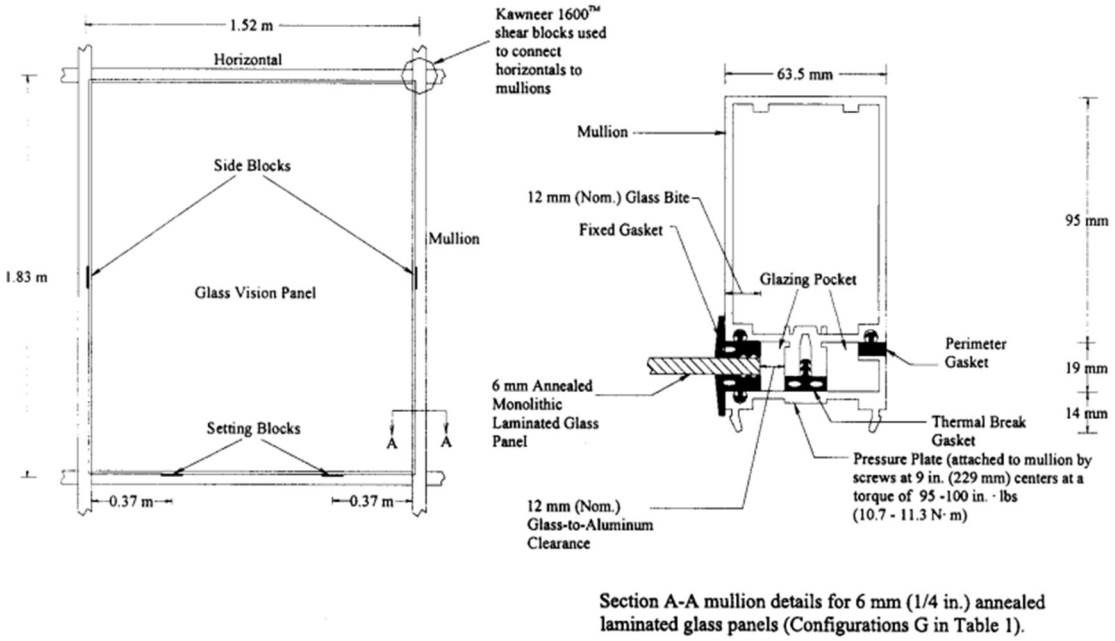

Figure A.4-3 Glazing details for the mid-rise aluminium curtain wall-framing system[7]

In order to reduce the computational burden of analyses, the cross-section of aluminium elements is simplified respect to the actual one represented in Fig. A.4-3. The simplification is allowed because it does not involve substantial changes in terms of characteristics of the section, also from the torsional point of view. The validation consisted of numerical analyses simulating crescendo test and performed for each configuration taking into account that the results from previous experimental campaigns aren't available in the literature, but the order of magnitude of the mean reference parameter (drift ratio = displacement/panel height), can be obtained from O'Brien et al. (2012) work.

[7] Figure reproduced with permission from (Memari et al. 2003) under the terms and conditions of CC-BY license agreement

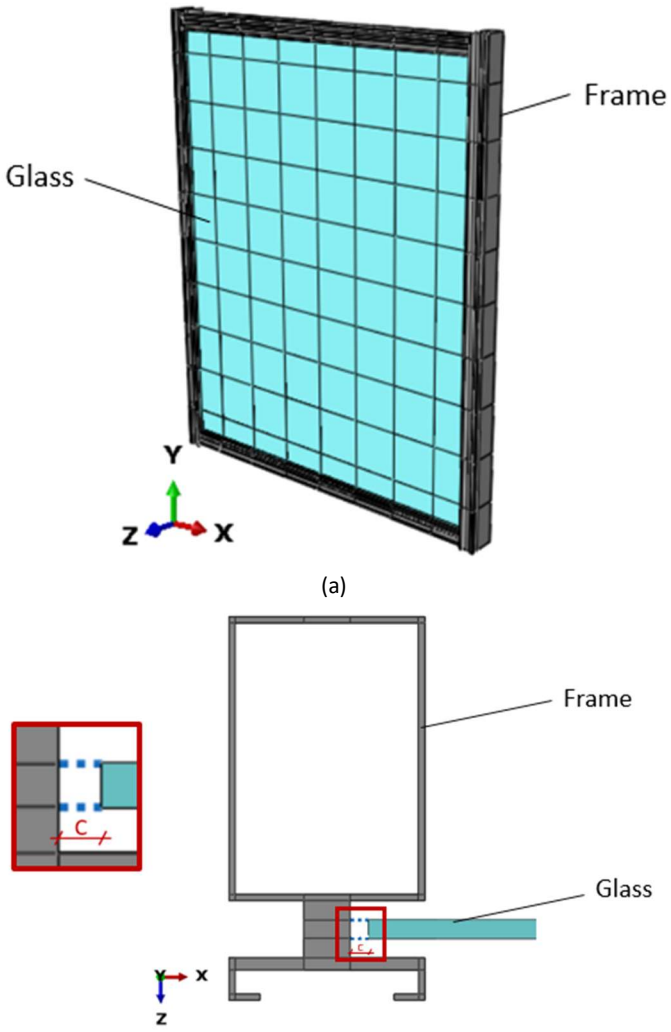

Figure A.4-4 Numerical model of (a) glass panel and (b) the schematic detail of glass-to-frame connection where *c* means nominal 'clearance'

A.4.3.2 Material characteristics

The glass shows a perfectly elastic and isotropic behaviour with brittle breakage. By not presenting yield, it does not have the possibility to redistribute the efforts as is the case for example in the case of aluminium. The mechanical properties in elastic field for glass and aluminium were characterized based on nominal product standards, thus resulting in E_g = 70 GPa and E_a = 69 GPa elastic moduli, ν_g = 0.23 and ν_s = 0.34 the corresponding Poisson ratio values and ρ_g = 2760 kg/m^3 and ρ_a = 2980 kg/m^3 the nominal density, respectively. Careful attention was paid for any possible fracture of materials, with $\sigma_{t,g}$ = 45 MPa (EN 572-2 2012) the characteristic tensile resistance of annealed glass and $\sigma_{y,a}$ = 150 MPa the yielding stress for aluminium. Moreover, in post-yielding field, for aluminium was considered a plastic behaviour with strain hardening as shown in Fig. A.5-5. Furthermore, a material model originally designed for reinforced concrete

elements exhibiting quasi-brittle behaviour was used to describe the post-breakage behaviour of glass. This model, known as the *concrete-damage plasticity* (CDP) model, is an updated version of the Drucker-Prager criterion proposed by Lubliner et al. (1989). Some numerical applications of this damage model to glass components can be found in Bedon et al.2016 and Bedon et al.2017. It incorporates isotropic compressive and tensile plasticity of concrete to capture its non-elastic behaviour while incorporating its isotropic damaged elasticity. The CDP model assumes that the primary failure mechanisms are tensile cracking and compressive crushing of the material. Scalar damage variables are employed to depict the constitutive behaviour of concrete. The figure shows that the yield surface's development is determined by equivalent plastic strains in both tension and compression. Two damage variables, d_t and d_c, are utilized to illustrate the reduction of elastic stiffness on the strain softening branch of the stress-strain curve and can range from zero to one, with zero representing an undamaged material and one indicating a complete loss of strength.

With regards to the laminated section, the peculiarities of a polymer interlayer are: viscosity; high sensitivity to temperature variations and humidity changes with a consequent deterioration. Since it is constrained to the glass through a chemical bond, the failure of laminated glass plates depends on the effectiveness of the connection. In this study, although the PVB is a hyper-elastic material with a hardening profile, Polyvinyl-butyral was modelled as an anisotropic and homogenous material and its constitutive law was assumed elastoplastic. The main mechanical parameters are reported in Table A.4-3.

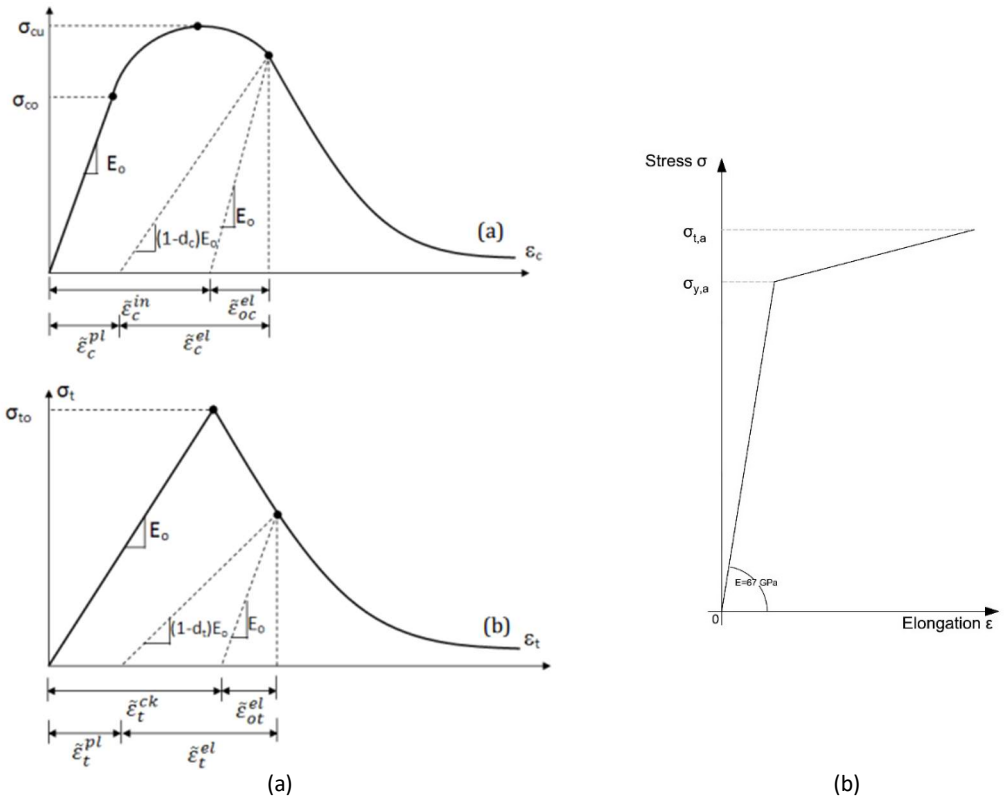

Figure A.4-5 Constitutive law of (a) glass under axial compressive (a) and tension(b) strength (Abaqus User Manual, 2008) and (b) aluminium.

Table A.4-3 Alluminium characteristics for FE model

Material	Elastic modulus	Poisson ratio	Yield stress	Plastic strain at yield point	Ultimate stress	Ultimate plastic strain
	[MPa]		[MPa]		[MPa]	
Aluminium	69000	0.34	150	0	190	0.08

Table A.4-4 Glass characteristics for FE model

Material	Elastic modulus	Poisson ratio	Tensile strength	Compressive strength	G_f	$U_{ck,t}=u_{ck,c}$
	[MPa]		[MPa]	[MPa]	[J/m^2]	[mm]
Glass	70000	0.23	45	1000	3	1.33 x 10^{-4}

A.4.3.3 Boundary conditions and interactions

At the initial step, the panel was restrained externally in order to allow its displacement in the plane, simulating the boundary conditions of the setup in the case of the dynamic racking test for calibrating the connector stiffness. Subsequently, for the application of the acceleration records at the lower transom, the degree of freedom in the excitation direction was inactivated.

With regard to the constraints between the different part of the *Assembly* model, two interactions have been created and defined with the aim of simulating the glass-frame and transom-mullion connections. Generally, there are several '*Connectors'* types provided in the Abaqus library, which are capable of connecting various regions of the model, with a connection between two points or a point and the ground. Moreover, the main advantages of using them relate to the easy convergence also by setting a connection between elements of different computational entities and the possibility of defining their properties by assigning a specific moment-curvature or stress-strain response in the connector section assignment. The transom-mullion connection was obtained by means of the *hinge* connector, which allows you to tie all degrees of freedom between two points, except the moment along a desired direction, this choice is managed through the definition of a local reference system, with the aim of lightening the analysis and reducing the computational burden.

Finally, the glass-frame connection models the behaviour of the perimeter gasket seal placed both along the inner and the outer face of the glass panel, by inserting *planar connectors* providing a slide-plane connection between two nodes and a revolute connection about the normal direction to the plane (1). In particular, the two connected nodes are bonded along directions 2 and 3 lying on the glass plane, and the corresponding stiffness can be calculated as a function of calibration analyses.

(a) (b)

Figure A.4-6 Planar connector type for glass-frame connection; and (b) hinge connector type for transom-mullion connection (Abaqus library)

The calibration method is developed with reference to the code ABAQUS and consisted of defining the connector stiffness as input data by comparison of 3D finite element model results with experimental data. Particularly, the outputs compared are in terms of maximum drift ratio calculated as the relative displacement (Δ) divided by h equals 1.6 m (see Fig. A.4-7 (a)).

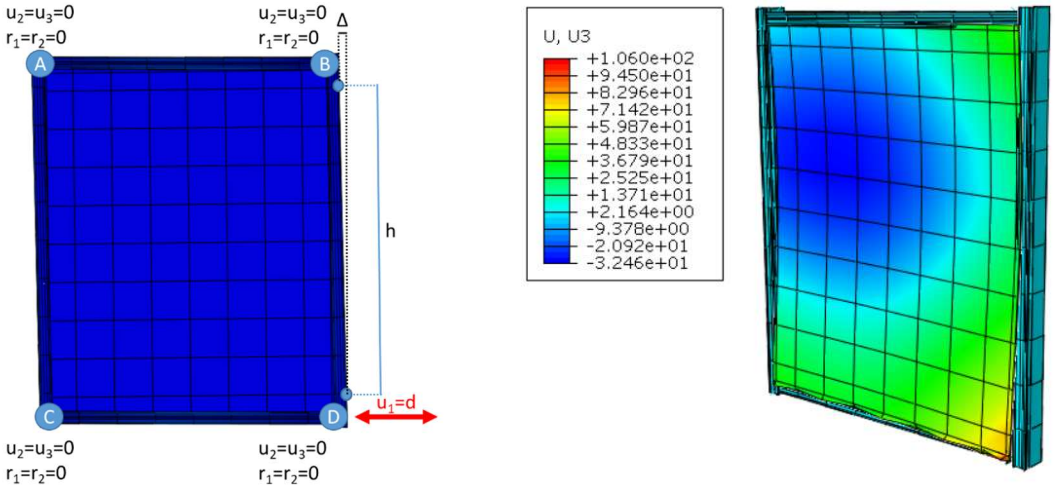

(a) (b)

Figure A.4-7 (a) FE model for calibration analyses and (b) a typical fallout limit state (measures in mm)

The actual experimental data aren't available for each configuration, but the median value provided by O'Brien et al. (2012) corresponds to the mean value of drift ratios by experimental dynamic racking tests. In Fig. A.4-8 and A.4-9 the simulation results in terms of relative displacement (Δ) as a function of time are shown.

Generally, the use of a few experimental outputs for the calibration of a numerical model, does not guarantee an adequate reliability of simulation results when the finite element model is extended to other configurations. Thus, the maximum values before the loss of numerical stability due to the fallout failure (see Fig. A.4-7 (b)) have been compared to drift ratio = 0.0107 for Configuration A and 0.0219 for Configuration C. In particular, after some iterations the best agreement between experimental and numerical results is provided by D22 and D33, mechanical characteristics of the planar connector, equal to 20 N/mm and 5 N/mm, respectively.

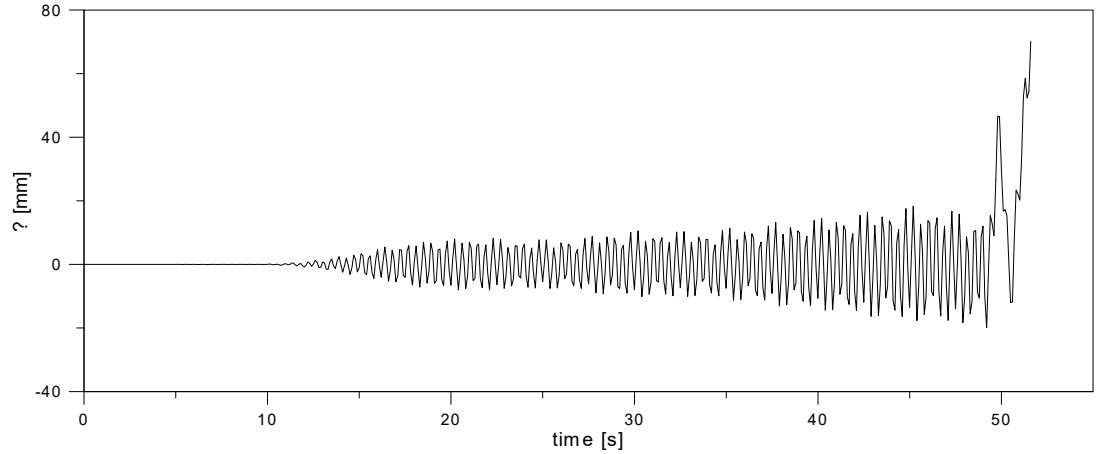

Figure A.4-8 3D representations of MRF structure from SAP2000

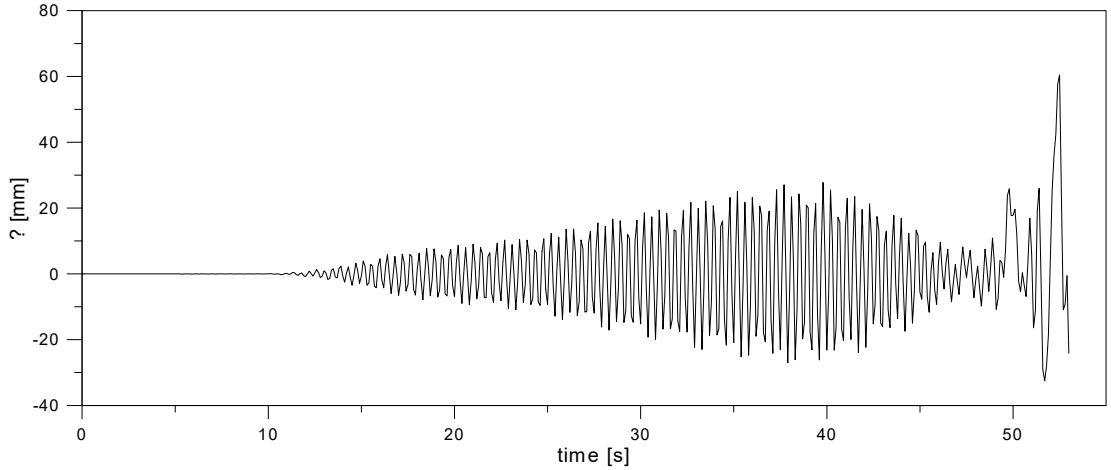

Figure A.4-9 3D representations of MRF structure from SAP2000

A.4.4 Case study 2: Full-scale application

The FEM results are a more accurate representation of reality than the simplified analytical calculations provided by previous studies. The goal of the Finite Element modelling is to investigate the influence of different configurations on the reliability of the fragility assessment of the panel and structur, and on the possibility of streamlining the computational effort. A detailed description of the newly designed full-scale application will be given in the following sections.

A.4.4.1 Primary steel frame

For the design of the four-story Moment Resisting Frame (MRFs) system corresponding to the primary structure, and then with the function of supporting building loads and statically connecting its parts, the basic design rules according to Eurocode 1998 for steel structures were used. In particular, linear dynamic analyses were performed by means of Sap 2000.v21 software (see Fig. A.4-10).

A.4 Finite Element Modelling

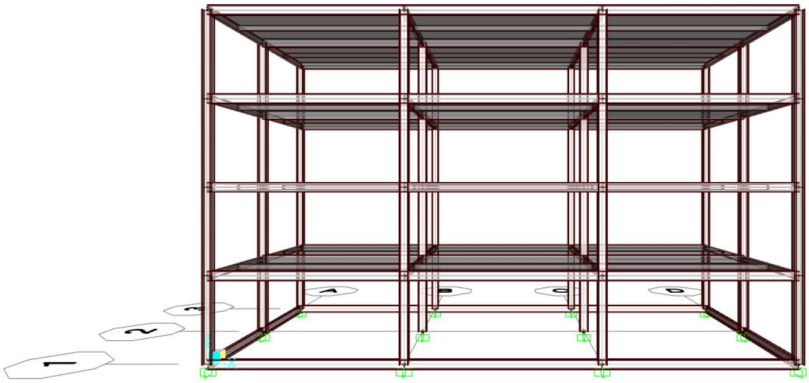

Figure A.4-10 3D representations of MRF structure from SAP2000

According to European practice, the elastic spectrum is defined as based on seismic input characteristics indicated in Section A.3.2.1, taking into account the magnitude ranges covered by the considered accelerograms and obtaining a Type 2 spectrum for soil type B (i.e., Table A.4-4 and Fig. A.4-11). Thus, the overall analysis of the structure is carried out by the elastic method. The effects of the actions have been evaluated under the hypothesis that the stress-strain behaviour of the material is indefinitely linear. Testing in the elastic range is feasible for all types of sections, taking into account, if necessary, local instability effects based on a section classification which is defined according to the width/thickness ratio of the plates, the state of stress and the strength class of the material.

Table A.4-5 Values of parameters describing the Type 2 elastic spectrum

Soil Type	S	T_B	T_C	T_D
A	1.0	0.05	0.25	1.2
B	1.35	0.05	0.25	1.2
C	1.5	0.10	0.25	1.2
D	1.8	0.10	0.30	1.2
E	1.6	0.05	0.25	1.2

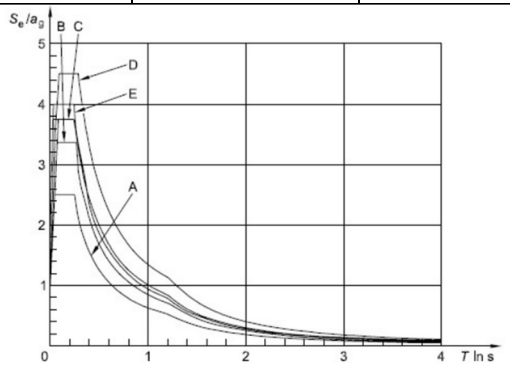

Figure A.4-11 Type 2 elastic response spectrum for soil types from A to E (Damping equals to 5%)

With regards to the geometry of the structure: the steel frame structure has a squared plane with 19.5×9.2m, three-bay by two-bay spans with length of 6.5m in X direction and 4.6m in Y direction (see Fig. A.4-12). Finally, the total height equal to 12 m is equally distributed, thus each story is 3 m high. This is a typical steel building designed and constructed according to the current design provisions and practices in Italy.

A.4 Finite Element Modelling

In the analysed structure, due to double symmetry in the x and y directions, the centre of mass CM and the centre of rigidity CR are both, at all levels, corresponding to the geometrical centre of the building floors. The loads acting on the floors, resulting from the loads analysis, were distributed on the load-bearing membranes according to their area of influence. The action due to the structural own weight has been combined with the others (permanent, accidental and earthquake loads) by the load combinations described by the code in order to obtain the probabilistic values to be used later in the validations. By considering a steel-concrete floor system, the dead load (i.e., weight of all structural and non-structural elements) was assumed equal to 2.73 kN/m^2 and live load equal to 2 kN/m^2 in case of residential building (i.e., category A). The effects of the seismic action are evaluated considering the masses associated with the following gravitational loads: $G+\psi_{Ei}Q$. The total design mass for one storey is 61887 kg.

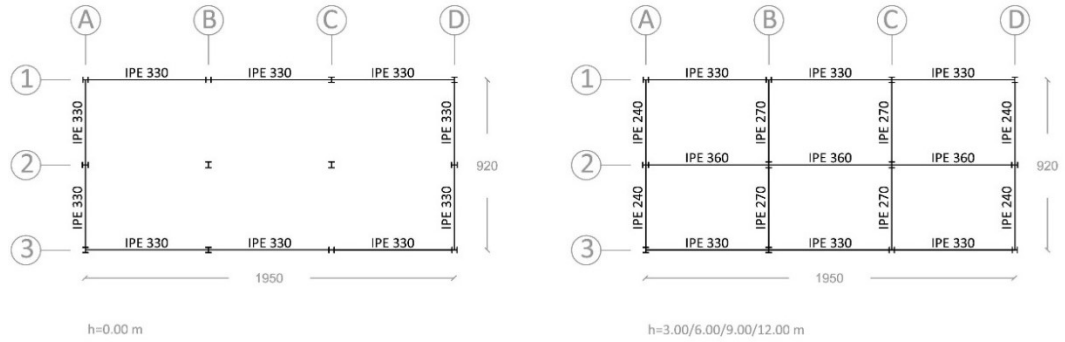

Figure A.4-12 MRF Structure in XY plane

Finally, the resulting sections have been dimensioned to ensure the crisis in the glass panel and therefore are oversized in relation to the seismic demand. The columns are made of HEB sections and the beams are made of IPE sections, but according to the capacity design approach some features, such as beam-to-column resistance hierarchy or drift limitations, strongly affect the final sizing of the members that are summarized in Table A.4-5 and Table A.4-6.

Table A.4-6 Sections of MRF system in X direction

Floor	X direction							
	Alignment 1 and 3				Alignment 2			
	Column		Beam		Column		Beam	
	External	Internal	External	Internal	External	Internal	External	Internal
I	HEB 300	HEB 300	IPE 330	IPE 330	HEB 340	HEB 340	IPE 360	IPE 360
II	HEB 300	HEB 300	IPE 330	IPE 330	HEB 340	HEB 340	IPE 360	IPE 360
III	HEB 300	HEB 300	IPE 330	IPE 330	HEB 340	HEB 340	IPE 360	IPE 360
IV	HEB 300	HEB 300	IPE 330	IPE 330	HEB 340	HEB 340	IPE 360	IPE 360

Table A.4-7 Sections of MRF system in Y direction

Floor	Y direction							
	Alignment A and D				Alignment B and C			
	Column		Beam		Column		Beam	
	External	Internal	External	Internal	External	Internal	External	Internal
I	HEB 300	HEB 340	IPE 240	IPE 240	HEB 300	HEB 340	IPE 270	IPE 270

II	HEB 300	HEB 340	IPE 240	IPE 240	HEB 300	HEB 340	IPE 270	IPE 270
III	HEB 300	HEB 340	IPE 240	IPE 240	HEB 300	HEB 340	IPE 270	IPE 270
IV	HEB 300	HEB 340	IPE 240	IPE 240	HEB 300	HEB 340	IPE 270	IPE 270

A.4.4.2 Geometric and material properties

In this study, dynamic FE analyses are conducted on a FE model for the four-storey steel frame structure (see Fig. A.4-13) by using Abaqus/CAE. In this context the façades along the perimeter of the structure have been modelled in order to address the actual seismic acceleration acting on the four vertices of the single squared panel.

For this reason, the modelling details are described in this section. The beams and columns embodied in steel primary structure consist of *beam elements*, that are one-dimensional elements in three-dimensional space that has stiffness associated with deformation of the only axis according to normal, tangential or torsional displacement components. Being a very complex Finite Element Model, it can be important to simplify the geometry in order to keep the analysis times contained. Thus, transoms and mullions were also included as beam elements; and glass panels as plane *shell elements*. The floor was modelled with the assumption of rigid as a *coupling constraint*, after the definition of the joint master as a reference point for each, corresponding to the centre of mass. In this case, all the degrees of freedom are constrained with a *structural distributing coupling* (see Fig. A.4-14 (a)) type to a reference point which coincides with the centre of mass for each storey and a total mass of 61887 kg was applied to it. The connection between the architectural glass curtain wall and the frame is considered rigid, as it turns out to be in real applications. For this reason, a *Beam Connector* (see Fig. A.4-14 (b)) was used by providing a rigid beam connection between two selected nodes chosen in correspondence of glass panel edges.

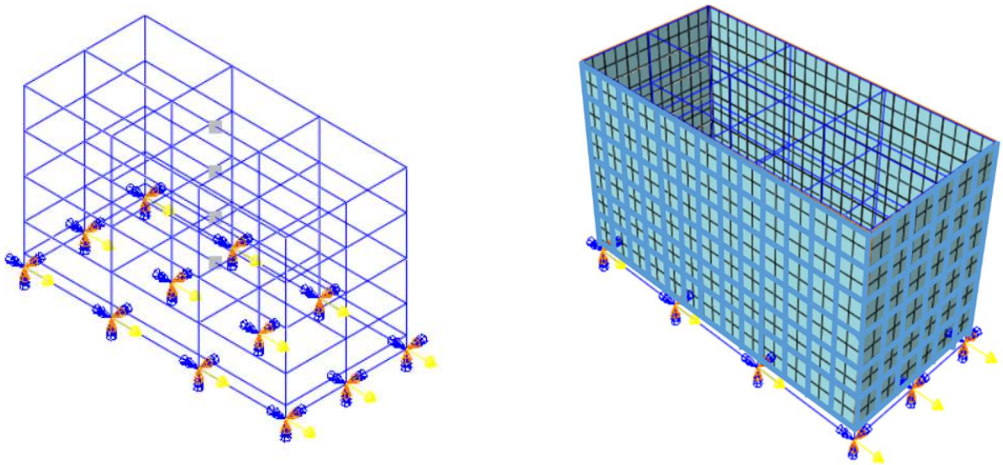

(a) (b)

Figure A.4-13 Abaqus model of (a) MRF structure and (b) with curtain-walls

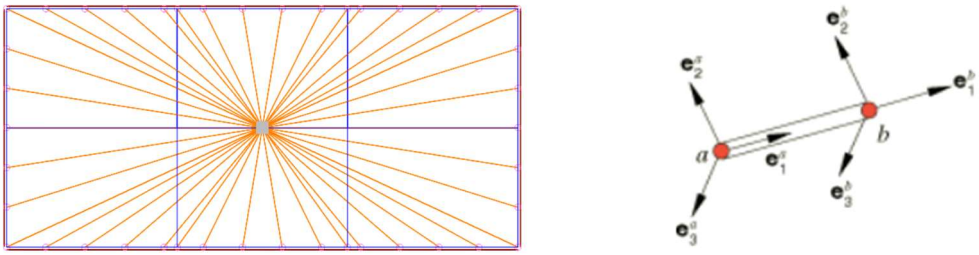

(a) b

Figure A.4-14 Distributing coupling constraint for 'rigid floor' assumption; and (b) beam connector type for façade frame-MRF connection (Abaqus library)

Finally, an elastic-linear behaviour and elastic-plastic behaviours were taken into account for glass, aluminium and steel, respectively, as reported in Table A.4-7. But given the geometry and the interactions, the material characterization is a fundamental step because in this case the damping was taken into account in the structure by introducing the Rayleigh coefficients. The full Rayleigh formulation is a linear combination of both mass and stiffness matrices or, in a simplified form, only stiffness proportional. This formulation leads, contrary to what happens in the frequency domain analysis, to a frequency-dependent damping that can more or less strongly affect the results of numerical analysis.

Starting from the system of equations (i.e., Eq. 32) which expresses the dynamic equilibrium of the overall structure, the solution can be achieved with two different integrations methods for which it is necessary to know the damping matrix [C]. In this sense, it's useful the Rayleigh formulation as expressed by Eq. 33.

$$[\mathrm{M}]\{\ddot{\mathrm{u}}\} + [\mathrm{C}]\{\dot{\mathrm{u}}\} + [\mathrm{K}]\{\mathrm{u}\} = -[\mathrm{M}]\{\mathrm{I}\}\ddot{\mathrm{u}}_{\mathrm{g}}(\mathrm{t}) \tag{32}$$

$$[\mathrm{C}] = \alpha_R[\mathrm{M}] + \beta_R[\mathrm{K}] \tag{33}$$

Where:

- [M], [C] and [K] are the mass matrix, the damping matrix and stiffness matrix, respectively;
- $\{\ddot{\mathrm{u}}\}$, $\{\dot{\mathrm{u}}\}$ and $\{\mathrm{u}\}$ are the acceleration vector, the velocity vector and the displacement vector, respectively;
- $\ddot{\mathrm{u}}_{\mathrm{g}}(\mathrm{t})$ represents the acceleration time-histories;
- $\{\mathrm{I}\}$ is the identity vector;
- α_R and β_R denotes Rayleigh coefficients.

Based on a modal analysis of the structure, according to a common procedure, two natural frequency values can be considered (ω_n and ω_m) corresponding to two natural periods (T_n and T_m) were considered and the coefficients were computed by Eq. 34 and Eq. 35 imposing the damping ratio ξ equals to 5%.

$$\alpha_R = \xi\frac{2\omega_{\mathrm{m}}\omega_{\mathrm{n}}}{\omega_{\mathrm{m}} + \omega_{\mathrm{n}}} \tag{34}$$

$$\beta_R = \xi \frac{2}{\omega_{\mathrm{m}} + \omega_{\mathrm{n}}} \tag{35}$$

Table A.4-7 Basic material parameters

Material	Elastic modulus	Poisson ratio	Yield stress	Plastic strain at yield point	Ultimate stress	Ultimate plastic strain
	[MPa]		[MPa]		[MPa]	
Aluminium	69000	0.34	150	0	190	0.08
Steel	210000	0.3	275	0	275	1
Glass	70000	0.25	45			
PVB	530	0.485	11	0	28	2

A.4.5 References

AAMA 501.6-01 (2001). “Recommended Dynamic Test Method for Determining the Seismic Drift Causing Glass Fallout From A Wall System”, AAMA, Schaumburg, IL, USA.

Bedon, C., and Louter, C, (2016). Finite-element analysis of post-tensioned SG-laminated glass beams with mechanically anchored tendons. *Glass Structures and Engineering*, 1, pp. 39-59.

Bedon C., and Louter, C, (2017). Numerical analysis of glass-FRP post-tensioned beams – Review and assessment. *Composite Structures*, 177, pp. 129-140.

Behr, R. A., Belarbi, A., and Culp, J. H., (1995a). Dynamic racking tests of curtain wall glass elements with in-plane and out-of-plane motions, *Earthquake Engineering and Structural Dynamics*, 24, pp.1-14.

Behr, R. A., Belarbi, A. (1996). “Seismic test methods for architectural glazing systems”. *Earthquake Spectra*, 12, pp.129-143.

Behr, R. A. (1998). “Seismic performance of architectural glass in mid-rise curtain wall”, *Journal of Architectural Engineering,* 4, pp.94-98.

EN 572-2:2012: Glass in building. Basic soda lime silicate glass products (2012).

Hilber, H. M., Hughes, T. J. R. (1978). “Collocation, dissipation and [overshoot] for time integration schemes in structural dynamics”. *Earthquake Engineering & Structural Dynamics*, 6(1), pp.99-117.

Memari, A. M., Behr, R. A., Kremer, P. A. (2003). “Seismic behavior of curtain walls containing insulating glass units”, *Journal of Architectural Engineering*, ASCE, 9, pp.70-85.

Memari, A. M., Behr, R. A., Kremer, P. A. (2004). “Dynamic racking crescendo tests on architectural glass fitted with anchored pet film”. *Journal of architectural engineering*, 10(1), pp.5-14.

Newmark, N. M. (1959). “A method of computation for structural dynamics”, *Journal of the engineering mechanics division*, 85(3), pp.67-94.

O’Brien, W. C., Memari, A. M., Kremer, P. A., Behr, R. A. (2012). “Fragility Curves for Architectural Glass in Stick-Built Glazing Systems”, *Earthquake Spectra*, 28(2), pp.639-665.

Simulia. ABAQUS v. 6.12 Computer Software and Online Documentation; Dassault Systems: Providence, RI, USA, 2017.

A.5 Discussion on the results

In this section, the results of the FEM model solving are reported, mainly in terms of probability cumulative functions, by providing a numerical method developed with detailed finite element models and based on tested configurations available in literature.

Generally, the seismic behaviour of the façades strictly depends on the seismic response of the primary structure and, in particular, they can be subjected to high stresses resulting from the inter-storey drift of the structure to which they are bound. It is possible to foresee, in fact, that the most difficult condition to consider, in the case of seismic analysis of the façades, is the in-plane drift, that is the relative displacement between two adjacent floors, which the façades must be able to withstand. At the same time, it is to be expected that this displacement will increase the stress of the glass sheets, given their fragile nature and rigid behaviour, while the frame having a globally ductile behaviour will be able to more easily follow the history of relative displacements, moving and deforming its shape. The main risks are the breakage of the glass sheets or the leakage of the panel from the façade plane and the consequent fall. In particular, it can happen that for the classic façade with mullions and transoms the vertical bearing elements tend to deform in their plane, causing on the infill changes of shape that cause breakages or expulsions from the plane.

As becomes clear from the previous chapters, the components constituting the overall building can be divided in two groups, and the derivation of the analytical fragility curves can be associated to the structural elements neglecting those that aren't involved in the designing process based on the seismic response. Although, non-structural elements have considered as secondary and, thus, expendable for structural capacity purposes, indirectly they contribute to the general response and represent a high share in the estimation of the vulnerability assessment's own losses. The probabilistic cumulative curves, as already mentioned, can be used to assess seismic performance of a structural system. In addition, since the combination of outputs is the basic concept of fragility for components, it is considered of great interest to contemplate an application of the predicted failure drifts for each CW-panel configuration on the overall building seismic response.

A.5.1 Description of numerical structural response

A.5.1.1 Full-scale application (CS#2)

In this context, as mentioned comprehensively in Section A.3.2, a Cloud analysis was carried out on the entire building. Thus, non-linear time-history analyses were

performed in Abaqus/CAE on the numerical FEM models thoroughly described in Section A.4 and the set of earthquake ground motion records used to define the seismic demand is already described in terms of characteristics measure parameter, such as magnitude (Mw), peak ground acceleration (PGA), or the spectral acceleration, ($S_a(T_1)$), which corresponds to the fundamental period of the structure.

Firstly, a modal analysis was carried out using Abaqus 6.11 linear perturbation frequency module. The higher frequency is 2.34 Hz, corresponding to a fundamental period of 0.43s in case of the steel frame alone, whereas T_1=0.39s after the application of glazing façade systems. The results from eigenvalue analysis show that the first period is in X-direction and for this reason the earthquake applied in the same direction will record the greatest shifts in the plane of the façade that are exactly those that are investigated for the analysis of the fragility of the curtain wall.

Fig. A.5-1 depicts a deformation example in X-direction of the model subjected to s#1 record (see Appendix A) in X-direction at the time corresponding to the displacement peak caused by the accelerogram. By way of example, the choice fell on the most significant input in terms of seismic demand. The unit of measure in Fig. A.5-1 (a) and (b) is the meter, then the maximum value of relative displacement between the top floor and the ground, in this case, is approximately around 6 cm for configuration #A and 5 cm for configuration #B and #C. Besides, also the deformation out-of-plane not appear to be negligible. Instead, it is worth to note by Fig. A.5-2 that there is a slight torsion which provides displacement out-of-plane in the millimetre range. At the same instant of time, Fig. A.5-3 and Fig. A.5-4 highlight separately the stress distributions in glass panels and in steel structure. The maximum value of the glass tensile stress is 28.5 MPa for configuration #A, 3.6 MPa for configuration #B and 3.4 MPa for configuration #C. The maximum value of the Von Mises stress for steel primary system is 250 MPa for configuration #A, 52 MPa for configuration #B and 40 MPa for configuration #C.

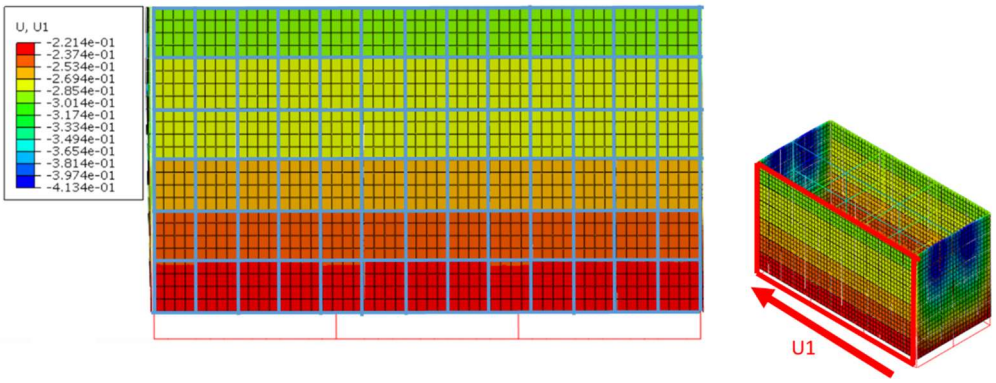

(a)

A.5 Discussion on the results

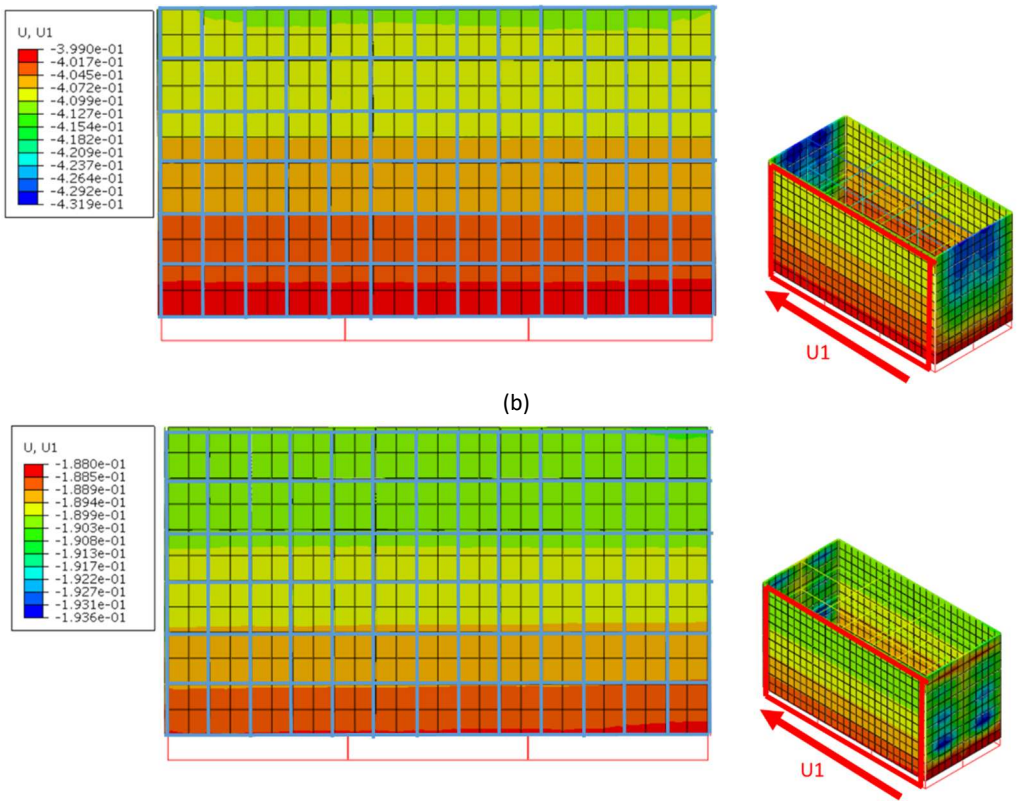

Figure A.5-1 Displacement distribution in X-direction for (a) Configuration #A; (b) Configuration #B and (c) Configuration C (measures in m)

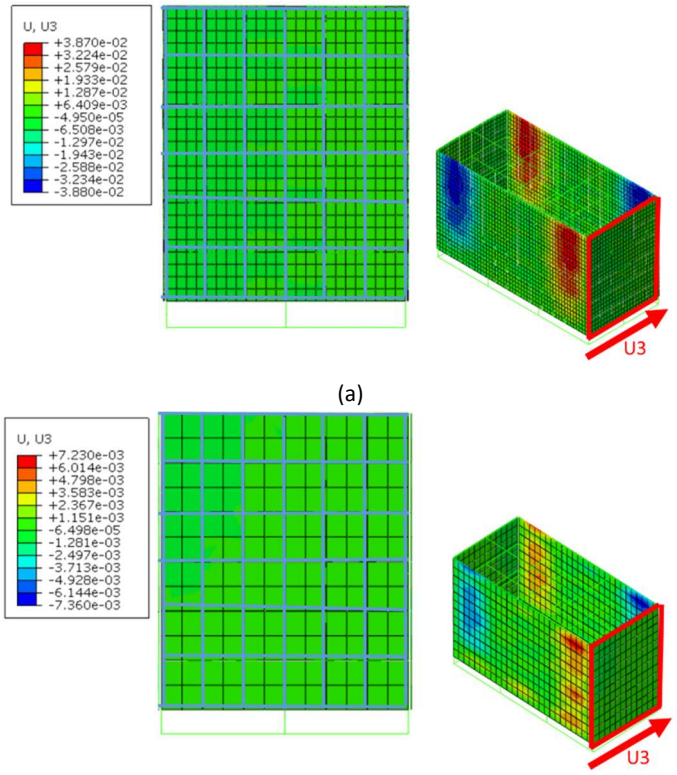

A.5 Discussion on the results

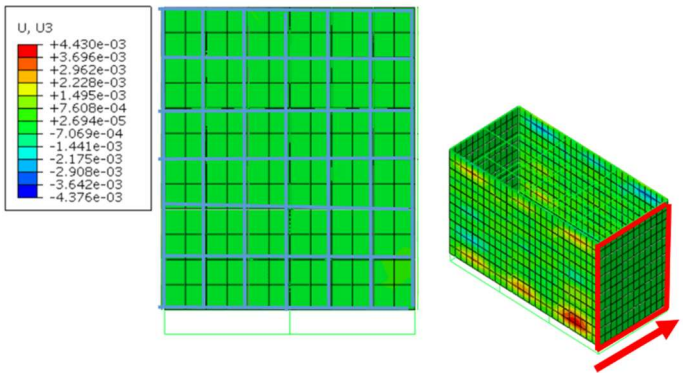

(c)

Figure A.5-2 Displacement distribution in Y-direction for (a) Configuration #A; (b) Configuration #B and (c) Configuration C (measures in m)

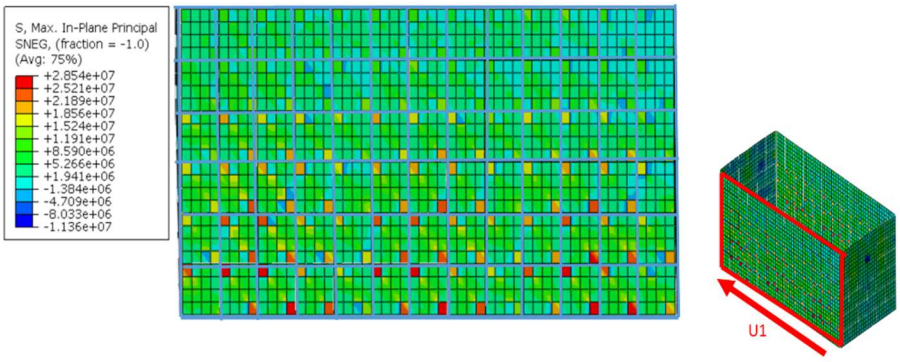

(a)

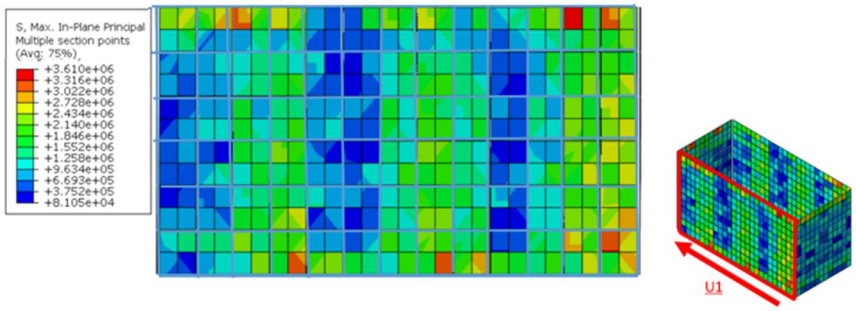

(b)

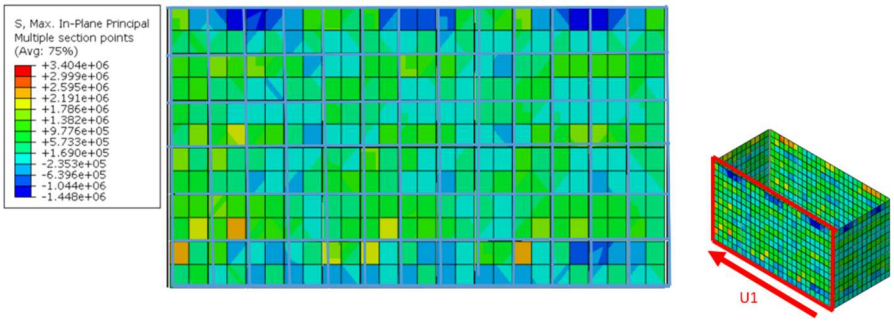

(c)

Figure A.5-3 Maximum in-plane principal stress distribution for glass panels in X-direction for (a) Configuration #A; (b) Configuration #B and (c) Configuration C (measures in MPa x 10e6)

A.5 Discussion on the results

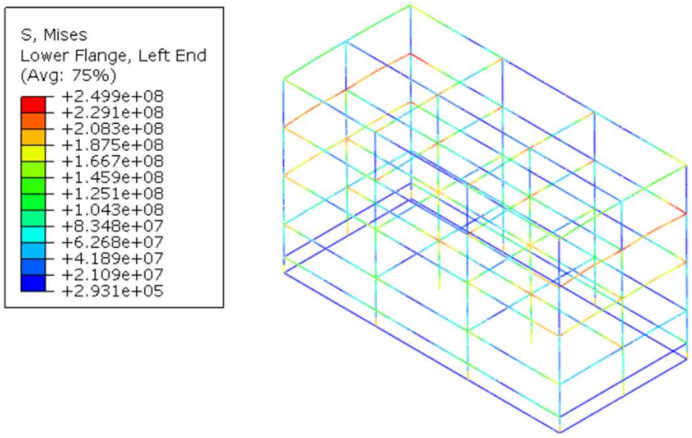

(a)

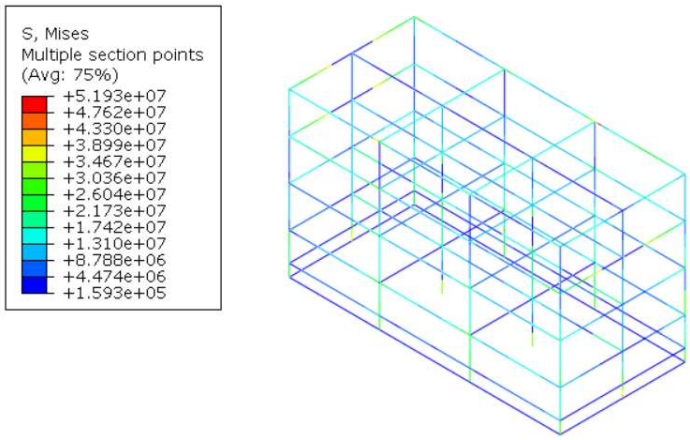

(b)

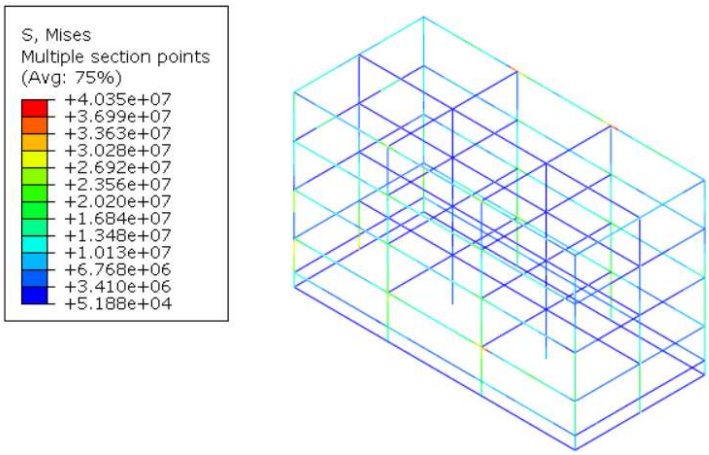

(c)

Figure A.5-4 Von Mises stress distribution for steel primary system in X-direction for (a) Configuration #A; (b) Configuration #B and (c) Configuration C (measures in MPa x 10e6)

A.5.1.2 Glass panels (CS#1)

The previous analysis on the entire structure allowed to implement of a fragility analysis for the single component taking into account that each panel is excited by 4 accelerations in its vertices that depends on its position in the structure, both in plane

and in height, as the dynamic response of the structural system to the lateral resistance is related to the shaking of the earthquake, the structural typology and the behaviour of the building. When the building deforms, all elements rigidly attached to the structure undergo the same displacements. Therefore, to the glazed architectural component (Case study #1) are applied the 4 top accelerations due to the 45 accelerograms considered for each configuration (see Fig. A.5-5). The seismic behaviour of the model calibrated on the results of the experimental tests allows to identify of two limit states concerning which the fragility curves for components will be constructed. DS1 corresponding to the achievement of the maximum tensile stress for glass and DS2 corresponding to the fallout and numerically to an out-of-plane displacement defined as $1/60L_{min}$ according to Table 7.11 (CNR-DT210 2013) as a function of the connection and glass types.

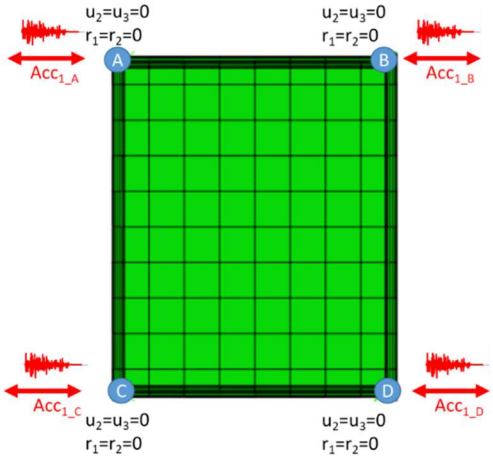

Figure A.5-5 FE model for dynamic analyses

To better clarify the results, for Configuration #A, in the following figures (i.e., Fig. A.5-7 and Fig. A.5-8) the maximum and minimum envelopes related to the distribution of tensile and compressive stresses in glass panel are reported for a single seismic event (i.e., s#5 in Fig. A.5-6). Afterwards further graphs including all performance outputs in terms of stress and strain are included.

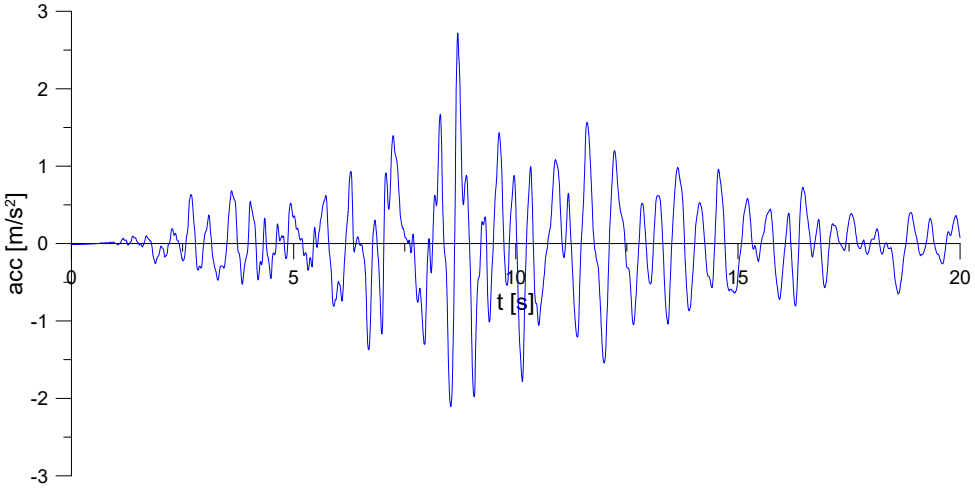

Figure A.5-6 Seismic record (s#5)

A.5 Discussion on the results

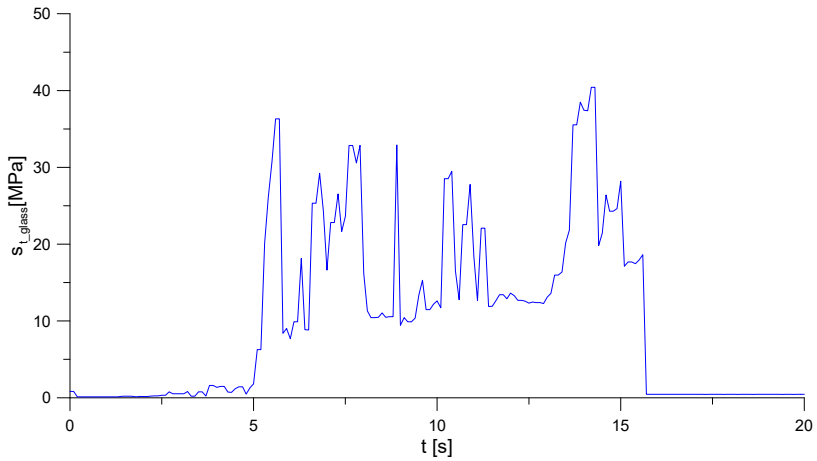

Figure A.5-7 Maximum envelope of glass tensile stress (Configuration #A)

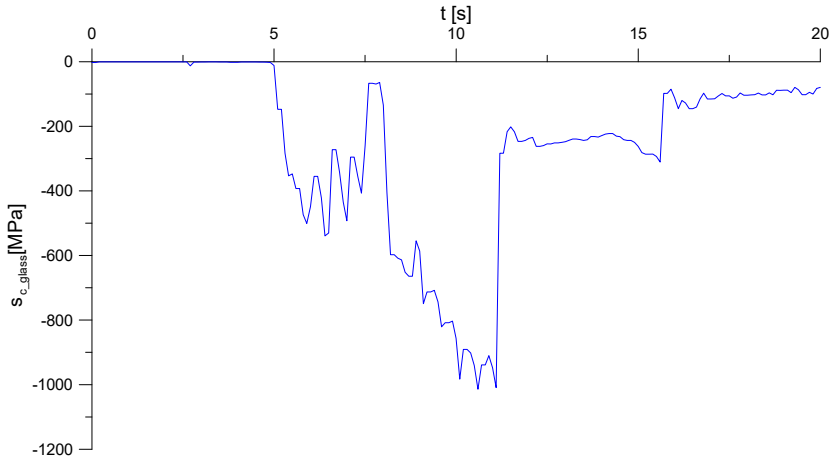

Figure A.5-8 Maximum envelope of glass compressive stress (Configuration #A)

In this case, the maximum value of $\sigma_{t,glass}$ and $\sigma_{c,glass}$ are reached at t=14.2s and t=10.6s respectively, while the second state of damage is drawn later as shown in Fig. A.5-9 (a). By the out-of-plane displacement trend depicted, it takes more than 15 seconds for the limit value of 25 mm (=1/60L_{min}) to be exceeded. Fig. 9 (b) illustrates the drift ratio, which is determined by the displacement between two vertices of the panel in its plane, and is calculated over the duration of the seismic input.

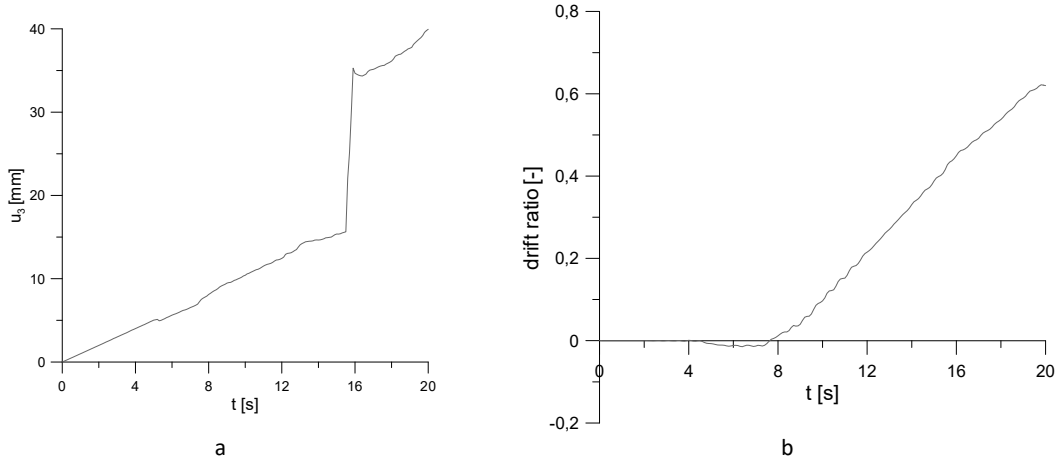

Figure A.5-9 Out-of-plane displacement (a) and in-plane drift (b) as functions of time

Moreover, Fig. A.5-10 illustrates the in-plane displacements and the stress distributions corresponding to the maximum tensile (on the left) and the maximum compressive stresses (on the right).

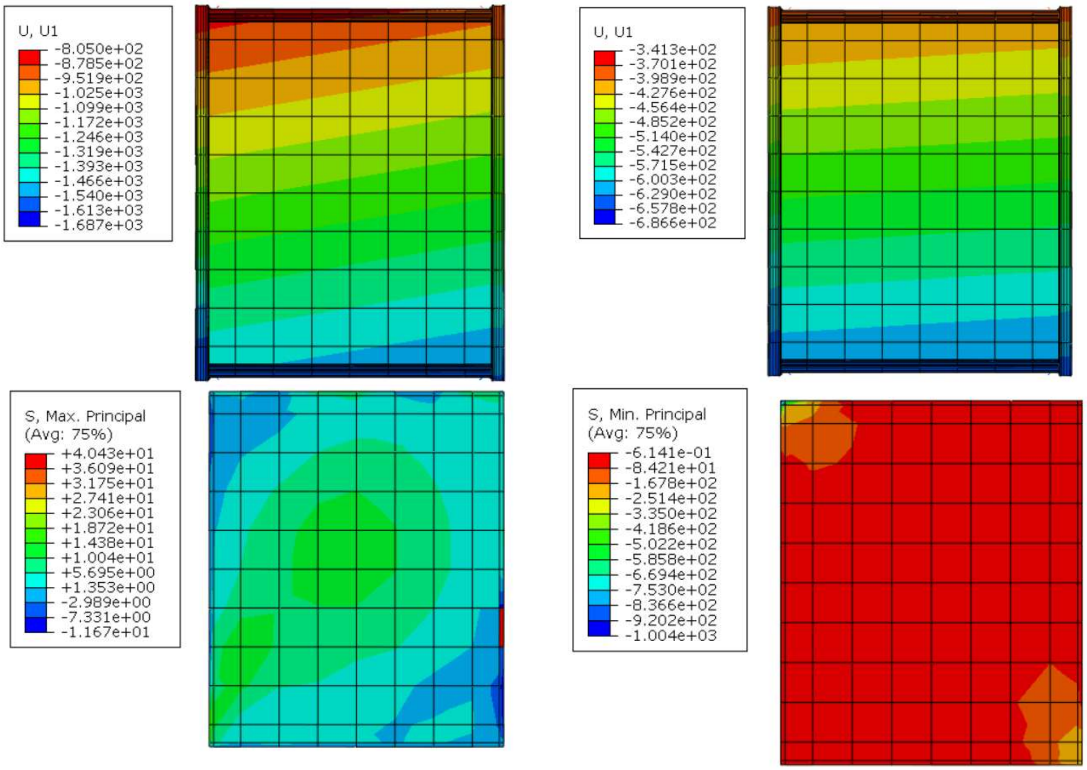

MAX TENSION : t=14.2s [acc=s#5] MAX COMPRESSION : t=10.6s [acc=s#5]

Figure A.5-10 Configuration #A: In-plane deformations [mm] and stresses distributions in glass panel [MPa] corresponding to the maximum tensile stress (on the left) and the maximum compressive stress (on the right)

At the same time, Configuration #B is analysed using the same accelerogram that was used in the previous numerical analysis (i.e., s#5). The maximum values of $\sigma_{t,glass}$ and $\sigma_{c,glass}$ are achieved at t=9.4s and t=9.1s respectively (see Fig. A.5-11 and Fig. A.5-12). Furthermore, the depicted trend of the out-of-plane displacement (see Fig. A.5-13 (a)) is comparable to the previous one (i.e., Fig. A.5-9 (b)), with less emphasis on the fall-out point.

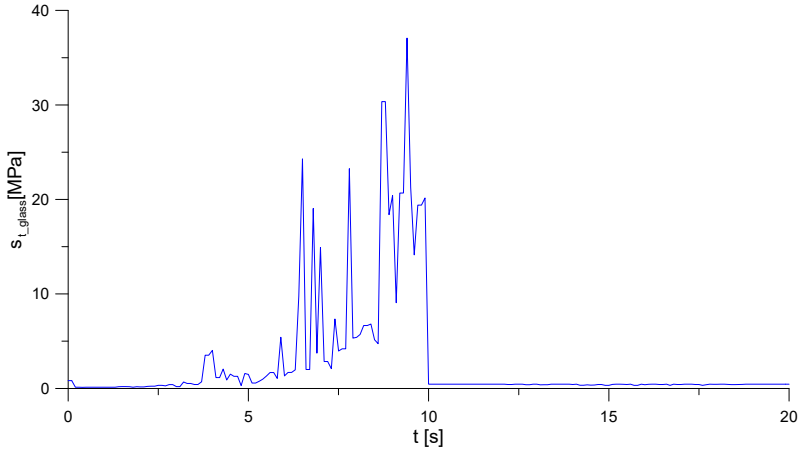

Figure A.5-11 Maximum envelope of glass tensile stress (Configuration #B)

A.5 Discussion on the results

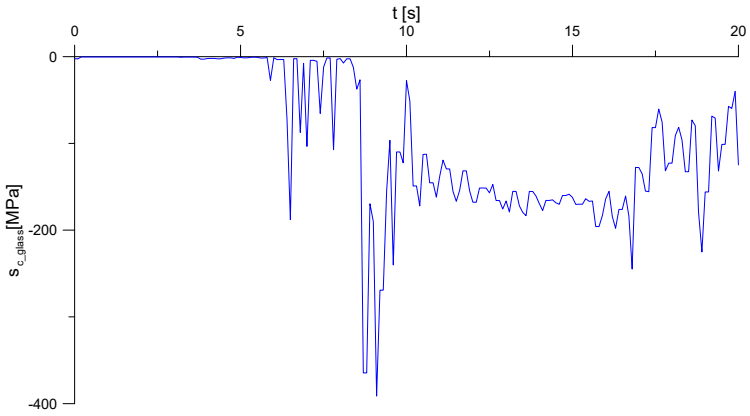

Figure A.5-12 Maximum envelope of glass compressive stress (Configuration #B)

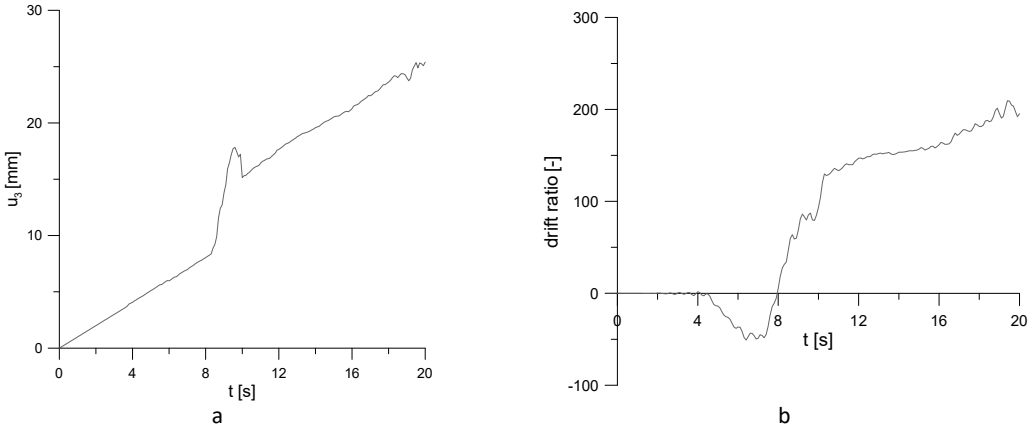

Figure A.5-13 Out-of-plane displacement (a) and in-plane drift (b) as functions of time

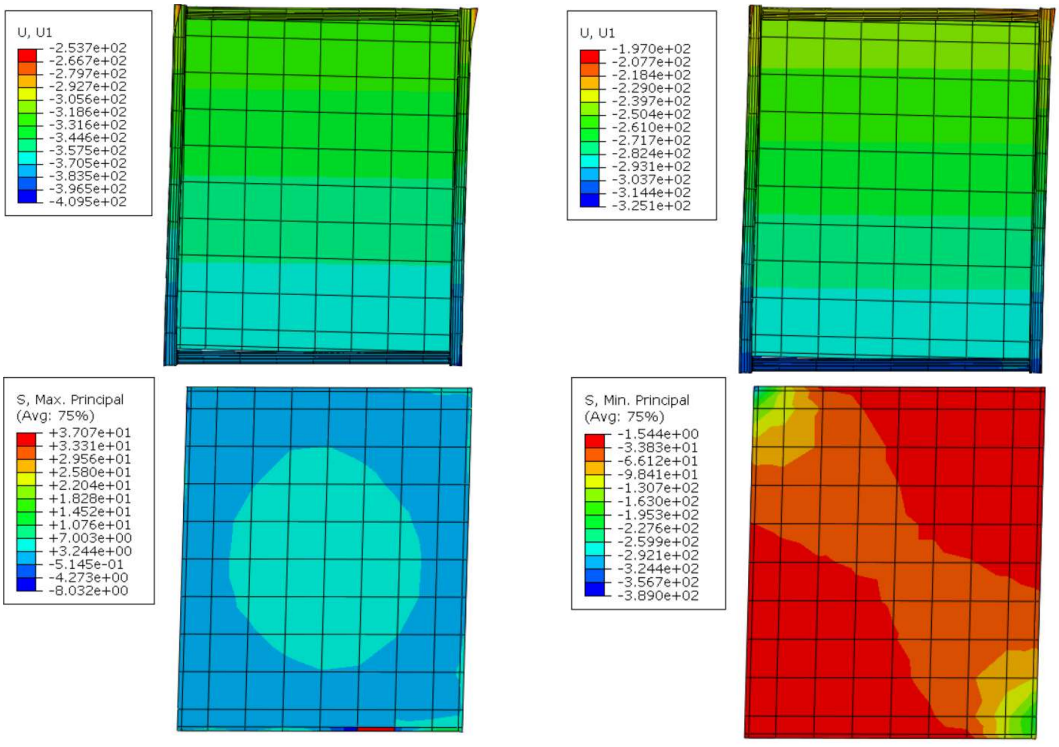

MAX TENSION : t=9.4s [acc=s#5] MAX COMPRESSION : t=9.1s [acc=s#5]

Figure A.5-14 Configuration #B: In-plane deformations [mm] and stresses distributions in glass panel [MPa] corresponding to the maximum tension (on the left) and the maximum compression (on the right)

In addition, Fig. A.5-14 shows the displacements and stresses at the time when maximum stress points occur, providing a clear depiction of the formation of the diagonal compressed strut, which is responsible for the out-of-plane instability that leads to the limit state of fall-out (DS2).

Finally, in the following figures (i.e., Fig. A.5-15) the summary of the final results of each dynamic analysis by using the finite element model is exposed in terms of maximum drift ratio for each configuration. It is worth mentioning that there is a significant difference between the outcomes obtained for the small-scale and full-scale applications, especially in the latter case, where the results are considerably minor as can be observed from the ratios, presented in the figure, less than 20%. It is worth emphasizing that the results are highly dependent on the specific case study and all the variables that may impact the response of such intricate components, including the connections, as well as the complexity of modelling the behaviour of glass, which also considers the post-failure domain.

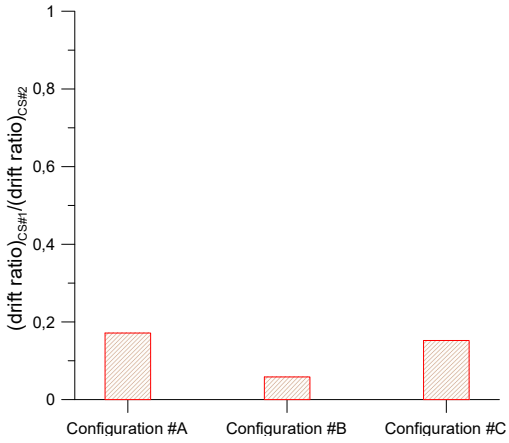

Figure A.5-15 Comparison of results between CS#1 and CS#2 in terms of in-plane maximum drift ratio for the specific seismic record (i.e., s#5)

A.5.2 Component fragility derivation

On the basis of the previous considerations, the Cloud Analysis was performed in Abaqus for each configuration in terms of non-linear time-histories analyses in order to obtain the seismic demand values of EDP under a set of ground motion records which can be represented by an appropriate intensity measure IM ($S_a(T_1)$ and PGA) by using unscaled accelerograms, or rather exactly the accelerations derived by the FE model of the entire structure, at the first level, caused by the same records indicated in Section A.3.2.1.

Since the fragility curve is a tool for the estimation of damage likely to occur during a seismic event, in this case a clarification of the investigated demand parameter and its limit value is necessary. By an accurate observation of the previous results, the cloud data exhibit an evident trend concerning the damage states in this range of seismic input. In particular, the mean of EDP parameter is approximately corresponding to the

predicted displacements derived by the empirical approach, based on the damage observed following a lateral action. Beyond doubt, this fragility development method produces fairly reliable results because they are directly related to the actual seismic behaviour of buildings; in many cases these approaches are useful for the validation of analytical methods and the calibration of hybrid fragility curves. Nevertheless, it is worth emphasizing that it is extremely difficult to generalise the results and to establish comparisons based on different methodologies or cases where the sample of the case studies analysed is too small and the aim is to facilitate the results or increase their applicability for a whole category of elements or systems, as in the case of this thesis. Therefore, a first study based on fragility assessment analyses carried out by O'Brien et al. (2012) was conducted by Nuzzo et al. (2020). In this last work, the same configurations that are the subject of this thesis were analysed, and subsequently, fragility functions were developed analytically based on the model proposed by Bouwkamp and Meehan (1960).

Firstly, Fig. A.5-8, Fig. A.5-9, Fig. A.5-10 and Fig. A.5-11 show the cloud data pairs (ln(EDP), ln(IM)). The associated linear regression analyses are based on the assumption of the EDP lognormal distribution in a logarithmic space (Cornell et al. 2002) and the parameters *a* and *b* that define the linear model can be easily derived applying the Maximum Likelihood Estimate based on the collection of data from the numerical simulations and the characteristics of the selected ground motion suite.

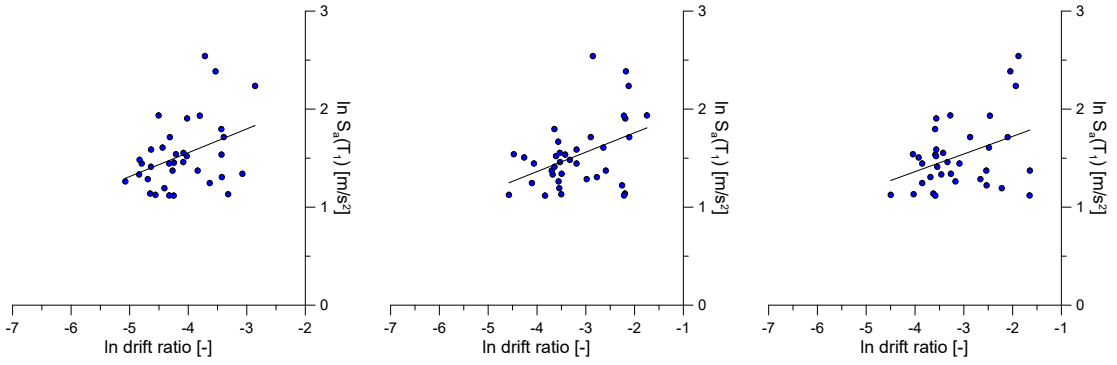

Figure A.5-16 Cloud data pair in bi-logarithmic plane in terms of IM=$S_a(T_1)$

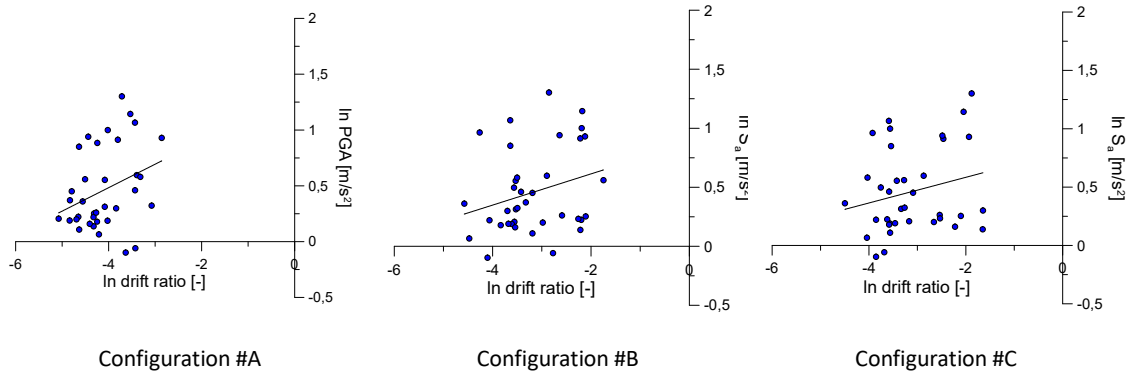

Figure A.5-17 Cloud data pair in bi-logarithmic plane in terms of IM=PGA

A.5 Discussion on the results

The linear regression parameters are summarised in Table A.5-2 for the selected configuration as explained in Section A.4.1. For the sake of clarity, the Configuration #A and #B differs in terms of glass-to-frame clearance and the Configuration #C is characterized by a laminated section keeping constant the clearance to 11 mm as the previous #C.

Table A.5-1 Summary of linear regression parameters

Configuration	IM=$S_a(T_1)$			IM=PGA		
	a	b	R^2	a	b	R^2
#A	2.5276	0.2431	0.1461	1.3247	0.2103	0.1012
#B	2.155	0.198	0.1805	0.8775	0.1321	0.0741
#C	2.0824	0.1801	0.1477	0.8035	0.1099	0.0516

In the present study, the panel drift ratio as the relative displacement between the top and the bottom of the modelled system divided up the vertical distance was chosen as EDP. In particular, as a first approximation, the assumed thresholds for this parameter are derived from the current regulations (see Section A.2.2) and reported in the following table.

Table A.5-2 Summary of the EDP-thresholds by current regulations in terms of drift

Code	EDP-thresholds = drift ratio [-]		
	Configuration #A	Configuration #B	Configuration #C
EC8	0.005		
NTC18	0.002		
FEMA450	0.007	0.026	0.026
JASS14	0.01		

Thus, it is assumed that an EDP-threshold is known (i.e., Table A.5-3) and its exceedance corresponds to the failure of the system. For immediacy of understanding, the definition of the structural fragility by using a Cloud Analysis and some mathematical steps are repeated below but the methodology is fully explained in Section A.3.2:

$$\mathrm{P}[\mathrm{IM_{CP}} < \mathrm{IM_i}] = \phi\left(\frac{\ln(\mathrm{IM_i}) - \mu_i}{\beta_i}\right) \tag{36}$$

$$\mathrm{P}[\mathrm{IM_{CP}} < \mathrm{IM_i}] = \Phi\left(\frac{(a + b\ln \mathrm{EDP_i}) - \mu_i)}{\beta_i}\right) \tag{37}$$

Where:

- μ_i is a median estimate of the seismic demand given the damage state value ds (by Eq. 24) and *a* and *b* are the regression model parameters;
- $\mathrm{EDP_i}$ is the generic value of the structural demand;
- β_i is the constant logarithmic standard deviation evaluated by Eq. 25 as per hypothesis residuals around the mean value are normally distributed with zero mean.

The fragility curves for each intensity measure are given below depending on the specific configuration investigated, the limit value for EDP as a function of the provisions expressed by worldwide technical codes, and the IM parameter considered (i.e., see Fig. A.5-18 and Fig. A.5-19). It is worth to note that the Italian code, like the European one,

is not able to provide acceptable vulnerability parameters by providing displacement limitations in the case of elements consisting of brittle and rigid materials connected to the primary structure. On the contrary, the American regulations are the only ones able to customize the Displacement Values (in terms of EDP) according to specific geometry and damage state (*ds*).

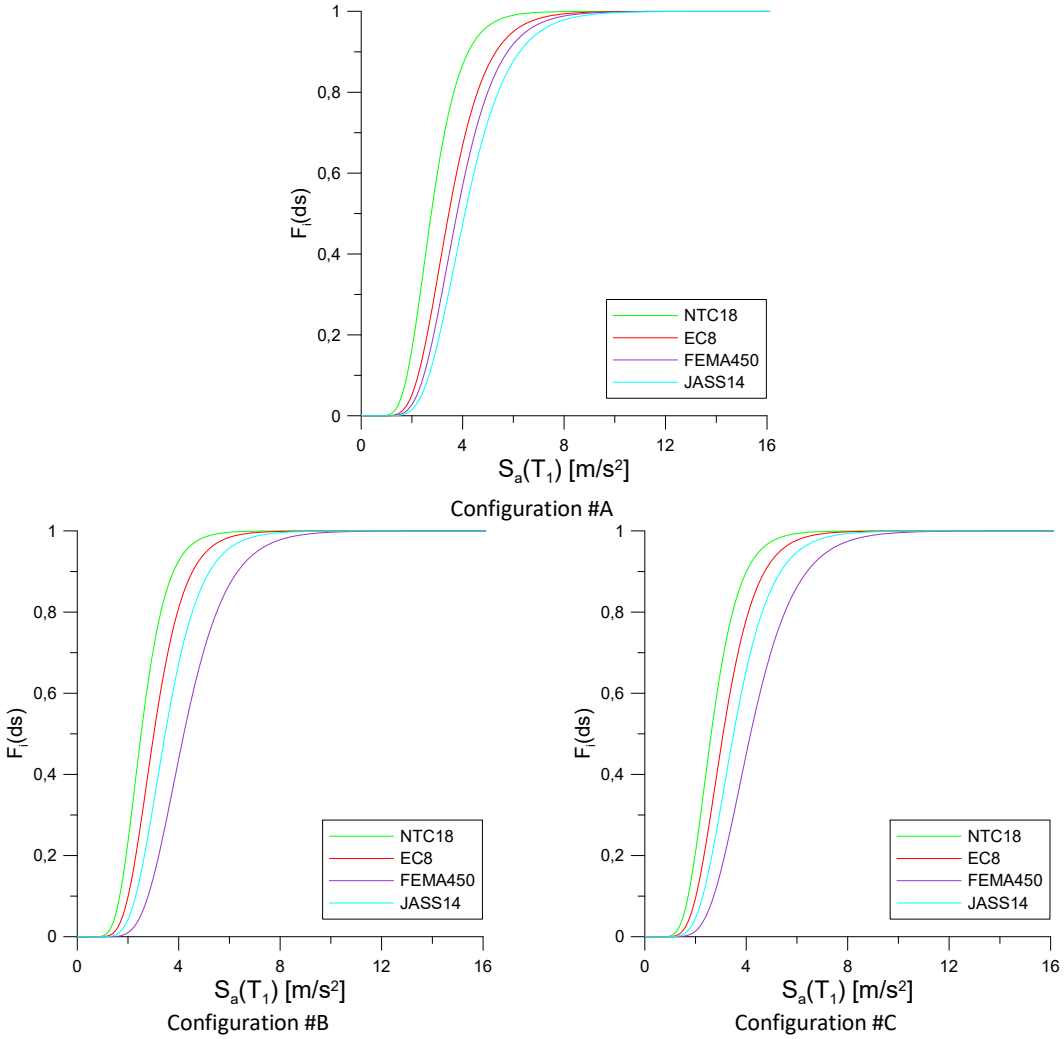

Figure A.5-18 Fragility curves based on different EDP-thresholds and IM=$S_a(T_1)$

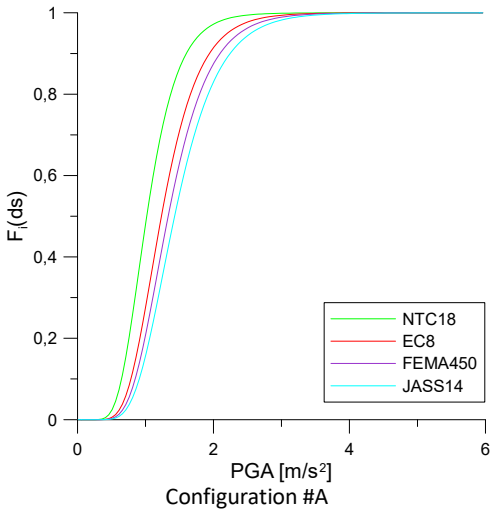

A.5 Discussion on the results

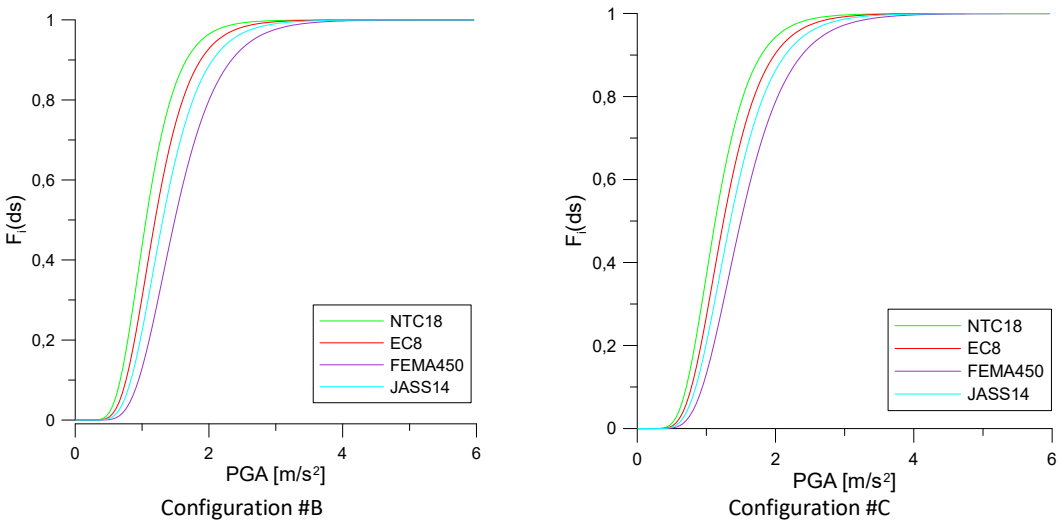

Figure A.5-19 Fragility curves based on different EDP-thresholds and IM=PGA

Finally, the investigation into the influence of the glass-to-frame clearance on the performance of the glass subjected to load in the plan is based on the proven sensitivity of the latter to the above-mentioned parameter, without, however, any study specifically analysing its effects. From the less recent study of Bouwkamp (1961), still taken as reference in the explanation of the behaviour of the façade under action in the plan, to the formulations present in the American code, many are the formulations that indicate the clearance like one of the parameters on which depends the answer in the final displacement of the system.

The findings for each configuration (i.e., C#A with c=3 mm and C#B with c=11 mm) attest that the clearance dimension has a significant meaning in the identification of EDP corresponding to the to the failure capacity of a glass panel. It goes that if the threshold of the *drift ratio* is lower, for instance for EDP-threshold by NTC18 (see Table A.5-2), the difference is less marked.

Another interesting observation can be achieved in comparing numerical fragility curves characterized by the same glass-to-frame clearance (c=11mm) but different glazing type, such as C#B with an AN-monolithic section and C#C with an AN-laminated section. The former has a thickness of 6mm, whereas the latter consists of two annealed glass sheets (2 x 3 mm of thickness) with a polyvinyl butyral interlayer pane in the middle, namely PVB, that is permanently bonded with use of heat and pressure in order to provide a strong chemical bonding. This is the reason why, as also proved by figures, the performance of a laminated glass is improved by the presence of structural safety margin.

As already mentioned, façades often cover large areas in the vertical plane, but it is not uncommon to find instances where glass panels are separated vertically within a single floor height. This can result in multiple panels being positioned vertically within one story. Subsequently, the formulation expressed below derives by a simple geometric problem:

A.5 Discussion on the results

$$\text{Drift ratio} = \frac{\delta}{\mathrm{h}} = \frac{\delta_{storey}}{\mathrm{h}_{storey}} \tag{38}$$

Where:

- δ and h denote the in-plane displacement and the height for the simple glass panel;
- δ_{storey} and h_{storey} denote the in-plane displacement and the height for the overall construction.

In Fig. A.5-20 (a) and (b), on the x-axis of the cloud data pairs for entire building, *drift ratio* corresponds to the value obtained by non-linear time histories analyses and the expression from Eq. 38 is perfectly satisfied as follows:

$$A = \frac{\delta}{\delta_{storey}} \sim \frac{\mathrm{h}}{\mathrm{h}_{storey}} = 0.6 \tag{39}$$

Moreover, it is considered that the best comparison can be made in terms of the intensity measure that can cause the attainment of the considered limit state (=*ds*). About the latter, it is important to define a unique parameter and threshold for both case studies, and thus, even in this discussion, the drift ratio was chosen as EDP.

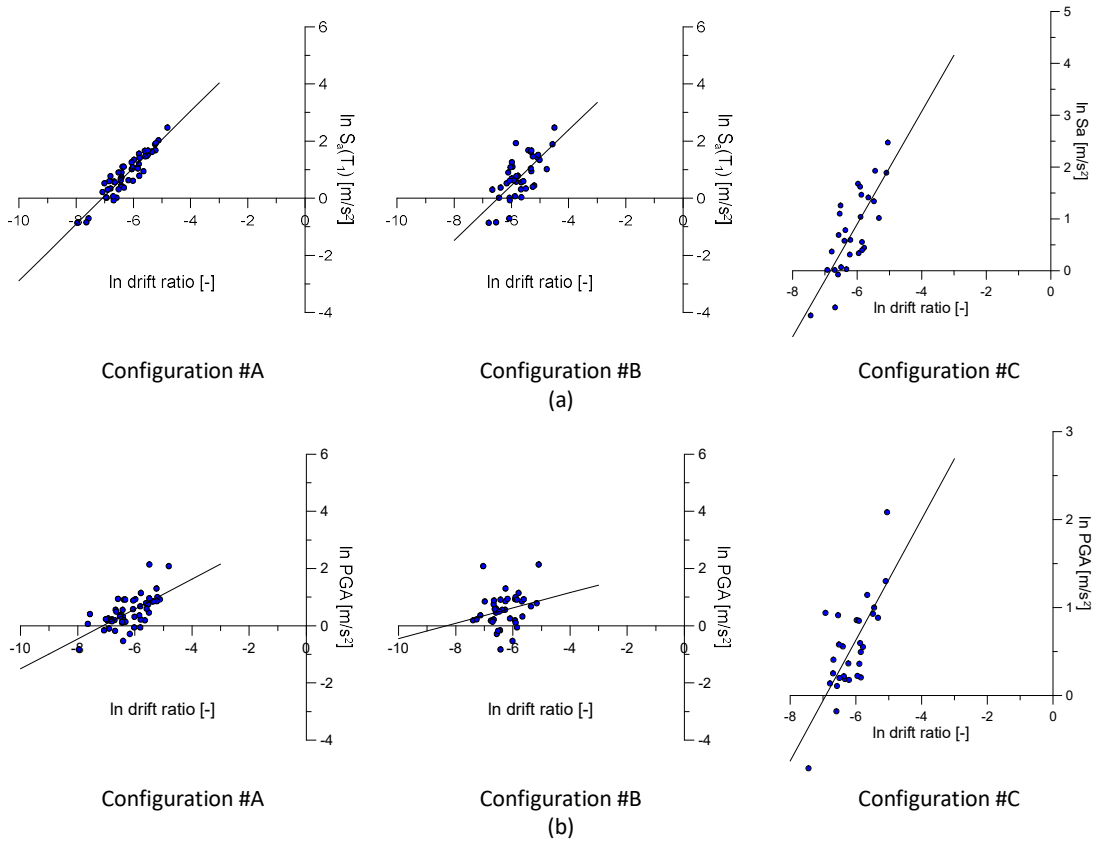

Figure A.5-20 Cloud data pairs for entire building in bi-logarithmic plane in terms of (a) IM=$S_a(T_1)$ and (b) IM=PGA

Finally, Fig. A.5-21 depicts fragility curves in terms of Sa and PGA evaluating the difference in the predicted failure values of the system. In the second case the linear regression parameters lead to the same mean. In this case, it appears there are no differences in considering the different CW configurations. On the contrary, the global

geometry affects the shape and parameters of a fragility function, even though the different section has less influence on the result.

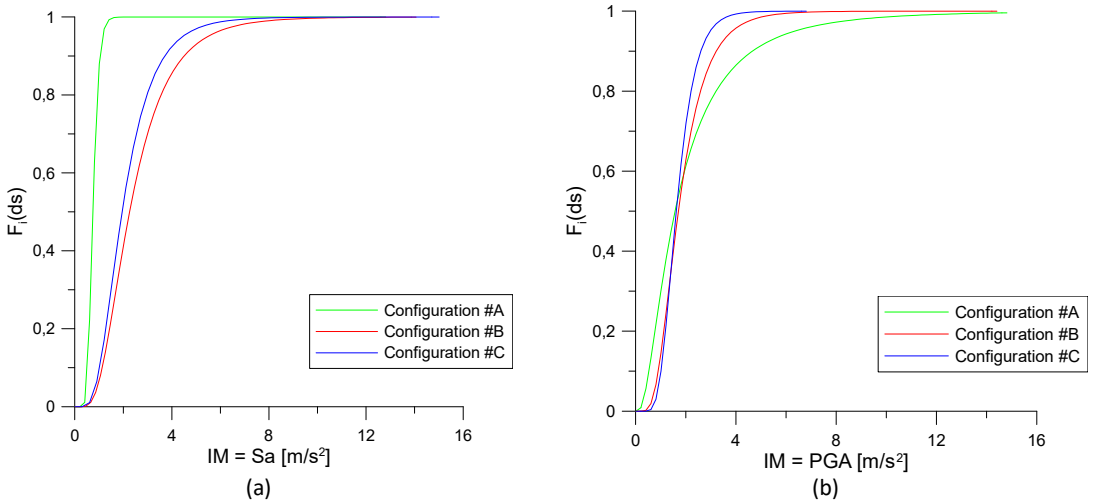

Figure A.5-21 Fragility curves for the curtain wall configuration with the same geometry in a 4-story building for Configuration #A, #B and #C in terms of (a) IM=$S_a(T_1)$ and (b) IM=PGA

In particular, in this last part of the Chapter A.5, a survey of the levels and modalities of application of fragility curves in the comparison between component and load-bearing structure as a whole was carried out.

Table A.5-3 Summary of linear regression parameters

Configuration	Fragility parameter	IM=$S_a(T_1)$			IM=PGA		
		CS#2	CS#1	ratio	CS#2	CS#1	ratio
#A	**μ**	6.806	4.179	1.629	2.811	1.448	1.941
	β	0.403	0.336	1.199	0.446	0.353	1.264
#B	**μ**	12.834	4.045	3.173	2.882	1.459	1.975
	β	0.545	0.319	1.712	0.581	0.353	1.646
#C	**μ**	38.538	4.776	8.069	10.700	1.627	6.575
	β	0.502	0.338	1.484	0.368	0.361	1.018

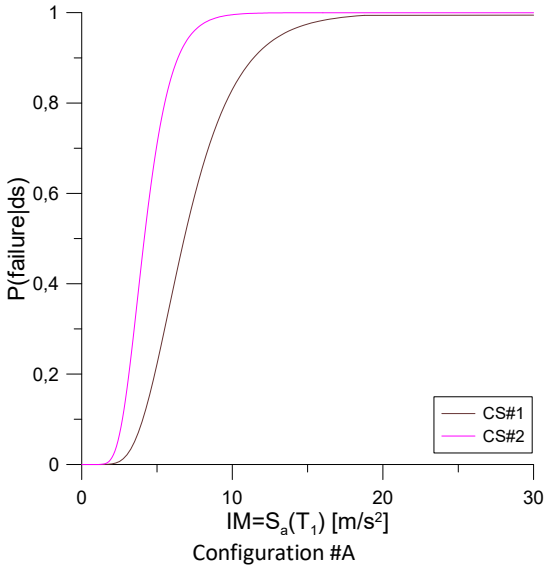

A.5 Discussion on the results

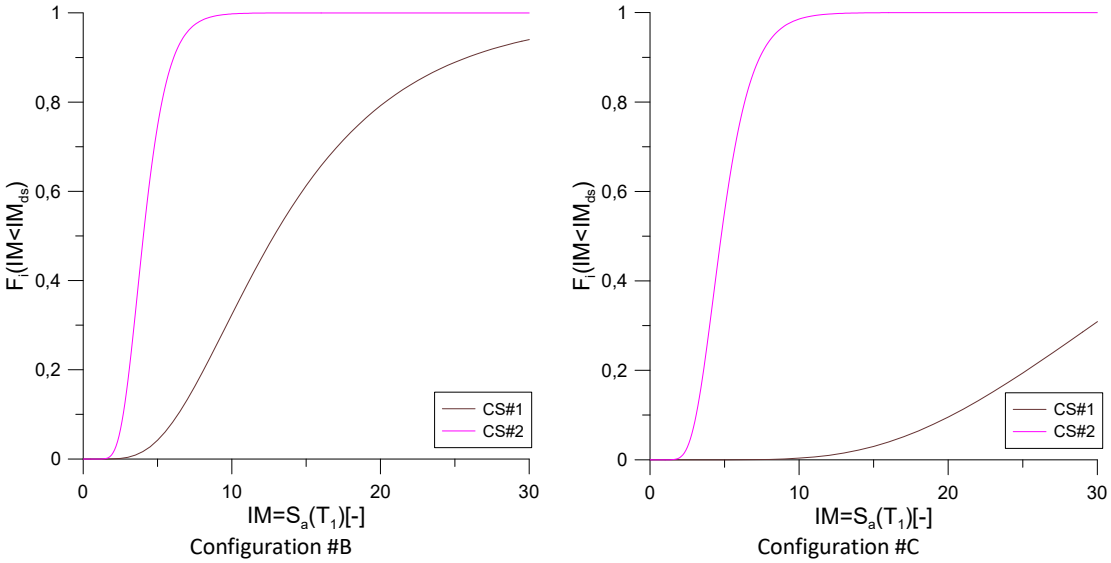

Figure A.5-22 Fragility curves based on the EDP-threshold by experimental results and IM=S_a

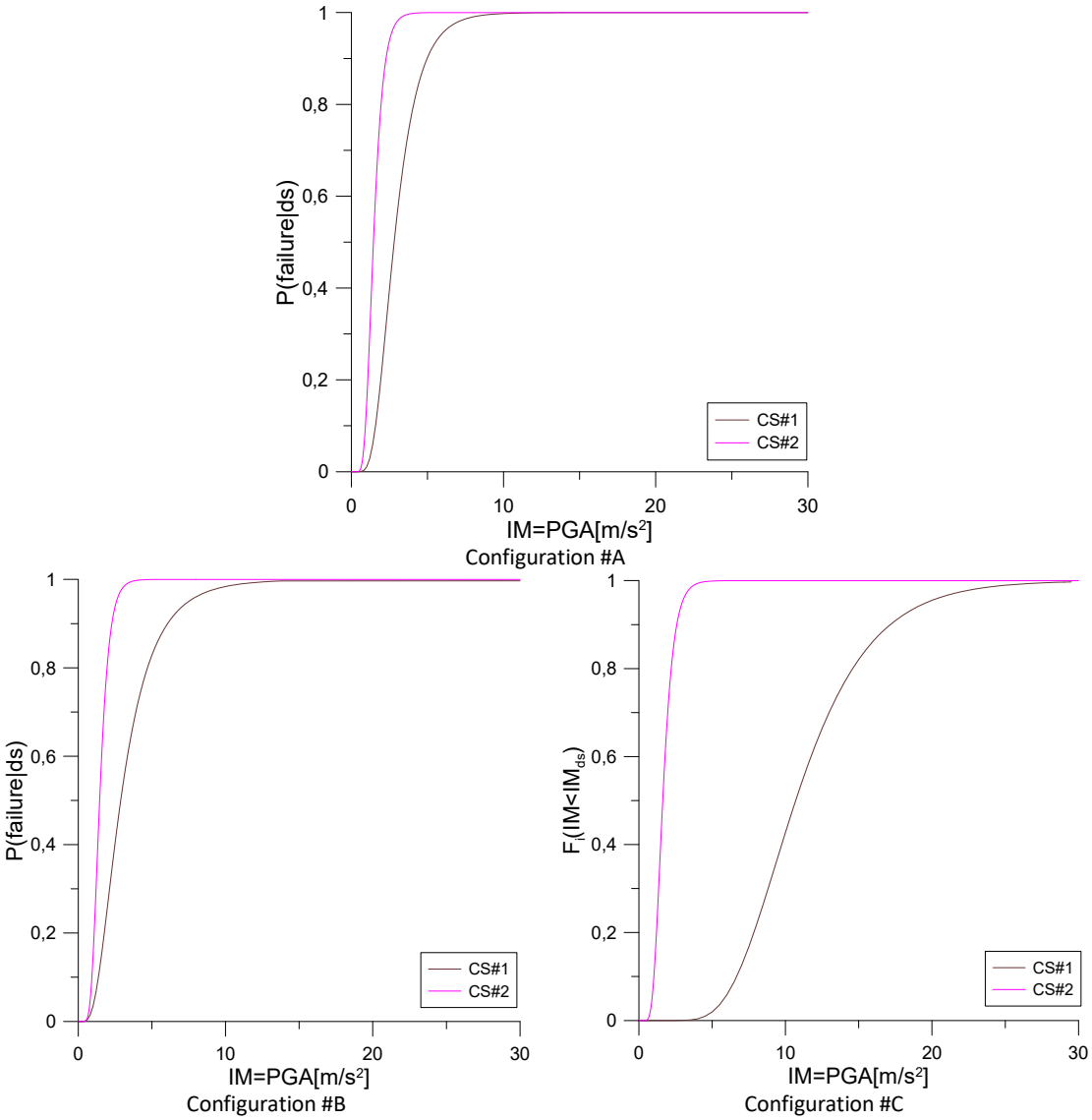

Figure A.5-23 Fragility curves based on the EDP-threshold by experimental results and IM=PGA

A.5 Discussion on the results

It must be stressed, however, that some of the conditions of the actual building taken to reference must be taken into account. In particular, the connections could influence the applicability of the numerical results going to modify the assumptions on which their derivation is based. The fact is that in many cases, the displacements that the façade will record during a seismic event will be slightly smaller than the storey-drift observed in the carrier frame. It can even be assumed, on the basis of past experiments and observations, that the vast majority of systems with mullions and transoms could even experience smaller drifts than the chassis itself throughout its lifetime, although there are several varieties of details related to the connection that will therefore present variable stiffness. This appears to be the reason why it was considered acceptable to disregard the influence of the connection in previous calculations. However, further studies in this direction could lead to even more detailed treatment of the seismic performance of glass façade elements. Furthermore, a fragility domain can be built for this specific full-scale application for each indicated damage state providing a useful tool to support the decision-making process of design and selection of CW components.

This section is an important contribution to understanding the research issue addressed, providing a comprehensive view of the results obtained. The understanding of both the individual and overall system behaviour is crucial in determining the factors that contribute to the failure modes and in predicting when damage is likely to occur under specific conditions. Besides, having this knowledge is essential in establishing the parameters that impact the failure modes and in determining the demand level at which a damage state is expected to take place.

A.5.3 References

Bouwkamp, J.G., Meehan, J.F. (1960). “Drift limitations imposed by glass”. *Proceedings of Second World Conference on Earthquake Engineering*, Tokyo, Japan, pp.1763-1778.

CNR. CNR-DT210. Istruzioni per la Progettazione, L’esecuzione ed il Controllo di Costruzioni con Elementi Strutturali di vetro; Guide for the Design, Construction and Control of Buildings with Structural Glass Elements; National Research Council of Italy (CNR): Roma, Italy, 2013. (In Italian).

Cornell, A. C., Jalayer, F., Hamburger, R.O. (2002). “Probabilistic basis for 2000 SAC Federal Emergency Management Agency steel moment frame guidelines.” Journal of structural Engineering. 128(4), p.526-532.

Nuzzo, I., Aiello, C., Bonati, A., Caterino, N., Coppola, O., Occhiuzzi, A. (2020). “Fragility curves of glass façades via analytical simplified modelling”. *Proceeding of 17th World Conference on Earthquake Engineering, 17WCEE*.

O’Brien, W. C., Memari, A. M., Kremer, P. A., Behr, R. A. (2012). “Fragility Curves for Architectural Glass in Stick-Built Glazing Systems”, *Earthquake Spectra*, 28(2), pp.639-665.

Part B: Experimental and numerical investigations on post-failure behaviour of glass fitted with ASFs

B.1 The use of ASFs in architectural glass

Recently, the impact of using PET-films in construction field, looking in particular at structural glass applications, has been investigated by several authors.

More in general, anti-shatter safety films (ASFs) are considered a common tool to increase the reliability of a structure in which glass element are involved. Given the typical brittle mechanical behaviour of this construction material, one of the main issues related to its structural performance is the sudden breakage and the manner in which it fails. The fragmentation of the material, function of the glass type and section as set out at the beginning of this dissertation (i.e., Section A.1.1), may represent a fairly serious danger to human life (Martins et al. 2012, Koper et al. 1999). In this context, the PET-films are a very widespread commercial product and therefore also very tested by manufacturers, but for which there are no technical documents or guidelines that regulate the applications. As far as the latter is concerned, the field of application is very wide, ranging from the automotive to the electronic industry; nonetheless, its primary purpose is to shield people from accidental, short-lived and high-intensity actions such as impacts or explosions (Van Dam et al. 2014). In fact, one of the first use in building dates back to the 1970s against terrorist attacks (IWFA).

At the same time, further advantages prove the usefulness and versatility of these elements, such as the possibility of reducing transparency until it is eliminated or improving the transmittance characteristics. These benefits also derive from the properties of the material that makes up the tape. From a chemical point of view, Polyethylene terephthalate (PET) can be an amorphous or a semi-crystalline thermoplastic polymer, but it is in fact very common in the ASF application field to combine to or more PET layers of them both, in order to exploit the characteristics of the first as well as the second. Among them, it is worth to note that PET material offers: good chemical resistance against acids; good adhesion and welding ability; high rigidity

and hardness; very low moisture absorption; good creep resistance and a high performance in terms of UV resistance or electrical properties at low prices compared to the replacement of glass components considered not sufficiently reliable structurally.

Nevertheless, it is not only tape that governs the behaviour and effectiveness of the application. Another element that makes up the film is of considerable interest and influences global performance is the pressure sensitive adhesive (PSA), which only requires slight pressure to adhere to clean glass surfaces. Concerning its performance in the overall composite application, the adhesion characterization is addressed in Chapter B.3 due to its paramount importance.

Finally, since manufacturer's warranty periods range from 10-15 years, depending on external conditions, the assessment of actual increased post-fracture strength is necessary over time and considering the humidity and temperature to which films are installed.

Figure B.1-1 Examples of PET-film actual applications

By considering the different glass types, ASFs are commonly applied on annealed glass due to the characteristic fracture patterns with cause a major danger in terms of irregularity in fragmentation resulting in sharp shards of any size ejected at different speeds depending on the external action. A similar argument can be made in the case of Heat-treated or Chemically strengthened glass, where typical crack patterns recall the previous typology, unlike the Tempered glass whose fragments are very small and blunt, causing therefore fewer consequences.

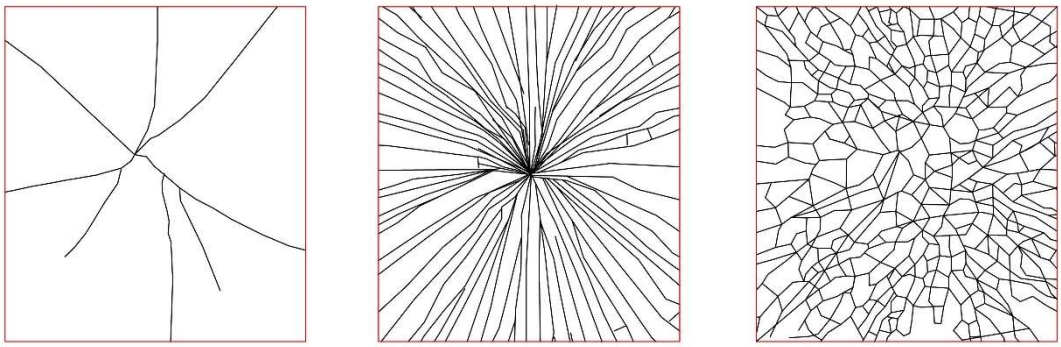

(a) (b) (c)

Figure B.1-2 Typical crack pattern for (a) annealed, (b) heat-streghtned and (c) tempered glass (figure © S. Mattei)

A literature study revealed that on this subject the research is poor or focused on investigating the response under impulsive and unpredictable actions. A ball-drop experimental program has been presented in (Figuli et al. 2021) for traditional glass windows. The use of protective films proved to offer increased safety levels to window elements, and thus to reduce potential risk for occupants. Several authors studied how to improve the performance of structural glass based on thin films (Caterino et al. 2017). Brueggeman et al. (2000) proposed an insulation system of panels to prevent damage. Other research studies were dedicated to the detection of efficient methods of the avoidance of severe consequences for customers, that is using PET-films applied on both sides of glass panels (Bárány et al. 2015) or on the external surface only (Thurston et al. 1992, Hutchinson et al. 2011). Memari et al. (2004) explored the influence of films through Racking Test Facility. The experiments demonstrated a greater strength for film-bonded glass elements, in addition to a limited ability to create flying debris, compared to ordinary glass members. On the other side, literature efforts are still rather limited towards the generalized quantification of advantages in using similar protective films, as well as towards the definition of basic mechanical properties. Talking about this aspect, it is worth to note that a major issue regarding the performance of ASFs is that the quality of mechanical properties at the interface is affected by many factors, such as intrinsic material properties, composition, processing method and operational conditions.

B.1.1 ASF composition

In Figure B.1-3, the basic constitutive materials of the glass fitted with anti-shatter film (ASF) (Mattei et al. 2022) is shown and the characterization phases are deeper explained in a specific Section (i.e., Chapter B.2). It is worth to note that the thickness of a PET-film is generally expressed in *mil* (IWFA) that is a non-SI unit of length, defined as one-thousandth of an inch and thus equal to 0.0254 mm.

The commercial multi-layer film, with a total thickness of 36 mil, consists of two layers of adhesives and two sheets of PET with thickness of 0.11 mm, on the external side (Layer 2), and 0.22 mm, in the inner part (Layer 1) with a high degree of transparency and low permeability, and characterized by similar glass transition temperature (T_g ~80°C) as obtained by the chemical characterization in Section B.5.1. As there are no significant differences between the two layers and the tensional fields to which they will be subjected in the various laboratory tests do not allow their separation, the overall tape is considered as a single and homogeneous material.

Furthermore, since all these components contribute to the behaviour of the glass equipped with safety window film construction as if it were a typical composite section despite we have very different thicknesses and characteristics, it is considered essential to study them all in more depth, treating them separately in the next paragraphs. The removable release liner is the only exception because this constituent has the aim of

protecting the PSA adhesive by environmental conditions, in fact it doesn't influence the mechanical behaviour of the system as it is removed before the installation of ASF onto the glass element.

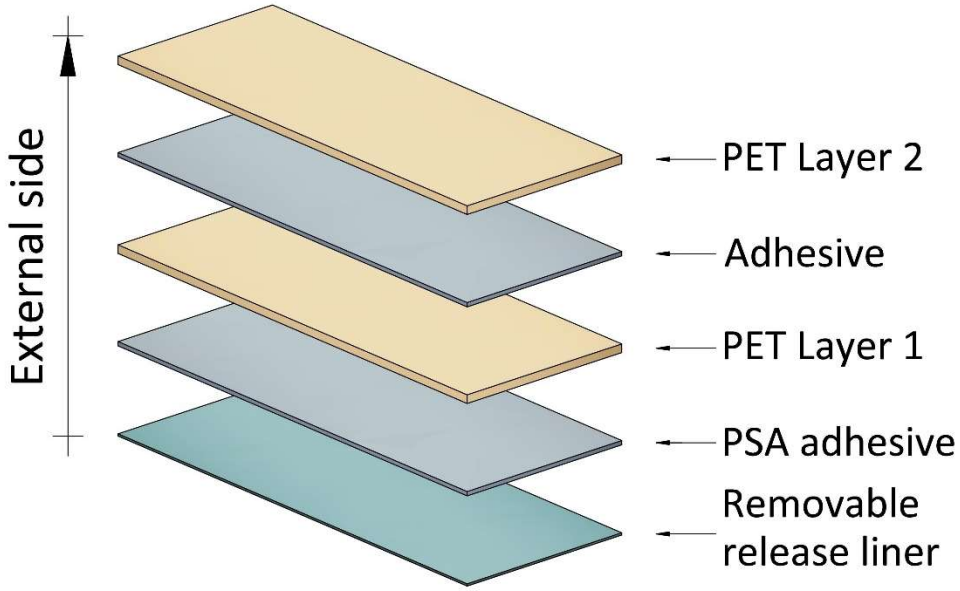

Figure B.1-3 Basic composition of the glass fitted with ASF[8]

B.1.1.1 Polyethylene terephthalate (PET) tape

Most of the known films are obtained from oil derivatives. In the field of lamination, paper converting and packaging, the main films used are: polypropylene (PP)*, polyethylene terephthalate (or simply polyester, abbreviation PET) and polyethylene (PE). The production of the main films starts from granules which, with the addition of additional ingredients such as sliding, antioxidants, stabilizers and various additives, are introduced into the extruder, a heated hollow cylinder that houses a worm screw inside. The extruder has the task of homogenizing and melting all the components. The compound obtained is pushed through a die which provides a continuous "plate" or "tube" of semi-molten polymer. To give the film the usual appearance, the plate is laminated in order to thin the thickness or compressed air is pushed inside the extruded to obtain a polymer bubble of the desired thickness. In addition to reducing the desired thickness, the film usually needs further processing. The most frequent are: orientation, to give the right mechanical and optical properties to the film and treatment, to make the film printable and suitable for receiving adhesives, inks, paints or lacquers.

Regarding the anti-shatter film applications, the choice falls undoubtedly on the PET material for the best mechanical characteristics.

[8] Figure reproduced with permission from (Mattei et al. 2022) under the terms and conditions of CC-BY license agreement

In fact, the thermoplastic polyester tape represents the only constituent which provides ensured mechanical characteristics to the coated glass absorbing the energy by plastic deformation after glass failure, and providing a residual strength in post-breakage field as well as significantly higher security holding the glass fragments together thank to the presence of PSA.

Unfortunately, any property is provided us by the commercial ASF manufacturer. Consequently, the mass density of PET material is given by literature and the needed mechanical parameters have been obtained by means of experimental tests.

B.1.1.2 Pressure sensitive adhesive (PSA)

Pressure adhesives are characterized by a solid form adhesive with permanent adhesiveness. Glueing is achieved by applying pressure to the adhesive film, hence the name Pressure Sensitive Adhesive (PSA). The more pressure is applied, the better the adhesion. Pressure adhesives are used for the coating of the materials to be bonded, as the joining of the materials can be carried out after the adhesive has been applied. Later, the union of materials can be made in a following period of time after the application of the adhesive and in a different place.

According to Fig. B.1-3, two adhesive types are combined in an anti-shatter film with different characteristics and purposes, both due to treatments or additives used. In this research study, the performed tests relate only the external version of PSA because the aim is the investigation on the adhesion parameters. The reason why the adhesion is so important concerns the efficiency of the bond between glass substrate and PET-tape, without which the influence of the film would be completely removed in terms of mechanical features.

However, precisely because adhesion is a parameter of fundamental interest, the mounting phase is crucial.

There are two types of lamination for films. To obtain a dry film, a layer of adhesive is applied on the film that at the time of lamination will be tempered through heated coated calender. Compared to non-adhesive films (wet films), dry films have several advantages from different points of view: less expensive laminators, faster starts, no glue group, coupled ready for subsequent processing in less time than wet, less environmental impact.

Thanks to its ease of operating, a slight pressure is widely sufficient in order to apply the dry PET-film, without forgetting to take into account the possibility of bubbles appearing on this surface, as well as a high probability of it folding together. In order to minimize the imperfections in the superimposition phase, the glass surface was treated and the period of time between the application and the removal of release liner layer was very short.

B.1.2 References

Bárány, T., Ronkay, F., Karger-Kocsis, J., Czigány, T. (2005). "In-plane and out-of-plane fracture toughness of physically aged polyesters as assessed by the essential work of fracture (EWF) method". *International journal of fracture*, 135(1), pp.251-265.

Brueggeman, J. L., Behr, R. A., Wulfert, H., Memari, A. M., Kremer, P. A. (2000). "Dynamic racking performance of an earthquake-isolated curtain wall system". *Earthquake spectra*, 16(4), pp.735-756.

Caterino, N., Del Zoppo, M., Maddaloni, G., Bonati, A., Cavanna, G., Occhiuzzi, A. (2017). "Seismic assessment and finite element modelling of glazed curtain walls". *Structural Engineering and Mechanics*, 61(1), pp.77-90.

Figuli, L., Papan, D., Papanova, S., Bedon, C. (2021). "Experimental mechanical analysis of traditional in-service glass windows subjected to dynamic tests and hard body impact". *Smart Structures and Systems*, 27(2), pp.365-378.

Hutchinson, T. C., Zhang, J., Eva, C. (2011). "Development of a drift protocol for seismic performance evaluation considering a damage index concept". *Earthquake Spectra*, 27(4), pp.1049-1076.

International Window Film Association (IWFA) - Safety/Security Window Film Draft PGC 020401, Martinsville, VA 24115.

Koper, K. D., Wallace, T. C., Hollnack, D. (1999). "Seismic analysis of the 7 August 1998 truck-bomb blast at the American embassy in Nairobi, Kenya". *Seismological Research Letters*, 70(5), pp.512-521.

Martins, L., Delgado, R., Camposinhos, R., Silva, T. (2012, June). "Seismic Behaviour of Point Supported Glass Panels". In *Challenging Glass 3: Conference on Architectural and Structural Applications of Glass*, Faculty of Civil Engineering and Geosciences, Delft University of Technology (p. 281).

Mattei, S., Cozzarini, L., Bedon, C. (2022). "Experimental and numerical peeling investigation on aged multi-layer anti-shatter safety films (ASFs) for structural glass retrofit". *Symmetry*, 14(1), 162.

Memari, A. M., Behr, R. A., Kremer, P. A. (2004). "Dynamic racking crescendo tests on architectural glass fitted with anchored pet film". *Journal of architectural engineering*, 10(1), pp.5-14.

Thurston, S. J., King, A. B. (1992). “Two-directional cyclic racking of corner curtain wall glazing”. Building Research Association of New Zealand.

Van Dam, S., Pelfrene, J., De Pauw, S., Van Paepegem, W. (2014). Experimental study on the dynamic behaviour of glass fitted with safety window film with a small-scale drop weight set-up. International Journal of Impact Engineering, 73, 101-111.

B.2 Experimental program

In this chapter the characterization of mechanical and chemical parameters involved in the overall performance is discussed. In addition to the need to quantify the quantities involved in the detailed analysis of the problem, these results are used for numerical modelling developed in the next chapter. The first section is dedicated to the assessment of mechanical behaviour of the tape alone, the PET-film or the coated glass. For the elastic properties (Young's modulus, E_{PET}, and yielding stress, $f_{y,PET}$) of PET tape, tensile tests were conducted according to standard (i.e., Section B.2.1.1); the adhesion properties were determined through peeling (i.e., Section B.2.1.2); and three-point bending tests were carried out on specimens consisted of glass fitted with ASF (i.e., Section B.2.1.3). Finally, the basic characterisation of materials is presented in the second section (i.e., Section B.2.2). In addition, a further investigation concerns the influence of accelerated ageing procedures on a limited number of specimens of PET-film and ASF fitted glass.

B.2.1 Static characterization

B.2.1.1 Tensile tests

The tensile test is, certainly, one of the most used to obtain fundamental quantitative information (Young's modulus, E, yield stress and strain, failure stress and deformation, etc.) describing the mechanical behaviour of a material subjected to uniaxial stress. Uniaxial deformation $\varepsilon = \Delta l/l_0$ produces a stress $\sigma = F/A_0$; where F is the force applied by a Schimadsu AGS-X Universal Testing Machine and A is the initial section of the specimen. The facility is interfaced to a computer by means of a software that manages the data acquisition.

According to ASTM D882-02 provisions, pure tensile tests on the thin multilayer PET-tape, sized 350 by 25 mm, are performed as shown in Fig. B.2-1. The specimen dimensions are in accordance with the requirements provided:

a) $L_{specimen} \geq 50 + L_{0\_grip}$ [mm];
b) $5 \leq B_{specimen} \leq 25.4$ mm;
c) $(B/t)_{specimen} \geq 8$.

Moreover, in order to minimize slippage at both ends, in correspondence to the grips an *'RS PRO Industrial Grade Adhesive 132633'* was applied for 50 mm of length.

Given the setup as in Fig. B.2-1, based on the standard, the tensile tests were conducted on 5 specimens with a constant rate of crosshead movement equal to 25.4 mm/min.

Figure B.2-1: Schematic setup for tensile test[9]

B.2.1.2 Peel Tests

The adhesion between the glass substrate and the PET-film was assessed through a peel test with a specific setup configuration. Generally, the adhesion characteristics can be addressed by several international standard methods that provide different test results for how the load is applied to the sample (such as geometry setup or speed-rate); but there are many similarities between the basic principles.

For example, from ASTM several peel tests are listed below:

- D1876, Peel Resistance of Adhesives (T-Peel Test);
- D3167, Floating Roller Peel Resistance of Adhesives;
- D1781, Climbing Drum Peel Test for Adhesives;
- D903, Peel or Stripping Strength of Adhesive Bonds;
- D2558, Evaluating Peel Strength of Shoe Sole-Attaching Adhesives.

All methods describe the use of rectangular samples with constant adherent thickness and large width-to-thickness ratio. Peeling shall be conducted in ordinary testing machines where the force is measured by a load cell. Thus, the test result is the peel force, which is the force per unit width of the adhesive.

In a peeling test, it is usual to specify parameters such as the thickness h and the width b of the delamination strip, called *peel arm*, the angle between the substrate and the direction of application of force, ϑ, and the speed of peeling; because they affect the final outputs.

Fig. B.2-2 shows the most common test patterns for peel testing as found in international standards. Peeling tests with a fixed substrate and the third one which is deformed by some angle (configuration known as peel test with fixed peel arm) can be

[9] Figure reproduced with permission from (Mattei et al. 2022a) under the terms and conditions of CC-BY license agreement

performed at different angles (typically from 45° to 180°). The main issue in performing a peeling test at angles different from 180° lies in maintaining the angle constant throughout the test. This can be achieved by appropriate setup for samples.

In a 180° peel test, the adherent is glued to a rigid substrate and placed at 180° with respect to its initial state. In any case, since peel resistance depends on the mechanical properties of the peel arm, comparisons between different peel tests are only possible when using a common peel arm.

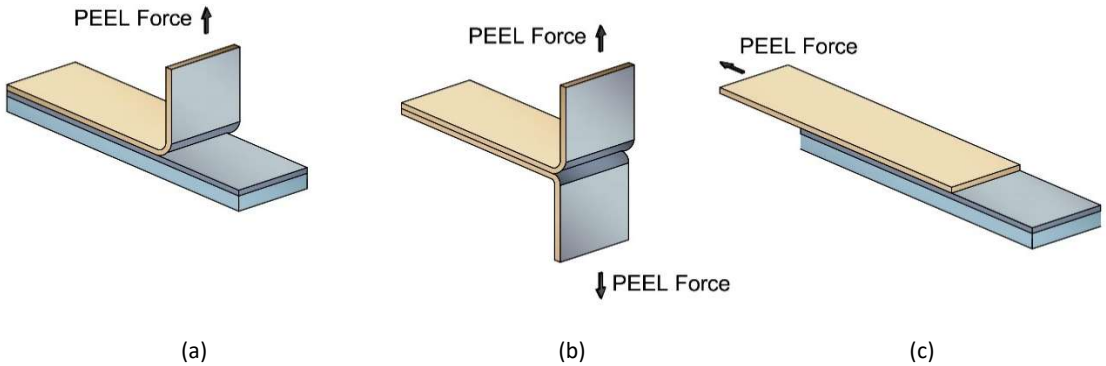

Figure B.2-2: Peel test configurations: (a) 90°peel test; (b) T-peel test and (c) 180° peel-test (figure © S. Mattei)

For this reason, it is of paramount importance to analyse the peculiarity of the performed peeling tests that lies in the setup configuration, as mentioned above. In this case, the peel angle (ϑ) is variable during the loading process since the substrate was fixed on the bottom part and a displacement-controlled rate was applied at the upper end of the peel arm (i.e., Fig. B.2-3). No technical document takes this condition into account, so an in-depth study in Section B.3 deals with the analysis of the influence of ϑ on the final result and the possible measures to be taken in the use of the classical formulations by the literature.

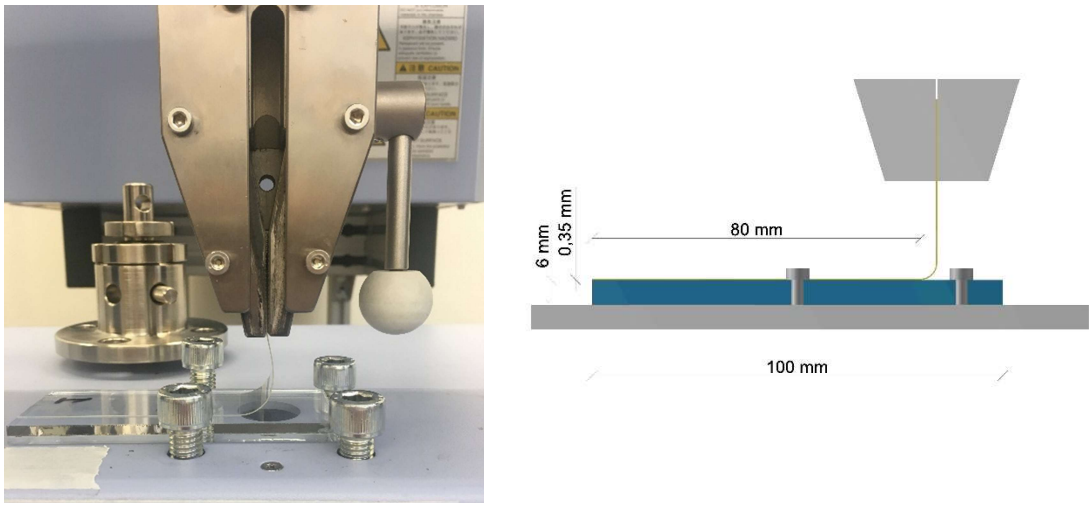

Figure B.2-3 Experimental setup of peel test (figure © S. Mattei)

With regards to the geometry of the 56 specimens involved, the film employed in the investigation has width of 25 mm, length of 120 mm and thickness of 0.36 mm. This

rectangular strips were obtained from the rolls of film, because it is generally available in this commercial form. The rigid substrate consists of annealed glass, sized 100 x 40 x 6 mm (width x depth x thickness).

B.2.1.3 Three-Point bending tests

This test was conducted to examine the bending behaviour of glass elements fitted with ASFs on the bottom face of specimens (see Fig. B.2-4). In this sense, 20 small-scale specimens were prepared and rested on two steel support, in the Shimadzu AGS-X universal testing machine (UTM), with a fixed curvature and without any restriction on rotational degrees of freedom in the loading plane. After placing the moving-crosshead in the mid-span point of the ideal beam avoiding pre-stress states, the 3PB test starts and a constant displacement-rate of 25.4 mm is applied by means of a loading edge. In addition, a protective shield between the test machine and the technicians is placed to avoid accidents at the failure.

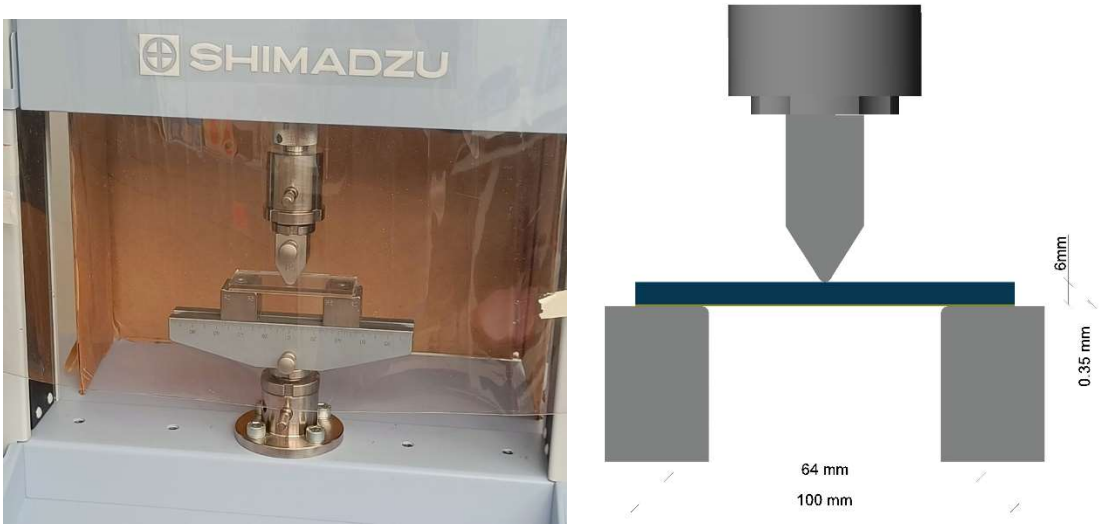

Figure B.2-4 Experimental setup of 3PB test (figure © S. Mattei)

Typical test results include:

a) bending elastic modulus;
b) stress and strain at the point of yield and at the rupture of the specimen.

With regard to this last point, the maximum bending stress for a rectangular homogenous cross section is computed as follows:

$$\sigma_{max} = \frac{\mathrm{M}}{\mathrm{I}} y = \frac{\frac{P}{2}\frac{l}{2}}{\frac{bh^3}{12}}\frac{h}{2} = \frac{Pl}{8}\frac{12h}{bh^3} = \frac{3}{2}\frac{Pl}{bh^2} \tag{41}$$

Where:

- P denotes the maximum force;
- l=64 mm as shown in Fig B.2-4;
- b and h represent the cross section dimensions.

Since the shear is also present in the most stressed section, the test results can be considered reliable if l >> h (generally, l/h ≥ 20) and thus the assumption of small deformation is still respected.

In this context, a theoretical discussion to provide a reliable solution for the deflection curve in the case of a composite section is addressed. In general, the composite sections consist of parts of different materials and a connection system appropriately sized. The degree of connection is the key parameter in the definition of the contributions included in assessing the structural capacity of the element. According to the Fig. B.2-5, three idealized situations can be distinguished depending on the actual efficiency of the constraint. Neglecting the influence of the adhesive layer and thus in the case of *'Null connection'*, between the two materials the shear stresses at the interface equal zero and the slippage isn't avoided. The bending behaviour of each component is based on its own mechanical parameters, thus the maximum bending force is computed as the sum of the two corresponding terms considering available Bernoulli's hypothesis of preserving the pane sections of a single component. Concerning the other limit condition, which provides a complete *'Rigid connection'*, the final section behaves as homogeneous. Obviously, the immediate output embodies a major bending stress due to the increase of the moment arm given the constant geometry.

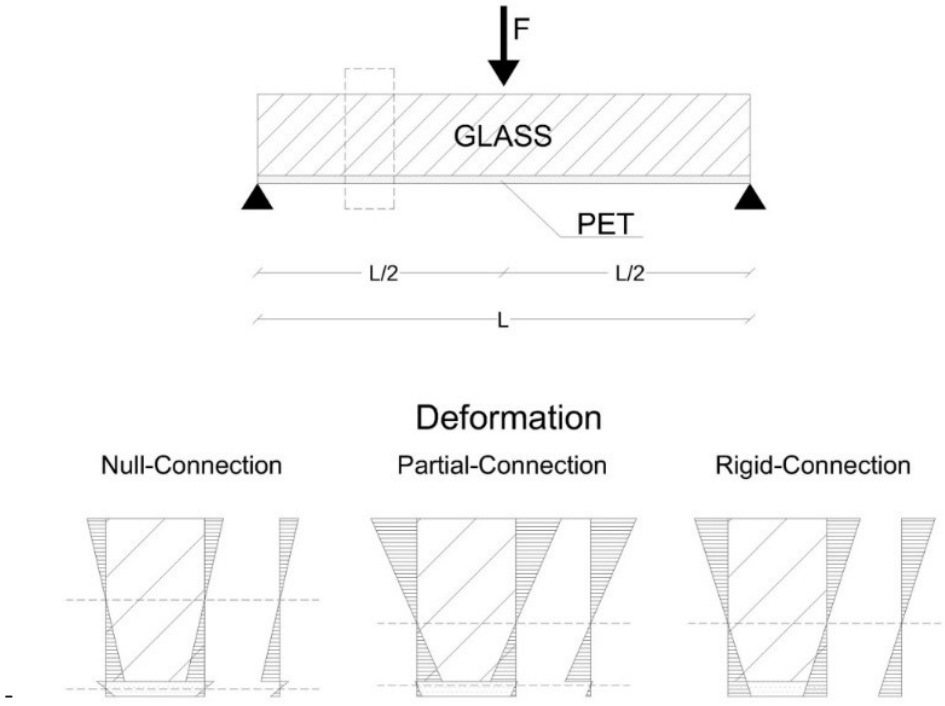

Figure B.2-5 Section deformation under bending loading in function of connection behaviour [10]

By a realistic point of view, the sliding shear stresses can't be neglected ranging from the minimum (zero stiffness connection) and the maximum value (infinite stiffness

[10] Figure reproduced with permission from (Mattei et al. 2022b) under the terms and conditions of CC-BY license agreement

connection). This bond type, named *'partial connection'*, represents all the intermediate conditions and Newmark et al. (1951) model them as individual constituent beam linked with axially deformable spring. Applying Newmark's theory to the case-study of a fitted glass element with ASF requires the following suitable assumptions:

- simply supported restrains;
- two different materials characterized by elastic-linear mechanical responses;
- uniform distribution of the connection along the length of the beam;
- constant geometries.

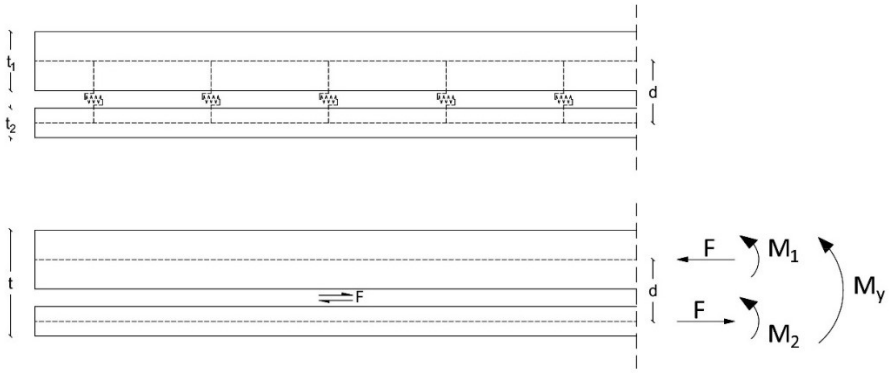

Figure B.2-6 Analytical model for composite beam with deformable connection (figure © S. Mattei)

The formulation of the bending deformation v(x) as by Eq. (42), was obtained by solving the fourth order differential equation describing the bending deformation.

$$v(x) = c_1\frac{x^2}{2} + c_2\frac{e^{\alpha^2 x}}{\alpha^4} + c_3 x + c_4 - \alpha^2\frac{M}{EJ_{full}}\frac{x^3}{6} - \frac{1}{2\alpha^4}\frac{M}{J_{full}}\frac{e^{2\alpha^2 x}}{2\alpha^2} \quad (42)$$

Where:

- M is the demand in terms of bending moment;
- the constant coefficients c_1, c_2, c_3 and c_4 derived by the integration procedure;
- α is computed as a function of various stiffness types = $\sqrt{\frac{K}{EA^*}\frac{EJ_{full}}{EJ_{abs}}}$;
- K is the stiffness of the connection = $\frac{G_{ad}b}{t_{ad}}$;
- G_{ad} is the tangential stiffness of the adhesive component;
- t_{ad} is the stiffness of the connection layer;
- EA* is the equivalent stiffness = $\frac{E_1A_1 * E_2A_2}{E_1A_1 + E_2A_2}$;
- EJ_{full} denotes the bending stiffness in case of rigid connection = $EJ_{abs} + EA^*d$;
- EJ_{abs} denotes the bending stiffness in case of null connection = $E_1J_1 + E_2J_2$;
- the subscripts 1 and 2 represent the glass and PET-tape, respectively.

B.2.2 Material investigation of PET-film

In this section, the material characterization is presented through physical-chemical analytical techniques with the aim of deriving the material properties of each constituent.

B.2.2.1 Differential Scanning Calorimetry

Differential Scanning Calorimetry (DSC) is the most widely used thermal analysis technique together with TGA, TMA and DMA.

DSC is an ideal method to determine thermal quantities, to study thermal processes and to characterize or simply compare two or more materials in a simple but extremely accurate way. Sample preparation is simple and requires only a small amount of material. In particular, it is used for quality control, research and development on materials. In fact, this technique is very useful to analyse and study polymers, such as thermoplastics, thermosets, elastomers and adhesives, food, pharmaceuticals and chemicals in general.

The experimental test consists of measuring the difference in the amount of energy (heat) absorbed or released by a sample from a reference during controlled heating or cooling of the sample, or in isotherm, and providing valuable information on process and application conditions, quality defects, identification, stability, reactivity, chemical safety and material purity. In this case, the test is performed with a Netzsch DSC 200 F3 Maia in nitrogen atmosphere at a heating rate of 10 K/min.

Finally, a graph is drawn where the heat flow (expressed in milliwatts) is reported as a function of the temperature of the sample, which is measured precisely throughout the process. The phase transitions that the sample undergoes determine peaks in the thermogram, the area of which corresponds to the enthalpy of the phenomenon involved.

The differential measurement of the system is important both theoretically and practically, because the signal is independent of all thermal effects external to the system that have an equal impact on the two samples, allowing the intrinsic behaviour of the material to be assessed independently of the test conditions.

B.2.2.2 Fourier Transform Infrared spectroscopy

The IR spectrum of any sample reflects its molecular composition - just like a chemical fingerprint. Both organic and inorganic chemical components contribute to the spectrum. The IR method is therefore particularly suitable for the identification of both pure compounds and complex materials. It is also possible to quantify individual components within the analysed material. For most samples, FT-IR analysis is performed without sample preparation and without the need for any consumables. Since the measurement times are generally less than a minute, its use saves time compared to traditional methods of chemical analysis.

Thus, a FT-IR system (in this case, a Thermo-Nicolet Nexus 470 spectrometer) allows in a few seconds the evaluation of the similarities of a raw material with a reference. This latter can be a certified standard or a previous batch and a minimum acceptability value of a raw material is defined. Finally, a good match is a guarantee of

quality of the new raw material; whereas a low match ratio is a first sign of non-compliance of the raw material.

b

Figure B.2-7 Thermo-Nicolet Nexus 470 spectrometer

B.2.3 Accelerated ageing protocols

As already mentioned, given the high sensitivity of PET towards the conditions of the external environment, the estimation of ageing influence on the ASF performance is of paramount importance, both in mechanical and adhesion terms. In particular, the specimens were exposed to a set of temperatures, moistures and ageing times as summarised in Table B.2-1, in case of peel tests, according to BS EN ISO 9142 (2003). Whereas, Table B.2-2 reports the ageing protocols developed specifically for laminated glass and investigated by Butchart and Overend (2017).

In particular, the different ageing conditions were chosen below the Tg (Glass transition temperature) and within the general range of temperatures to which architectural glass element is exposed on-site.

Table B.2-1 Ageing protocols and summary of tested specimens for peel tests

Specimen #	T	Ageing time	Displacement rate
	°C	h	mm/min
1-4	23	-	25.4
5-9	50	3	25.4
10-14	50	24	25.4
15-19	50	72	25.4
20-24	50	168	25.4
25-29	70	3	25.4
30-34	70	24	25.4
35-39	70	72	25.4
40-44	70	168	25.4

Table B.2-2 Ageing protocols and summary of tested specimens for peel tests

Specimen #	T	Ageing time	Displacement rate
	°C	h	mm/min
HU-2/HU-5	50	336	25.4
HT-11/ HT-15	100	2	25.4

B.2 Experimental program

HU-6/HU-10	50	336	1000
HT-16/ HT-20	100	2	1000

B.2.4 References

ASTM D882 - 02 - Standard Test Method for Tensile Properties of Thin Plastic Sheeting.

ASTM D1876 - Peel Resistance of Adhesives (T-Peel Test).

ASTM D3167 - Floating Roller Peel Resistance of Adhesives.

ASTM D1781 - Climbing Drum Peel Test for Adhesives.

ASTM D903 - Peel or Stripping Strength of Adhesive Bonds.

ASTM D2558 - Evaluating Peel Strength of Shoe Sole-Attaching Adhesives.

ISO 9142:2003 - Adhesives — Guide to the selection of standard laboratory ageing conditions for testing bonded joints.

Butchart, C., Overend, M. (2017). "Influence of Aging on Post-Fracture Performance". *Proceedings of Glass Performance Days Conference* 2017.

Mattei, S.; Cozzarini, L.; Bedon, C. (2022a). Experimental and numerical peeling investigation on aged multi-layer anti-shatter safety films (ASFs) for structural glass retrofit. *Symmetry*, 2022, 14(1), 162.

Mattei, S., Cozzarini, L., Bedon, C. (2022b). "Pre-and Post-Failure Experimental Bending Analysis of Glass Elements Coated by Aged Anti-Shatter Safety Films". *Challenging Glass Conference Proceedings* (Vol. 8).

Newmark, N.M., Siess, C.P., Viest, I.M. (1951). "Tests and analysis of composite beams with incomplete interaction", *Proc. Soc. Exp. Stress Anal*., 9(1), pp.75-92.

B.3 Adhesion: theoretical approach

This section introduces the main concepts regarding adhesion between polymers focusing on Pressure Sensitive Adhesives (PSAs). In addition, some basic concepts are introduced to describe both the toughness of an adhesive and the analysis of the peeling test; and, contextually, a brief review concerning the main theoretical methods used for the characterization of adhesives is provided.

B.3.1 Fracture mechanics basics applied to peel test

The connections between two or more materials have always been the subject of discussion in the academic and industrial environment, as we try to exploit the best properties of each of them in various fields. In addition to the classic methods used in the engineering field, such as bolting, nailing and welding, the application of adhesives begins to catch on bringing with it advantages and disadvantages. For instance, improved corrosion resistance, the possibility of combining materials of different natures also in unusual configurations and a more uniform distribution of load over a larger area, against lower durability if not with special attention or less shear and tension stresses than many metals.

There are many fields of application for adhesives, from aerospace to chemical engineering. Since adhesion between polymers and glass is the subject of this chapter, it is of paramount importance to review the theory behind the delamination process, the parameters that describe it and the formulations derived.

Contrary to what was initially thought, the adhesion between an adhesive and the substrate is due to the forces of attraction between molecules and atoms, which can be measured by surface tension forces. In this sense, Kinloch (Kinloch 1980, Kinloch et al. 1994, Kinloch 1997) developed the first studies in which the adhesive energy, defined as the required energy to separate the two element involved in the delamination phenomenon, is treated with a fracture mechanics approach.

In fracture mechanics, the formalism of continuous mechanics is used: details of the molecular structure of the polymer are ignored and this is seen as a single body with particular physical properties. In the first half of 1900, Griffith demonstrated that the theoretical stress for the fracture of a brittle solid had to be on the order of one-tenth of Young's module. However, from the experimental results this prediction appeared largely oversized (Griffith 1921). The reason for these low failure stresses was the presence of small imperfections in the material due to the manufacturing process, acting as concentrators of stress. This is easily described in materials that deform in an elastic linear manner, such as glass material.

B.3 Adhesion: theoretical approach

Due to the impossibility of using the closed-form solutions of fracture mechanics in a microscopic scale problem, Kinloch et al. (1994) focus on solving the calculation of G by applying a balance of energies involved in the peeling mechanics.

This approach is based on an energy-type criterion and describes the propagation of a fracture in terms of converting the work performed (W) by an external force and available elastic energy (U) stored in the sample creating an interfacial area described by a free surface energy (G).

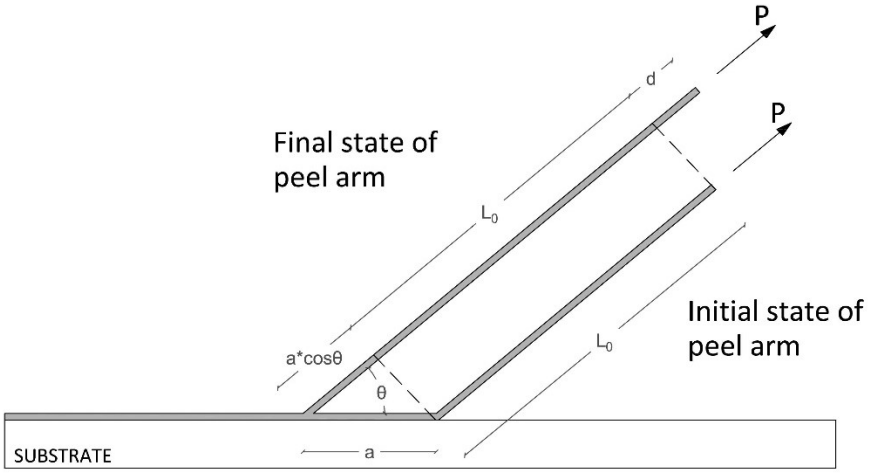

Figure B.3-1 Geometric configuration of peel test (figure © S. Mattei)

More in detail, given the geometry of the mathematical problem by Fig. B.3-1, the external work (W) can be computed as equal to the product of the external peel force (P) and its travel distance (d). Furthermore, when the peel angle is considered as constant, d is calculated with a trivial estimation as follows:

$$\mathrm{d} = (1 + \varepsilon_a + \cos\vartheta)\mathrm{a} \tag{43}$$

Where: ϑ is the constant peel angle; a represents the peeling distance and ε_a denotes the inelastic contribute to the elongation of the peel arm.

Consequently, W can be re-formulated in a final form as:

$$\mathrm{W} = \mathrm{P}(1 + \varepsilon_a + \cos\vartheta)\mathrm{a} \tag{44}$$

According to Kinloch's approach, the primary assumptions are related to the mechanical behaviour of the tape, and to the setup geometry characterized by a minimum number of variables neglecting speed-rate test or multilayer section of the tape.

Based on the aforementioned hypotheses, the external work corresponds to the sum of the energy of fracture (U_a), the energy dissipated during the elongation (U_s+U_{dt}) and the bending of the tape (U_{db}). Eq. 45 is derived by substituting these three energy terms in energy per unit area of peel propagation (a x b):

$$\mathrm{W} = \mathrm{U_a} + \mathrm{U_s} + \mathrm{U_{dt}} + \mathrm{U_b} = (\mathrm{G_a} + \mathrm{G_s} + \mathrm{G_{dt}} + \mathrm{G_b})\mathrm{ab} \tag{45}$$

Where a is, again, the peeling distance involved in delamination and b is the width of the film.

When considering the upper and lower bound in mechanical behaviour of tape in tension and bending, the fracture energy can be calculated as $G_a^{\infty E}$ by Eq. (46) in case of an infinite tensile stiffness and zero bending stiffness, or as in Eq. (47) in the opposite case. It is worth to highlight that both equations do not contain parameters related to the mechanical behaviour of the film because such hypotheses make the problem of only geometric character and purely elastic.

$$G_a^{\infty E} = \frac{P}{b}(1 - \cos\vartheta) \tag{46}$$

$$G_a^{eb} = \frac{P}{b}(1 + \varepsilon_a - \cos\vartheta) - h_s \int_0^{\varepsilon_a} \sigma \, d\varepsilon \tag{47}$$

Where h_s denotes the thickness of the tape, σ and ε are stress and strain in the peel arm due to the peel force (P), respectively.

In some configurations, more than in others, generally the effects of flexural deformation in the tape cannot be neglected because of their magnitude. The energy losses per unit area (G_{bd}), occurring near the crack front for a plastic or viscoelastic material, has to be taken into account in the evaluation of total fracture energy as follows:

$$G_a = \frac{P}{b}(1 + \varepsilon_a - \cos\vartheta) - h_s \int_0^{\varepsilon_a} \sigma \, d\varepsilon - G_{db} \tag{48}$$

The most critical step in assessing the adhesive energy in accordance with fracture mechanics basics is the estimation of G_{db} due to the necessary evaluation of the deformation during the loading and unloading cycles. It is defined as function of the area under a complete cycle in terms of bending moment and rotations (see Fig. B.3-2).

$$G_{db} = \frac{Area}{b} \tag{49}$$

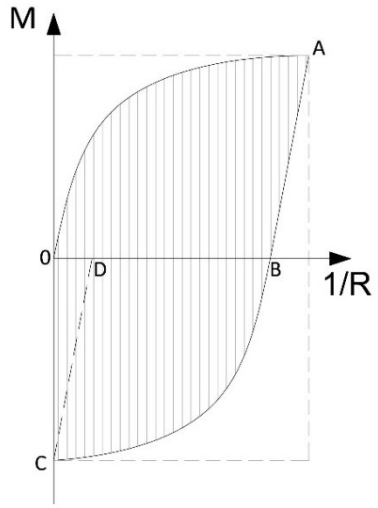

Figure B.3-2 Bending moment diagram vs bending radius for peeling

B.3 Adhesion: theoretical approach

Since the deformation of an assumed elastoplastic material (with a work-hardening behaviour) in this context falls in large-displacement field, based on a range of possible deformation types of film upon loaded and unloaded, a detailed work by Kinloch et al. (1994) embodies the derivation process of the reported following equations (from Eq. (50) to Eq. (55)).

According to the first case the peel arm behaves as elastic during loading and unloading processes. In the second case, the loading phase involves plastic deformations. Finally, Case#3 provides for plastic deformations in both processes.

Case#1:

$$\frac{\mathrm{G_{db}}}{\mathrm{G^{e}_{max}}} = 0 \tag{50}$$

$$\frac{\mathrm{G_{a}^{\infty E}}}{\mathrm{G^{e}_{max}}} = \frac{(1-\cos\vartheta)}{[1-\cos(\vartheta-\vartheta_0)]}\frac{k_0^2}{3} \tag{51}$$

Case#2:

$$\frac{\mathrm{G_{db}}}{\mathrm{G^{e}_{max}}} = (1-\alpha)\left[\frac{k_0^2}{3} + \frac{2(1-\alpha)^2}{3k_0} - 1\right] \tag{52}$$

$$\frac{\mathrm{G_{a}^{\infty E}}}{\mathrm{G^{e}_{max}}} = \frac{(1-\cos\vartheta)}{[1-\cos(\vartheta-\vartheta_0)]}\frac{k_0^2}{3} \tag{53}$$

Case#3:

$$\frac{\mathrm{G_{db}}}{\mathrm{G^{e}_{max}}} = f_1(k_0) \tag{54}$$

$$\frac{\mathrm{G_{a}^{\infty E}}}{\mathrm{G^{e}_{max}}} = \frac{(1-\cos\vartheta)}{[1-\cos(\vartheta-\vartheta_0)]} f_2(k_0) \tag{55}$$

Where k_0 is the ratio between two radius of curvature, R_1/R_0, in which the former corresponds to the onset of plastic yielding and the latter is the initial one; ϑ_0 represents the root rotation. This latter parameter is also a strong function of the bending moment at the peel front. Finally $\mathrm{G^{e}_{max}}$ is the maximum value of stored elastic energy when the tape's material behaviour falls in the totally linear elastic branch and is function of E (Young's modulus) and ε_y (deformation at yielding point):

$$\mathrm{G^{e}_{max}} = \frac{1}{2}\left(E\varepsilon_y^2 h\right) \tag{56}$$

B.3.2 Application of the classic approach to the specific peel test configuration

It is of great interest to apply the classic approach to derive the fracture energy in case of the configuration geometry as indicated in Fig. B.3-2, with the aim of generalizing the theoretical formulations and avoiding the results dependency on test setup.

B.3 Adhesion: theoretical approach

Since it is not possible to describe the variation of the peel angle during the delamination observed in laboratory, which is a function of several factors (i.e., speed-rate, mechanical parameters of the tape and adhesion of PSA), the algebraic problem is discretized starting from the Kinloch formulations. Consequently, Eq. (46) and Eq. (47) are reformulated for each unit of time in the data acquisition from experimental test and reported below (Mattei et al. 2022) in case of elastic film elongation but neglecting the bending deformation:

$$G_a^{\infty E} = \sum_{i=0}^{i=t-1} \frac{1}{b}\left[\frac{f_{i+1}}{\sin\ \theta_{i+1}}(1-\cos\theta_{i+1}) - \frac{f_i}{\sin\ \theta_i}(1-\cos\theta_i)\right] \tag{57}$$

$$G_a^{eb} = \sum_{i=0}^{i=t-1} \frac{1}{b}\left[\frac{f_{i+1}}{\sin\ \theta_{i+1}}\left(1+\varepsilon_{a(i+1)}-\cos\theta_{i+1}\right) - \frac{f_i}{\sin\ \theta_i}(1+\varepsilon_{ai}-\cos\theta_i)\right] - h_s E\frac{{\varepsilon_a}^2}{2} \tag{58}$$

Where *i* and *i+1* represent the two consecutive time steps whereas *t* is the total test time.

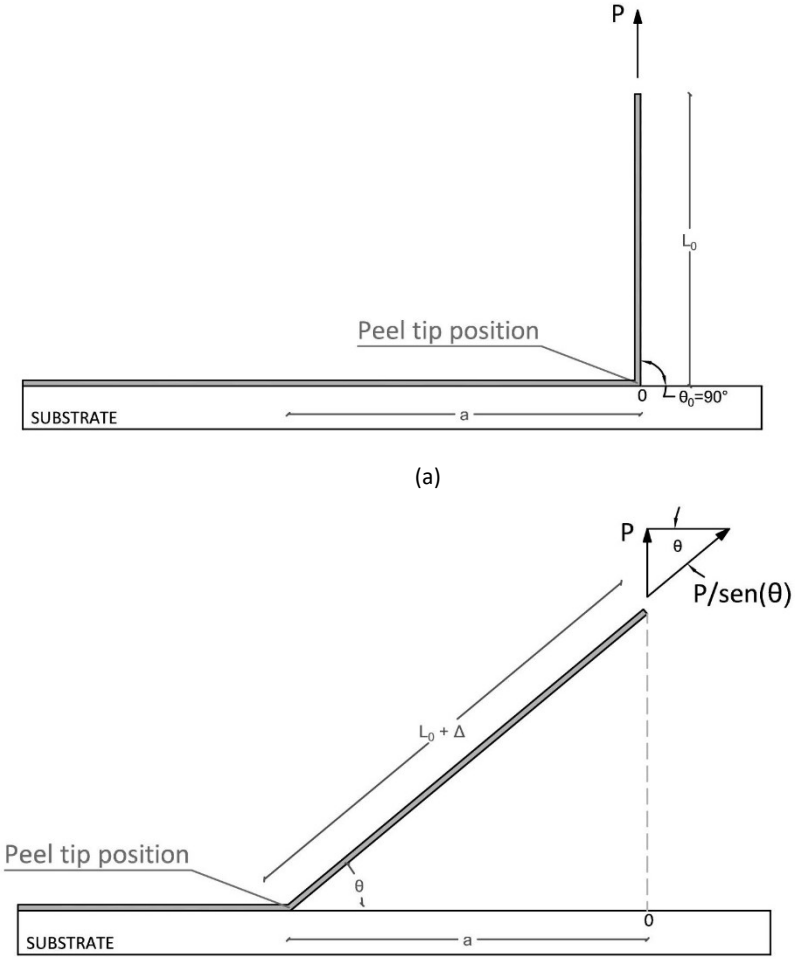

Figure B.3-3 Configuration of peeling process at (a) t=0 and (b) t=i (figure © S. Mattei)

B.3 Adhesion: theoretical approach

The overall applied methodology follows the same steps of the Kinloch's 'array' for defining the fracture energy, G_a. For the sake of clarity, the iterative method is presented in the following points:

1- $G_a^{\infty E}$ by Eq. (57);
2- G_a^{eb} by Eq. (58);
3- G_{max}^{e} by the original Eq. (56) due to its complete independence from geometric parameters;
4- Identification of the suitable Case# by means of some defined conditions below:
   Case#1 if $0 < k_0 < 1$
   Case#2 if $1 < k_0 < 2(1-\alpha)/(1-2\alpha)$ or $\alpha \geq 0.5$
   Case#3 if $k_0 > 2(1-\alpha)/(1-2\alpha)$ and $\alpha < 0.5$

Polymers behaviour is usually well described by Case#3, but at this magnitude of the forces involved in the peeling mechanism, Case#1 is the best representation of PET-tape behaviour.

B.3.3 References

Griffith, A. A. (1921). “The phenomena of rupture and flow in solids”. *Philosophical Transactions of the Royal Society B: Biological Sciences*. A 221, pp.163-198.

Kinloch, A.J. (1980). “The science of adhesion”. *Journal of Material’s Science*, 15, pp.2141-2166.

Kinloch, A.J., Lau, C.C., & Williams, J.G. (1994). The peeling of flexible laminates. *International Journal of Fracture*, 66, 45-70.

Kinloch, A.J. (1997). “Adhesive in engineering. Proceedings of the Institution of Mechanical Engineers”. *Part G: Journal of Aerospace Engineering*, vol 211.

Mattei, S., Cozzarini, L., Bedon, C. (2022). “Experimental and numerical peeling investigation on aged multi-layer anti-shatter safety films (ASFs) for structural glass retrofit”. *Symmetry*, 14(1), 162.

B.4 Finite Element Modelling

In this chapter, the main purpose is the calibration of a Finite Element Model with the ability to carefully reproduce peeling phenomena and predict mechanical bending responses of coated glass with anti-shatter films. In this regard, quasi-static numerical simulations in the commercial calculation code Abaqus/Explicit v.6.12 (2017) were performed. In this regard, this chapter focuses on a detailed description of geometries and materials properties with a particular emphasis on the modelling of the adhesive layer with the Cohesive Zone Model, available in the library of the used software.

B.4.1 Geometric and material proprieties

B.4.1.1 Peel Test simulations

The geometry of the 3-dimensional model was reproduced properly by the experimental setup (see Fig. B.2-3), through *C3D8R* solid elements for the majority of involved components. The eight-node linear brick element with a reduction integration (*C3D8R*) differs from the original (*C3D8*) in the number of integration points. In the former case, thus, small dimensions are required in the region where a stress concentration would be assessed. For simply matters of numerical times of parametric analyses, the portion of the tape initially not in direct contact with the glass substrate, namely tape backing, was modelled with four-node shell elements (*S4R*) with the same thickness of 0.35 mm. At the interface between 2D and 3D film representations, the *shell-to-solid* constraint was introduced in order to implement the boundary condition of material continuity. In the assembly mesh, 29751 elements were used with 39027 nodes. In Fig. B.4-1 the two-steps of analysis are shown. In the first step the manual positioning of the peel arm at ϑ_0=90° was simulated. Otherwise it would be considered by the software as a fixed pre-deformation of the material on the bending peel-front. This modelling was performed considering a static problem, whereas the second quasi-static step analysis was carried out using the dynamic implicit solver because it reproduced the experimental peeling procedure.

The material input parameters, as summarised in Table B.4-1, have been provided depending on the specific behaviour constitutive law chosen. The tape was modelled by the tensile test outcomes as an elastoplastic material with a work-hardening feature by taking into account the influence of the accelerated ageing protocols. Despite the fact that the glass was considered as a linear elastic material, it is worth noting that during the test it behaves as a rigid solid and the deformation occurs in the only PET + PSA system.

Glass substrate and ASF were modelled separately, as mentioned above, and bonded employing a *cohesive* interaction whose specific cohesive zone law will be derived later in this chapter.

Table B.4-1 Basic material characteristics assumed in FEM simulations of peel test

Material	Elastic modulus	Poisson ratio	Yield stress	Plastic strain at yield point	Ultimate stress	Ultimate plastic strain
	[MPa]		[MPa]		[MPa]	
Glass	70000	0.23	45			
PET	3310	0.49	90	0	134	0.8

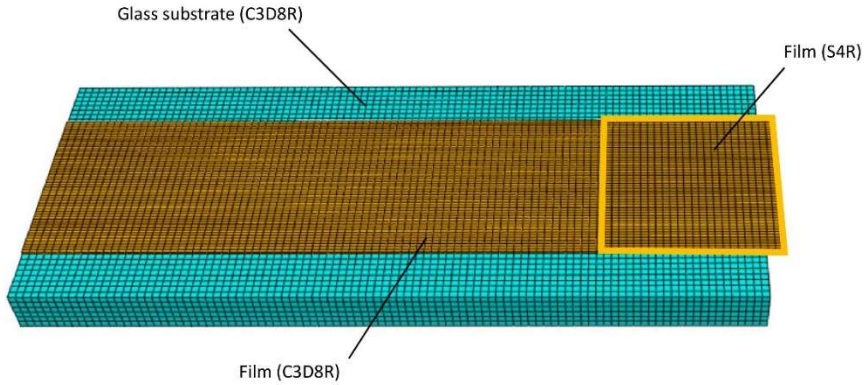

(a)

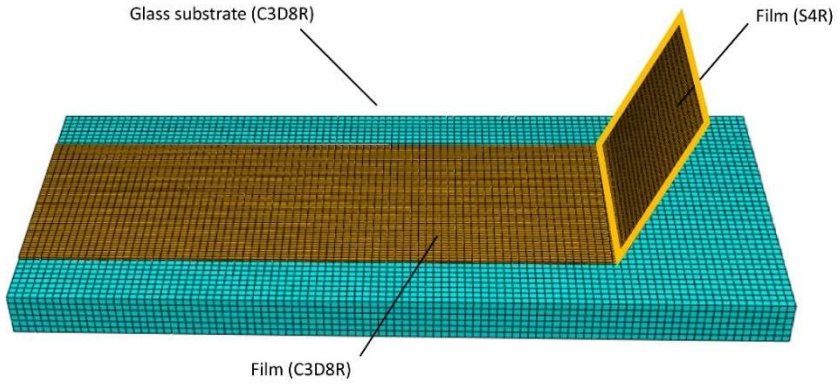

(b)

Figure B.4-1 Finite Element Models for (a) positioning step and (b) numerical simulation of experimental peel test

B.4.1.2 Three-Point bending test simulations

With regards to the numerical simulations of small-scale specimens of glass fitted with safety films subjected to a force applied at the mid-span, the modelling phase is roughly the same as the previous case-study excluding the test setup geometry. The schematic pattern of the three-point bending test, as shown in Fig. B.4-2, consist of a glass rectangular specimen, with dimensions of 10 x 4 x 0.6 mm (L x B x t), that is completely coated by the ASF at the bottom surface and placed on two steel supports assumed as discrete rigid elements (R3D4). These latter cylinder have the original

curvature of the machine components in order to avoid stress concentrations. A general interaction between all the unrestrained contact surfaces with a normal and a tangential behaviour that simulate the sliding phenomenon without interpenetration was defined. Abaqus *cohesive elements* (COH3D4) were used at the interface to model PSA adhesive and the behaviour properties are fully investigated in the following section of this chapter.

Finally, a total number of 6972 solid elements constitutes the final assembly and the application of the constant displacement-rate takes place through the upper cylinder with the same geometric and material characteristics.

The material properties are briefly reported in Table B.4-2. In this context, the assumption of linear elastic behaviour for glass is unsuitable because of the importance of assessing the residual post-fracture strength in an intrinsically destructive test. For this reason, the annealed glass was modelled through the *brittle cracking* constitutive law characterized by the definition of the Mode I fracture energy from literature (Bedon et al. 2017). In addition, the sub-options *brittle shear* and *brittle failure* are used to describe the post-cracking field based on a reduction of tangential stiffness by using the power law form of the shear retention model by Eq. (59) as a function of the p exponent equals to 2, and the maximum magnitude of the deformation (e_{max}^{ck}) equals to 0.01.

$$\rho\left(e_{nn}^{ck}\right) = \left(1 - \frac{e_{nn}^{ck}}{e_{max}^{ck}}\right)^{p} \tag{59}$$

Where e_{nn}^{ck} is the crack opening strain.

Table B.4-2 Basic material characteristics assumed in FEM simulations of 3PB test

Material	Elastic modulus	Poisson ratio	Yield stress	Plastic strain at yield point	Ultimate stress	Ultimate plastic strain	Fracture energy	e_{max}^{ck}
	[MPa]		[MPa]		[MPa]		[J/m²]	
Glass	70000	0.23	45				3	0.01
PET	3310	0.49	90	0	134	0.8		

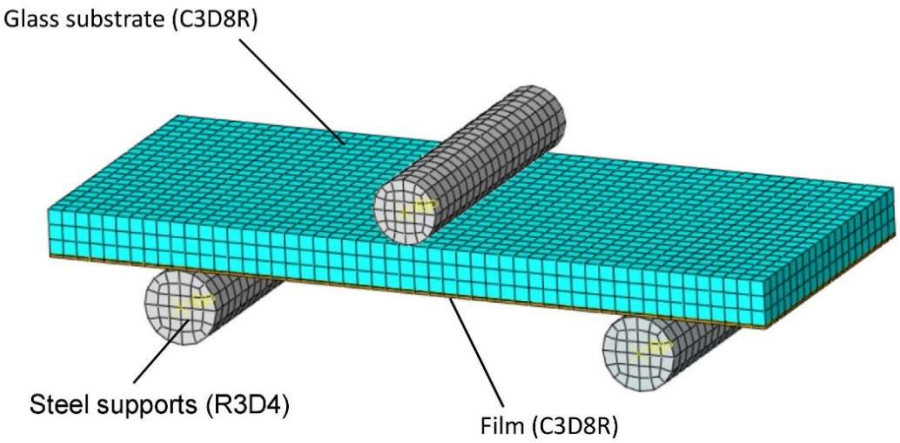

Figure B.4-2 Finite Element Models for numerical simulation of experimental 3PB test

B.4.2 Cohesive Zone Model (CZM)

As mentioned above, this paragraph will describe the Cohesive Zone Model used for PSA characterization. Generally, an adhesive layer can be modelled as a *cohesive element* or a *surface* (Bedon et al. 2018, Rahulkumar et al. 2000, Vocialta et al. 2018). The behaviour behind both typologies of numerical simulation of what observed in the experimental campaign is defined by means of the same description parameters. The main difference between the two technique consists in a primary assumption in drafting the cohesive element (*COH3D4*). In fact, being intended for bonded interfaces, the thickness should be small enough in order to be considered as irrelevant. Otherwise, for the purpose of the final result the complete solid modelling is required.

In such cases, the constitutive response of the adhesive layer is defined by means of a *traction-separation law*. According to this behaviour model, the three components of the nominal traction stress vector, $\{t\}$, are related to the three corresponding separation directions: n=normal traction, s and t= shear tractions (see Fig B.4-3). By definition, traction stresses are computed as the ratios between traction forces and the nominal area; whereas the corresponding separation measures are merely obtained as the relative displacements divided by the adhesive thickness. The latter is considered equals to 1 in such a way as to be made equal to the nominal strain since this is defined as the ratio between the above separation and the thickness of the adhesive.

The Fig B.4-3 shows the development of the adhesion behaviour during the delamination process. The first branch is completely linear elastic up to the maximum value of the nominal traction, t, corresponding to the initiation of the crack propagation. Instead, the following part of the model denotes the degradation of the adhesion and can be described by many different formulations: linear; exponential; power law; etc..

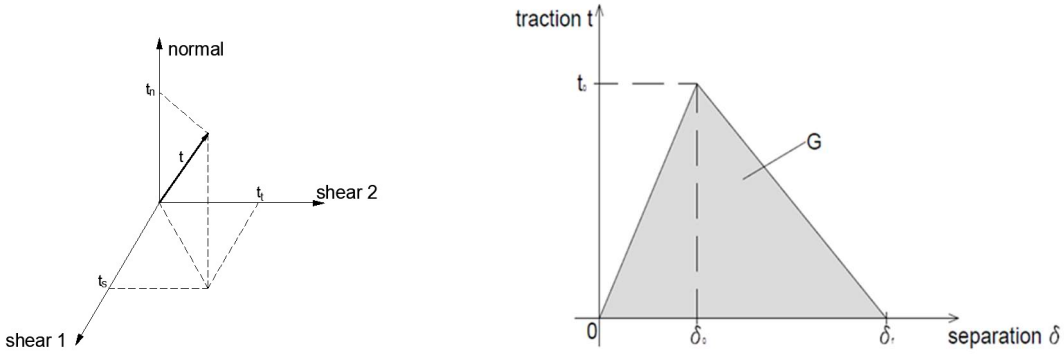

Figure B.4-3 Triangular traction-separation law for cohesive zone model (figure © S. Mattei)

The elastic behaviour is provided by the following matrix equation:

$$t = E\varepsilon = K\delta = \begin{Bmatrix} t_n \\ t_s \\ t_t \end{Bmatrix} = \begin{bmatrix} K_{nn} & K_{sn} & K_{nt} \\ K_{ns} & K_{ss} & K_{st} \\ K_{nt} & K_{st} & K_{tt} \end{bmatrix} \begin{Bmatrix} \delta_n \\ \delta_s \\ \delta_t \end{Bmatrix} \quad (60)$$

In case of uncoupled behaviour between the direction components, the off-diagonal terms can be considered as null values and the Eq. (60) re-written as:

B.4 Finite Element Modelling

$$t = E\varepsilon = K\delta = \begin{Bmatrix} t_n \\ t_s \\ t_t \end{Bmatrix} = \begin{bmatrix} \frac{E_{adh}}{t_{adh}} & 0 & 0 \\ 0 & \frac{G_{adh}}{t_{adh}} & 0 \\ 0 & 0 & \frac{G_{adh}}{t_{adh}} \end{bmatrix} \begin{Bmatrix} \delta_n \\ \delta_s \\ \delta_t \end{Bmatrix} \quad (61)$$

Where: K is the stiffness matrix.

Concerning the damage evolution, the theoretical issue consists of three assumptions related to overall final adhesive response: the damage initiation criterion by Abaqus library; the propagation law and the ability to consider the failed elements at the next integration steps or not (*deletion* feature). Firstly, several damage initiation criteria are available in the numerical software based on solely tractions or separations. The general rule consists in the achievement of 1, that corresponds to the onset of the crack. In this study, a maximum nominal stress (MAXS) criterion was considered:

$$\max\left\{\frac{\langle t_n \rangle}{t_n^0}; \frac{t_s}{t_s^0}; \frac{t_t}{t_t^0}\right\} \quad (62)$$

Where:

- t_n and t_n^0 represent the normal traction at a general integration step and at the peak of traction-separation law, respectively;
- t_s and t_s^0 represent the s-shear traction at a general integration step and at the peak of traction-separation law, respectively;
- t_t and t_t^0 represent the t-shear traction at a general integration step and at the peak of traction-separation law, respectively;
- the bracket in the formulation, $\langle \dots \rangle$, namely the Macaulay brackets, mean that a pure compressive deformation can't provide the damage initiation.

The damage evolution is monitored by a scalar parameter, *D*, ranging from 0 (='no damage' condition) to 1 ('total failure' condition). This latter case signifies a zero stiffness for a cohesive element, and a lost cohesive bond in the specific node for a cohesive surface.

D acts as a reduction factor for stiffness in every direction following these equations:

$$t_n = \begin{cases} (1-D)\bar{t_n} & \text{for } \bar{t_n} \geq 0 \\ t_n & \text{otherwise} \end{cases} \quad (63)$$

$$t_s = (1-D)\bar{t_s} \quad (64)$$

$$t_t = (1-D)\bar{t_t} \quad (65)$$

Where $\bar{t_n}$; $\bar{t_s}$ and $\bar{t_t}$ represent the ideal stress components in case of 'no damage' condition.

Moreover, the software supplies an energy-based or a displacement-based option to define the trend of the last branch of the traction-separation response. In the first case, the

input parameter is G that represents the area under the curve, whereas the former case the ultimate separation corresponds to the intersection of the cohesive response model and the x-axis is used.

B.4.3 References

Simulia. ABAQUS v. 6.12 Computer Software and Online Documentation; Dassault Systems: Providence, RI, USA, 2017.

Bedon, C., Louter, C. (2017). “Numerical analysis of glass-FRP post-tensioned beams–Review and assessment”.*Composite Structures*,*177*, pp.129-140.

Bedon, C., Machalická, K., Eliášová, M., Vokáč, M. (2018). “Numerical modelling of adhesive connections including cohesive damage”. *Challenging Glass Conference Proceedings*, Vol. 6, pp.309-320.

Rahulkumar, P., Jagota, A., Bennison, S. J., Saigal, S. (2000) “Cohesive element modeling of viscoelastic fracture: application to peel testing of polymers,” *International Journal of Solids and Structures*, vol. 37, no. 13, pp. 1873-1897.

Vocialta, M., Corrado, M., Molinari, J.-F., (2018). “Numerical analysis of fragmentation in tempered glass with parallel dynamic insertion of cohesive elements,” *Engineering Fracture Mechanics*, vol. 188, pp. 448-469.

B.5 Discussion on the results

B.5.1 Film results

B.5.1.1 Material properties

Fig. B.5-1 shows the thermograms on the three material layers constituting the tape of the film: Layer 1, 2 and 3 numbered in ascending order from the outermost, considering the adhesive as the inner side (the curves are green, blue and red respectively). In the graph is reported the Heat Flow (mW/mg) as a function of temperature (°C). It's clear that there are no significant differences between layers: the temperature of the melting peak is about T_m=257°C, according to ISO 11537-3. These outputs suggest that the constituent material is a semi-crystalline PET being in line with the typical values in the literature [30], whereas layer 2 is characterized by the presence of a second polymer indicated by a further melting peak, of a lower intensity, at 243°C. This value could represent a polymer that is, generally, blended with PET: PBT (polybutylene terephthalate) or PTT (polytrimethylene terephthalate).

Finally, the determination of glass transition temperature is the last step in the description of the basic properties useful in this characterisation in accordance with ISO 11537-2. T_g is equal to 80 °C for all PET layer, and this is an information of paramount importance in assessing the influence of accelerated ageing procedures.

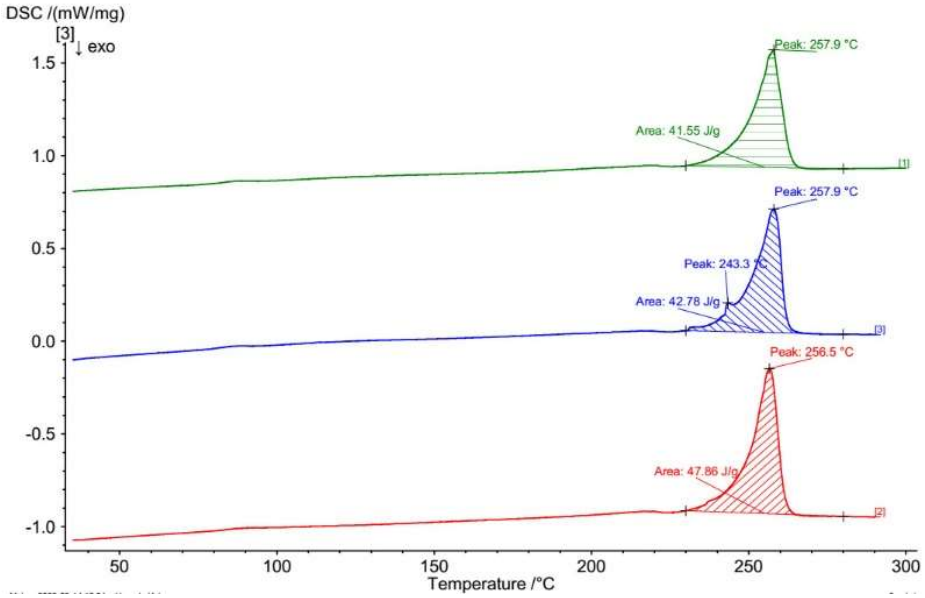

Figure B.5-24: DSC curves for each PET layers: layer-1 (green), layer-2 (blue) and layer-3 (red) [11]

[11] Figure reproduced with permission from (Mattei et al. 2022b) under the terms and conditions of CC-BY license agreement

B.5 Discussion on the results

In Fig. B.5-2 and Fig. B.5-3, FT-IR spectra for PET sheets and adhesive layers are shown respectively. In the first case, the vibrational bands indicated by vertical lines are in good agreement with those relatives to the PET material. It is worth to note that one exception involves the external side of layer 3 for which the difference can be associated to a possible surface treatment with an amine according to the specific bands. Finally, the two adhesive types are characterized by the equivalent chemical composition demonstrated by the correspondence between the peaks. Moreover, the chemical groups specified by the vibrational bands are typical in constituting commercial PSA adhesives (Mapari et al. 2021; Marquez et al. 2020).

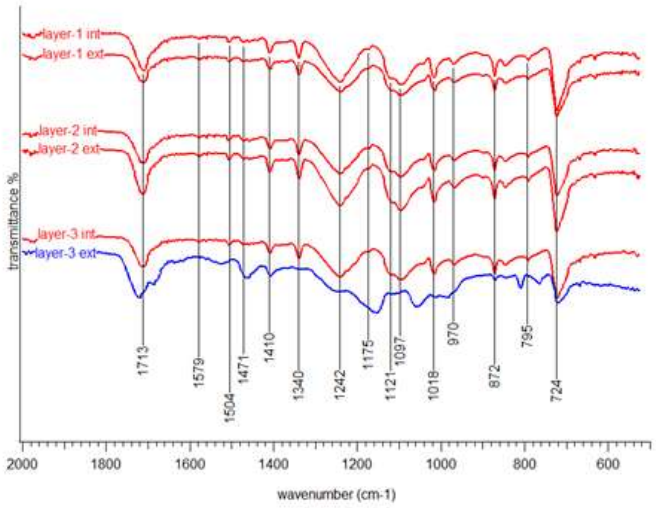

Figure B.5-2 FTIR spectra of layer 1,2 and 3. Layers 1 and 2 (both sides) and layer-3 (internal side)[12]

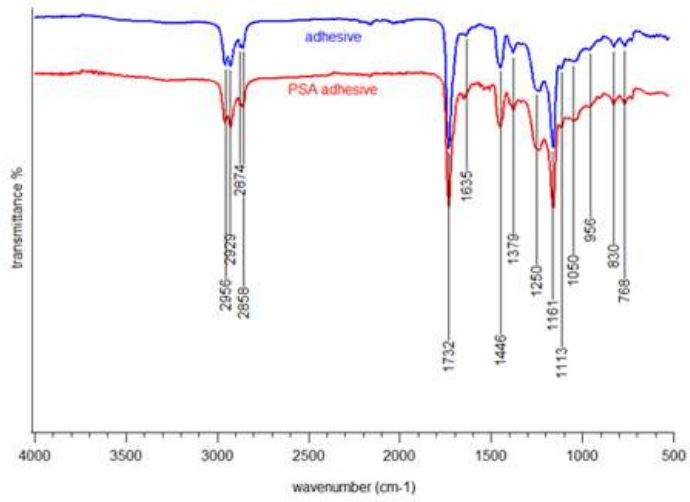

Figure B.5-3 Vibrational bands identified on the adhesive between the layers and on the PSA adhesive [13]

[12] Figure reproduced with permission from (Mattei et al. 2022b) under the terms and conditions of CC-BY license agreement

[13] Figure reproduced with permission from (Mattei et al. 2022b) under the terms and conditions of CC-BY license agreement

An additional Fourier Transform Infrared spectroscopy was performed on aged safety films in order to investigate possible modifications in chemical compositions. However, the result spectra of both materials after ageing procedures do not show any thermal oxidation.

B.5.1.2 Mechanical properties of PET: tensile test

Since the overall goal of this investigation is to derive the modified mechanical properties concerning the glass fitted with anti-shatter films, the knowledge of basic mechanical parameters of the tape, as well as the adhesion properties, are necessary to calibrate the cohesive zone model (CZM) response for the simulation of the experimental tests in Abaqus/CAE.

Tensile tests were carried out on 5 specimens, as shown in Fig. B.5-4(a), and the outputs in terms of force-displacement curve, and the corresponding stress-deformation curves, are reported in Fig. B.5-4(b). Both types of curves have a trend characterized by a first linear stretch, whose initial slope gives the value of the Young modulus, a yielding phase and a last plastic portion with a certain slope that defines a characteristic hardening described by a second slope much lower than the first. During the test of the total multi-layered film, a separation between only two of the three PET-sheets occurred. In particular, during the yielding phase the amorphous PET, the orientation of the molecules is changed, causing a loss of transparency.

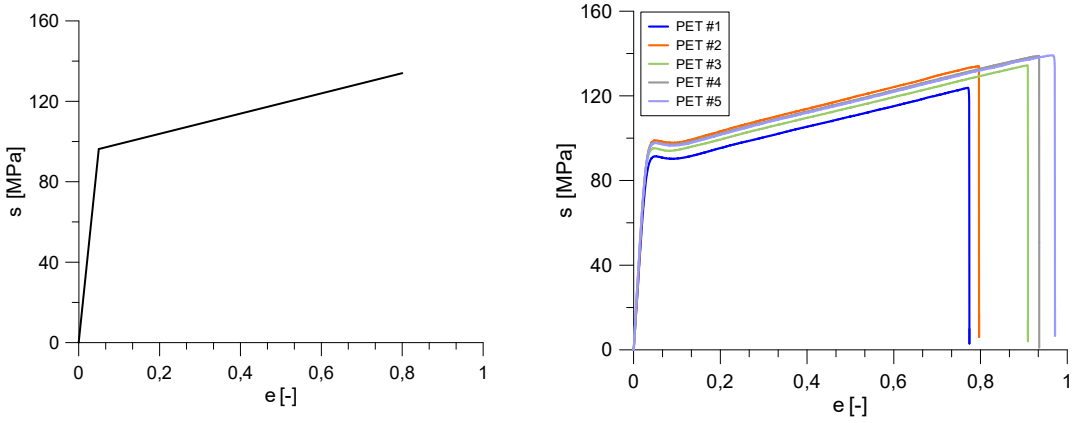

(a)

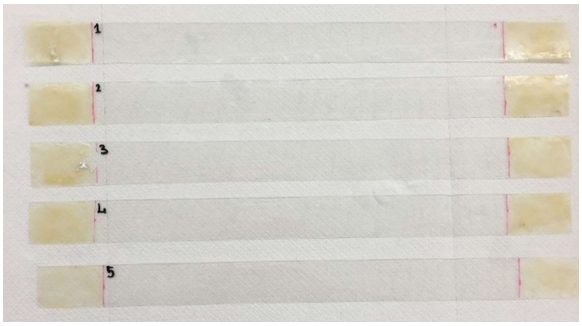

(b)

Figure B.5-4 (a) PET tape specimens (b) Experimental stress-strain curves and (on the top right) mechanical behaviour model (on the bottom right)

B.5 Discussion on the results

Finally, the data obtained from tensile tests are processed to obtain an average of experimental curve and its schematization as bilinear. The main parameters, corresponding to those used in the ideal model of PET tape in Abaqus, are summarized in Table B.5-1.

Table B.5-1 PET basic material characteristics

Material	Elastic modulus	Poisson ratio	Yield stress	Plastic strain at yield point	Ultimate stress	Ultimate plastic strain
	[MPa]		[MPa]		[MPa]	
PET	3310	0.49	96	0	134	0.8

In addition to the above considerations, it is important to consider that several properties of a polymeric material can be affected by physical ageing. For this reason, a literature review concerning the influence of accelerated ageing on PET material allows to understand the actual reduction of mechanical parameters with regard to the values of temperature and exposure time.

Based on fracture data (within a temperature range between 23°C and 70°C) provided by Arkhireyeva and Hashemi (2002) by means of tensile tests performed on PET films, the necessary values at significant temperatures, 50°C and 70°C, are obtained through a curve fitting of the experimental outputs (see Fig. B.5-5). In addition, to assess the degradation over time, a study conducted Oreski et al. (2005) contributes in addressing the effect of physical ageing after the damp heat test. Since the exposure period in the latter case is longer than the maximum considered in this investigation, a calculation in terms of percentage reduction of E1 and E2 (corresponding to elastic and hardening branches respectively) is made for each T_{ageing}, and the same percentages are applied to the values obtained previously. In Fig. B.5-6 are depicted all the mechanical behaviours for various aged PET materials used in numerical simulations. The decrease of tensile properties is evident although the glass transition temperature, T_g, is never reached or exceeded.

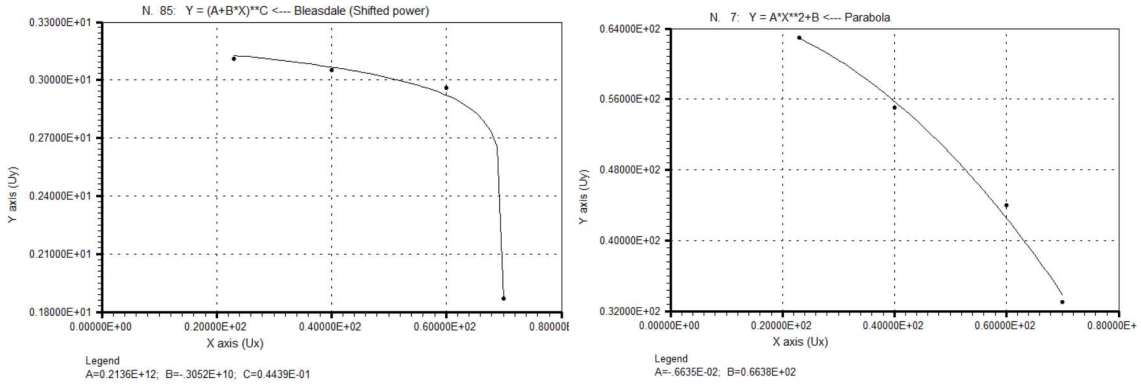

(a) (b)

Figure B.5-5 (a) (T; E) [°C; GPa] (b) (T; σ_Y) [°C; MPa]

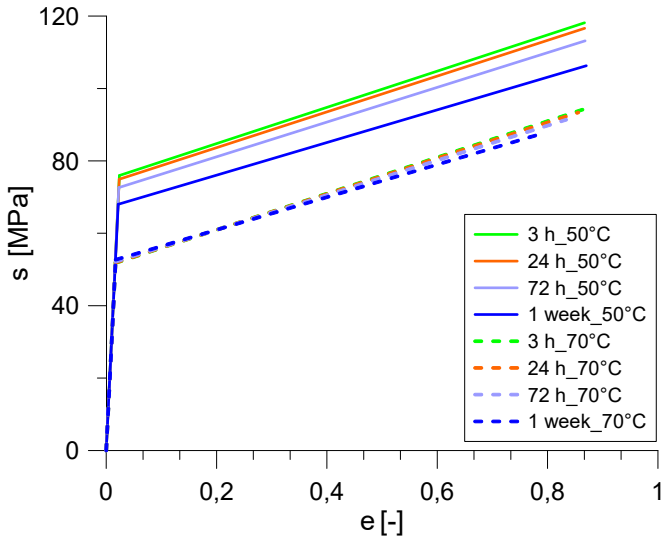

Figure B.5-6 Vibrational bands identified on the adhesive between the layers and on the PSA adhesive

B.5.1.3 Adhesion properties of PSA: peel test

Generally, a peel configuration with a constant peel angle results in a force-time curve that will tend to stabilize providing what is called peel resistance, which is calculated as the average of the steady-state portion of the overall curve. By definition, peel strength is the force needed to "peel" an adhesive film from any given surface. In case of temporary application, as is that of the ASF, the adhesion of the peel must remain in balance between its positioning with proper adhesion and ease of removal taking into account that generally the adhesion strength of the peel builds up over time, if adverse conditions do not come into play.

In this matter, please note that the peculiar configuration, as already mentioned in Section B.2.1.2, does not have a constant geometry in terms of angle, but this latter parameter decreases with ever lower speed from 90°C (initial position) to 34°C (final position). Thus, towards the end of the test, the steady-state region is less visible because it continues to increase slightly.

Figure B.5-7 (a) shows the (P_v-d) curves by the load cell data from universal tensile machine; where P_v represents the vertical value of the load, whereas the peel force is defined as the component in the direction of the peel arm as follows:

$$P_{peel} = P_v \operatorname{sen} \vartheta \tag{66}$$

In the previous formulation, ϑ is carefully estimated by verifying at each instant of time the following expression:

$$\left(l_0 + \frac{y_i - y_0}{\operatorname{sen} \vartheta_i}\right)^2 = (y_0 + y_i)^2 + d_i^2 \tag{67}$$

Where: l_0 is the initial length of the peel arm; y_i and y_0 represent the vertical lengths, starting from the bottom of the substrate, corresponding to the generic instant

of time (i) and t=0s, respectively; ϑ_i is the peel angle and d_i denotes the imposed displacement.

The actual peel force P_{peel} is, instead, gained as the average of P_{peel} shown in Fig. B.5-7 (b) in the steady-state region roughly recognized. Moreover, the mean value relative to the unaged sample is about 4.4 kN.

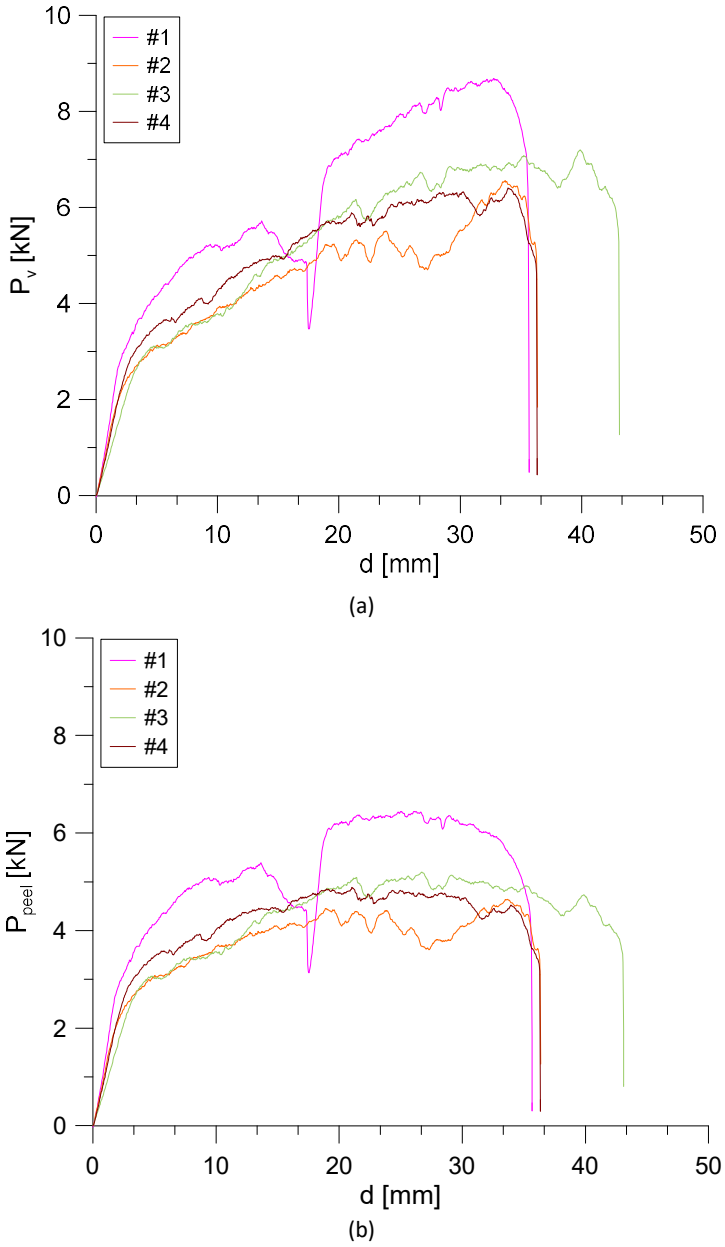

Figure B.5-7 Figure 14. Peel curves of unaged samples (specimens 1-4) in terms of (a) Pvert and (b) its component along peel arm direction.

Effects of accelerated ageing

The experimental results of the peeling tests (Force vs Displacement) at different ageing temperatures are shown in Fig. B.5-8. Instead, Fig. B.5-9 depicts the post-processed curves computing P_{peel} by Eq. 60. The shape of curves is quite similar for each

specimen in a specific sample: the peel force increases initially up the onset of interface delamination. At the same time, for the purposes of comparing between the initial and secondary slope values (distinguishing the chart in two main portions), these are almost very similar regardless of a particular ageing time or temperature.

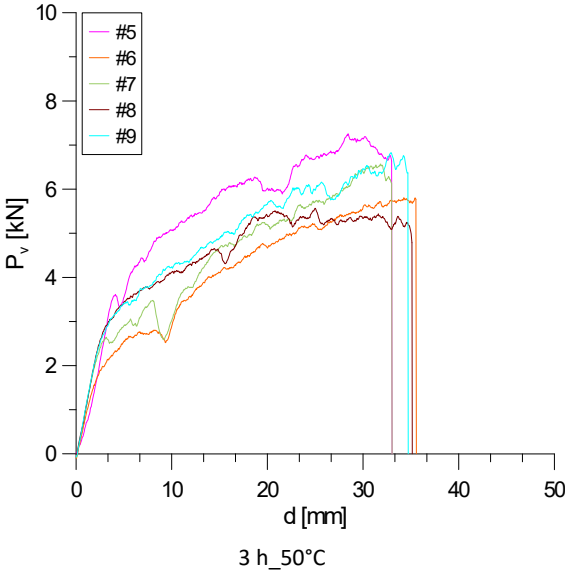

3 h_50°C

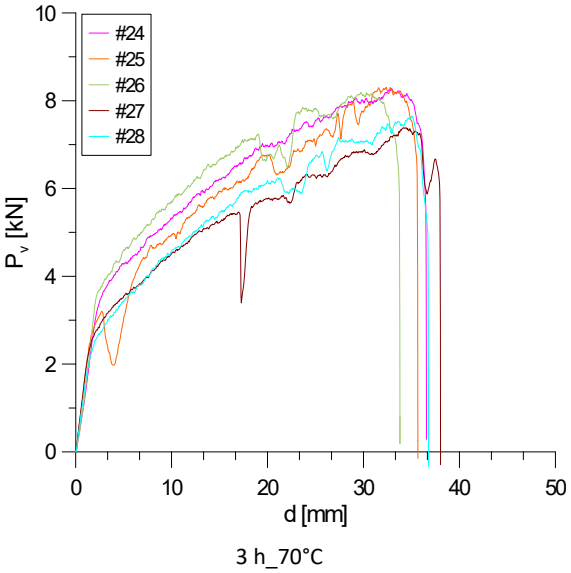

3 h_70°C

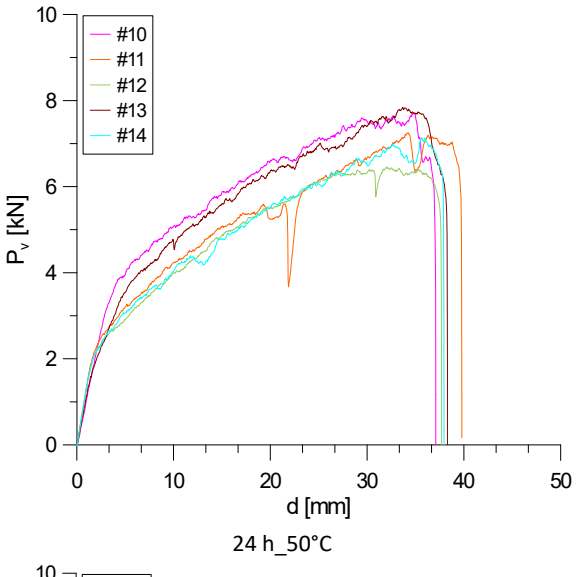

24 h_50°C

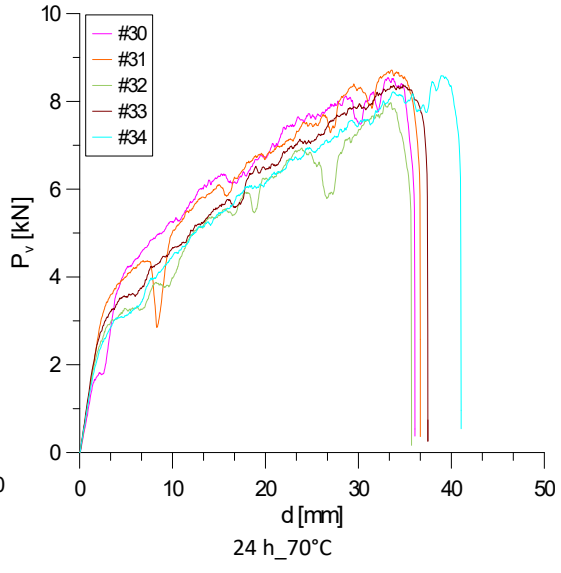

24 h_70°C

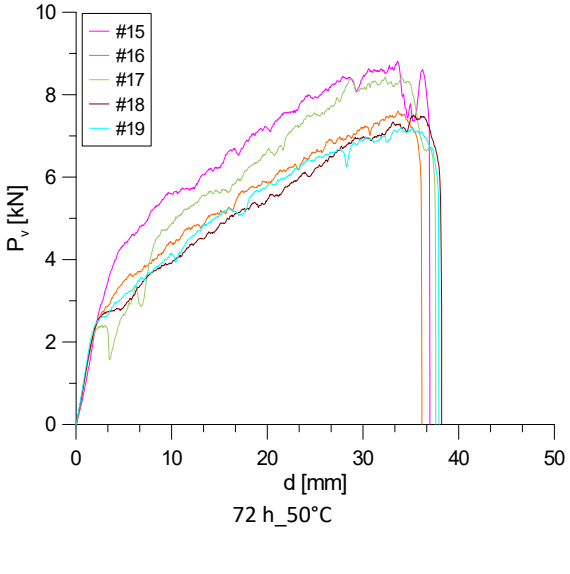

72 h_50°C

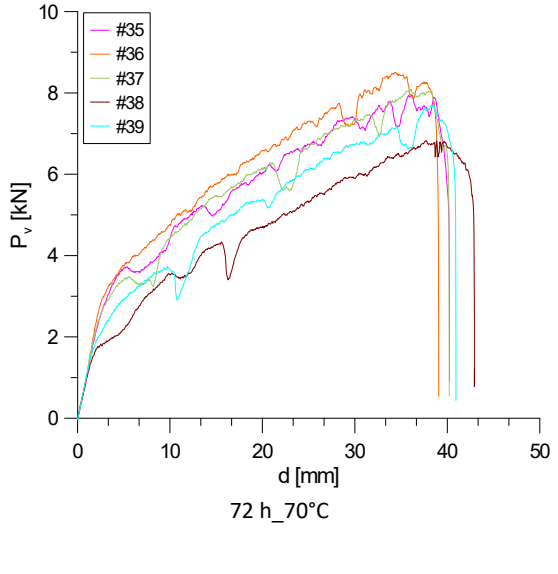

72 h_70°C

B.5 Discussion on the results

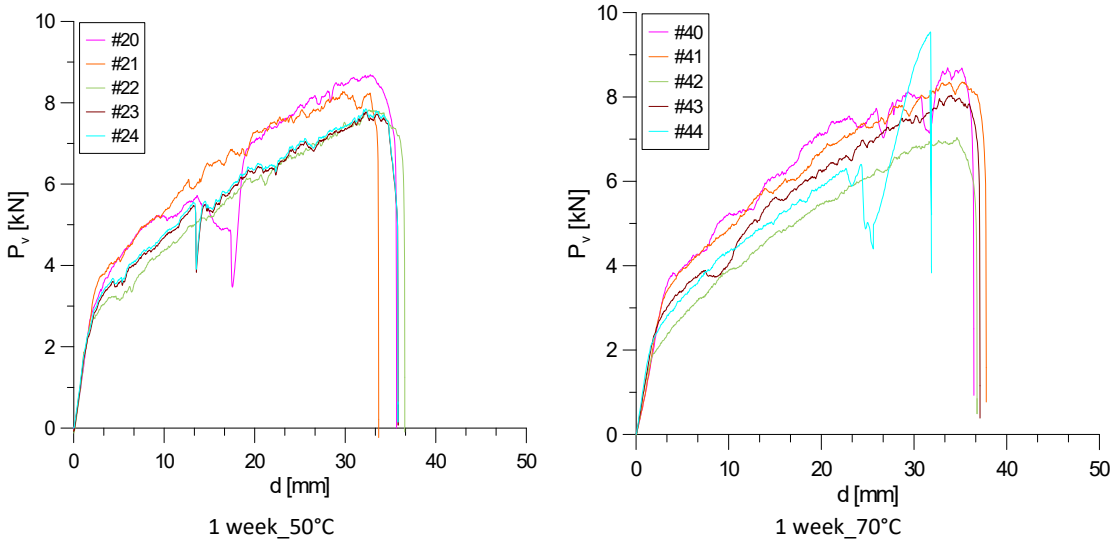

Figure B.5-8 Original experimental results in terms of peel curves (d; P_v) for unaged and aged samples (specimens from #1 to #44)

The experimental curves in terms of P_{peel} are shown in Fig. B.5-8.

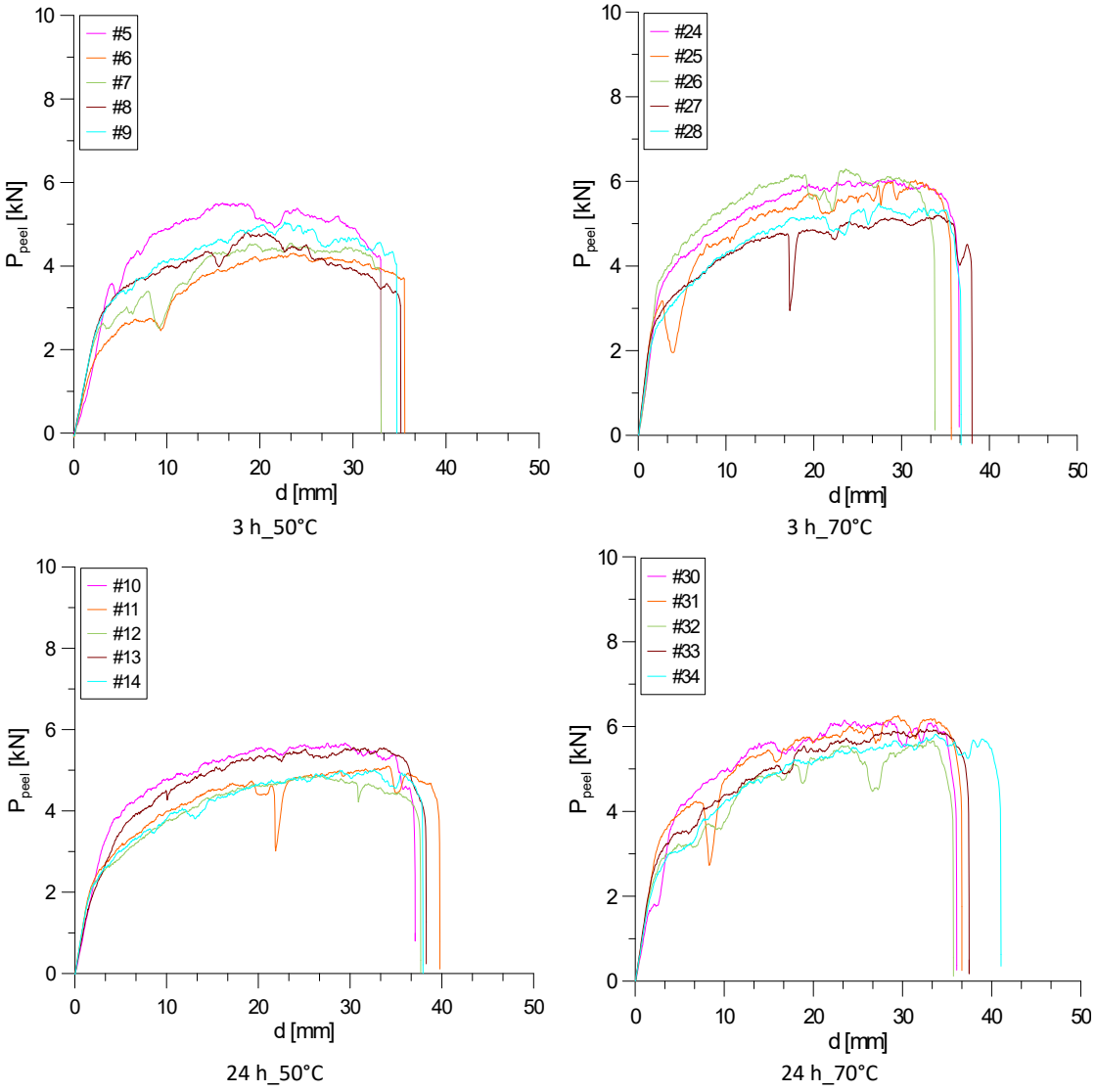

B.5 Discussion on the results

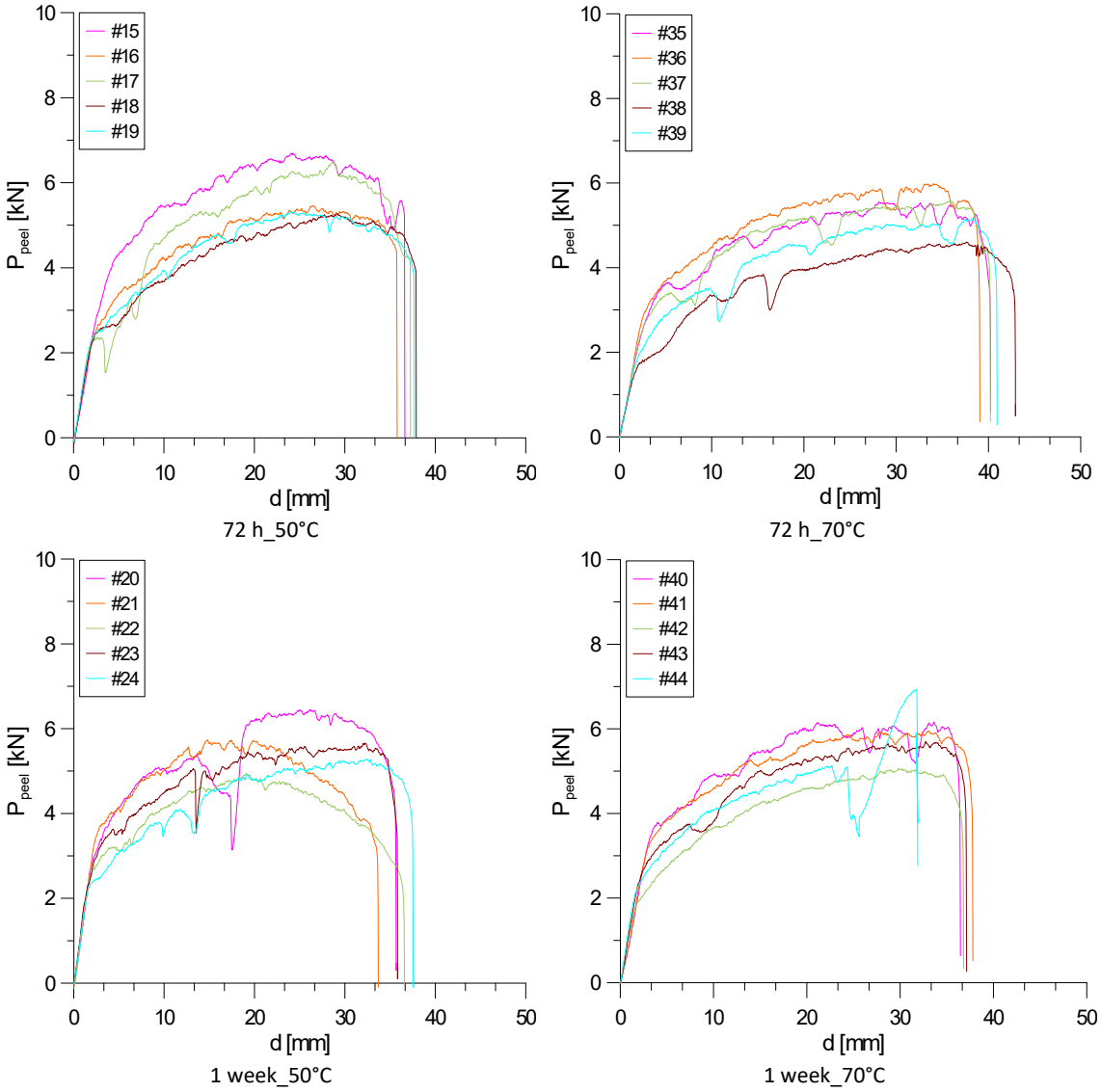

Figure B.5-9 Adjusted experimental results in terms of peel curves (d; P_{peel}) for unaged and aged samples (specimens from #1 to #44)

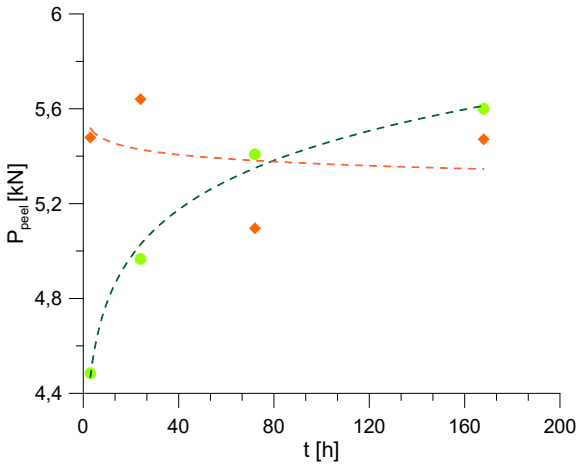

Figure B.5-10 Peel force-as a function of ageing time: T_{ageing}=50°C (green) and T_{ageing}=70°C (orange)

The first observation on the effects of ageing procedures concerns the results in terms of peel resistance. A positive trend is registered in the case of T equal to 50 °C,

and on the contrary, a less marked change can be observed with the second higher temperature. However, it seems that the resistance to peeling tends to stabilize and never change its value again, if not by a little, for very high ageing times and even that it tends to similar values whatever the temperature at which the specimen is exposed. Contrary to what one might guess, peel strength values do not always increase depending on the exposure period regardless of temperature; but the maximum value is detected at 24 h in case of T=70°C, as the proximity to the glass transition tempering value causes a decrease in the stiffness of the PET tape.

With regard to the effect of ageing on fracture energy, some considerations will be provided after performing a detailed calibration analyses of the numerical model for peeling tests, as described in Section B.4.1.1, on the experimental output curves previously discussed. As in the experimental procedure, the numerical simulations were conducted by imposing a displacement at the end of the tape backing with the same constant peel rate of 25.4 mm/min.

In particular, the calibration consists in changing G parameters in Cohesive Zone Model (CZM) neglecting the Mode II component of G and maintaining constant the other stress parameters in the three directions, the components of the traction vector were assumed to be equal. The diagrams in Fig. B.5-11 show the better correlation of analytical peel curves and the corresponding numerical simulations through Abaqus software, for each aged specimen.

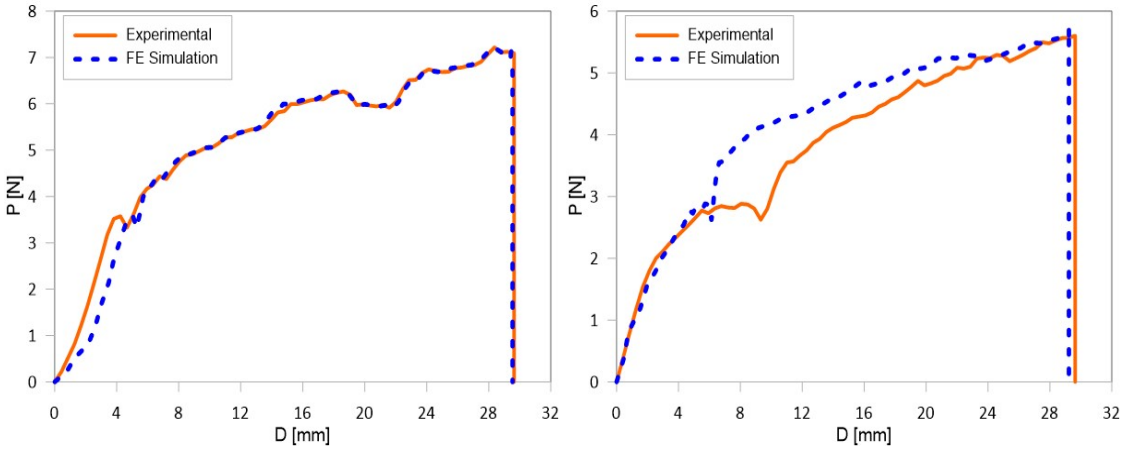

B.5 Discussion on the results

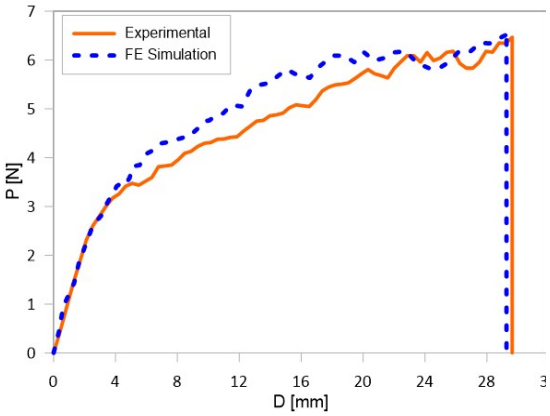

#9

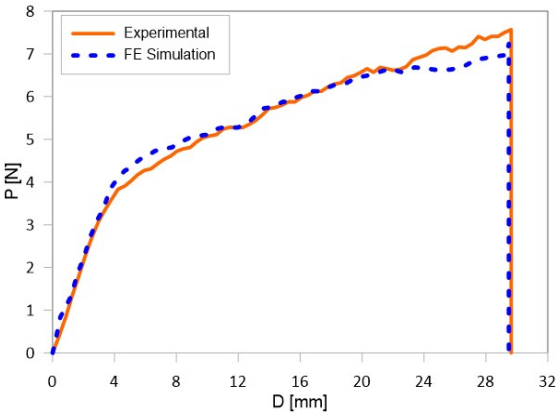

#10

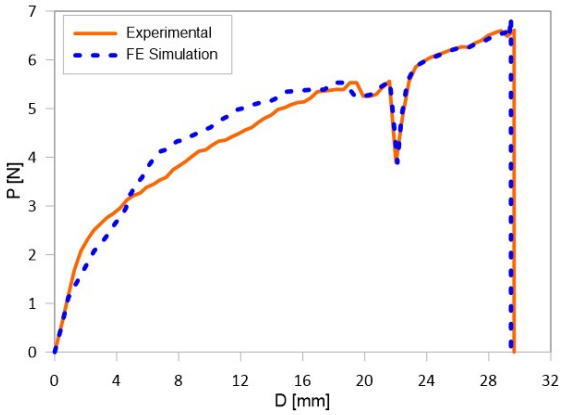

#11

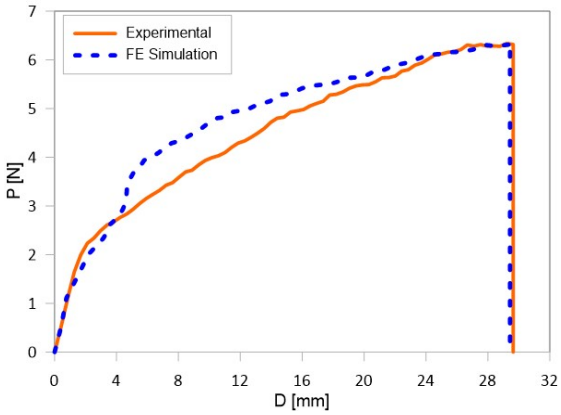

#12

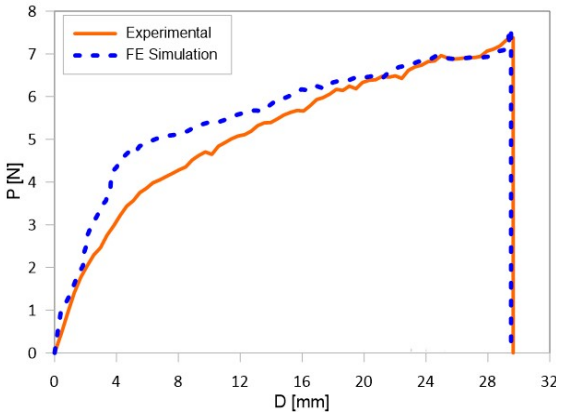

#13

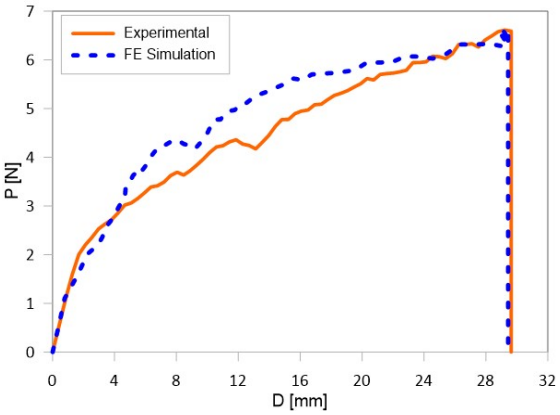

#14

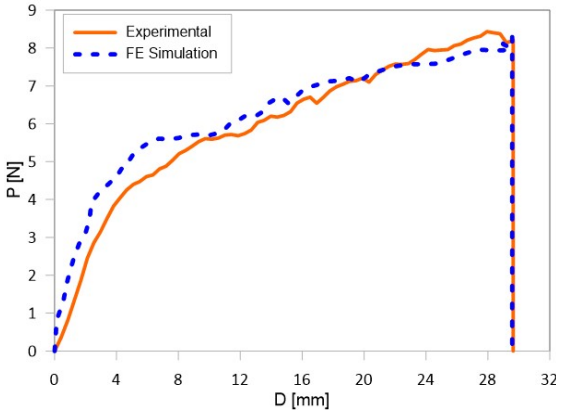

#15

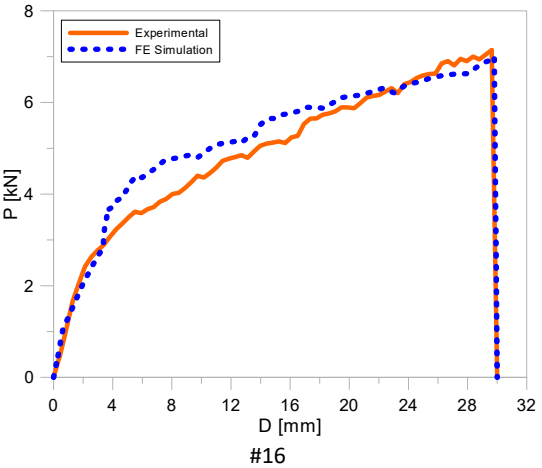

#16

B.5 Discussion on the results

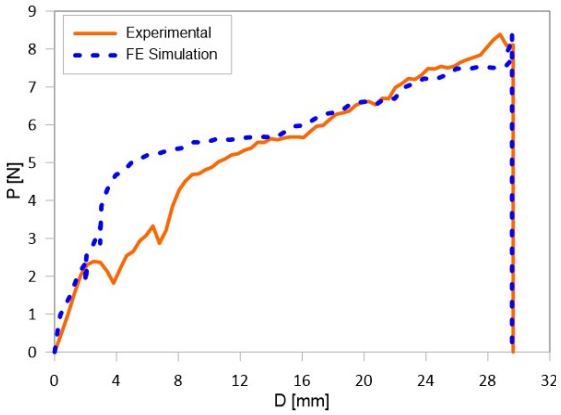

#17

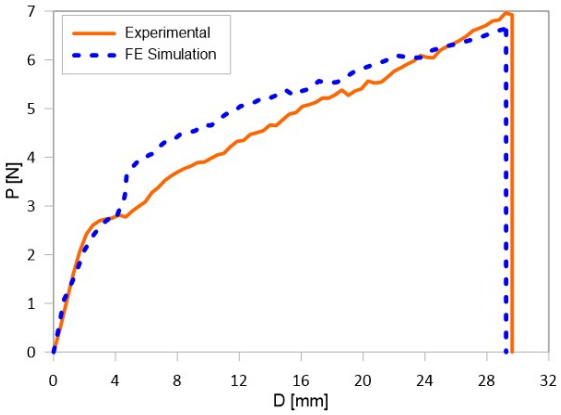

#18

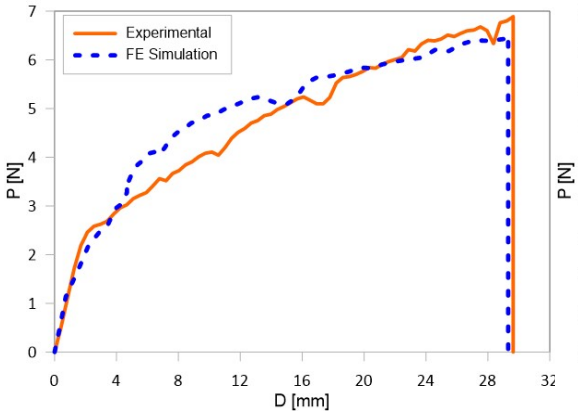

#19

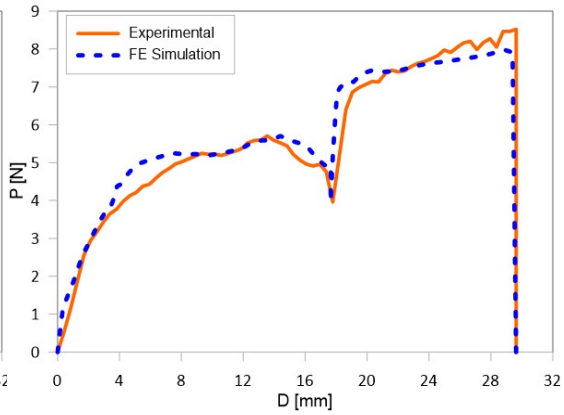

#20

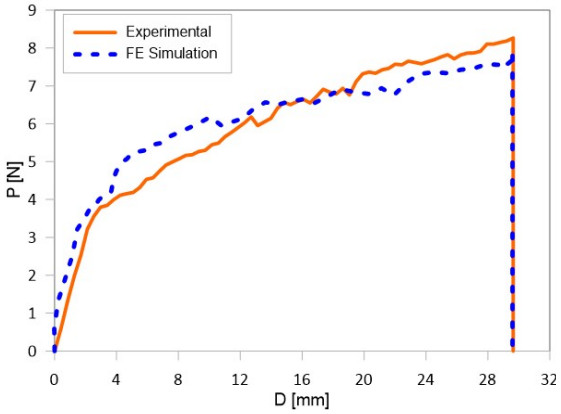

#21

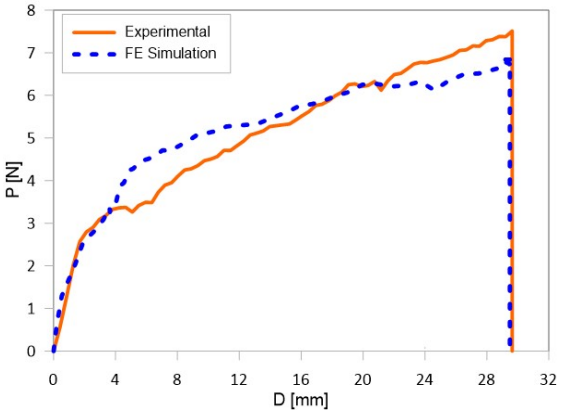

#22

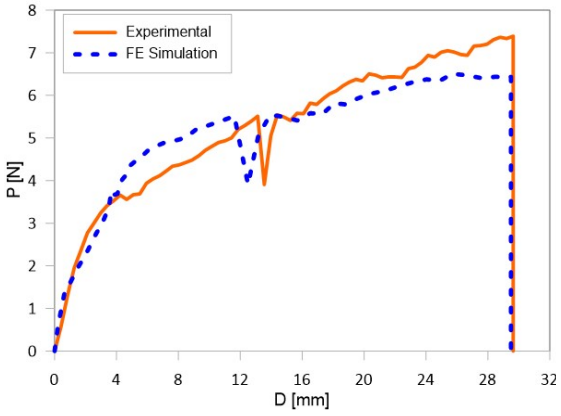

#23

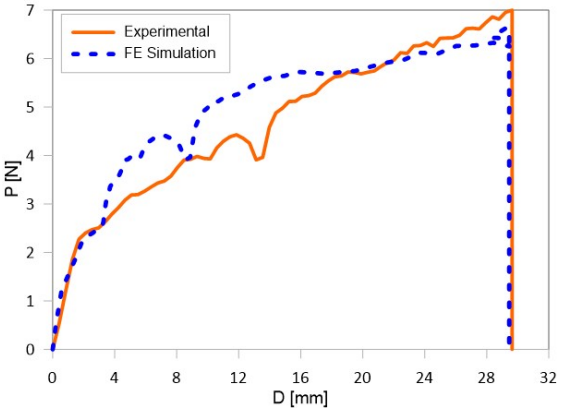

#24

B.5 Discussion on the results

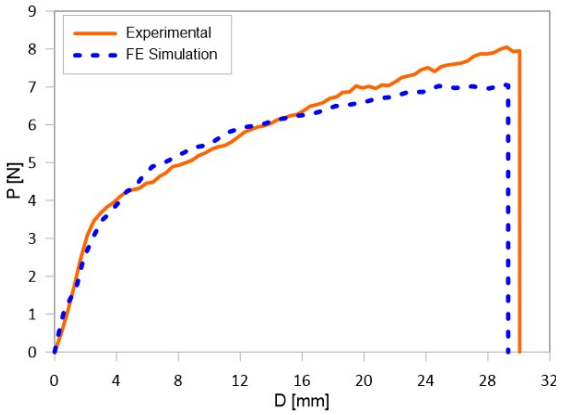

#25

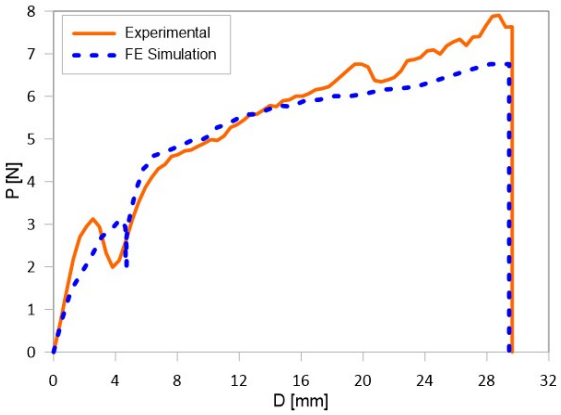

#26

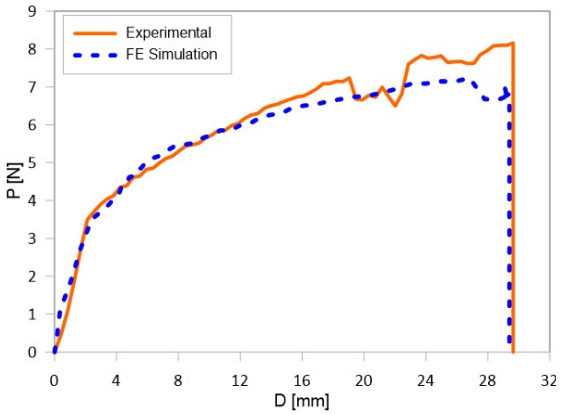

#27

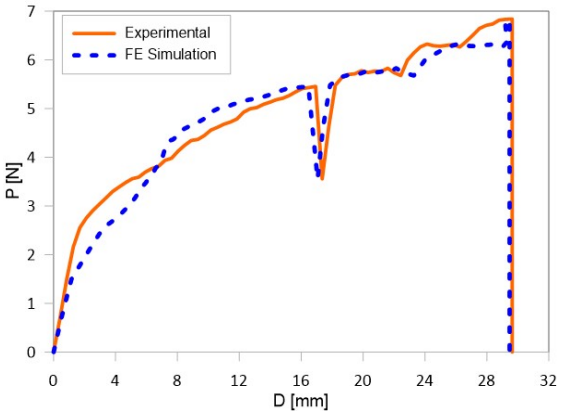

#28

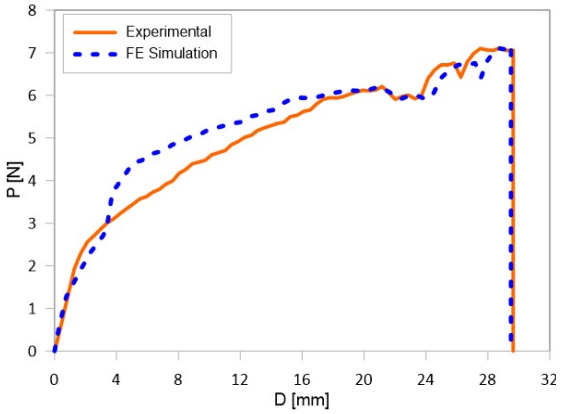

#29

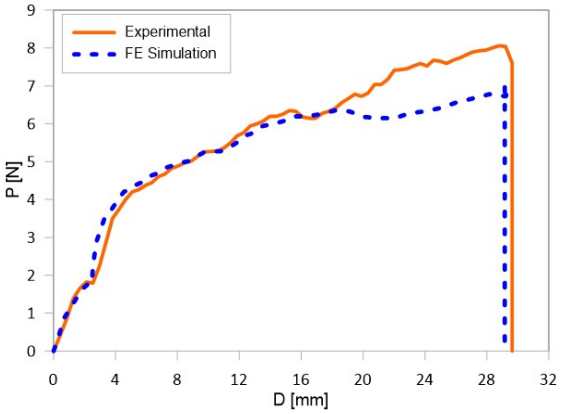

#30

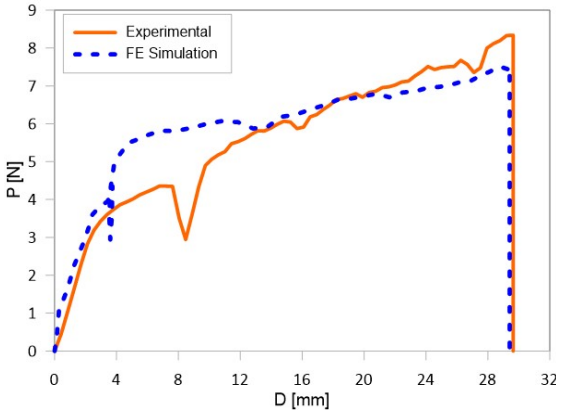

#31

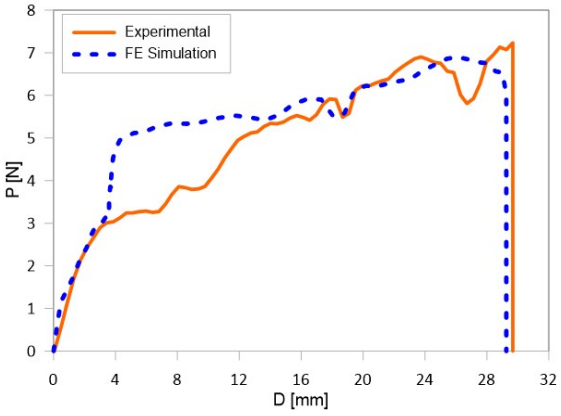

#32

B.5 Discussion on the results

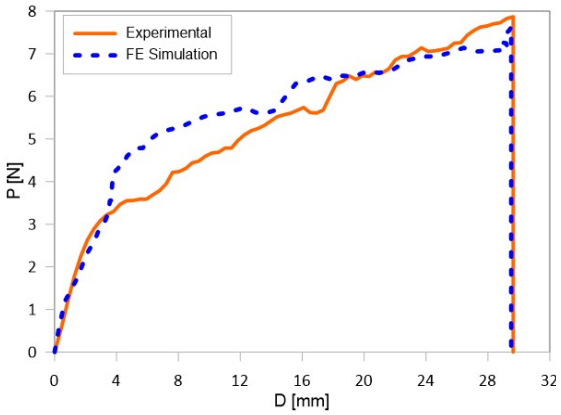

#33

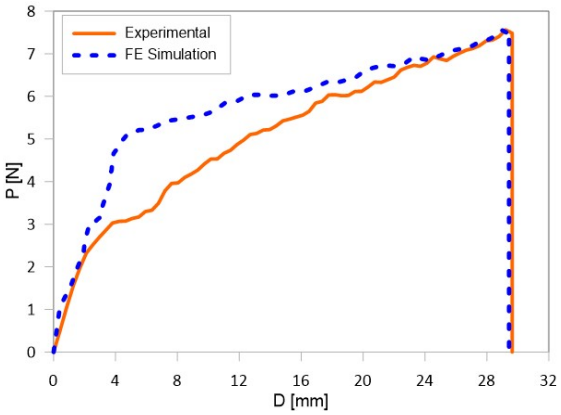

#34

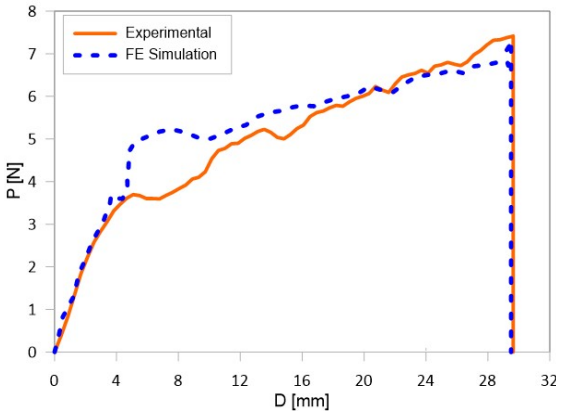

#35

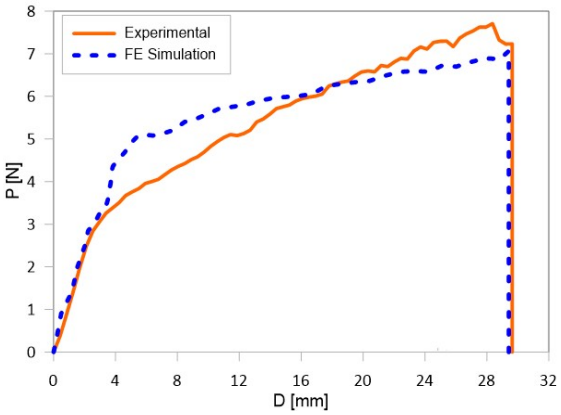

#36

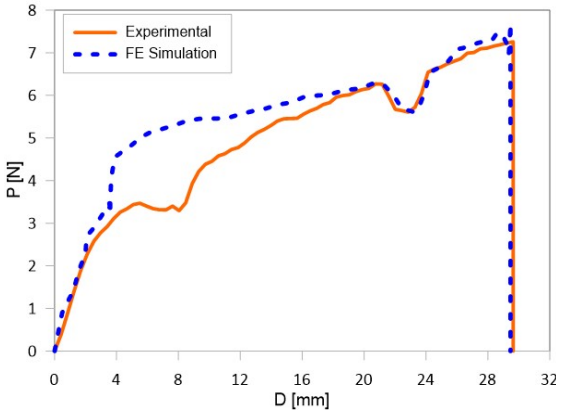

#37

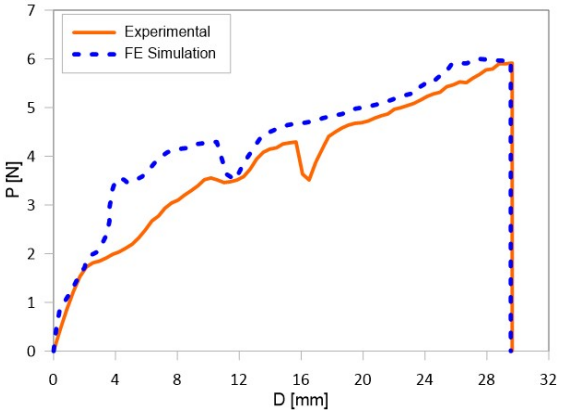

#38

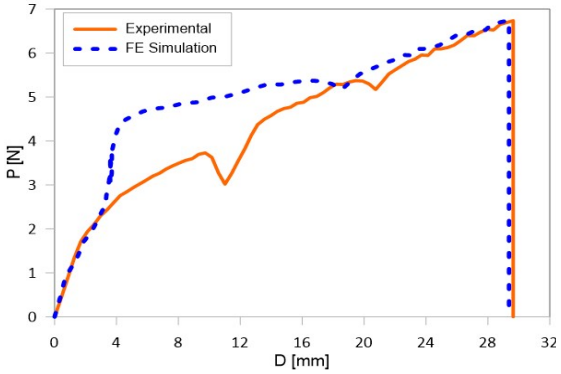

#39

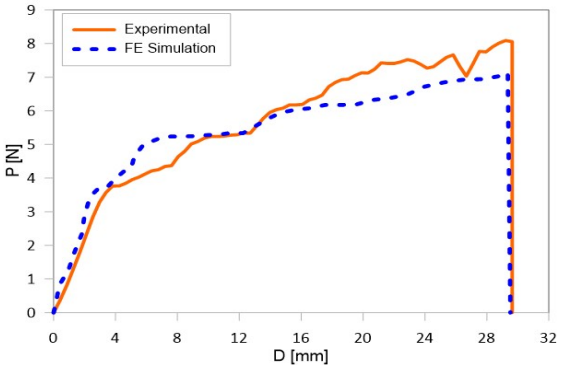

#40

B.5 Discussion on the results

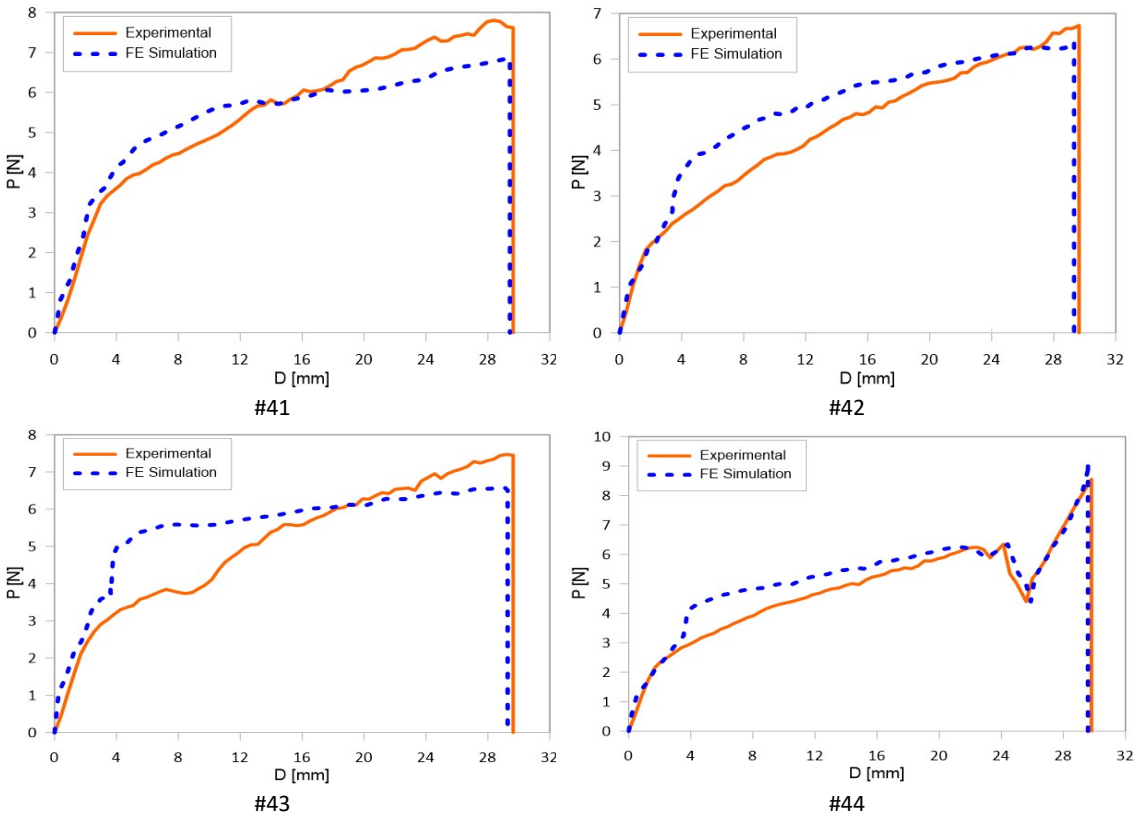

Figure B.5-11 Comparison between experimental and numerical peel-curves for each testing aged specimen

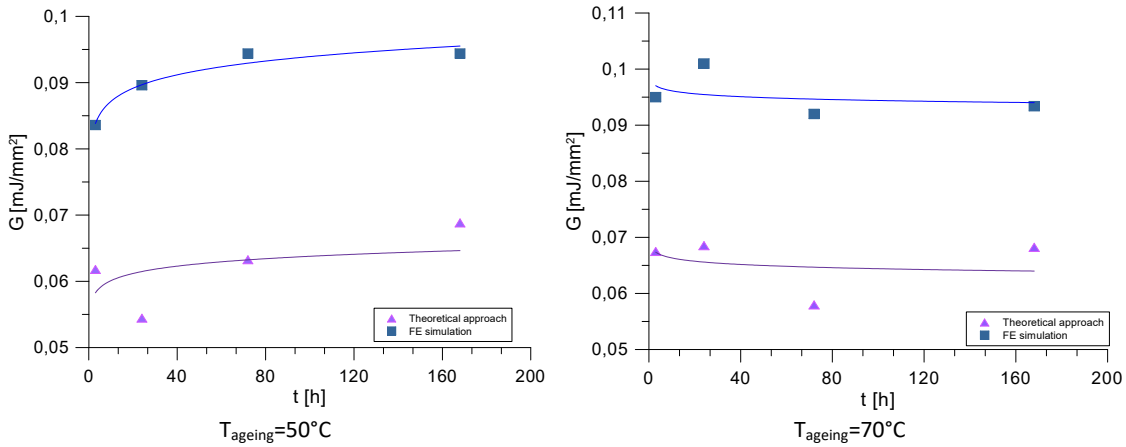

Figure B.5-12 Comparison between experimental and numerical fracture energy values (G) for both the ageing temperatures

As a complete picture of the variations in fracture energy due to accelerated aging, the Figure shows the average values for each set of 5 specimens, then for each temperature and exposure period, both those calculated analytically using the approach described in Section B.3.2 and those obtained from the calibration analysis described above. It is very interesting that the trend of the improvement, in terms of peel strength,

is almost faithfully reproduced. Consequently, it is confirmed that the study and analysis of these two parameters can lead to the same conclusion about adhesive performance.

Fig. B.5-12 illustrates that the fracture energy values according to the theoretical approach have led to forecasts of about 30% lower than FE simulations; although the correlations exposed in Fig. B.5-11 provide a generally good agreement.

Effects of peel-rate

For the assessment of the influence of the displacement-rate, the initial crosshead velocity was doubled and tripled, resulting in the following speeds: 25.4, 50.8, 76.2 mm/min and no ageing was applied to the samples; but they were all simply stored at room temperature. For each rates, the sample consists of four specimens were tested as summarized in Table B.5-2.

Table B.5-2 PET basic material characteristics

Specimen #	T	Ageing time	Displacement rate
	°C	h	mm/min
1/4	23	-	25.4
1-1/1-4	23	-	50.8
2-2/2-4	23	-	76.2

Generally, the peel-rate influence is significant in delamination phenomena because of the intrinsic characteristics of a polymeric material whose mechanical behaviour is strictly dependent on the loading rate. In fact, Alfano and Musto proposed in some papers (2013 and 2015) a treatment that takes into account the viscoelastic behaviour of the film and is based on changing the scalar parameter, D, which indicates the degree of damage in Abaqus.

Fig. B.5-13 shows the experimental curves from peeling tests for v = 50.4 and 76.2 mm/min; and the following two charts (see Fig. B.5-14 and Fig. B.5-15) elucidate on the overall influence of the peel speed in terms of mean values of energy fracture and peel resistance for each sample. As was easy to expect, according to several literature data, average peel force increases with increasing peel rate but to a very small extent indeed. In this regard, the trend shown in the figures proves the modified adhesion characteristics defining a clear dependency of all significant parameters. From an analytical and a numerical point of view, experimental tests and FE simulations demonstrate that doubling the value of v provided by standard indications shows a slight increase in the parameter, either P_{peel} or G. Whereas, when v continues to increase, the curves tend to a sort of horizontal limit value of about 5 kN in case of peel strength, 0.9 mJ/mm^2 and 0.76 mJ/mm^2 for adhesive fracture energy by Abaqus calibration analyses and by theoretical approach respectively.

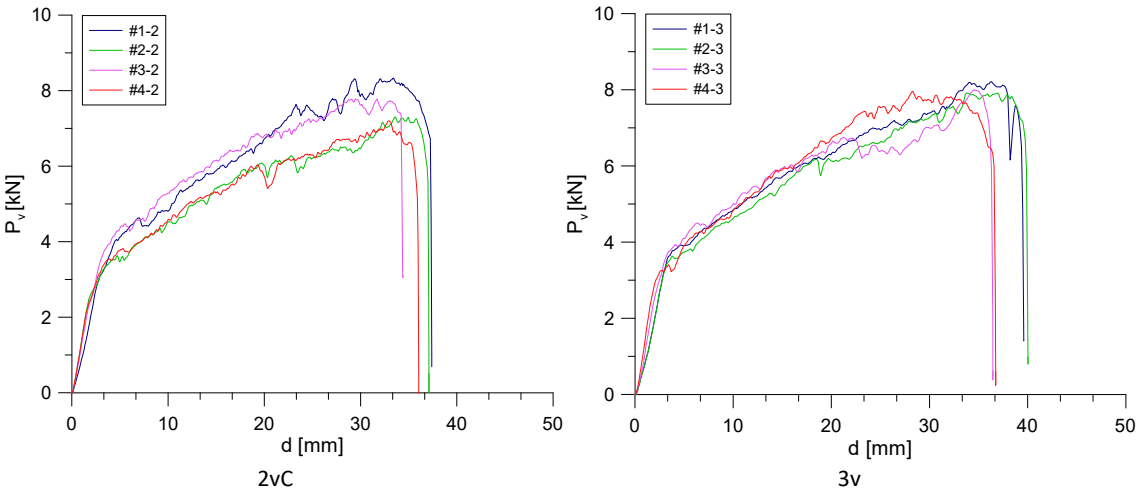

Figure B.5-13 Comparison between experimental and numerical peel-curves at different peel rates

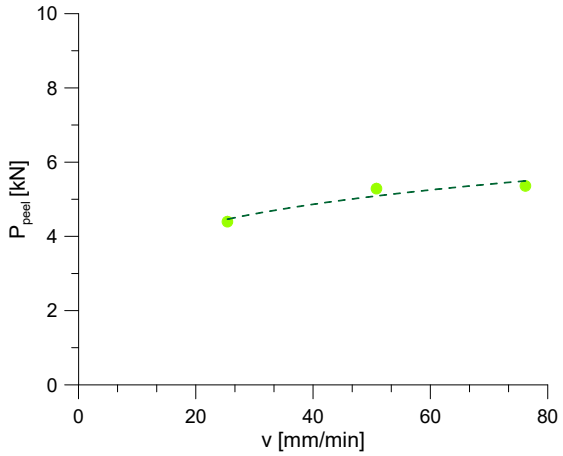

Figure B.5-14 Peel force as a function of peel rate

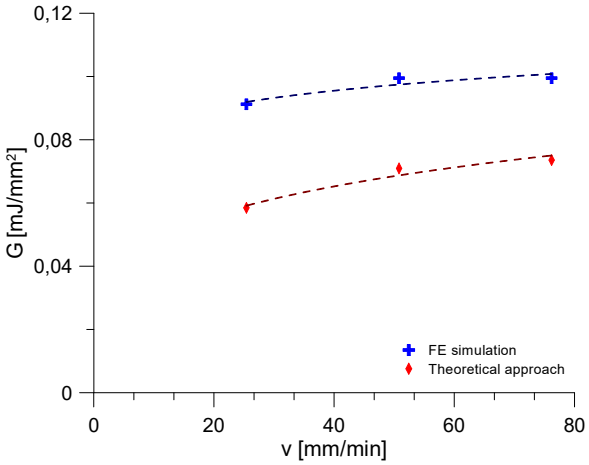

Figure B.5-15 Energy fracture with respect to different peel rate by experimental and numerical tests.

Furthermore, the peel-rate is of paramount importance in the delamination process of a viscoelastic film. Generally, it is possible to distinguish high or low-speed transitions in this type of process. In the first case, it is a transition from a condition of high adhesion to a sharp decrease in the fracture energy in the case of behaviour called stick-slip, a usual condition in the case of elastomeric type PSA (Kaeble 1964, Gent et al.

1969). This behaviour is due to a stiffening of the adhesive caused by the approach of its rubber-glass transition. Kaelble (1964), in particular, provides a quantitative interpretation of the effect of the rapid growth of the elastic modulus on the behaviour of the adhesive as it approaches its glass transition temperature Tg. The peel strength reaches a maximum and then a region is observed where the peel strength decreases as the peel speed increases. This negative slope gives a direct explanation of the instability commonly called "stick slip".

In case of low-speed transition, it can be considered as a transition from a cohesive to an interfacial fracture, or better, from liquid-like to rubber-like behaviour.

In particular, the evidence of the transition from cohesive to adhesive is usually stated by the presence of residual traces on the substrate. On the contrary, by a visual inspection, in this test program any visible portion of adhesive is present the glass support and the fracture occurs between the interface of adhesives and adherent in a cohesive failure.

B.5.2 ASF fitted glass results

The strength properties of 20 small-scaled specimens were computed by means of three-point bending tests, as defined in Section B.4.1.2. The experimental curves are shown in Fig. B.5-16 as a function of different ageing procedures, as explained in Section B.2.3.

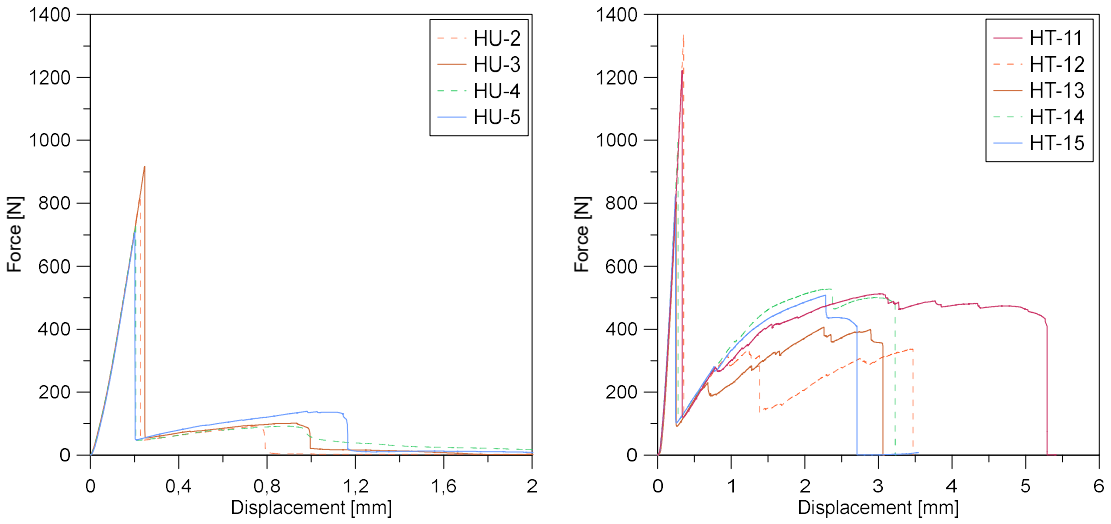

Figure B.5-16 Load-displacement curves at low-speed rate: Ageing protocols (a) High Humidity and (b) High Temperature[14]

In both cases, the force increases by following an elastic linear branch up to its maximum value in load-displacement curve, F_{max}., corresponding to the achievement of

[14] Figure reproduced with permission from (Mattei et al. 2022b) under the terms and conditions of CC-BY license agreement

glass tensile stress. Then, a sudden drop of force was observed that almost vanishes and then starts to grow again thanks to the presence of the ASF that, holding together the fragments, allows a kind of interlocking phenomenon among those of greater dimensions. The shape of the curves in the charts is very similar to a bending behaviour of a glass laminated cross section. The maximum strength values in the second region can be called F_{res} and represent an additional resistance of a glass section that in other circumstances would have collapsed in a brittle way. This is the reason why is so important to assess the actual benefit in increasing the post-breakage behaviour of a monolithic annealed glass, for example.

In addition, the fine-tuning three-dimensional model built in Abaqus and a parametric numerical analysis was carried out with the aim of addressing the calibration of a parameter set for the definition of cohesive behaviour (such as fracture energy, G, and cohesive stiffness, K). The study on the influence of the aforementioned cohesive factors lead to detect that higher K values result in increasing slope of the ascending section of the post-elastic region; whereas the adhesive fracture energy the fracture energy governs the second section of this portion by modifying the residual force value from which it can be drawn.

The general worthy correlation between the numerical and the experimental results are shown in Fig. B.5-17 in terms of mean curves by considering the adhesion characteristics in Table B.5-3

Table B.5-3 Cohesive characteristics in Finite Element Model

Ageing protocol	G	Eij/Kij
	J/m²	J/m²
HU	10	3
HT	250	20

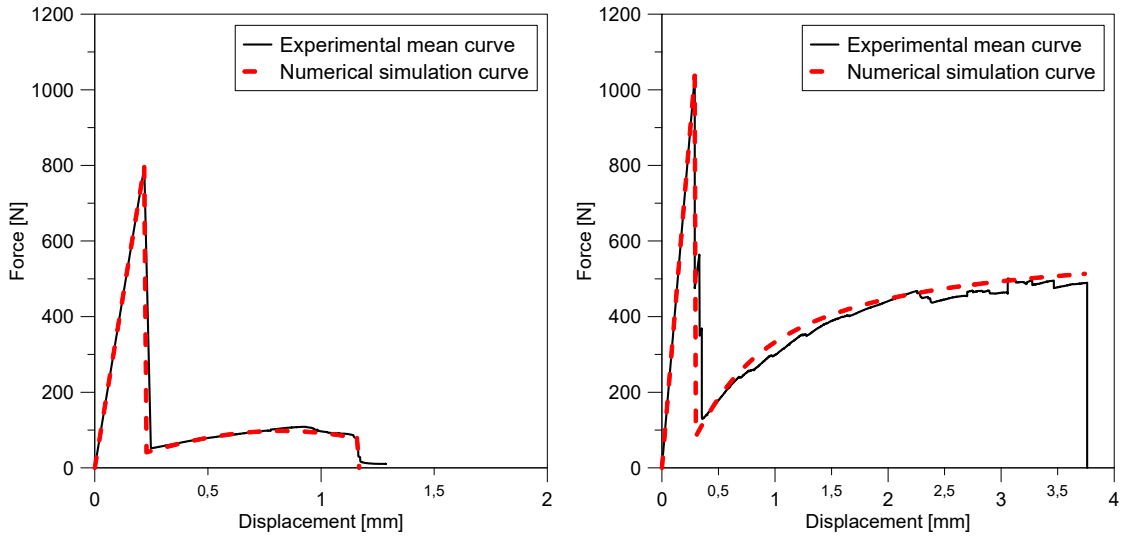

Figure B.5-17 Comparison between load-displacement curves at low-speed rate by means of FE model and of experimental tests at (a) High Humidity and (b) High Temperature ageing

B.5 Discussion on the results

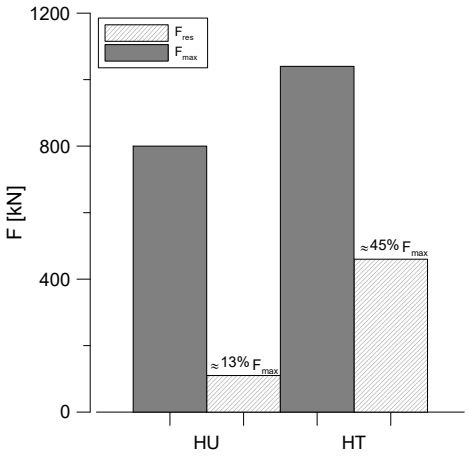

Figure B.5-18 F_{max} and F_{res} with respect to different ageing protocols

Fig. B.5-18 highlights the difference observed between the maximum load values before and after the glass breakage, represented by the ratio indicated in percentage.

Furthermore, an analytical approach was employed to determine the tangential stiffness of the adhesive layer in the elastic phase. The approach involved equating the vertical displacement (d) measured by the testing machine to the value calculated by Eq. 38 for the mid-span section. The resulting value was approximately 0.87 MPa.

Additionally, the effect of loading speed was investigated, as it can impact the evolution of cracking in brittle materials. Under low loading regimes, a single dominant crack can form from a critical defect, causing rapid development and eventual collapse of the section. The shielding effect of this crack can prevent the formation of other cracks. As loading rate decreases, the glass will break at a lower stress. Conversely, high loading rates can cause a large number of cracks to form simultaneously, leading to complete fragmentation of the material. The second testing-speed, equal to 1 m/min, corresponds to this condition, and the load-displacement curves from experimental 3PB tests are presented in Fig. B.5-20 as a function of ageing protocols.

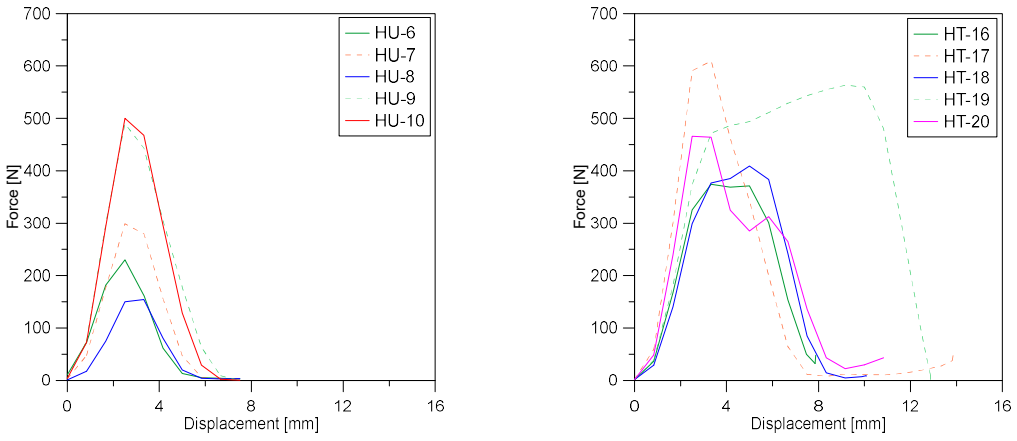

Figure B.5-19 Load-displacement curves at high-speed rate: Ageing protocols (a) High Humidity and (b) High Temperature[15]

[15] Figure reproduced with permission from (Mattei et al. 2022b) under the terms and conditions of CC-BY license agreement

Furthermore, Fig. B.5-20 illustrates the relationship between strain energy and adhesive fracture energy, as determined by cohesive element analysis. The strain energy is calculated as the area under the curve until the point of glass cracking. It is noteworthy that the initial curve (HU-ageing), shows an increasing trend that eventually stabilizes at the experimentally derived value (K_{el_Exp}). The intersection of the numerical results for a range of G values and the horizontal lines representing experimental data yields consistent fracture energy values of 100 J/m^2 and 150 J/m^2 for HU and HT ageing, respectively.

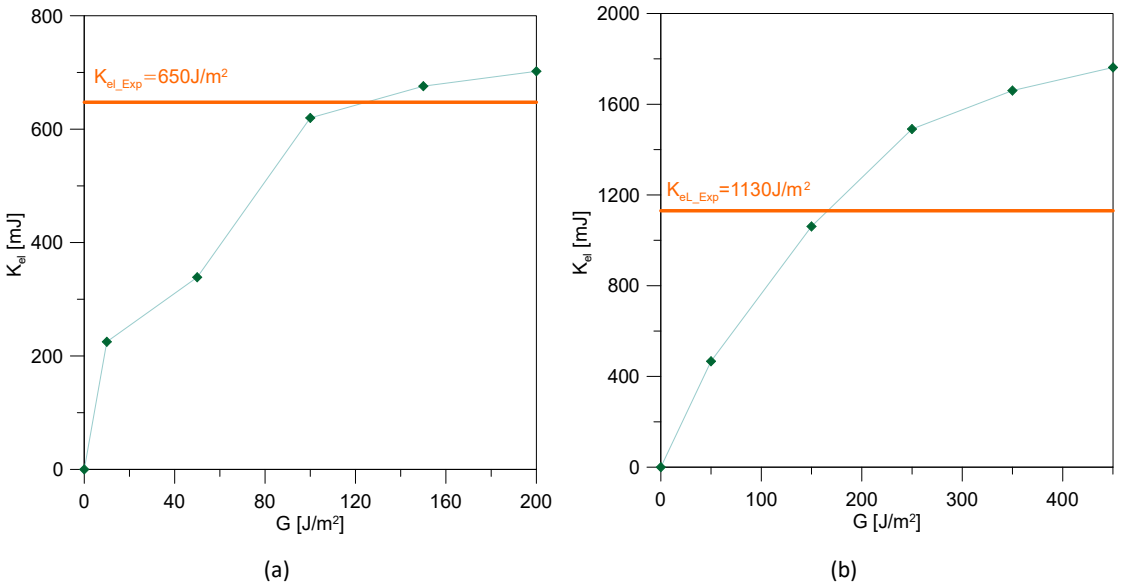

Figure B.5-20 K_{el} at (a) High Humidity and (b) High Temperature ageing

B.5.3 References

Arkhireyeva, A., Hashemi, S. (2002). “Effect of temperature on fracture properties of an amorphous poly(ethylene terephthalate) (PET) film”. *Journal of Materials Science and Technologies*, 37, pp.3675-3683.

Gent, A. N., Petrich, R. P. (1969). “Adhesion of viscoelastic materials to rigid substrates", *Proc. Roy. Soc. A* 310, pp.433-448.

Kaelble, D.H. (1964). “Theory and Analysis of peel adhesion: Rate-temperature dependence of viscoelastic interlayers", *Journal of colloid science*, 19, pp.413-424.

Mapari, S., Mestry, S., Mhaske, S.T. (2021). “Developments in pressure-sensitive adhesives: a review, *Polymer Bulletin*, 78, pp.4075-4108.

Marquez, I., Alarcia, F., Velasco, J.L. (2021). “Synthesis and Properties of Water-Based Acrylic Adhesives with a Variable Ratio of 2-Ethylhexyl Acrylate and n-Butyl Acrylate for Application in Glass Bottle Labels”. *Polymers*, 12(2), 428.

Mattei, S., Cozzarini, L., Bedon, C. (2022b). “Pre-and Post-Failure Experimental Bending Analysis of Glass Elements Coated by Aged Anti-Shatter Safety Films”. *Challenging Glass Conference Proceedings* (Vol. 8).

Musto, M., and Alfano, G. (2013). “A novel rate-dependent cohesive-zone model combining damage and visco-elasticity”. *Computers and Structures*, 118, pp.126-133.

Musto, M., and Alfano, G. (2015). “A fractional rate-dependent cohesive zone model”. *International Journal for Numerical Methods in Engineering*, 103(5), pp.313-341.

Oreski, G., Wallner G.M. (2005). “Delamination behaviour of multi-layer films for PV encapsulation”. *Solar Energy Materials & Solar Cells*, 89, pp.139-151.

Conclusions

This chapter comprises an overview of the conclusions of this research activity based on the above summarized results.

Concerning 'Part A', the study of literature has made it possible to identify the shortcomings and the topics that need special attention nowadays, and the seismic performance of a structural glass systems is certainly one of the aspects whose knowledge is most required. Within the context of the general PBD approach, the derivation of specific fragility curves for an exterior façade system, considered a secondary component, is a key step for estimating the rate of earthquakes leading the entire existing structure to reach a performance limit state. By definition, these functions can have a dual purpose and also provide a measurement of seismic performance according to a probabilistic method, relating the state of damage (as a function of a parameter arbitrarily chosen as significant) and a quantitative measure of seismic intensity and taking into account different types of uncertainties.

In this perspective, the state-of-the-art examined existing procedures for assessing fragility by focusing on the functions achieved in previous years with the aim of providing a valid alternative approach by using detailed finite element modelling. In particular, the Cloud method has been chosen for many advantages, including a lower computation burden compared to IDA, despite the fact that non-linear dynamic type analyses are still required, and the use of real accelerograms that allows taking into account the uncertainties related to the seismic action (i.e., record-to-record). Since the development approaches used in the reference studies for constructing fragility curves, explained in Chapter A.5, are based on geometric solutions or laboratory tests, the influence of input characteristics is an additional information.

The probabilistic fragility functions were developed for four different glazing configurations that were selected from a large database of experimental tests carried out at the Department of Architectural Engineering in the "Pennsylvania State University". Providing comparisons and considerations on the ability of the numerical procedure to grasp the critical aspects observed in the laboratory was the first target in this part. The vulnerability analysis of glass curtain walls remains an unresolved subject, despite the lack of regulations and adequate research on probabilistic functions that can accurately represent all of the uncertainties that influence their structural response. As a consequence, from the resulting numerical fragility curves, it is concluded that the structural response in terms of EDP is highly affected by the level of detail of the 3D numerical model. The main limitation concerns the lack of specific material definition for glass and the complexity in considering a mechanical strength after cracking, that is the post-breakage behaviour.

Moreover, since it is a common knowledge that the glass-to-frame clearance and the glass type affect the seismic performance of a glass system, these parameters are chosen as representatives of the distinctive characteristics of the investigated systems. In the first case, it is confirmed that the lower the clearance value and the higher the probability of collapse. Since this type of configuration is the most rigid, it achieves lower horizontal displacement values (corresponding to a specific limit state) before reaching the damage threshold with a lower rotation capacity before contact with the frame. Regarding the second factor, trends in the data showed that laminated glass type have higher glass fallout capacity than monolithic unit. Another interesting outcome was provided in terms of consistent displacement limitations for the entire building externally covered with a mullion-to-transom façade by reasonably considering a rigid frame-to-structure connection. However, the influence of its deformability could be assed with further investigations.

Because of these considerations, the numerical fragility method based on Cloud analyses should be used with caution in the definition of seismic performance and the estimation of uncertainties should be considered in a probabilistic manner to increase its reliability. Furthermore, the present work has to perceived as a preliminary study with the goal of evaluating fragility functions for glazing curtain walls taking into account a limited number of investigated case-studies.

With regard to the second part of this thesis (Part B), the mechanical behaviour of non-aged and aged safety films in glass applications was studied on the basis of the results by an experimental campaign that were post-processed with theoretical approaches. Furthermore, finite element numerical modelling techniques were used for supporting the characterization methods.

Firstly, a characterization on the construction of anti-shatter film (ASF) has been experimentally conducted through DSC and FT-IR, whereas for a mechanical characterization three different tests were performed: pure tensile tests on the only thin tape, peel tests to assess the adhesion of the PSA between the PET-film and glass substrate, and 3-point bending tests to evaluate the mechanical bending response of a glass fitted with ASF and quantify the increased post-breakage capacity.

Generally, one of the main characteristic parameters of adhesion between film and glass is the adhesion fracture energy, G, representing the energy required to bond the films to the substrate. In accordance with the interpretation of fracture mechanics at the peel testing of flexible laminates, the data analysis was carried out by using a modified analytical approach to take into account the non-standard test setup and providing a method for calculating G even under typical and representative conditions of reality. Consequently, a three-dimensional FE models were built in Abaqus/CAE to support these outcomes and calibration analyses were carried out on each experimental curve by using the Cohesive Zone Modelling (CZM) technique.

Conclusions

In analytical and numerical field, the dependence of fracture energy (G), peel force (P_{peel}) and residual capacity of the glass+ ASF sample (F_{res}), on the displacement rate (v), temperature (T) and period of exposure (t) in reference to the selected aging protocols was addressed. The simulated mechanical behaviour from the peel test and 3-Point-Bending test simulations corresponded well with the experimental results. On the contrary, although the general trend of G (according to the different test conditions investigated) corresponds between FE simulations and values calculated analytically, the numerical results are always lower with a deviation of about 20-30% according to test. In the future, possible extension of the present study should properly estimate the failure mode of the examined PSA model and the cyclic response of PET-film samples could be assessed to measure the dissipation capacity by considering a variable root rotation.

Nomenclature

α_R	Rayleigh coefficients
β_R	Rayleigh coefficients
β	Measure of uncertainty
β_i	Standard deviation of the natural logarithm derived
γ_a	Importance factor
δ_{xA}	Deflection at level x of structure
δ_{yA}	Deflection at level y of structure
Δ_{aA}	Allowable story drift for structure
Δ_{clear}	Drift causing contact between the glass panels and the frame
$\Delta_{fallout}$	Off-plane displacement
ε	Uniaxial deformation
ε_a	Inelastic contribute to the elongation of the peel arm
θ	Peel angle
θ_0	Root rotation
μ_{IM}	Median for IM parameter given EDPi
ν	Reduction factor to account for the lower return period for damage limitation
ν_a	Poisson ratio of aluminium
ν_g	Poisson ratio of glass
ξ	Damping ratio
ρ	Nominal density
ρ_a	Nominal density of aluminium
ρ_g	Nominal density of glass
ρ_{PVB}	Nominal density of PVB
σ	Uniaxial stress
σ_{max}	Maximum elastic Bending stress by three-point bending test
$\sigma_{y,a}$	Yielding stress for aluminium
$\sigma_{t,a}$	Ultimate stress for aluminium
$\sigma_{tk,g}$	Characteristic tensile resistance of annealed glass
ϕ	Standard normal cumulative distribution function
[C]	Damping matrix
[K]	Stiffness matrix
[M]	Mass matrix
{I}	Identity vector
{u}	Displacement vector
$\{\dot{u}\}$	Velocity vector
$\{\ddot{u}\}$	Acceleration vector
3PB	Three-point bending test
a	Peeling distance

Nomenclature

a_g	Peak ground acceleration on type A ground
a_p	Component amplification factor
A_0	Initial section of the specimen
ASFs	Anti-shatter films
b	Width of the glass panel
$B_{specimen}$	Width of the specimen
c	Clearance
c_1	Clearance between the vertical glass edges and the frame
c_2	Clearance between the horizontal glass edges and the frame
C_p	Horizontal design coefficient of the part (NZS 4219:2009)
C_{pH}	Horizontal response factors (NZS 4219:2009)
C_{pV}	Vertical response factors (NZS 4219:2009)
C_{vd}	Vertical design action coefficient for the period of the system (NZS 4219:2009)
d	Travel distance
D_p	Relative seismic displacements
E	Elastic modulus
E_g	Elastic modulus of glass
E_s	Elastic modulus of aluminium
EA*	Equivalent stiffness
EDP_i	Engineering demand parameter
EJ_{full}	Bending stiffness in case of rigid connection
EJ_{full}	Bending stiffness in case of null connection
F_a	Horizontal seismic force
F_{pH}	Horizontal seismic force (NZS 4219:2009)
F_{pV}	Vertical seismic force (NZS 4219:2009)
FT-IR	Fourier Transform Infrared spectroscopy
g	Gravitational acceleration
G	Free surface energy
G_{ad}	Tangential stiffness of the adhesive component
h	height of the glass panel
H	Building height measured from the foundation level
I	Moment of inertia
IM	Intensity measure
IDR	Inter-storey drift
K	Stiffness
l_0	Initial length of the specimen
I_p	Component response modification factor
L_{min}	Smallest mesh element dimension
$L_{specimen}$	Length of the specimen
M	Bending moment
P	Peel force

Nomenclature

PET	Positron emission tomography
PSA	Pressure sensitive adhesive
PVB	Polyvinyl-butyral
q_a	Behaviour factor of the element
R_a	Magnification factor
R_p	Risk factor (NZS 4219:2009)
s_1 ... s_{60}	Acceleration records
S_a	Seismic coefficient applicable to non-structural elements
S_{DS}	Short-period spectral acceleration parameter
t	Thickness of element
t_{ad}	Stiffness of the connection layer
t_{adh}	Thickness of adhesive
T_1	Fundamental vibration period of the construction in the direction considered
T_a	Fundamental vibration period of the non-structural element
T_g	Glass transition temperature
T_r	Return period
u	Displacement
$\dot{u}$	Velocity
$\ddot{u}$	Acceleration time-histories
U	Elastic energy
U_a	Energy of fracture
U_{db}	Energy dissipated during the bending of the tape
UV	Ultra-Violet
W	External work
W_a	Weight of the structure
W_p	Weight of the non-structural element
Z	Height of the centre of gravity measured from the foundation level

List of Figures

Part A: Numerical fragility assessment of glazing curtain-walls

Figure A.1-1 Chemical composition of soda-lime glass and borosilicate glass (Schittich et al. 2007; GRANTA 2014) _____ *10*

*Figure A.1-2 Schematic image of a float line (figure © S. Mattei)*_____ *10*

Figure A.1-3 Connection detail between glass beams _____ *13*

Figure A.1-4 Primary glass frames. _____ *13*

*Figure A.1-5 Glass shells – (a) glass pedestrian walkway in Basilica of Aquileia, Italy; (b) glass roof at metropolitan train-station 'Aeroporto do Oporto: Francisco Sá Carneiro', Portugal; (c) glass stair tower in hotel facility in Marotta Italy; (d) glass-steel stair in residential building in Sant'Agata De' Goti, Italy (photos © S. Mattei)*_____ *15*

Figure A.1-6 Two practical example of glass balustrades in residential buildings, (photos © S. Mattei) _____ *16*

Figure A.1-7 Glass curtain-walls – (a) Unitized system , (b) Mullions and transom system; (c) and (d) Point-supported systems (photos © S. Mattei) _____ *18*

*Figure A.2-1 (a) Glazing damage in Chile, after the 8.8 Chile Earthquake (2010) (FEMA E-74_Figure 6.3.1.4-3); (b) Impact damaged façade at the entrance of the Corte de Apelaciones de Talca , after the 8.8 Chile Earthquake (2010) (FEMA E-74_Figure 6.3.6.1-2); (c) Damaged glazing system in San Francisco (1989), after Loma Prieta earthquake [https://www.earthquakecountry.org/step1/largewindows/ ; California Seismic Safety Commission]*_____ *31*

Figure A.2-2 In plane drift mechanism of the framed CW: (a) Rigid horizontal movement of the panel; (b) Deflection of frame by panel horizontal movement; (c) Combined horizontal and rotation movement (figure © S. Mattei) _____ *33*

Figure A.2-3 Dynamic racking test facility (AAMA 501.6) _____ *39*

Figure A.3-1 Seismic risk definition as the convolution of parameters (figure © S.Mattei) ___ *45*

*Figure A.3-2 Flowing chart for estimating seismic vulnerability by analytical method*_____ *49*

Figure A.3-3 Fragility curves corresponding to a specific damage states for the same building class _____ *50*

Figure A.3-4 Flow-chart on the numerical implementation of the analytical fragility function *53*

Figure A.3-5 Response spectra of the chosen records _____ *55*
Figure A.4-1 The entire time history of the crescendo test _____ *60*
Figure A.4-2 Racking facility and setup used for the mid-rise CW testing _____ *61*
Figure A.4-3 Glazing details for the mid-rise aluminium curtain wall-framing system _____ *65*
Figure A.4-4 Numerical model of (a) glass panel and (b) the schematic detail of glass-to-frame connection where c means nominal 'clearance' _____ *66*
Figure A.4-5 Constitutive law of (a) glass under axial compressive (a) and tension(b) strength (Abaqus User Manual, 2008) and (b) aluminium. _____ *67*
Figure A.4-6 Planar connector type for glass-frame connection; and (b) hinge connector type for transom-mullion connection (Abaqus library) _____ *69*
Figure A.4-7 (a) FE model for calibration analyses and (b) a typical fallout limit state (measures in mm) _____ *69*
Figure A.4-8 3D representations of MRF structure from SAP2000 _____ *70*
Figure A.4-9 3D representations of MRF structure from SAP2000 _____ *70*
Figure A.4-10 3D representations of MRF structure from SAP2000 _____ *71*
Figure A.4-11 Type 2 elastic response spectrum for soil types from A to E (Damping equals to 5%) _____ *71*
Figure A.4-12 MRF Structure in XY plane _____ *72*
Figure A.4-13 Abaqus model of (a) MRF structure and (b) with curtain-walls _____ *73*
Figure A.4-14 Distributing coupling constraint for 'rigid floor' assumption; and (b) beam connector type for façade frame-MRF connection (Abaqus library) _____ *74*
Figure A.5-1 Displacement distribution in X-direction for (a) Configuration #A; (b) Configuration #B and (c) Configuration C (measures in m) _____ *80*
Figure A.5-2 Displacement distribution in Y-direction for (a) Configuration #A; (b) Configuration #B and (c) Configuration C (measures in m) _____ *81*
Figure A.5-3 Maximum in-plane principal stress distribution for glass panels in X-direction for (a) Configuration #A; (b) Configuration #B and (c) Configuration C (measures in MPa x 10e6) *81*
Figure A.5-4 Von Mises stress distribution for steel primary system in X-direction for (a) Configuration #A; (b) Configuration #B and (c) Configuration C (measures in MPa x 10e6) ___ *82*
Figure A.5-5 FE model for dynamic analyses _____ *83*
Figure A.5-6 Seismic record (s#5) _____ *83*
Figure A.5-7 Maximum envelope of glass tensile stress (Configuration #A) _____ *84*
Figure A.5-8 Maximum envelope of glass compressive stress (Configuration #A) _____ *84*
Figure A.5-9 Out-of-plane displacement (a) and in-plane drift (b) as functions of time _____ *84*

Figure A.5-10 Configuration #A: In-plane deformations [mm] and stresses distributions in glass panel [MPa] corresponding to the maximum tensile stress (on the left) and the maximum compressive stress (on the right) _____ *85*
Figure A.5-11 Maximum envelope of glass tensile stress (Configuration #B) _____ *85*
*Figure A.5-12 Maximum envelope of glass compressive stress (Configuration #B)*_____ *86*
Figure A.5-13 Out-of-plane displacement (a) and in-plane drift (b) as functions of time _____ *86*
*Figure A.5-14 Configuration #B: In-plane deformations [mm] and stresses distributions in glass panel [MPa] corresponding to the maximum tension (on the left) and the maximum compression (on the right)*_____ *86*
Figure A.5-15 Comparison of results between CS#1 and CS#2 in terms of in-plane maximum drift ratio for the specific seismic record (i.e., s#5) _____ *87*
*Figure A.5-16 Cloud data pair in bi-logarithmic plane in terms of IM=$S_a(T_1)$*_____ *88*
*Figure A.5-17 Cloud data pair in bi-logarithmic plane in terms of IM=PGA*_____ *88*
Figure A.5-18 Fragility curves based on different EDP-thresholds and IM=$S_a(T_1)$ _____ *90*
Figure A.5-19 Fragility curves based on different EDP-thresholds and IM=PGA _____ *91*
Figure A.5-20 Cloud data pairs for entire building in bi-logarithmic plane in terms of (a) IM=$S_a(T_1)$ and (b) IM=PGA _____ *92*
Figure A.5-21 Fragility curves for the curtain wall configuration with the same geometry in a 4-story building for Configuration #A, #B and #C in terms of (a) IM=$S_a(T_1)$ and (b) IM=PGA ____ *93*
Figure A.5-22 Fragility curves based on the EDP-threshold by experimental results and IM=S_a *94*
Figure A.5-23 Fragility curves based on the EDP-threshold by experimental results and IM=PGA _____ *94*

Part B: Experimental and numerical investigations on post-failure behaviour of glass fitted with ASFs

Figure B.1-1 Examples of PET-film actual applications _____ *98*
Figure B.1-2 Typical crack pattern for (a) annealed, (b) heat-streghtned and (c) tempered glass (figure © S. Mattei) _____ *98*
Figure B.1-3 Basic composition of the glass fitted with ASF _____ *100*
Figure B.2-1: Schematic setup for tensile test _____ *105*
Figure B.2-2: Peel test configurations: (a) 90°peel test; (b) T-peel test and (c) 180° peel-test (figure © S. Mattei) _____ *106*
*Figure B.2-3 Experimental setup of peel test (figure © S. Mattei)*_____ *106*

Figure B.2-4 Experimental setup of 3PB test (figure © S. Mattei) _____ *107*

Figure B.2-5 Section deformation under bending loading in function of connection behaviour _____ *108*

Figure B.2-6 Analytical model for composite beam with deformable connection (figure © S. Mattei) _____ *109*

Figure B.2-7 Thermo-Nicolet Nexus 470 spectrometer _____ *111*

Figure B.3-1 Geometric configuration of peel test (figure © S. Mattei) _____ *115*

Figure B.3-2 Bending moment diagram vs bending radius for peeling _____ *116*

Figure B.3-3 Configuration of peeling process at (a) t=0 and (b) t=i (figure © S. Mattei) ____ *118*

Figure B.4-1 Finite Element Models for (a) positioning step and (b) numerical simulation of experimental peel test _____ *122*

Figure B.4-2 Finite Element Models for numerical simulation of experimental 3PB test _____ *123*

Figure B.4-3 Triangular traction-separation law for cohesive zone model (figure © S. Mattei) _____ *124*

Figure B.5-12: DSC curves for each PET layers: layer-1 (green), layer-2 (blue) and layer-3 (red) _____ *128*

Figure B.5-2 FTIR spectra of layer 1,2 and 3. Layers 1 and 2 (both sides) and layer-3 (internal side) _____ *129*

Figure B.5-3 Vibrational bands identified on the adhesive between the layers and on the PSA adhesive _____ *129*

Figure B.5-4 (a) PET tape specimens (b) Experimental stress-strain curves and (on the top right) mechanical behaviour model (on the bottom right) _____ *130*

Figure B.5-5 (a) (T; E) [°C; GPa] (b) (T; σ_y) [°C; MPa] _____ *131*

Figure B.5-6 Vibrational bands identified on the adhesive between the layers and on the PSA adhesive _____ *132*

Figure B.5-7 Figure 14. Peel curves of unaged samples (specimens 1-4) in terms of (a) Pvert and (b) its component along peel arm direction. _____ *133*

Figure B.5-8 Original experimental results in terms of peel curves (d; P_v) for unaged and aged samples (specimens from #1 to #44) _____ *135*

Figure B.5-9 Adjusted experimental results in terms of peel curves (d; P_{peel}) for unaged and aged samples (specimens from #1 to #44) _____ *136*

Figure B.5-10 Peel force-as a function of ageing time: $T_{agein}g$=50°C (green) and $T_{agein}g$=70°C (orange) _____ *136*

Figure B.5-11 Comparison between experimental and numerical peel-curves for each testing aged specimen _____ *142*
Figure B.5-12 Comparison between experimental and numerical fracture energy values (G) for both the ageing temperatures _____ *142*
Figure B.5-13 Comparison between experimental and numerical peel-curves at different peel rates _____ *144*
Figure B.5-14 Peel force as a function of peel rate _____ *144*
Figure B.5-15 Energy fracture with respect to different peel rate by experimental and numerical tests. _____ *144*
Figure B.5-16 Load-displacement curves at low-speed rate: Ageing protocols (a) High Humidity and (b) High Temperature _____ *145*
Figure B.5-17 Comparison between load-displacement curves at low-speed rate by means of FE model and of experimental tests at (a) High Humidity and (b) High Temperature ageing ___ *146*
Figure B.5-18 F_{max} and F_{res} with respect to different ageing protocols _____ *147*
Figure B.5-19 Load-displacement curves at high-speed rate: Ageing protocols (a) High Humidity and (b) High Temperature _____ *147*
Figure B.5-20 K_{el} at (a) High Humidity and (b) High Temperature ageing _____ *148*

Appendix A

Figure Appendix.A- 1 s#1_TK-1999-0415 _____ *ii*
Figure Appendix.A- 2 s#2_TK-1999-0077 _____ *ii*
Figure Appendix.A- 3 s#3_IT-1980-0012 _____ *ii*
Figure Appendix.A- 4 s#4_TK-1999-0415 _____ *ii*
Figure Appendix.A- 5 s#5_TK-1998-0063 _____ *iii*
Figure Appendix.A- 6 s#6_GR-1981-0001 _____ *iii*
Figure Appendix.A- 7 s#7_ME-1979-0003 _____ *iii*
Figure Appendix.A- 8 s#8_EMSC-20161030_0000029 _____ *iii*
Figure Appendix.A- 9 s#9_TK-1999-0415 _____ *iii*
Figure Appendix.A- 10 s#10_TK-1999-0077 _____ *iii*
Figure Appendix.A- 11 s#11_TK-1999-0077 _____ *iv*
Figure Appendix.A- 12 s#12_EMSC-20160824_0000006 _____ *iv*
Figure Appendix.A- 13 s#13_EMSC-20160824_0000006 _____ *iv*
Figure Appendix.A- 14 s#14_HR-1990-0007 _____ *iv*

List of Figures

Figure Appendix.A- 15 s#15_ME-1979-0003 _____ *iv*
Figure Appendix.A- 16 s#16_EMSC-20161030_0000029 _____ *iv*
Figure Appendix.A- 17 s#17_TK-1999-0415 _____ *v*
Figure Appendix.A- 18 s#18_TK-1999-0077 _____ *v*
Figure Appendix.A- 19 s#19_EMSC-20160824_0000006 _____ *v*
Figure Appendix.A- 20 s#20_GR-1999-0001 _____ *v*
Figure Appendix.A- 21 s#21_TK-1999-0077 _____ *v*
Figure Appendix.A- 22 s#22_EMSC-20161030_0000029 _____ *v*
Figure Appendix.A- 23 s#23_AM-1988-0001 _____ *vi*
Figure Appendix.A- 24 s#24_GR-1988-0020 _____ *vi*
Figure Appendix.A- 25 s#25_TK-1999-0077 _____ *vi*
Figure Appendix.A- 26 s#26_GR-1993-0023 _____ *vi*
Figure Appendix.A- 27 s#27_IT-1984-0004 _____ *vi*
Figure Appendix.A- 28 s#28_EMSC-20161030_0000029 _____ *vi*
Figure Appendix.A- 29 s#29_TK-1999-0077 _____ *vii*
Figure Appendix.A- 30 s#30_EMSC-20161026_0000095 _____ *vii*
Figure Appendix.A- 31 s#31_EMSC-20161026_0000095 _____ *vii*
Figure Appendix.A- 32 s#32_EMSC-20161026_0000095 _____ *vii*
Figure Appendix.A- 33 s#33_EMSC-20161026_0000095 _____ *vii*
Figure Appendix.A- 34 s#34_ME-1979-0012 _____ *vii*
Figure Appendix.A- 35 s#35_TK-2002-0008 _____ *viii*
Figure Appendix.A- 36 s#36_GR-1997-0019 _____ *viii*
Figure Appendix.A- 37 s#37_TK-1998-0063 _____ *viii*
Figure Appendix.A- 38 s#38_GR-1997-0014 _____ *viii*
Figure Appendix.A- 39 s#39_EMSC-20120610_0000062 _____ *viii*
Figure Appendix.A- 40 s#40_IT-1980-0012 _____ *viii*
Figure Appendix.A- 41 s#41_EMSC-20130108_0000044 _____ *ix*
Figure Appendix.A- 42 s#42_GR-1981-0003 _____ *ix*
Figure Appendix.A- 43 s#43_EMSC-20161026_0000077 _____ *ix*
Figure Appendix.A- 44 s#44_IT-1978-0004 _____ *ix*
Figure Appendix.A- 45 s#45_MK-1994-0004 _____ *ix*

List of Tables

Part A: Numerical fragility assessment of glazing curtain-walls

Table A.1-1 Main physical properties of soda-lime silicate and borosilicate glass 11
Table A.1- 2 Summary of element classes as a function of consequences classes 20
Table A.2- 1 Damage limitation criteria in EC 8-1 35
Table A.2-2 Damage limitation criteria in NTC-18 36
Table A.2-3 Coefficients for Architectural Components (FEMA 450 2003) 37
Table A.2- 4 Values for the allowable story drift (FEMA 450 2003) 38
Table A.2-5 Reference limitations based on JASS14 (1996) 40
Table A.2-6 Parts classification criteria 40
Table A.2-7 Part response factors 41
Table A.4-1 Configuration characteristics (O'Brien et al. 2012) 60
Table A.4-2 Geometric characteristics of the investigated configuration 61
Table A.4-3 Alluminium characteristics for FE model 68
Table A.4-3 Glass characteristics for FE model 68
Table A.4-4 Values of parameters describing the Type 2 elastic spectrum 71
Table A.4-5 Sections of MRF system in X direction 72
Table A.4-6 Sections of MRF system in Y direction 72
Table A.4-7 Basic material parameters 75
Table A.5-1 Summary of linear regression parameters 89
Table A.5-2 Summary of the EDP-thresholds by current regulations in terms of drift 89
Table A.5-3 Summary of linear regression parameters 93
Table B.2-1 Ageing protocols and summary of tested specimens for peel tests 111
Table B.2-2 Ageing protocols and summary of tested specimens for peel tests 111
Table B.4-1 Basic material characteristics assumed in FEM simulations of peel test 122
Table B.4-2 Basic material characteristics assumed in FEM simulations of 3PB test 123
Table B.5-1 PET basic material characteristics 131
Table B.5-2 PET basic material characteristics 143
Table B.5-3 Cohesive characteristics in Finite Element Model 146

Scientific publications

Update to 01.31.2023

Scientific papers

- Mattei, S.; Cozzarini, L.; Bedon, C. (2023). Numerical simulation and modelling of thin anti-scattering films for glass. *In revision.*

- Mattei, S.; Bedon, C. (2022). Seismic demand assessment of structural glass systems based on simplified methods". Bulletin of Geophysics and Oceanography Vol, 2022, 63(4), pp. 639–658.

- Mattei, S.; Cozzarini, L.; Bedon, C. (2022). Experimental and numerical peeling investigation on aged multi-layer anti-shatter safety films (ASFs) for structural glass retrofit. Symmetry, 2022, 14(1), 162.

- Mattei, S.; Cozzarini, L.; Bedon, C. (2022). Pre-and Post-Failure Experimental Bending Analysis of Glass Elements Coated by Aged Anti-Shatter Safety Films. CertBond COST Action CA18120 Vol. 8 (2022): Challenging Glass 8.

- Mattei, S.; Fasan, M.; Bedon, C. (2021). On the use of cloud analysis for structural glass members under seismic events. Sustainability, 2021, 13(16), 9291.

- Mattei, S.; Bedon, C. (2021). Analytical fragility curves for seismic design of glass systems based on cloud analysis. Symmetry 2021, 13(8), 1541.

- Bedon, C.; Mattei, S. (2021). Facial expression-based experimental analysis of human reactions and psychological comfort on glass structures in buildings. Buildings, 2021, 11(5), 204.

- Bedon, C.; Mattei, S. (2021). Remote facial expression and heart rate measurements to assess human reactions in glass structures. Advances in Civil Engineering, 2021, 2021, 1978111.

- Mattei, S.; Bedon, C. (2021). Multistep Experimental Calibration of Mechanical Parameters for Modelling Multilayer Antishatter Safety Films in Structural Glass Protection. Mathematical Problems in Engineering Volume 2021, 2021, 6714418.

- Mattei, S.; Bedon, C. (2021). Development of analytical fragility curves for structural glass frames by using Cloud Analysis. MATEC Web of Conferences, 2021.

- Santo, D.; Mattei, S.; Bedon, C. (2020). Elastic Critical Moment for the Lateral–Torsional Buckling (LTB) Analysis of Structural Glass Beams with Discrete Mechanical Lateral Restraints. Materials 2020, 13(11), 2492.

- Mattei, S.; Bedon, C. (2020). Lateral Torsional Buckling (LTB) analysis of structural glass beams with discrete mechanical lateral restraints (LRs). Proceedings of the First Poster Competition on Materials Science 2020.

Conference papers

- Mattei, S.; Cozzarini, L.; Bedon, C. (2022). “Comparison between numerical and empirical derivation methods of component fragility functions”. 41° Convegno Nazionale del Gruppo Nazionale di Geofisica della Terra Solida (GNGTS). *In revision.*

- Mattei, S.; Cozzarini, L.; Bedon, C. (2022). “Pre- and post-failure experimental bending analysis of glass elements coated by aged Anti-shatter Safety Film”. CGC8- Challenging Glass Conference 8.

- Mattei, S.; Bedon, C. (2022). “Fragility assessment of glass components by Single-Degree of Freedom approximation”. 40° Convegno Nazionale del Gruppo Nazionale di Geofisica della Terra Solida (GNGTS).

- Mattei, S.; Bedon, C. (2021). Analytical fragility method to assess seismic behavior of glass panels”. 39° Convegno Nazionale del Gruppo Nazionale di Geofisica della Terra Solida (GNGTS).

Appendix A

This appendix shows the chosen seismic signals, in terms of ground acceleration, used in the Cloud analyses described in Section A.3.2

In addition, the data relating to them are presented in tabular form in order to provide a clear reading of the diagrams

Record #	Event ID	Date (Year/Month/Day)	Soil Type	M_w	R (km)	PGA (m/s^2)
s#1	TK-1999-0415	1999/11/12	C	7.3	36.1	8.0
s#2	TK-1999-0077	1999/08/17	C	7.6	101.2	3.7
s#3	IT-1980-0012	1980/11/23	B	6.9	33.3	3.1
s#4	TK-1999-0415	1999/11/12	A	7.3	32.3	2.5
s#5	TK-1998-0063	1998/06/27	C	6.2	48.2	2.7
s#6	GR-1981-0001	1981/02/24	B	6.6	32.0	2.4
s#7	ME-1979-0003	1979/04/15	A	6.9	62.9	2.5
s#8	EMSC-20161030_0000029	2016/10/30	B	6.6	45.2	1.8
s#9	TK-1999-0415	1999/11/12	A	7.3	34.7	1.3
s#10	TK-1999-0077	1999/08/17	B	7.6	89.6	1.6
s#11	TK-1999-0077	1999/08/17	C	7.6	109.3	1.8
s#12	EMSC-20160824_0000006	2016/08/24	A	6.0	32.9	2.4
s#13	EMSC-20160824_0000006	2016/08/24	C	6.0	45.7	2.6
s#14	HR-1990-0007	1990/11/27	A	5.5	56.9	1.2
s#15	ME-1979-0003	1979/04/15	C	6.9	143.7	1.7
s#16	EMSC-20161030_0000029	2016/10/30	B	6.6	30.9	2.3
s#17	TK-1999-0415	1999/11/12	A	7.3	30.3	1.2
s#18	TK-1999-0077	1999/08/17	C	7.6	96.8	1.6
s#19	EMSC-20160824_0000006	2016/08/24	D	6.0	45.5	1.2
s#20	GR-1999-0001	1999/09/07	E	5.9	263.4	1.4
s#21	TK-1999-0077	1999/08/17	B	7.6	90.8	1.3
s#22	EMSC-20161030_0000029	2016/10/30	B	6.6	44.3	1.1
s#23	AM-1988-0001	1988/12/07	C	6.7	36.2	1.8
s#24	GR-1988-0020	1988/10/16	C	-	40.4	0.8
s#25	TK-1999-0077	1999/08/17	C	7.6	80.7	1.2
s#26	GR-1993-0023	1993/06/13	C	5.3	58.5	0.4
s#27	IT-1984-0004	1984/05/07	B	5.9	63.8	1.2
s#28	EMSC-20161030_0000029	2016/10/30	C	6.6	31.0	1.1
s#29	TK-1999-0077	1999/08/17	B	7.6	42.8	1.4
s#30	EMSC-20161026_0000095	2016/10/26	B	5.9	39.1	1.2
s#31	EMSC-20161026_0000095	2016/10/26	C	5.9	51.4	1.5
s#32	EMSC-20161026_0000095	2016/10/26	B	5.9	35.2	1.1
s#33	EMSC-20161026_0000095	2016/10/26	B	5.9	33.3	0.9
s#34	ME-1979-0012	1979/05/24	B	6.2	33.3	2.6
s#35	TK-2002-0008	2002/02/03	C	6.5	64.7	0.9
s#36	GR-1997-0019	1997/11/18	C	6.4	38.3	1.2
s#37	TK-1998-0063	1998/06/27	B	6.2	64.8	1.3

Appendix A

s#38	GR-1997-0014	1997/10/13	A	6.5	51.4	1.2
s#39	EMSC-20120610_0000062	2012/06/10	B	5.8	124.2	1.4
s#40	IT-1980-0012	1980/11/23	B	6.9	47.1	1.4
s#41	EMSC-20130108_0000044	2013/01/08	C	5.8	116.2	1.7
s#42	GR-1981-0003	1981/03/10	C	5.4	60.7	0.5
s#43	EMSC-20161026_0000077	2016/10/26	B	5.5	30.0	0.9
s#44	IT-1978-0004	1978/04/15	C	6.0	33.0	1.3
s#45	MK-1994-0004	1994/09/01	B	6.1	47.6	0.8

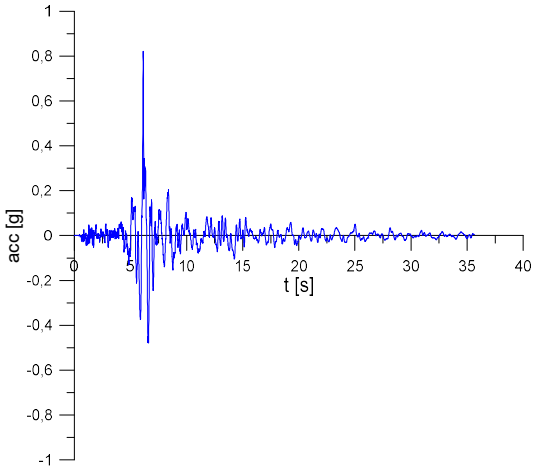

Figure Appendix.A- 1 s#1_TK-1999-0415

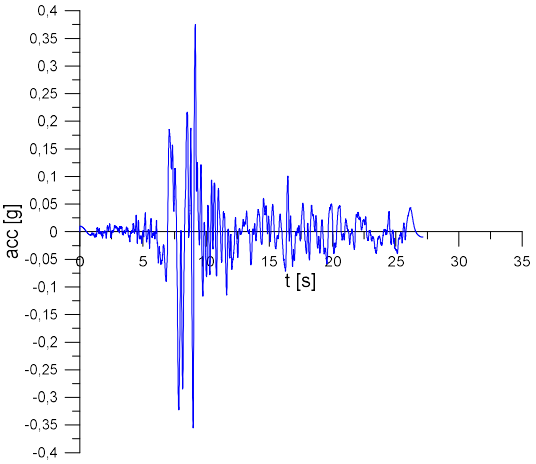

Figure Appendix.A- 2 s#2_TK-1999-0077

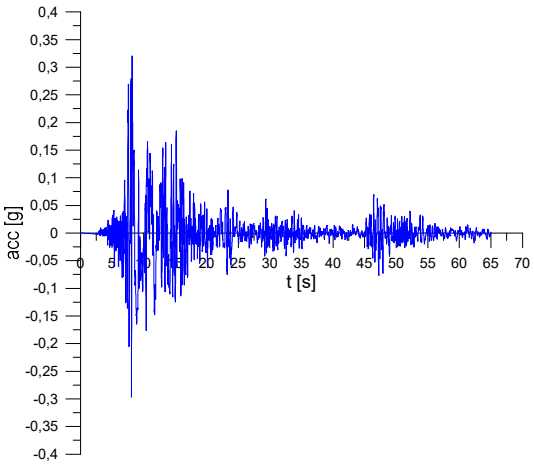

Figure Appendix.A- 3 s#3_IT-1980-0012

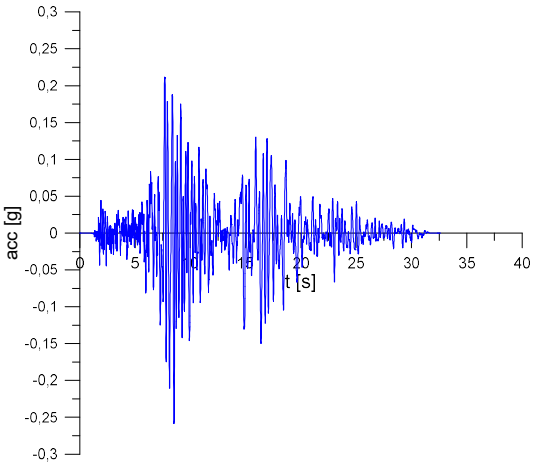

Figure Appendix.A- 4 s#4_TK-1999-0415

Appendix A

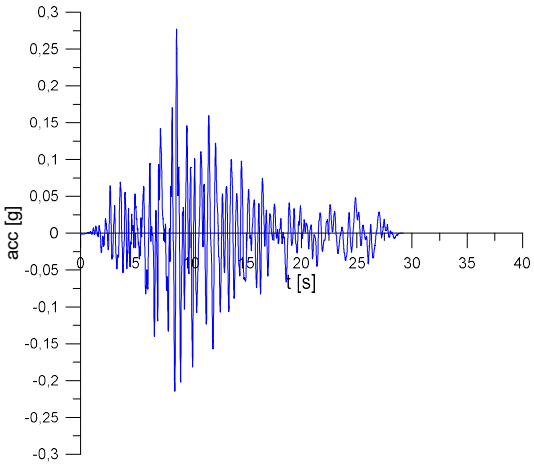

Figure Appendix.A- 5 s#5_TK-1998-0063

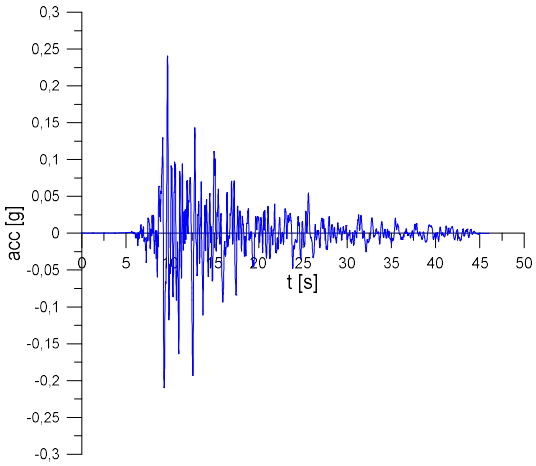

Figure Appendix.A- 6 s#6_GR-1981-0001

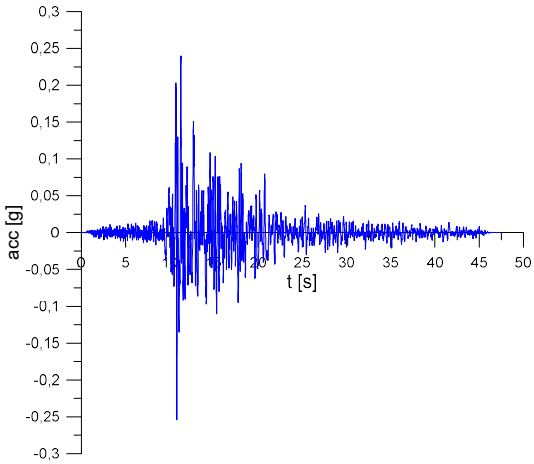

Figure Appendix.A- 7 s#7_ME-1979-0003

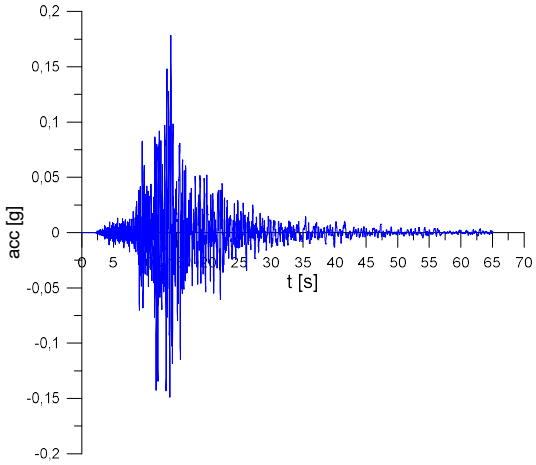

Figure Appendix.A- 8 s#8_EMSC-20161030_0000029

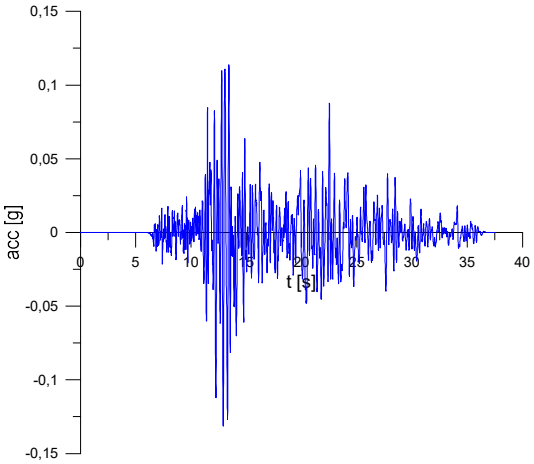

Figure Appendix.A- 9 s#9_TK-1999-0415

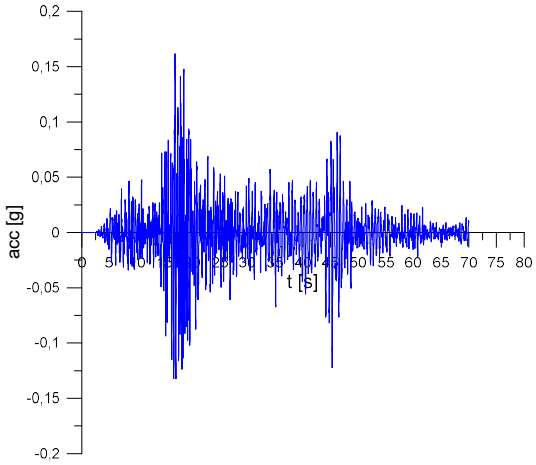

Figure Appendix.A- 10 s#10_TK-1999-0077

Appendix A

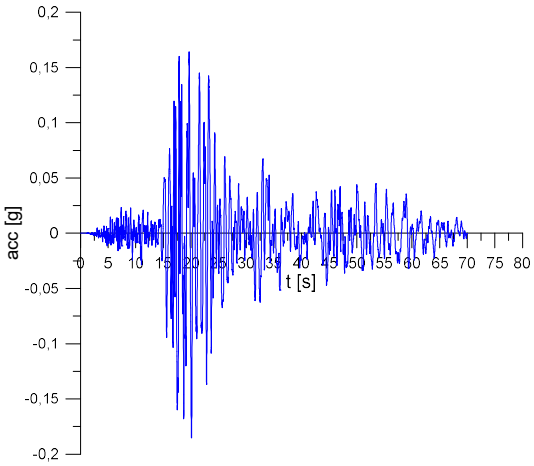

Figure Appendix.A- 11 s#11_TK-1999-0077

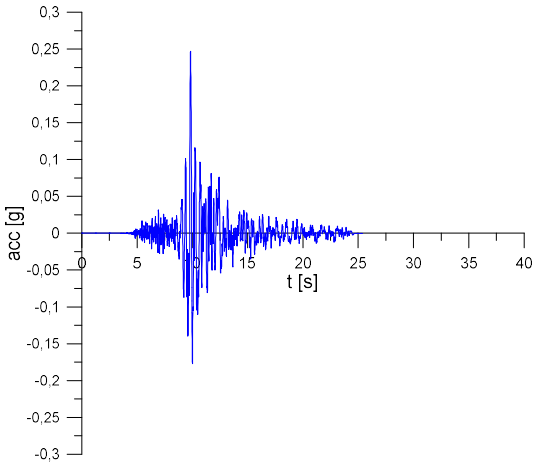

Figure Appendix.A- 12 s#12_EMSC-20160824_0000006

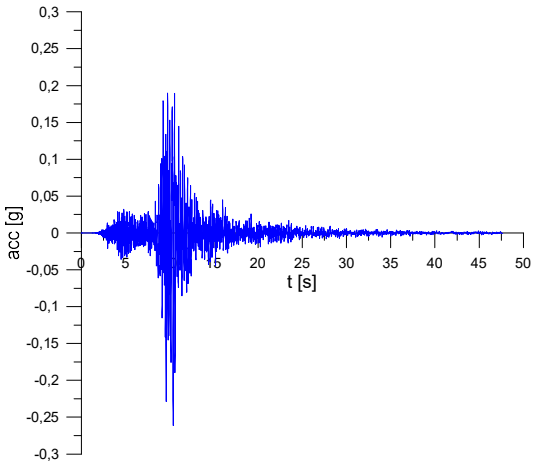

Figure Appendix.A- 13 s#13_EMSC-20160824_0000006

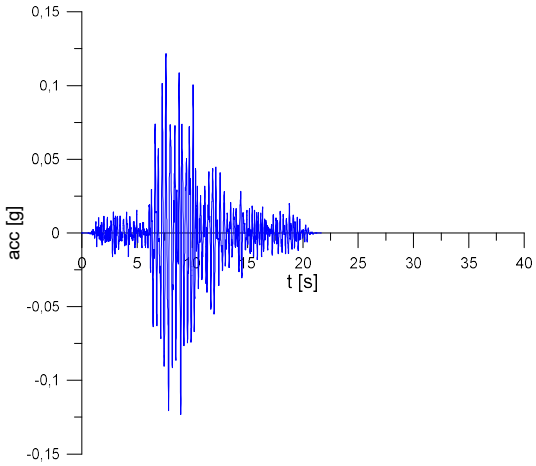

Figure Appendix.A- 14 s#14_HR-1990-0007

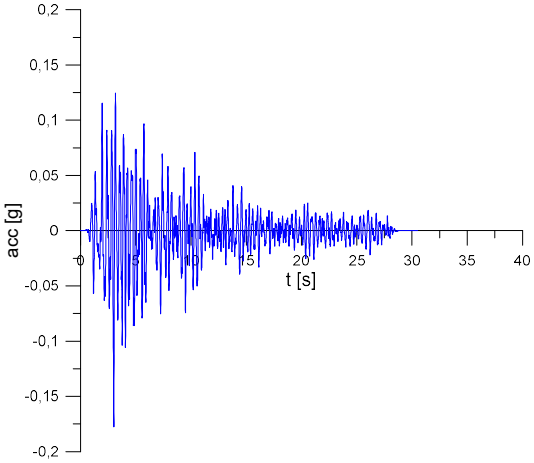

Figure Appendix.A- 15 s#15_ME-1979-0003

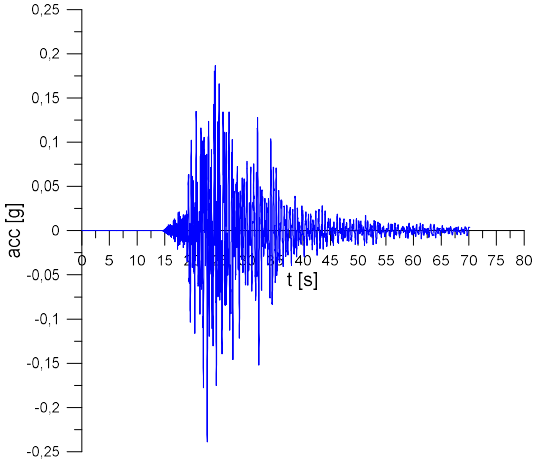

Figure Appendix.A- 16 s#16_EMSC-20161030_0000029

Appendix A

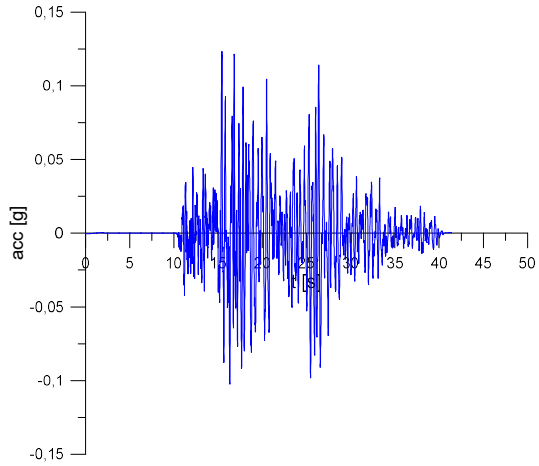

Figure Appendix.A- 17 s#17_TK-1999-0415

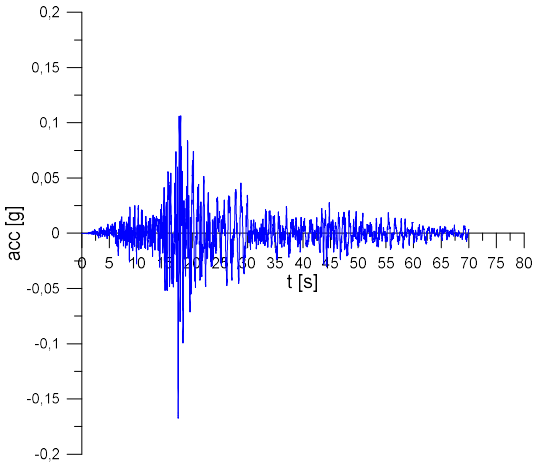

Figure Appendix.A- 18 s#18_TK-1999-0077

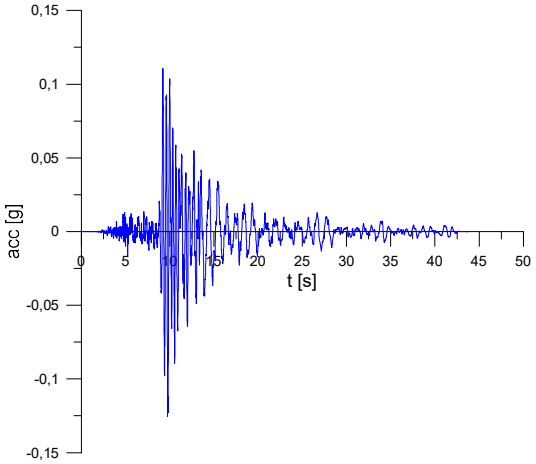

Figure Appendix.A- 19 s#19_EMSC-20160824_0000006

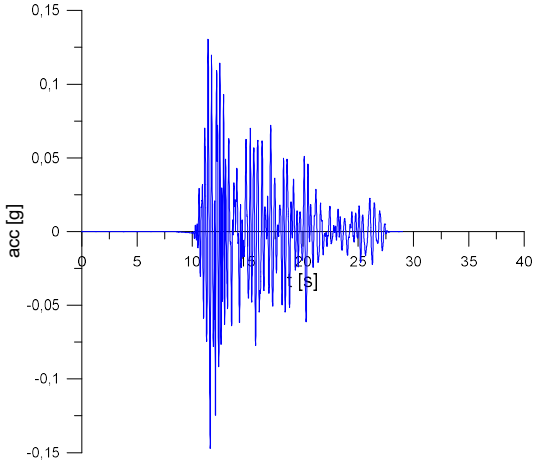

Figure Appendix.A- 20 s#20_GR-1999-0001

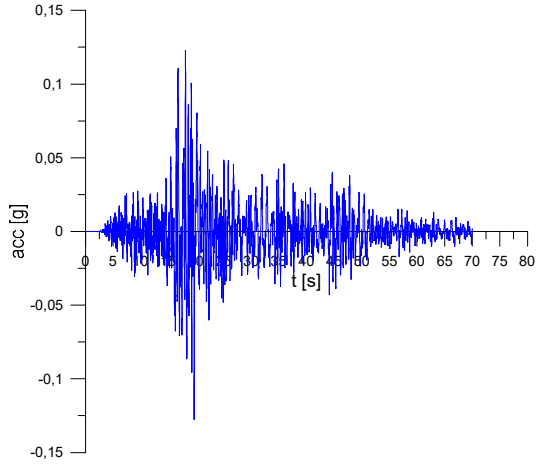

Figure Appendix.A- 21 s#21_TK-1999-0077

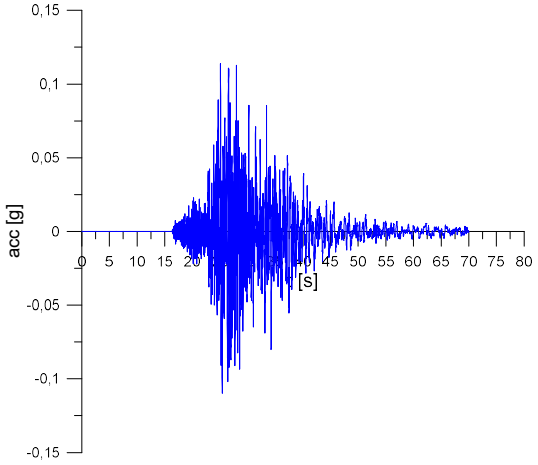

Figure Appendix.A- 22 s#22_EMSC-20161030_0000029

Appendix A

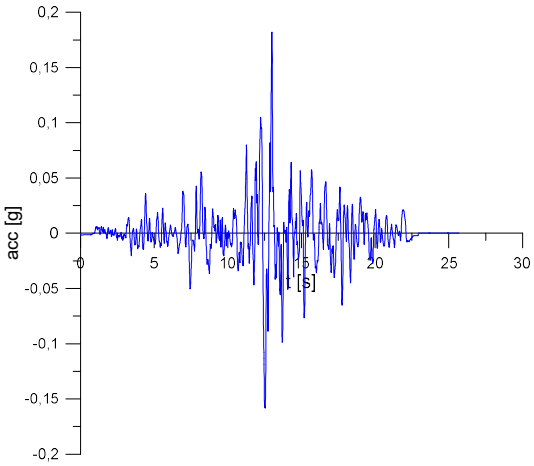

Figure Appendix.A- 23 s#23_AM-1988-0001

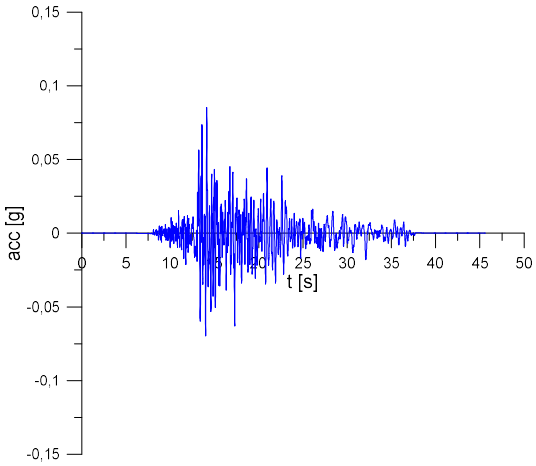

Figure Appendix.A- 24 s#24_GR-1988-0020

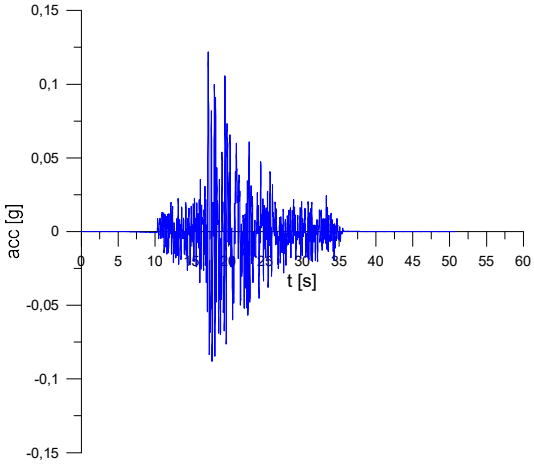

Figure Appendix.A- 25 s#25_TK-1999-0077

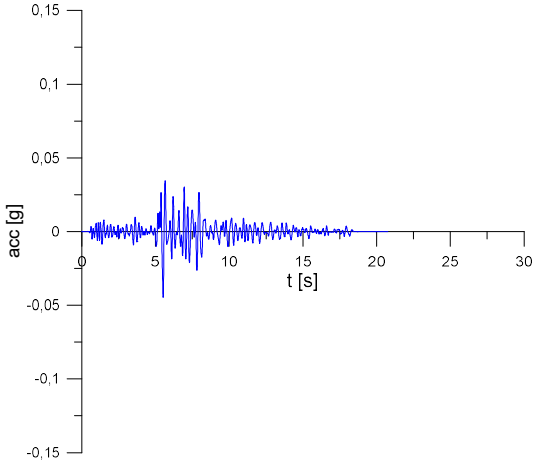

Figure Appendix.A- 26 s#26_GR-1993-0023

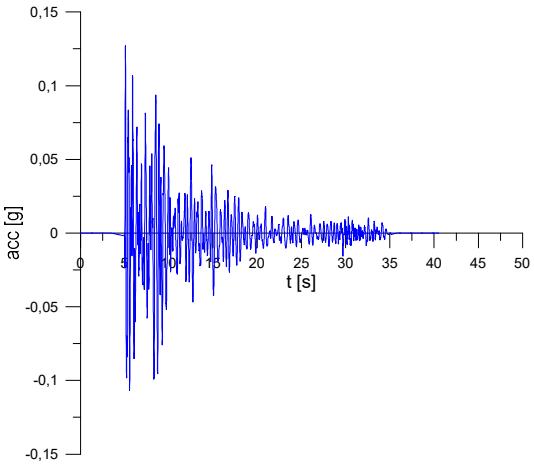

Figure Appendix.A- 27 s#27_IT-1984-0004

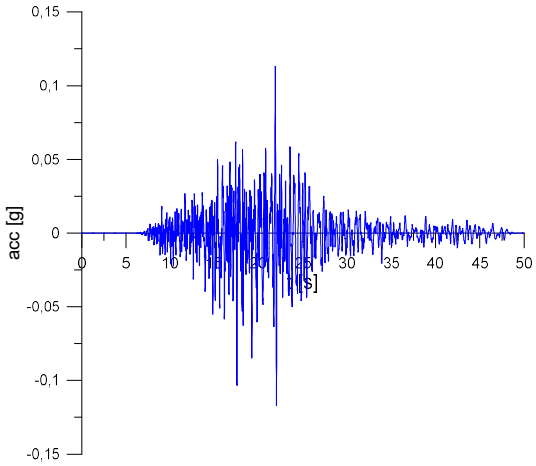

Figure Appendix.A- 28 s#28_EMSC-20161030_0000029

Appendix A

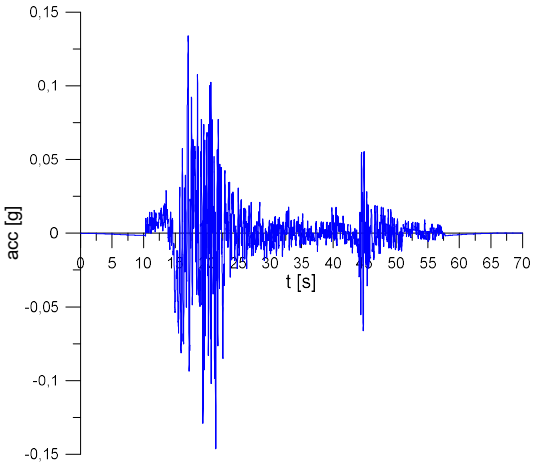

Figure Appendix.A- 29 s#29_TK-1999-0077

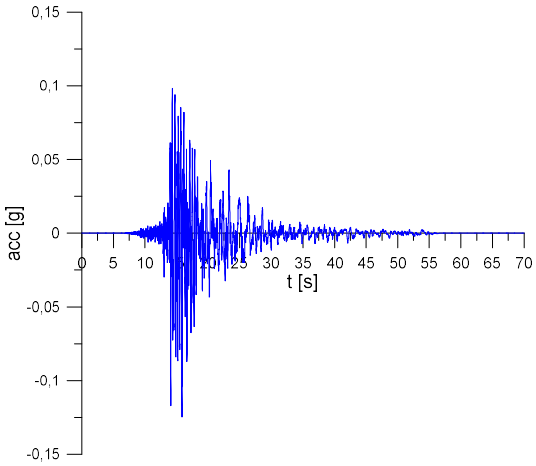

Figure Appendix.A- 30 s#30_EMSC-20161026_0000095

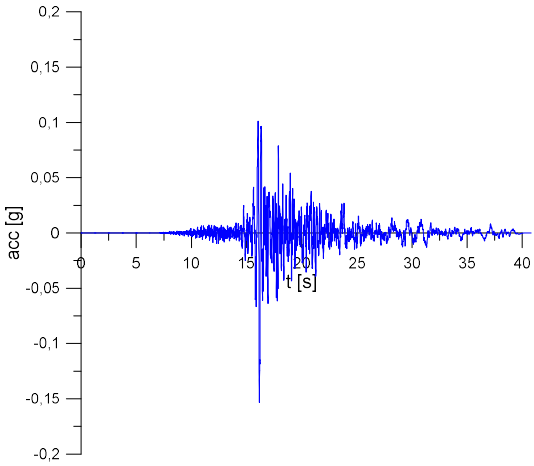

Figure Appendix.A- 31 s#31_EMSC-20161026_0000095

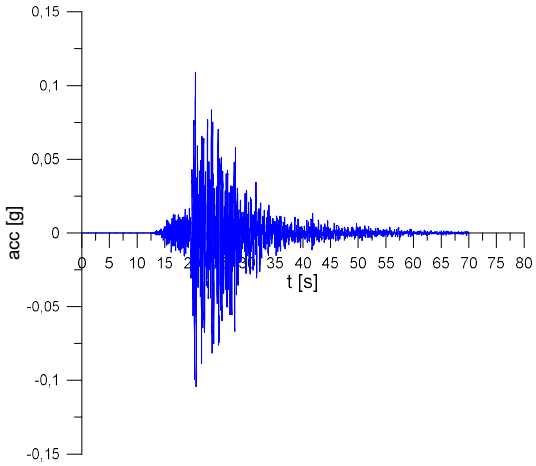

Figure Appendix.A- 32 s#32_EMSC-20161026_0000095

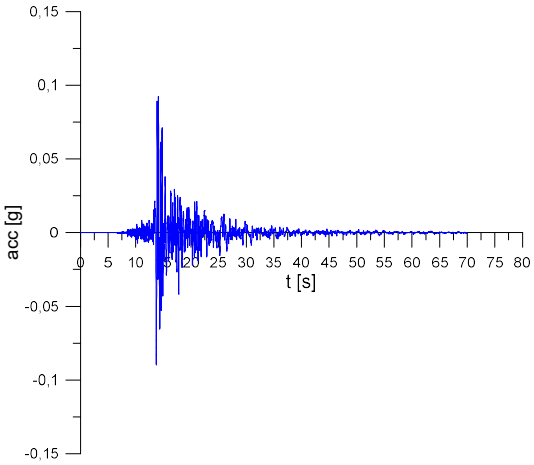

Figure Appendix.A- 33 s#33_EMSC-20161026_0000095

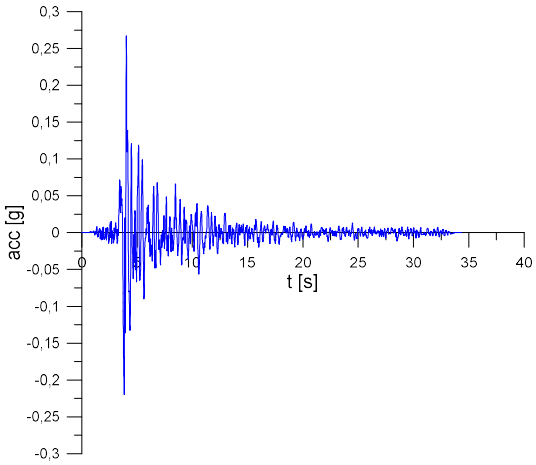

Figure Appendix.A- 34 s#34_ME-1979-0012

Appendix A

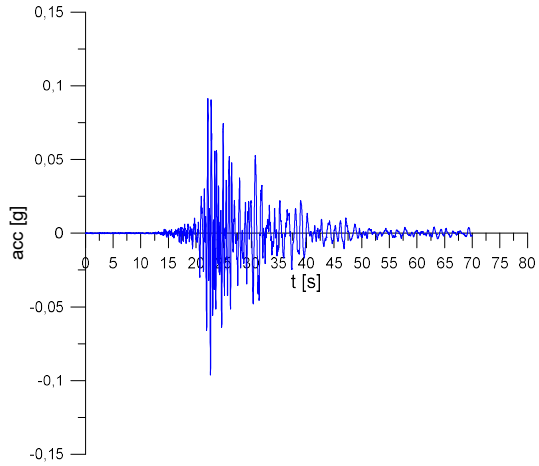

Figure Appendix.A- 35 s#35_TK-2002-0008

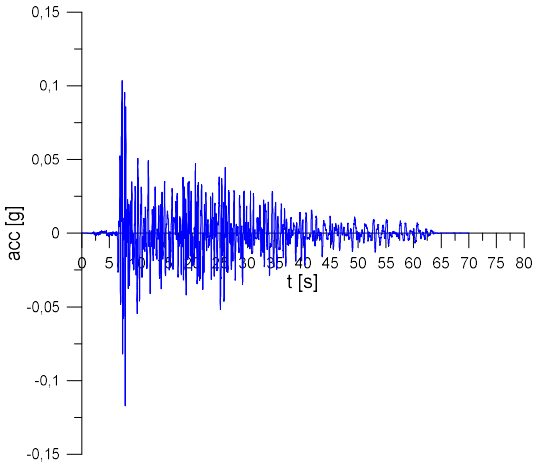

Figure Appendix.A- 36 s#36_GR-1997-0019

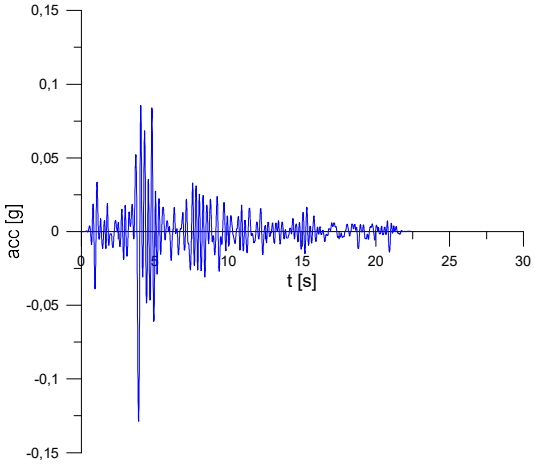

Figure Appendix.A- 37 s#37_TK-1998-0063

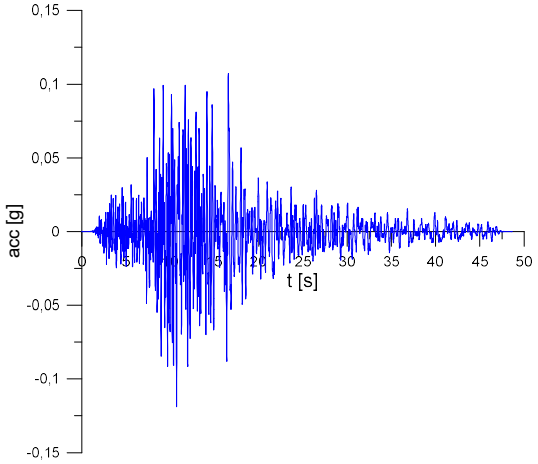

Figure Appendix.A- 38 s#38_GR-1997-0014

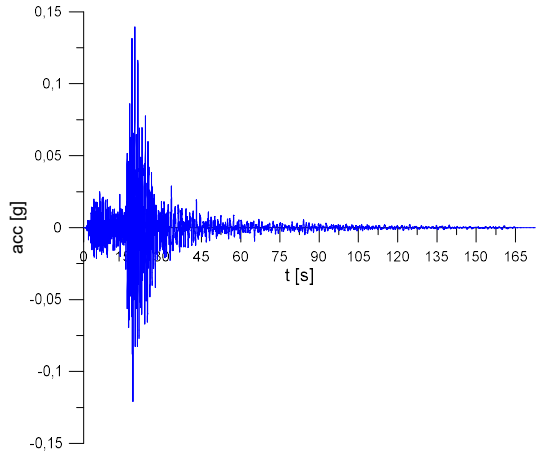

Figure Appendix.A- 39 s#39_EMSC-20120610_0000062

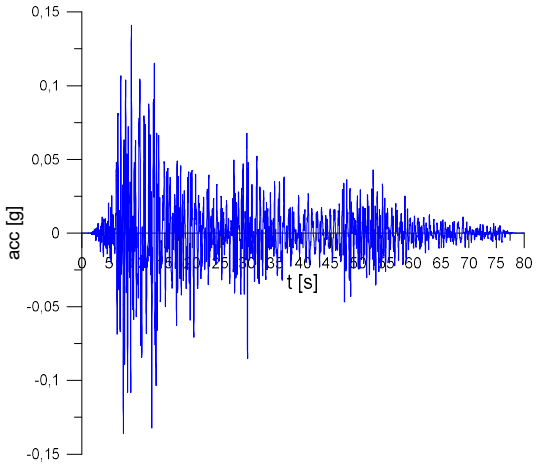

Figure Appendix.A- 40 s#40_IT-1980-0012

Appendix A

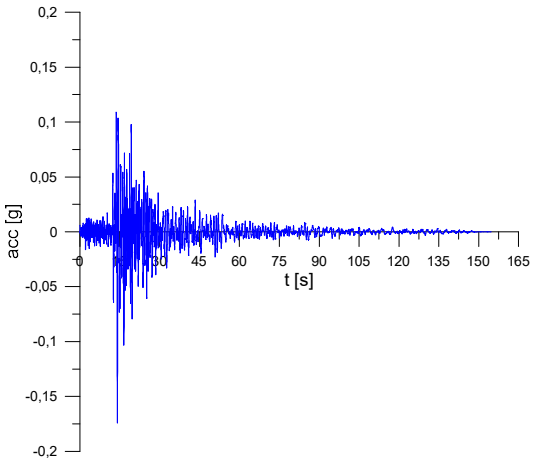

Figure Appendix.A- 41 s#41_EMSC-20130108_0000044

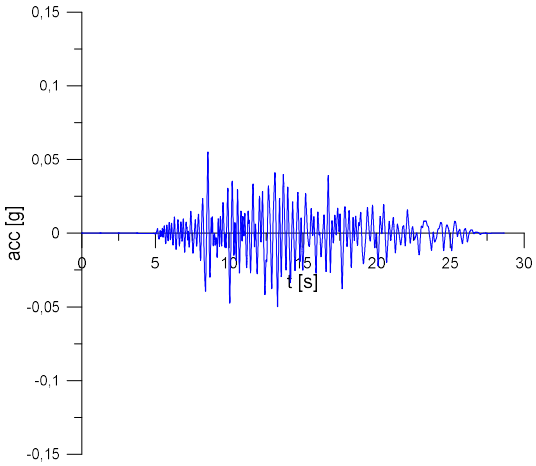

Figure Appendix.A- 42 s#42_GR-1981-0003

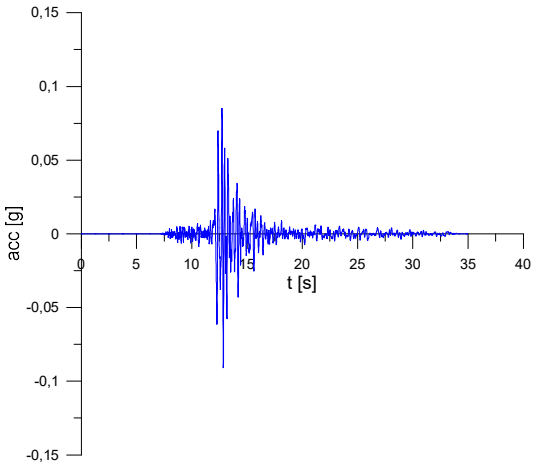

Figure Appendix.A- 43 s#43_EMSC-20161026_0000077

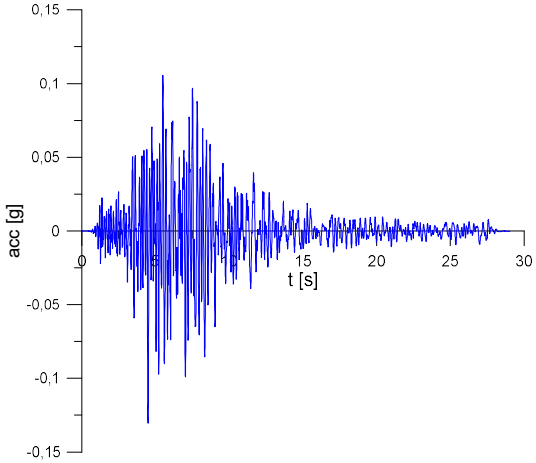

Figure Appendix.A- 44 s#44_IT-1978-0004

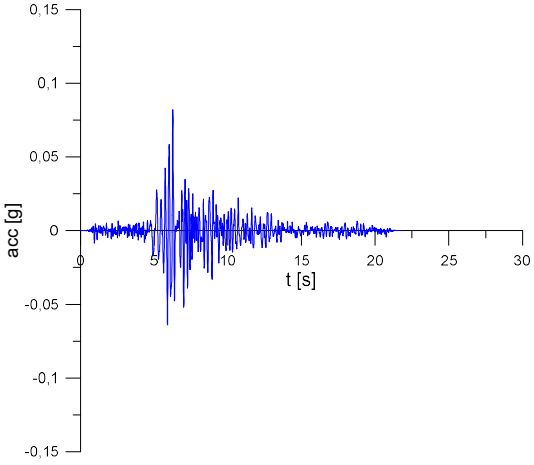

Figure Appendix.A- 45 s#45_MK-1994-0004